UNIVERSIDADE ESTADUAL DE CAMPINAS
Faculdade de Engenharia Elétrica e de Computação

Jhair Stivel Acosta Sarmiento

Optimization of overhead transmission lines with multiple circuits at different voltage levels on the same tower

Otimização de linhas de transmissão aéreas com vários circuitos em diferentes níveis de tensão na mesma torre

Campinas

2021

Jhair Stivel Acosta Sarmiento

Optimization of overhead transmission lines with multiple circuits at different voltage levels on the same tower

Otimização de linhas de transmissão aéreas com vários circuitos em diferentes níveis de tensão na mesma torre

Thesis presented to the School of Electrical and Computing Engineering of the University of Campinas in partial fulfillment of the requirements for the degree of Doctor in Electrical Engineering, in the area of Electrical Energy.

Tese apresentada à Faculdade de Engenharia Elétrica e de Computação da Universidade Estadual de Campinas como parte dos requisitos exigidos para a obtenção do título de Doutor em Engenharia Elétrica, na Área de Energia Elétrica.

Supervisor: Prof. Dr. Maria Cristina Dias Tavares

Este trabalho corresponde à versão final da tese defendida pelo aluno Jhair Stivel Acosta Sarmiento e orientada pela Profa. Dra. Maria Cristina Dias Tavares

Campinas

2021

Ficha catalográfica
Universidade Estadual de Campinas
Biblioteca da Área de Engenharia e Arquitetura
Rose Meire da Silva - CRB 8/5974

Ac72o

Acosta Sarmiento, Jhair Stivel, 1990-
Optimization of overhead transmission lines with multiple circuits at different voltage levels on the same tower / Jhair Stivel Acosta Sarmiento. – Campinas, SP : [s.n.], 2021.

Orientador: Maria Cristina Dias Tavares.
Tese (doutorado) – Universidade Estadual de Campinas, Faculdade de Engenharia Elétrica e de Computação.

1. Otimização multiobjetivo. 2. Linhas elétricas aéreas - Transmissão. 3. Computação evolutiva. 4. Transitórios (Eletricidade). 5. Arco elétrico. I. Tavares, Maria Cristina Dias, 1962-. II. Universidade Estadual de Campinas. Faculdade de Engenharia Elétrica e de Computação. III. Título.

Informações para Biblioteca Digital

Título em outro idioma: Otimização de linhas de transmissão aéreas com vários circuitos em diferentes níveis de tensão na mesma torre
Palavras-chave em inglês:
Multiobjective optimization
Overhead power lines - Transmission
Evolutionary computing
Transients (Electricity)
Electric arc
Área de concentração: Energia Elétrica
Titulação: Doutor em Engenharia Elétrica
Banca examinadora:
Maria Cristina Dias Tavares [Orientador]
Maria Teresa Nunes Padilha de Castro Correia de Barros
Aniruddha Madhukar Gole
Fernando Augusto Moreira
Marco Aurélio de Oliveira Schroeder
Data de defesa: 24-02-2021
Programa de Pós-Graduação: Engenharia Elétrica

Identificação e informações acadêmicas do(a) aluno(a)
- ORCID do autor: https://orcid.org/0000-0002-0345-998X
- Currículo Lattes do autor: http://lattes.cnpq.br/6143987038747533

COMISSÃO JULGADORA - TESE DE DOUTORADO

Candidato: Jhair Stivel Acosta Sarmiento. RA: 153771
Data de defensa: 24 de Fevereiro de 2021
Titulo da Tese: Optimization of overhead transmission lines with multiple circuits at different voltage levels on the same tower.

Profa. Dra. Maria Cristina Dias Tavares (Presidente)
Profa. Dra. Maria Teresa Nunes Padilha de Castro Correia de Barros
Prof. Dr. Aniruddha Madhukar Gole
Prof. Dr. Fernando Augusto Moreira
Prof. Dr. Marco Aurélio de Oliveira Schroeder

A Ata de Defesa, com as respectivas assinaturas dos membros da Comissão Julgadora, encontra-se no SIGA (Sistema de Fluxo de Dissertação/Tese) e na Secretaria de Pós-Graduação da Faculdade de Engenharia Elétrica e de Computação.

I would like to dedicate this work to my family, wife and friends.

Acknowledgements

There are many people that deserve my acknowledgment for helping me in some way to complete this research and face this process. Without their help it would be more difficult complete my goals.

First, I would like to thank to my family. In spite of being far away, they were always concerned about my welfare and happiness. They were with me whenever I needed.

Certainly, I would like thank to my beloved wife, Katherine Romero. She was also my friend, support and partner in many hard and happy moments. Thank you to give me love, happiness and peace. Without you this process would be lonely and harder.

Third, I want to thank to my supervisor Maria Cristina Tavares. Her support was really valuable. Without her certainly I would not be in this point. She is the person who allowed me to begin and complete this dream since 2014, when I started my Master studies, until now that I am finishing my D.Sc.. Thank you very much for allowing me to be here and evolve as professional and as human being.

Fourth, I want to thank all my friends and laboratory partners. Many of you have contributed in my life and/or in my research. I wish to give special thanks to Sebastian because he was always concerned about my welfare and helped me every time that I needed. Also I wish to thank specifically to Javier and Ozenir who help me to solve several doubts and advance in my research.

Fifth, I want to acknowledge Prof. Aniruddha Gole from University of Manitoba. He guided during my research in Canada, and we have interesting conversations that helped me to improve the research.

Sixth, I want to thanks my friends in Canada, Massimo, Ishan and Ajinkya who helped me to overcome the fact of being far away from my family.

Finally, I wish to thank the Brazilian Institutions CAPES, CNPq and the São Paulo Research Foundation (FAPESP) for supporting my research and helping me to disclosure the results. Thanks to the financial support, this research and my internship abroad was possible.

This study was financed in part by the Coordenação de Aperfeiçoamento de Pessoal de Nível Superior – Brasil (CAPES) - Finance Code 001. This study was financed in part by the São Paulo Research Foundation (FAPESP), grant #2015/26096-0 and #2019/16263-7. Note that the opinions, hypotheses and conclusions or recommendations expressed in this material are the responsibility of the author(s) and do not necessarily reflect the vision of FAPESP.

"We keep moving forward, opening new doors, and doing new things, because we're curious and curiosity keeps leading us down new paths."

(Walt Disney)

Abstract

Multi-circuit lines are a good way to increase the transmitted power using a lesser or similar right of way (ROW) than single-circuit parallel transmission lines. Although double-circuit and multi-circuit transmission lines have been used over the last years, there are few studies about non-conventional multi-circuit multi-voltage transmission lines. Thus, in the present research, it is proposed a mathematical model to increase the surge impedance loading (SIL) level of each circuit, and reduce the total costs, ROW, and height of the towers, by optimizing the tower characteristics through evolutionary computing.

The model is solved with two approaches: The weighted sum method and a modified version of the Non-dominated Sorting Genetic Algorithm II (NSGA-II). As a result, it were obtained several non-conventional multi-circuit transmission lines with single, double, triple, and quadruple circuits with an overall improvement in the range of 66 to 152% computing all objectives.

After initial results, it was observed that the phase sequence of each circuit in the tower has an important impact on the electric field of the transmission lines, and therefore, in the tower ROW and height. With this optimization, the overall objective function value sum was increased in the best of the cases by almost 30%, because of the additional ROW and height reduction.

Regarding the transient behavior, it was observed that each circuit disturbs the others during switching or faults in their own circuits. However, with the addition of the phase sequence optimization, it was observed a reduction in the overvoltage level.

Later, neutral reactors schemes were also optimized, aiming to have a successful single-phase auto-reclosing (SPAR). As a result, reductions of up-to 50% in the arc extinction time were achieved.

The final part of this research included the secondary arc current (SAC) minimization as a constraint in the mathematical model related to the optimization of the multi-circuit lines. As a result, new optimized transmission lines ready to perform SPAR were achieved. These lines, present SACs with up-to 61% faster arc extinction times.

Finally, since the transmission lines satisfy all constraints and have up-to 88% lower ROW than conventional lines, we considered that they are good options to implement in actual transmission line projects that have to deal with severe environmental restrictions.

Keywords: Multi-objective optimization; multi-circuit transmission lines; multi-voltage transmission lines; secondary arc; transient response.

Resumo

Os circuitos múltiplos são uma boa maneira de aumentar a potência transmitida nas linhas usando a uma faixa de servidão (ROW) menor ou similar às de linhas de transmissão paralelas de circuito simples. Embora as linhas de transmissão de circuito duplo e circuito múltiplo tenham sido usadas nos últimos anos, existem poucos estudos sobre linhas de transmissão não convencionais em múltiplos circuitos com diferentes níveis de tensão (multi-tensão).

Assim, nesta pesquisa foi proposto um modelo matemático para aumentar a potência característica (SIL) de cada circuito, e reduzir os custos totais, ROW e altura das torres, otimizando a geometria dos feixes através da computação evolutiva.

A otimização foi feita usando duas abordagens: O método da soma ponderada e uma versão modificada do Algoritmo Genético de Ordenação Não Dominada II (NSGA-II). Como resultado, foram obtidas várias linhas de transmissão não-convencionais com circuitos simples, duplos, triplos e quádruplos com uma melhoria geral na faixa de 66 a 152% ao somar todos os objetivos.

Após os resultados iniciais, observou-se que a sequência de fases de cada circuito na torre tem um impacto importante no campo elétrico no solo e, portanto, no ROW e na altura. Incluindo mais este parâmetro, o valor da soma das funções objetivos foi aumentado em quase 30% no melhor dos casos, devido à redução adicional do ROW e de altura da torre.

Em relação à resposta transitória, observou-se que os circuitos na mesma torre têm impacto sobre os demais durante manobras ou falhas em seus próprios circuitos. No entanto, com a adição da otimização da sequência de fase, observou-se uma diminuição nas sobretensões.

Configurações diferentes de reatores de neutro foram otimizadas também, com o propósito de conseguir sucesso do religamento monopolar automático. Como resultado, reduções de até 50% no tempo de extinção do arco foram atingidas.

A parte final desta pesquisa incluiu a minimização da corrente de arco secundário como restrição no modelo matemático. Como resultado, as novas linhas de transmissão apresentam tempos de extinção de arco até 61% mais rápidos.

Finalmente, uma vez que as linhas de transmissão satisfazem todas as restrições e têm ROW até 88% menor do que as linhas convencionais, elas podem ser consideradas boas opções para serem implementadas nos novos projetos de linhas de transmissão.

Palavras-chaves: Otimização multi-objetivo; linhas de transmissão multi-circuito; circuitos multi-tensão; arco secundário; resposta transitória.

List of Figures

List of Tables

Contents

1 Introduction

1.1 Motivation and importance of the research

The increasing of the power demand and the necessity of an efficient use of the land has led the attention of the researchers towards alternatives to transmit more power in narrow spaces. In some cases, the legal and environmental requirements for obtaining the rights-of-ways (ROW) can be so high that it could result in an extremely large time delay. Thus, one of the alternatives is the use of compact transmission lines with modified bundle geometries. The special bundle configuration allows to increase the capacitance of the line and therefore its power capacity, also known as Surge Impedance Loading (SIL). The lines with increased capacity are know as High SIL lines (HSIL).

The second alternative is the use of more than one circuit in the same tower. These towers, known as multi-circuit transmission lines, considerably reduce the right of way (ROW) and increase the power capacity. Furthermore, more than one utility could share the same tower, leading to the possibility of having more than one voltage level at the same tower. These lines, known as multi-circuit multi-voltage transmission lines, attracted attention of the research community in recent years, and some of them have been built in real projects. A detailed review of HSIL, multi-circuit lines, and multi-circuit multi-voltage transmission lines is presented in chapter 2.

As a third alternative, a combined solution of the alternatives 1 and 2, have been proposed in this research. Thus, the proposed solution is to use multi-circuit multi-voltage transmission lines with increased power capacity. However, as any project, the economical part is important, being necessary to find a good trade-off between the costs of the project and other objectives.

To obtain the desired transmission lines, the problem was modeled as an optimization problem, looking for the increasing of the power capacity (SIL), while reducing the cost, right of way and height of the tower. Also, several electrical and mechanical constraints were considered. The mathematical model that formalizes the optimization problem is presented in chapter 4. It involves the solution of a complex mixed-integer non-linear mathematical problem.

In the literature there are different techniques to solve optimization problems. They can be classified mainly in two big groups: classical optimization and heuristic optimization. In classical optimization it is necessary to have a complete mathematical model of the problem, including all decision variables on the objective function. However,

in some cases the mathematical model does not exist, is not derivable, or is too complex to compute with classical techniques. In these cases, the heuristics techniques are a good optimization option, because they do not need that a complete mathematical model of the problem exists.

To solve the proposed mathematical model, algorithms based on evolutionary computing were used. The most popular are the population techniques as genetic algorithms (GA), evolutionary algorithms (EA), genetic programming, evolutionary programming, among others. The bases of these kind of algorithms are presented in chapter 3. Currently, GAs and EAs are used combining some of their features. Therefore, in this research the term GA and EA are used without distinction. Although the heuristics algorithms do not ensure obtaining the global optimal, the advantage is that they allow to solve complex problems in tractable times and do not require a continuous and derivable mathematical function.

Initially, the optimization was solved as a mono-objective problem using a genetic algorithm and the weighted sum approach, i.e., the objectives were normalized, then, a weight was assigned to each objective, and finally the value of each objective was added. Later, the problem was solved as a multi-objective problem, using the Non dominated sorting genetic algorithm (NSGA-II). With the NSGA-II, Pareto optimal solutions were identified. Since the problem is complex, non-linear and the selected evolutionary methods require dealing with populations of solutions, parallel computing was used to decrease the processing time. Both algorithms were coded from scratch in the programming language *Matlab*.

The advantage of the NSGA-II over the GA is that it allows to obtain the Pareto solutions in a single execution, whereas to achieve the same result with the GA multiple runs with different weight for the objectives should be used. The algorithms description and analyses are presented in chapter 5, whereas the results of the optimization processes are in chapter 6. Optimized transmission lines up-to 152% better than conventional parallel single-circuit transmission lines were obtained.

To be able to use the optimized transmission lines in actual projects it was necessary to characterize the lines for different operation conditions. From the steady state characterization of the electromagnetic environment[1], presented in chapter 7, it was identified that the phase sequence/arrangement have an important influence on the electric field. Hence, the phase sequence can modify the electric field on the surface of the sub-conductors and under the line. As a result, the height of the tower and the right of way can be controlled (changed) with the correct phase arrangement.

[1] The characterization was done solving the mathematical equations related to the electric field, and validated via simulation in *COMSOL Multiphysics*.

Accordingly, it was decided to introduce the phase sequence in the optimization model. It was included in chapter 8. The inclusion of the phase sequence transformed the problem into a mixed-integer non-linear optimization problem inside a permutation based space, increasing the complexity of the problem. However, significant improvements were achieved. The new lines, with optimized phase sequence, showed results up-to 30% better than when the optimization was done without considering the phase sequence. The main reason of the increment of the objective function value was the reduction of the right of way and tower height.

Continuing with the characterization of the new transmission lines under different operative conditions, transient studies in *PSCAD*[2] were performed. The studies are available in chapter 9. Different scenarios such as line energization, load rejection, and faults were investigated. The results showed that the overvoltages are more severe in the proposed lines than in single circuit lines. The reason is the proximity of the circuits and the high coupling capacitance, result of increasing the power capacity. However, the phase sequence also showed a positive influence, helping to reduce the overvoltages to some extent. The results presented during these analyses evidenced the necessity of a further study of the protection system. However, it was not performed during this research, being considered for future works.

Additionally, in lines with multiple-circuits and multiple-voltages it is very important to maintain the power flow most of the time, because the interruption of the power flow could yield important economical losses. Therefore, techniques like the single-phase auto-reclosing (SPAR), which allows maintaining most of the power flow during transient single-phase faults, are very useful. Accordingly, alternatives to obtain a feasible SPAR in the optimized lines were investigated. Initially, in chapter 10, different schemes for neutral reactors were proposed. Since there are no mathematical models to select the parameters of the proposed neutral reactors, and the conventional four-legged reactor design does not consider the coupling between circuits, the parameters of the reactors were obtained through optimization. As a result, it was evidenced that all the neutral reactor schemes using optimal parameters can reduce the secondary arc currents (SAC) in the multi-circuit transmission lines to similar values. Therefore, even with the four-legged reactor it is possible to reduce the SAC as long as the values of the reactor parameters are optimized. The results of the optimization of the neutral reactors showed SACs with up-to 68% lower values than when using the reactor parameters calculated with conventional formulas.

The final part of this research, presented in chapter 11, considered the design of optimized transmission lines with high probability of success of the SPAR. To achieve

[2] All *PSCAD* simulations were automated with *Python* through the *PSCAD automation library*.

these lines, the SAC was included in the mathematical model as a constraint. As a result, new lines with high probability of SPAR success were obtained. The transmission lines obtained with this method not only improves the SIL, costs, ROW, and tower height, but also presented SAC extinction times up-to 61% faster than the optimized lines obtained without consider the SAC during the optimization process.

As a result of the research project, some articles in journals and congress were published. Also, a patent request was deposited and a program developed in *C#* was registered at the INPI (Brazilian Institute of Industrial Patents). The language C# was chosen to achieve a C like speed and have an user friendly interface, without much difficulty.

1.2 Objectives

This research was developed to achieve the following objectives.

1.2.1 General Objective

Develops a methodology that allows obtaining optimal transmission lines with multiple circuits operating at the same or different voltage level at the same tower.

1.2.2 Specific objectives

1. Reduce the environmental impact of new overhead transmission line projects by proposing compact towers with optimized bundles and multiple circuits on the same tower.

2. Develop a clear methodology to increase the overhead transmission line capacity of lines with several circuits and same or different voltage levels at the same tower.

3. Characterize the electromagnetic and transient behavior of circuits sharing the same tower.

4. Propose feasible overhead transmission lines configuration different from those presented in previous researches.

5. Make the designed transmission lines feasible under different electrical conditions.

1.3 Research contributions

The main contributions of this research are summarized in the following list:

- A mathematical model to properly formalize the optimization problem associated with multi-circuit multi-voltage transmission lines.
- A methodology to optimize multi-circuit transmission lines using evolutionary computing.
- A model able to optimize the individual position, number and type of conductors in multi-circuit lines, producing geometries of any type and not restricted to specific geometries as in other researches.
- New optimized multi-circuit transmission lines different from previous literature, presenting good values related to each one of the objective functions.
- An algorithm easily scalable to optimize transmission lines up-to four circuits at different voltage levels.
- A multi-objective approach to the optimization problem to help in the a posteriori decision making process through Pareto Fronts and parallel coordinated plots.
- Optimization of the phase sequence in multi-circuit transmission lines, which yield further ROW reductions and SIL increments.
- Optimization of neutral reactors to reduce the secondary arc current in multi-circuit transmission lines.
- Optimized transmission lines ready to perform single-phase auto-reclosing (SPAR) with success.

1.4 Publications, patents and extra activities performed during the research

During the development of the research, some publications directly or indirectly linked to the main topic were done or are under development. In the next list you can see that the focus was the optimization of: single circuit transmission lines, multi-circuit transmission lines, allocation of fault indicators, positioning of shielding wires for rural electrification, and secondary arc mitigation.

- Journal articles published:
  - Acosta, J. S, Tavares, M.C. and Gole, A., "Neutral Reactor Structures for Improved Single Phase Auto Reclosing in Non-conventional Multi-circuit

Multi-voltage Transmission Lines.", In: IEEE Transactions on Power Delivery (Early Access), February 2021. DOI: 10.1109/TPWRD.2021.3059269.

- Acosta, J. S., and Tavares, M.C., "Optimal selection and positioning of conductors in multi-circuit overhead transmission lines using evolutionary computing". In :Electr. Power Syst. Volume 180, March 2020, 106174. DOI:10.1016/j.epsr.2019.106174.
- Acosta, J. S., and Tavares, M.C., "Multi-Objective optimization of overhead transmission lines including the phase sequence optimization", ELSEVIER, International Journal of Electrical Power & Energy Systems, Volume 115, February 2020, 105495. DOI: https://doi.org/10.1016/j.ijepes.2019.105495.
- Acosta, J. S., and Tavares, M.C., "Methodology for optimizing the capacity and costs of overhead transmission lines by modifying their bundle geometry", Volume 163, Part B, October 2018, Pages 668-677, Special Edition of Electric Power Systems Research ELSEVIER. DOI: 10.1016/j.epsr.2017.10.005.
- Chaves J. S., Acosta, J. S., and Tavares, M.C. "Optimal transmission line coupling generation system design for rural electrification". In: IEEE Transactions on Power Delivery (Early Access), August 2020. DOI: 10.1109/TPWRD.2020.3017376.
- Acosta, J. S. and Lopez, J. C. and Rider, M. J., "Optimal Multi-Scenario, Multi-Objective Allocation of Fault Indicators in Electrical Distribution Systems Using a Mixed-Integer Linear Programming Model", in IEEE Transactions on Smart Grid. Volume: 10 , Issue: 4 , July 2019. DOI: 10.1109/TSG.2018.2862905.

- Conferences articles published/presented by the author:

  - Pretti, F., Acosta, J. S., and Tavares, M.C., "Cálculo dos parâmetros do arco elétrico em sistemas de corrente contínua utilizando teoria de identificação de sistemas", Cong. Bras. Aut. (CBA), virtual, 2020.
  - Dias, O., Acosta, J. S., and Tavares, M.C., "Análise do Religamento Monopolar em Linhas de Transmissão Não Convencionais", Simp. Bras. Sist. Eletr. (SBSE), virtual, 2020.
  - Pereira, T., Santiago, J.A., Acosta, J. S., and Tavares, M.C., "Influence of Corona Effect on Severe Overvoltages due to Critical Fault on Half-Wavelength Transmission Line", Simp. Bras. Sist. Eletr. (SBSE), virtual, 2020.
  - Acosta, J. S., and Tavares, M.C., "Many-objective optimization of multi-circuit multi-voltage transmission lines with natural computing", poster presented at

the Deep Learning and Reinforcement Learning Summer School, July 24th to August 2nd, Edmonton, Alberta, Canada, 2019.

- Acosta, J. S., and Tavares, M.C., "Transient behaviour of non-conventional multi-circuit power lines with different voltages levels at the same tower", International Conference on Power Systems Transients - IPST 2019, Perpignan, France, June 16-20, 2019.
- Acosta, J. S., and Tavares, M.C., "Enhancement of overhead transmission line capacity through evolutionary computing", IEEE T&D PES Conference and Exposition Latin America, September 18-21 2018 in Lima, Peru, 2018.
- Acosta, J. S., and Tavares, M.C., "Optimization of high-voltage transmission lines by modifying the bundle geometry", VII Simpósio Brasileiro de Sistemas Elétricos (SBSE 2018), 12th-16th May 2018 in Niterói-RJ, Brazil, 2018.
- Acosta, J. S., and Tavares, M.C., "Transient Behavior of High Surge Impedance Loading Transmission Lines", in the 20th International Symposium on High Voltage Engineering, Buenos Aires, Argentina, August 27 – September 01, 2017.

- Articles submitted to journals:
  - Acosta, J. S, Tavares, M.C. and Gole, A., "Optimizing multi-circuit transmission lines for single-phase auto-reclosing", submitted to ELSEVIER Electric Power Systems Research (special edition of the IPST 2021), 2020.
  - Pretti, F., Acosta, J. S, and Tavares, M.C., "Parameter Estimation of DC Black Box Arc Models using Genetic Algorithms", submitted to ELSEVIER Electric Power Systems Research (special edition of the IPST 2021), 2020.

- Patents and computer programs:
  - Computer program registered at INPI (Brazilian Patent Agency): Collector Line Optimizer. Brazil, 2019. Register No. BR512020000597-7.
  - Patent deposited at INPI: Method for generating non-conventional geometries of transmission towers with multiple circuits at the same tower (in Portuguese). Brazil, 2019. Patent deposit No. BR 10 2019 027645 2.
  - Computer program registered at INPI: Multi-circuit Multi-voltage Transmission Line Optimizer. Brazil, 2019. Register No. BR512019002331-5.
  - Patent deposited at INPI: Method for increasing the power capacity in overhead transmission lines by modifying the bundle geometry (in Portuguese). Brazil, 2017. Patent deposit No. BR 10 2017 004723 7.

- Extra activities during the Phd:
  - Design of an optimized single-circuit transmission line for the company Voltalia. The goal was to increase the power capacity to reduce the size of the capacitive shunt compensation used for power factor correction.
  - Visiting scholar from 24/11/2019 to 02/09/2020 at the University of Manitoba, Winnipeg, Canada, through FAPESP BEPE program, supervised by Prof. Aniruddha Gole. The topic of the research was "Parallel simulation of electromagnetic transients and secondary arc mitigation in non-conventional multi-circuit multi-voltage transmission lines".

1.5 Thesis structure

This document is organized as follows.

In chapter 1 an introduction to the problem solved in this research is given.

In chapter 2, a brief overview of the methods to increase the transmission line capacity and reduce the ROW is presented. The basic characteristics of lines with increased power capacity and multi-circuit lines are also presented in this chapter.

In chapter 3, the definition of multi-objective optimization problems is given. Furthermore, heuristics techniques to solve this kind of problems are explained.

In chapter 4, the mathematical model that defines the optimization problem solved in this research is defined.

In chapter 5, the optimization methods used in this research are explained in detail.

In chapter 6, the resulting optimized transmission lines are presented.

In chapter 7, the electromagnetic behavior of the optimized transmission lines is performed.

In chapter 8, following the results of the previous chapter, the importance of the phase arrangements is evidenced and the lines are optimized considering the phase sequence of each circuit.

In chapter 9, a study of the transient behavior of some optimized transmission lines is presented.

In chapter 10, the secondary arc current (SAC) is investigated and neutral reactors alternatives are optimized for reducing the SAC.

In chapter 11, the SAC is included in the mathematical model and new transmission lines with adequate SAC levels are obtained.

In chapter 12, the conclusions are summarized and investigations for future works are proposed.

Finally, since this research uses parallel computing techniques, which are not well known in the power system area, an explanation of how to use parallel computing in PSCAD program is presented in the Appendix.

2 Developments on non-conventional transmission lines

With the continuous growing of population density, power demand, and environmental requirements, the transmission line projects should use the land in an efficient way. Through the history, some researches have focused their investigations in alternatives to solve this problem, finding two main approaches. The first one, is the use of non-conventional transmission lines, i.e., transmission lines with a non-conventional geometric configuration. The second one, is the use of more than one circuit in the same tower. Both approaches can effectively increase the power capacity of the transmission lines and have their own advantages and disadvantages. Thus, a brief overview of these alternatives are presented in this chapter. Also, the key aspects that define the non-conventional transmission lines and multi-circuit transmission lines are explained.

2.1 History of the alternatives to transmit more energy in the transmission lines

The first approach to transmit more energy in the transmission lines adopted the use of bundle conductors, i.e., more than one conductor per phase, increasing the positive sequence line shunt capacitance and decreasing the positive sequence line series inductance, and therefore, increasing the natural power of the line or Surge Impedance Loading (SIL) (THOMAS, 1909). Thus, more power could be transmitted using a very similar Right of Way (ROW). As related in (ABETTI, 1958) and (SANDELL *et al.*, 1963), the first investigations on bundle conductors used two to five conductors per phase, with bundles of 0.457 m in the American standards and 0.4 m in the European standards.

Later investigations proposed the use of transmission lines with closer phases (compact lines) and non-conventional bundles (ALEXANDROV; PODPORKYN, 1991). The SIL increasing in the former research considered limitations by the electric field on the surface of the conductors and the non-uniformity of the electric field distribution on the conductors. These investigations showed that the SIL in transmission lines between 35 kV to 200 kV lines can be increased using closer phases. According to the authors, the distance between phases can be maintained using insulator spacers in a span. Therefore, it will not yield insulation problems. They also showed that important SIL increments can be obtained with more sub-conductors, reporting an increment of 300 MVA in a 220 kV when using 5 sub-conductors instead of 2. Then, a mathematical analysis of the capacitance

of the transmission line allowed to conclude that an uniform charge distribution along the conductors could be obtained by stretching the outer phases' bundles and shrinking the inner phase bundle. This non-conventional bundle configuration allowed the authors to increase the SIL 4 times. However, the investigations in (ALEXANDROV; PODPORKYN, 1991) only considered circular bundles in transmission lines with flat configurations.

Based on the previous works several approaches to increase the SIL were developed. In (SALARI, 1993) the objective was to increase the SIL and maintain balance between the charge and current distribution on the sub-conductors inside predefined geometries such as circular and elliptic, resulting in a computer program named *OTLIN*, later known as *ELEKTRA*. The optimization, made with an heuristic method, included constraints related to the electric and magnetic fields under the transmission lines. Maximum SIL increments close to 60% were reported. However, the bundle sizes are considerable big ($>$ 2 m) yielding mechanical stress. Also, only phases in horizontal configuration were considered. In (Gomes Junior, 1995) the previous work was extended to also analyze bundles with vertical dispositions, but still with flat phases. In that research SIL increments of almost 20% were reported. However, bundles with more than 10 m were considered, which in practical situations are almost not feasible.

In (MACIEL, 2013) an approach using classical optimization with the gradient method was presented. In that research, the objective function was reduce the positive line reactance, which yielded SIL increments. As in the previous cases, only horizontal phases were optimized and bundles bigger than 2 m were considered. However, the location of the conductors is not fixed to circular shapes. It will depends on the direction given by the gradient. The major drawback of the research is that the optimization based on the gradient is extremely dependent of the initial point, so it is easy to be attracted by a local optimal.

Meanwhile, in (SARMIENTO; TAVARES, 2016) it was used an heuristic algorithm that yielded to geometries that do not followed any fixed form. In that research, the bundle size was limited to 1.5 m. Also, the position, type and number of conductors were optimized at the same time. The optimization was divided in two parts. The first one tries to obtain good initial solutions to avoid be attracted by a local optimal. The second one produces the optimized lines using as a starting point the initial conditions obtained in the first part.

The drawback of all the previous works was that they only considered the SIL increasing without taking into account other items as the cost. Therefore, in (ACOSTA; TAVARES, 2017) the methodology proposed in (SARMIENTO; TAVARES, 2016) was extended to a multi-objective problem, aiming to SIL increasing and cost reduction. The

multiple objectives were modeled as a mono-objective problem through the normalization of the individual objectives. The optimization yielded optimized transmission lines that not only had increased the SIL, but also minimized costs.

As a result of the researches in non-conventional lines, some high SIL (HSIL) lines are in operation in countries such as Brazil, United States, Russia and China. Some examples are a 230 kV HSIL transmission line in Recife, a 230 kV HSIL transmission line in Paulo Afonso, a 330 kV line in Russia and a 230 kV HSIL transmission line between in Banabuiú and Fortaleza. The power capacity of the HSIL line was 25% higher than a conventional line, saving millions of dollars per year because of the reductions in the power losses and in the towers' weight. In United States, the company BOLD has patented HSIL lines and has won several awards (KOEHLER *et al.*, 2016; GHASSEMI, 2019).

Another approach to make a better use of the land is the use of multi-circuit overhead power lines, i.e., several circuits constructed in the same tower sharing the same ROW. With multi-circuit transmission lines the power capacity can be multiplied according to the number of circuits in the tower, using a ROW similar to the one in single-circuit transmission lines.

The use of multi-circuit transmission lines is increasing in the last years. In several countries such as Germany, India, Japan and China the use of double or quadruple circuits is common, and in rare cases six circuit lines have been built. In United States, 47% of the 220 kV lines are double-circuit lines, whereas 52% of the 345 kV lines are double-circuit lines. In England, all the 400 kV lines are in double-circuit. In Japan 90% of the 500 kV lines and all 1000 kV are double-circuit lines. In Russia and China there are also compact 500 kV double-circuit lines (LI *et al.*, 2020). The largest overhead double circuit transmission line, built in 1999, is the Kita-Iwaki power line, operating at 500 kV with a height of 108 m and a ROW of 38 m.

The behavior of multi-circuit transmission lines has been characterized in several researches (WANG *et al.*, 2012b; NOVITSKIY; WESTERMANN, 2012). Specific topics such as protection (AGRASAR *et al.*, 1997; ZUO; KURIBYASHI, 2003), lightning performance (LIEW; THUM, 1993; ZHEREN *et al.*, 2010; WANG *et al.*, 2012a; LI *et al.*, 2012; ZHAO *et al.*, 2014), electromagnetic behavior (GUIHONG *et al.*, 2008; LIU *et al.*, 2013), transient behavior (KIZILCAY; NEUMANN, 2007) and secondary arc current extinction (YANG *et al.*, 2015) have been studied for overhead multi-circuit AC power lines. Even researches on multi-circuit DC lines have been made (LI *et al.*, 2008). Currently, some attention has been focused on hybrid AC/DC multi-circuit transmission lines (WEI *et al.*, 2013; MACKOW *et al.*, 2015; MALICKI *et al.*, 2016).

In some cases, more than one voltage level can be used in the same tower.

Thus, the transmission lines become Multi-circuit Multi-voltage Transmission lines (MCMVTLs). Some of those lines are in operation over the world (REICHELT *et al.*, 1996; KIZILCAY; NEUMANN, 2007; MACKOW *et al.*, 2015; LI *et al.*, 2018; KOCOT, 2019). However, lines with different voltages levels have complex electromagnetic interactions (GUIHONG *et al.*, 2008; NOVITSKIY; WESTERMANN, 2012; LIU *et al.*, 2013) that could lead to current unbalances (Yang Changhui *et al.*, 2011; Haisheng Liang *et al.*, 2016; LI *et al.*, 2021), affect the lightning protection (XI *et al.*, 2014), and increase the secondary arc current (SAC) and transient recovery voltage (TRV) (SUN *et al.*, 2008; LV *et al.*, 2011; YANG *et al.*, 2015) during a single-phase tripping. Nonetheless, most of these problems can be mitigated by selecting the optimal phase sequence (LI, 2017; TANG *et al.*, 2018).

In recent researches, multi-circuit multi-voltage transmission lines operating at 138/230 kV have been optimized using a multi-objective approach solved with evolutionary computing, using fixed tower shapes (RIBEIRO *et al.*, 2017). At the moment in which this document was written, the investigation of (RIBEIRO *et al.*, 2017) is the only additional research that considers the optimization of multi-circuit multi-voltage transmission lines. However, the optimization made by the authors only considers the bundles in fixed tower shapes and just for 138 and 230 kV. With a broader perspective, the present research included additional considerations such as the phase sequence, secondary arc current, voltage levels from 230 to 1000 kV, no restrictions on the tower and circuit shapes, and additional objective functions.

2.2 Characteristics of non-conventional transmission lines

Non-conventional transmission lines can be obtained by modifying different aspects such as the position, type and number of sub-conductors in the bundle. For instance, Figs. 2.1 to 2.3 show the SIL and the electric field at the surface of the sub-conductors as a function of the number of wires in the bundle, bundle radio, and distance between phases. As can be seen, the SIL can be increased by reducing distance between phases, or increasing the number of wires in the bundle or the bundle radio. However, there are some limitations to increase the SIL. Some of them can be physical, economical, or electrical. As an example, the electric field in Figs. 2.1 to 2.3 evidences that most of the techniques to augment the SIL also yield greater electric field values, which produce Corona effect and power losses. Therefore, the SIL increasing must be done considering many physical, economic, and electric aspects.

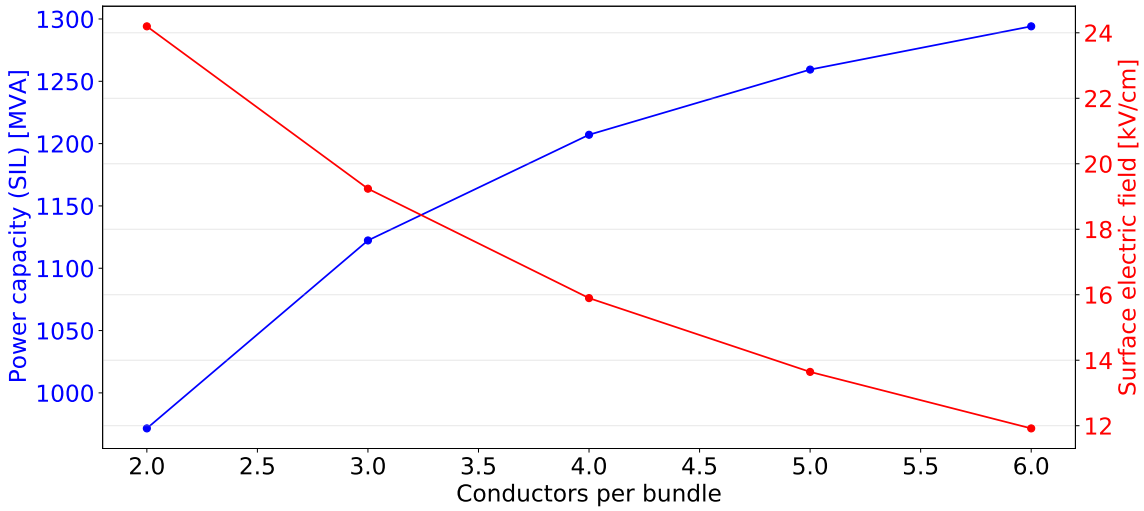

Figure 2.1 – SIL vs number of sub-conductors/bundle in a 500 kV transmission line.

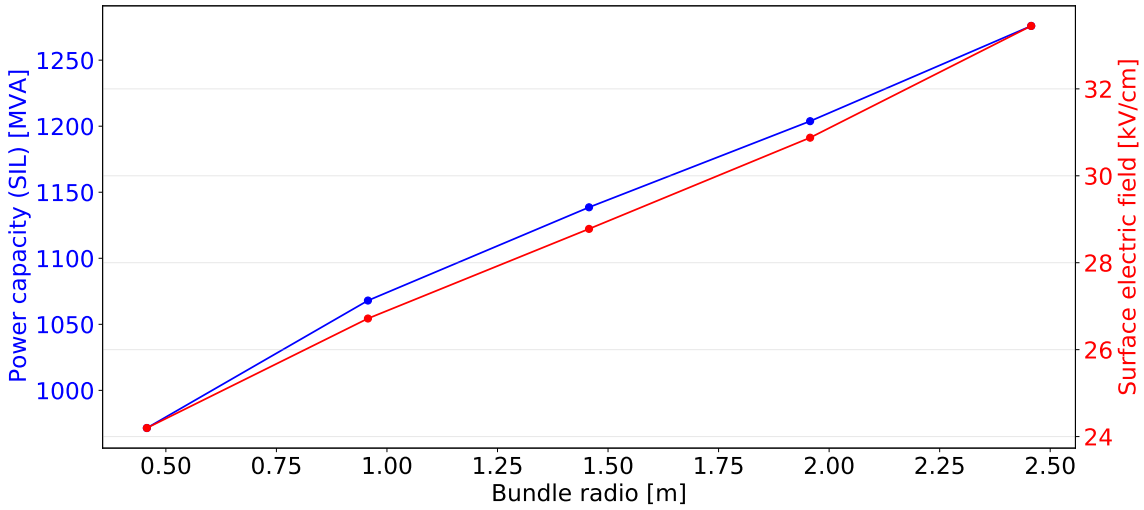

Figure 2.2 – SIL vs bundle radius in a 500 kV transmission line.

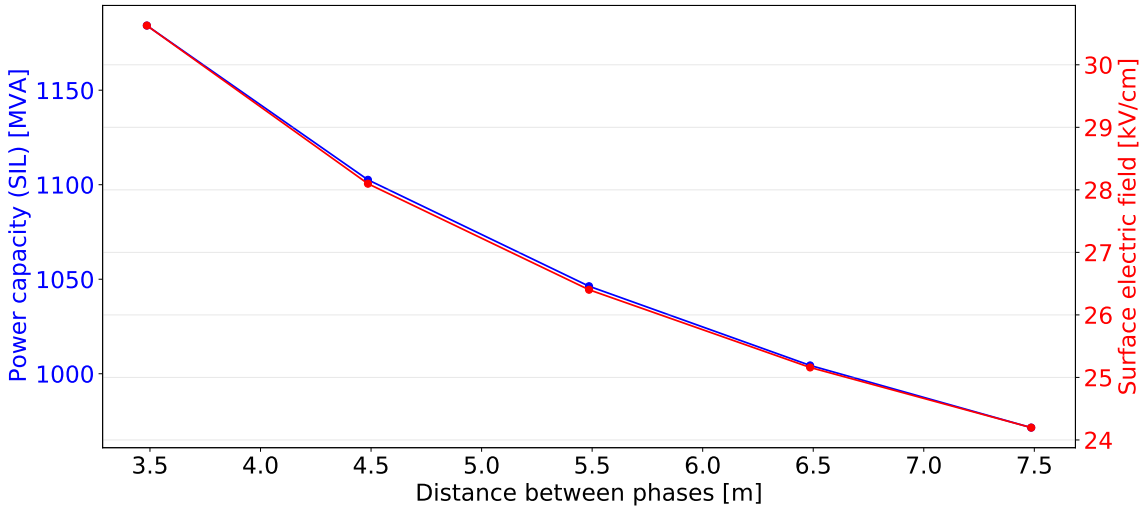

Figure 2.3 – SIL vs phase distance in a 500 kV transmission line.

A 500 kV non-conventional transmission line may look as the one in Fig. 2.4. That line was obtained after an optimization process following the methodology presented in this research in the next chapters. Note that the line is combining all the modifications presented before. You can clearly see that the general shape of the transmission line is an inverted delta, which is different from conventional horizontal lines. Also, the sub-conductors in the bundle are located in a non circular shape, presenting an evident difference in the outer phases. Finally, note that the bundle size is bigger than the one in conventional transmission lines (457 or 400 mm).

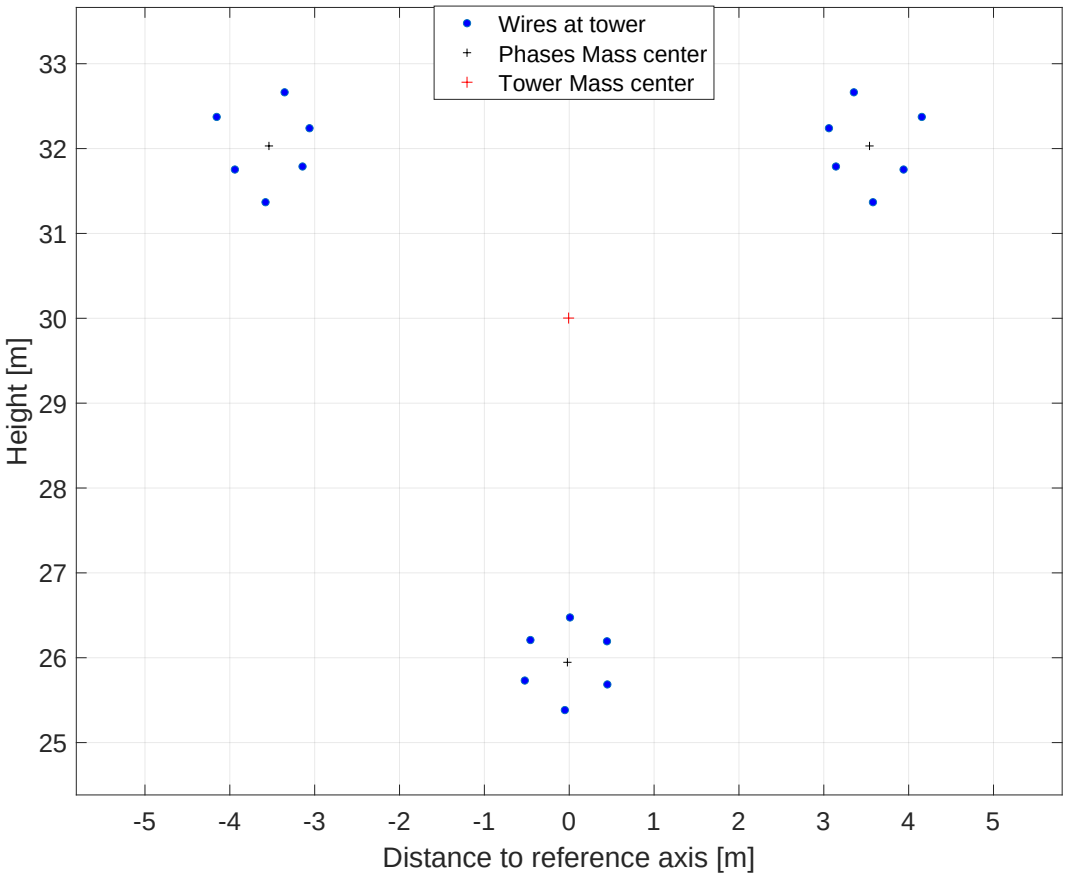

Figure 2.4 – Optimized 500 kV transmission line.

With all the modifications described before, the non-conventional transmission line presents a SIL of approximately 1500 MW, which is almost 50% greater than the SIL of conventional transmission lines. As you can see, the advantages regarding to the SIL are evident. It also presents advantages regarding to the the right of way, which is almost 40% smaller than in a conventional 500 kV transmission line. However, the transmission line optimization also leads to some challenges. Firstly, since the phases are close, it is necessary to ensure that they will not approach even more along span. For this goal, spacers could be used along the span. The other challenge is the physical construction of the line, because there are no standard conductor hardware and attachments for this

type of line. We hope that future investigations address the mechanical feasibility of these lines.

2.3 SIL increasing with multi-circuit transmission lines

Increasing the SIL per line width is straightforward by using multi-circuit transmission lines. Considering transmission lines like the one in Fig. 2.5, it is evident that the power of four parallel transmission lines can be transmitted using the same width of a single circuit line, now with four circuits in a vertical structure.

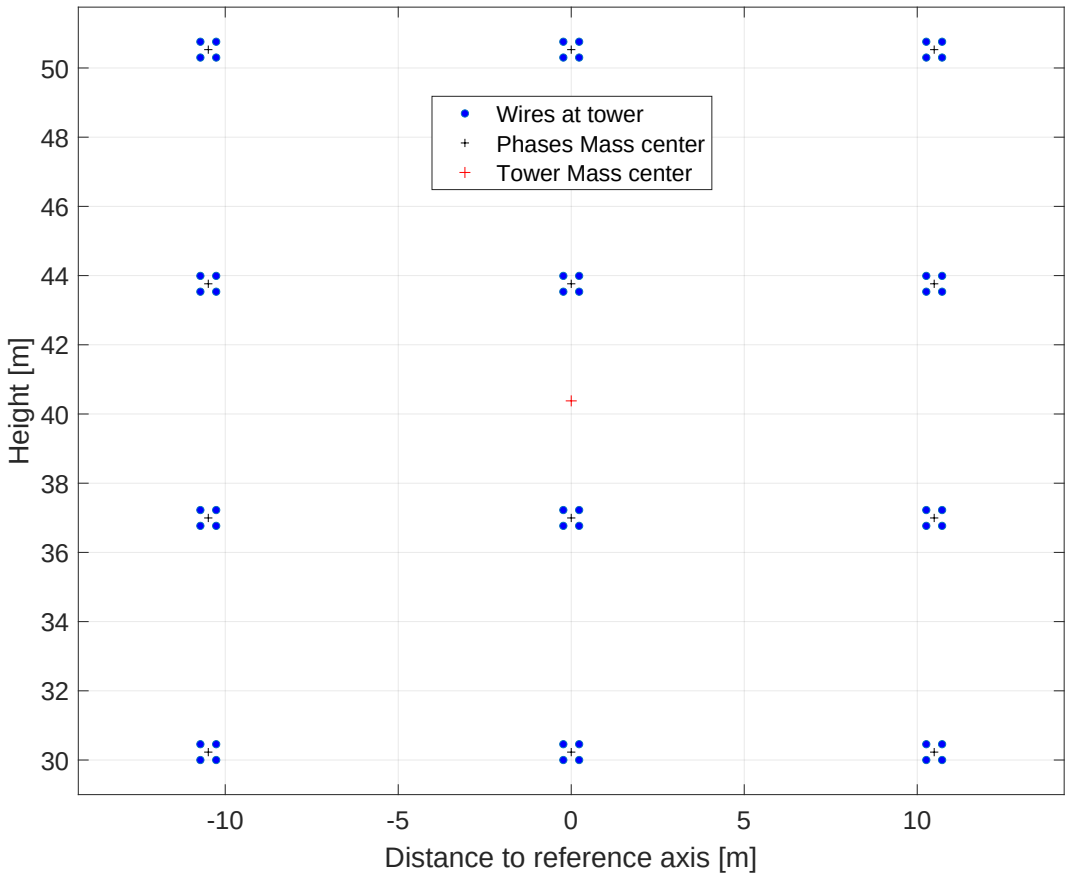

Figure 2.5 – Example of a quadruple-circuit transmission line.

However, it is important not to misunderstand width with ROW. The ROW of high power transmission lines mainly depends on the electric field above the soil under the transmission lines. For example, the ROW of a single-circuit transmission line is given by Fig. 2.6, where as for the line in Fig. 2.5 it is given by the electric field in Fig. 2.7. In this research, the end of the ROW is given by the distance where the electric field measured at 1.5 m above of the soil is lower than 1.6 kV/m (Electric Power Research Institute, 2005). As you can see, the ROW of the quadruple-circuit transmission line is larger than the ROW of the single-circuit line. That is because the additional circuits are increasing the

electric field under the line. However, when compared the multi-circuit lines with parallel lines, important ROW reductions are obtained. Hence, in double circuit lines the ROW is 41% smaller; in triple-circuit lines, the ROW is 55% smaller; and in quadruple-circuit lines, the ROW is 63% smaller.

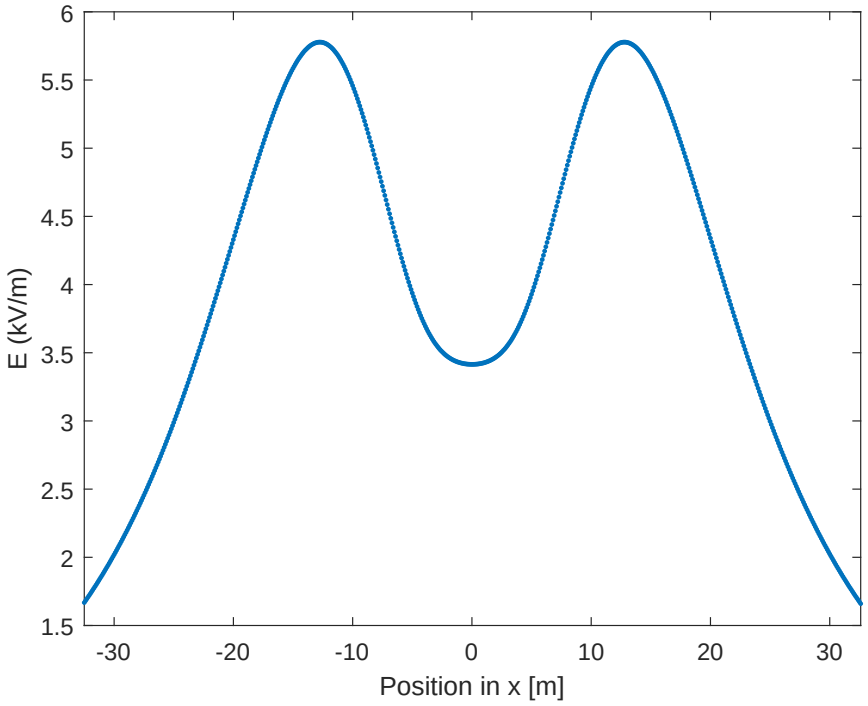

Figure 2.6 – Electric field under a conventional 500 kV transmission line.

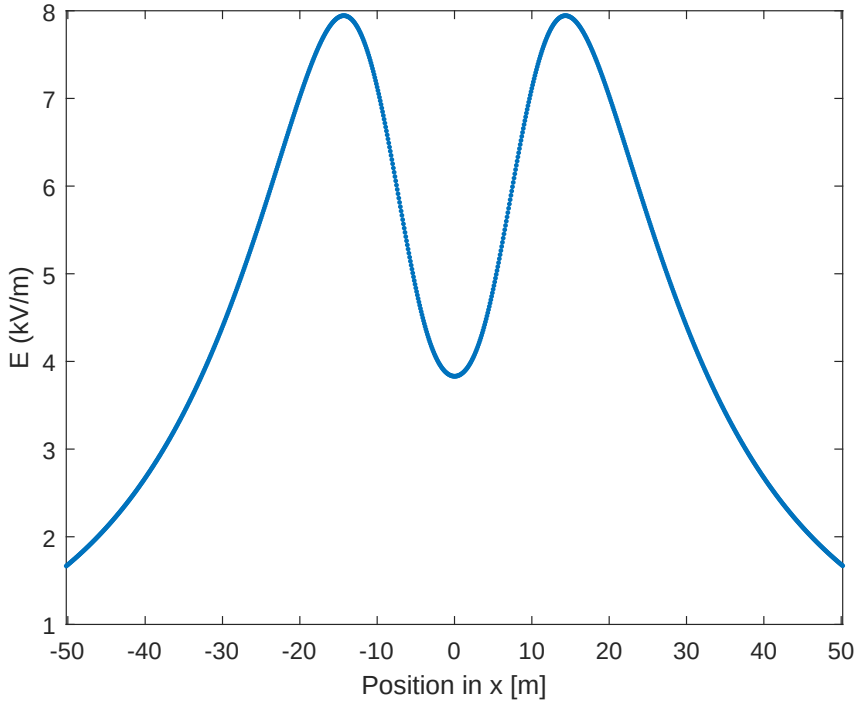

Figure 2.7 – Electric field under the quadruple circuit 500 kV transmission line of Fig. 2.5.

In multi-circuit transmission lines it is possible to combine different voltage levels. In this case, the ROW will be severely affected mainly by the circuits with higher voltages. Also, the mutual coupling will be higher and problems related to Corona phenomenon could appear. Therefore, designing this kind of transmission lines is a challenge, but the advantages regarding to the SIL and ROW are considerable.

The disadvantages of using multi-circuit transmission lines are: 1) The tower height and weight could be very high; 2) The electromagnetic fields are stronger and the transient overvoltages could be more severe; 3) It is difficult to enable features like the single-phase auto reclosing; and 4) The protection system must be specialized. During this research, some solutions to these problems are proposed.

2.4 SIL increasing combining the former approaches

In this research we propose the use of an algorithm and a mathematical model to optimize multi-circuit transmission lines with different voltage levels above 230 kV at same tower. The optimization is initially done by modifying the position and type of each wire through evolutionary computing. Then, the phase sequence was also used as a decision variable. In the end, the secondary arc current was included as a constraint in the mathematical model. The mathematical model has four objective functions: maximize SIL and minimize: costs, ROW and tower's height. Two approaches were used to solve the problem. In the first one, the individual objective functions were aggregated and modeled as a mono-objective function. In the second one, the problem was solved without transforming it into a mono-objective problem. As result, improved compact multi-circuit transmission lines with good electrical, economic and mechanical characteristics were obtained.

As an example, a transmission line like the one in Fig. 2.8 could be obtained at the end of the optimization process. The optimized transmission line has two circuits operating at 230 kV and two circuits operating at 500 kV. The value of the desired objectives (SIL, ROW, cost and height) is shown at the top of the image. Compared with parallel single-circuit lines, the optimized transmission line has 53% greater SIL and 75% lower ROW. However, the cost and tower height will be higher. As will be explained in the next chapters, we are dealing with a multi-objective problem, so it is not possible to improve all the objectives at the same time. Therefore, some solutions have more benefits for one of the objectives. In particular, the selected line has a large SIL at the price of increasing the cost of the line.

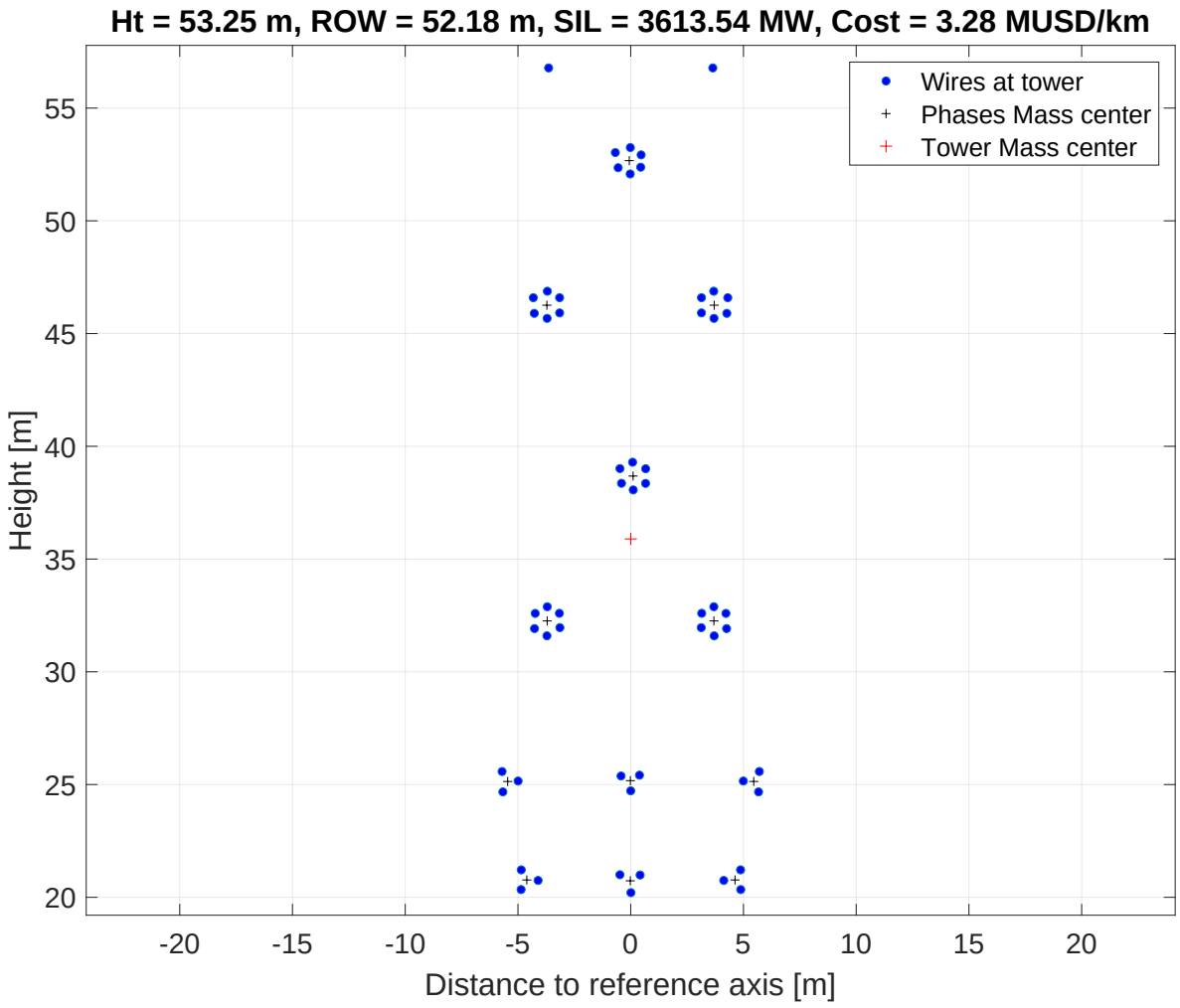

Figure 2.8 – Optimized quadruple-circuit transmission line with 2 circuits operating at 230 kV and 2 circuits operating at 500 kV.

The next chapters of this document will show the mathematical model, characteristics, and the necessary steps for obtaining transmission lines like the one in the example.

3 Multi-objective optimization

In this chapter, it is explained what a multi-objective optimization problem is, and some of techniques to solve these kind of problems are presented. In real life, many problems can be modeled as a multi-objective problem. Therefore, it is important to know concepts like Pareto dominance and Pareto optimal solutions. A simple example of a multi-objective problem can be taken from common situations. Suppose that your old cellphone is broken and you need to buy a new one. Certainly, you would like to get the best cellphone available on the market. However, your budget is limited. In this situation, there is a trade-off between price and performance of the cellphone. Now, the problem is how to select the device considering the available budget. As you can guess, there are many options, and there is not a single solution. However, in a simple situation like this, a feasible solution is to buy the most expensive phone that you can afford. Nonetheless, in complex problems finding the best solutions it not straightforward and specialized methods should be used. Thus, techniques like the ones explained in this chapter are useful to solve a wide variety of multi-objective problems.

3.1 Multi-objective problems

A general constrained multi-objective problem can be formulated as in (3.1) to (3.3). The m objective functions $f_m(\chi)$ are in (3.1) where χ is a vector composed of the decision variables. Equation (3.2) represents the equality constraints and (3.3) the inequality constraints.

$$\min(f_1(\chi), f_2(\chi), ..., f_m(\chi)) \tag{3.1}$$

Subjected to:

$$g(\chi) = c \tag{3.2}$$

$$h(\chi) \leq d \tag{3.3}$$

Note that (3.1) was formulated as a minimization problem. However, to solve maximization problems it is enough to invert the signs of the objective functions, meanwhile the rest of the formulation remains equal.

In multi-objective problems there exist two spaces: the decision space and the objective space. The decision space contains the solutions, e.g., the optimized tower characteristics, such as wire type, positions, etc. Meanwhile, the objective space contains the evaluation of the solutions for all objectives, e.g., SIL, costs, etc. In multi-objective optimization it is desired to get well-distributed solutions in both spaces. This allows to have diverse solutions with prominent exploration of both spaces.

Commonly, in multi-objective problems an objective is in conflict with one or more objectives. Therefore, improving one of them implies making another worse. For example, in this research it is not possible to increase the SIL without increasing the costs. In order to choose the best solutions for this kind of problems it is necessary to find the *Pareto optimal* solutions, or in other words, the solutions whose objective functions can not be further improved without deteriorating some of the other objectives. Hence, it is necessary to know the concept of Pareto dominance. The Pareto dominance is formally defined in theorem 3.1.

Theorem 3.1 (Pareto dominance) *A solution* $\boldsymbol{u}$ *dominates a solution* $\boldsymbol{v}$ *if for all objectives* $\boldsymbol{u}$ *is better or equal than* $\boldsymbol{v}$ *and in at least one objective* $\boldsymbol{u}$ *is better than* $\boldsymbol{v}$*. Mathematically, for minimization* $\boldsymbol{u}$ *dominates* $\boldsymbol{v}$ *(denoted as* $\boldsymbol{u} \prec \boldsymbol{v}$*) if* $\forall i \in \{1, \cdots, k\}$, $u_i \leq v_i$ *and* $\exists i_0 \in \{1, \cdots, k\} \mid u_{i_0} < v_{i_0}$.

To illustrate the Pareto dominance concept, an imaginary Pareto front of the line optimization problem, aiming to increase the SIL and decrease the costs (i.e., a maximization-minimization problem) is presented in Fig. 3.1. Note that the red crosses are the dominated solutions whereas the blue asterisks are the non-dominated solutions, i.e., all the red solutions are dominated by one or more blue solutions. Therefore, there are no other solutions better than the blue solutions in both objectives at the same time.

There are different methods to solve multi-objective problems. We can divide those methods in two groups. The first one deals with the multi-objective problem as it is, finding the *Pareto optimal* solutions without making any transformation, whereas the second transforms the multi-objective problem into a mono-objective problem. Hence, the *Pareto Front* is not directly obtained in the former case.

Transforming a multi-objective problem into a mono-objective problem is a straightforward technique that often is done by normalizing the objectives and combining them into a single one, using a weighting factor for each objective. However, the weights are arbitrarily chosen and can change the final solution, as consequence of an a priori choice. Another approach to transform the problem into a single-objective function is to

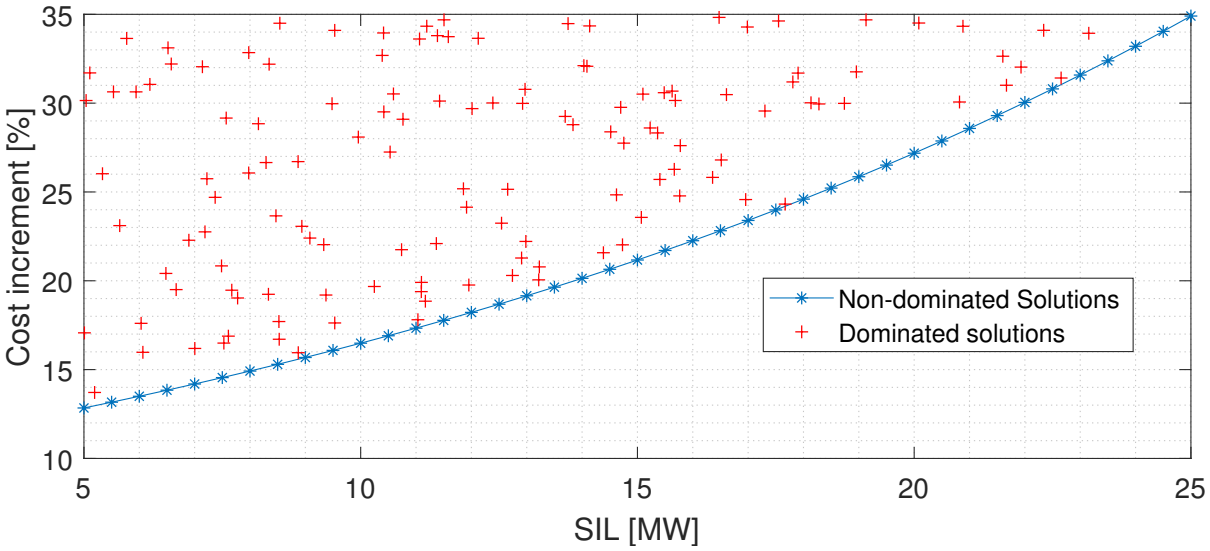

Figure 3.1 – Example of possible Pareto Front behavior of transmission lines.

set all but one objective as constraints. Nevertheless, the constraints limits are chosen in an arbitrary way.

On the other hand, when the problem is not transformed, the identification of the Pareto optimal solutions is required. The drawback is that the more objectives the more computational time is used. Additionally, as can be deduced from Fig. 3.1 it is not possible to observe the Pareto front when more than three objectives are analyzed (even Pareto fronts with three objectives are not common).

Classical optimization (i.e., methods that use differential calculus to optimize continuous and differentiable functions) allows to solve multi-objective problems, however they have several disadvantages. One of them is that the mathematical model has to be well defined in a closed form. However, in many real applications the model is not even known. Also, when the problem is not convex the complexity of the model is increased and finding the global optimal solution is not granted. Additionally, since classical methods work with single solutions, they are highly dependent of the initial conditions and the size of the steps used during each actualization of the decision variables. Therefore, the solution can be easily attracted by a local optimum.

Since the evolutionary algorithms are population methods that overcome most of the drawbacks of classical methods, they were chosen in this research. Even if they do not guarantee obtaining the global optima, they have the capacity of yielding good solutions. In particular, genetic algorithms and the non-dominated sorting genetic algorithm II (NSGA-II) were used in this research.

3.2 Genetic algorithms (GA)

The GAs are heuristic bio-inspired optimization techniques. They are based on the concept of evolution proposed by Charles Darwin. Thus, along the generations the species evolve, being more adapted to the environment. The individuals more adapted within their population have more chances to transmit part of their genetic material to the next generation through reproduction process. The new generations also have a random possibility of suffering an unexpected variation on their genetic material, improving or deteriorating their performance on the environment. Therefore, since the individuals with better performance have more chances to survive, the population after several generations will be mainly composed with the more adapted individuals.

In GAs, the individuals in the decision space are represented as chromosomes. The process of combining genetic material is represented with the crossover operator. The random variation of the genetic material is represented with the mutation operator. The performance of the individuals is known as the fitness. Finally, the selection of the individuals that will compose the next generation is determined by the natural selection operator.

It is possible to represent or codify many problems as a chromosome (e.g., images, sounds, words, etc.) as shown in Fig. 3.2 in which the features of each element are represented by $\mathbf{X}_1$ to $\mathbf{X}_n$ (e.g., $\mathbf{X}_2$ can be the feature that defines dog skin color). This representation is known as genotype whereas as the phenotype is the manifestation of the genotype (e.g., a specific frequency in a sound wave). The genotype can contain any type of variables such as binary, integer, real, permutations, trees, etc. However, according to their representation it will be necessary to use different type of genetic operators, increasing or decreasing the complexity of the problem.

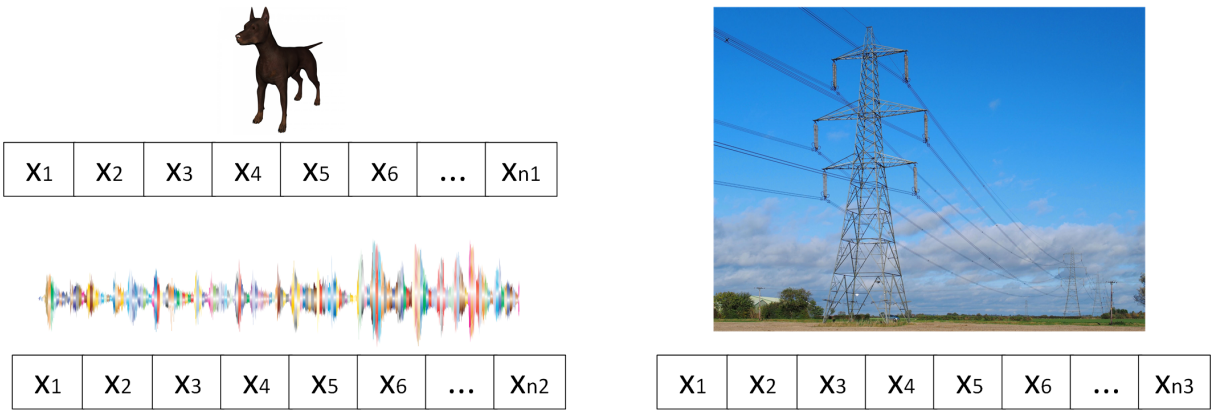

Figure 3.2 – Representation of different elements as a chromosome.

Since GAs are population methods, i.e., they work with more than one solution at the same time, they have a good possibility of making a good exploration of the solution

space, helping to avoid local optima.

A general flux diagram of the GAs is presented in Fig. 3.3. As can be seen, the process begins with the generation of an initial population, denoted as *parents/progenitors*. Then, it is applied the crossover and mutation operator, yielding a new population denoted as *sons/offspring*. Later, both population are evaluated according to their fitness. After that, the operator of natural selection is applied and a new population is selected. The natural selection operator can be applied to the union of parents and sons or only to the sons. However, this selection has different implications in the final results. Finally, when the new population is created the stopping condition is verified. If the stopping condition is satisfied the algorithm ends, otherwise the new population is denoted as parents and the process is repeated from the crossover and mutation operator for several generations until satisfying the stopping condition. The stopping condition usually is a number of generations or some fitness value.

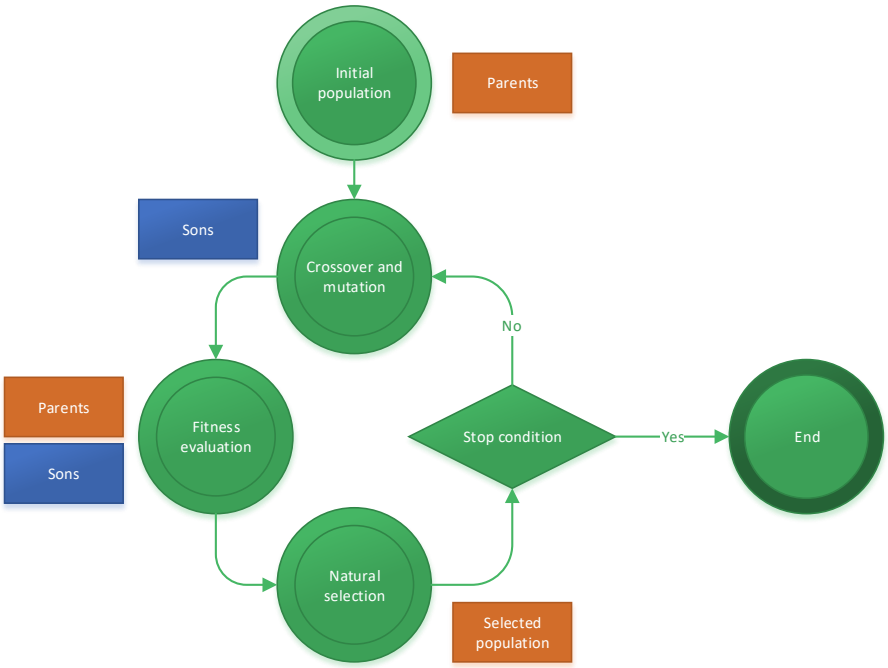

Figure 3.3 – Flux diagram of a general GA.

More details of each part of GAs are given in the following sections.

3.2.1 Initial population

The initial population is the starting point of the GAs. Depending on their values the algorithm could find or not a valid solution. Commonly, the initial population is initialized randomly. This allows to have a high diversity on the population (i.e., solutions that are different between them). However, in complex cases a random population can

produce solutions in the decision space that are outside of the feasible region. At this point there are some options: 1) with the operators try to ensure that all the solutions are inside the feasible region; 2) use some technique to turn feasible an unfeasible solution; 3) remove from the population all unfeasible solutions; 4) use the solutions no matter if they are feasible or not, but penalize the fitness of the unfeasible solutions. The problem with approaches 1) and 2) is that they can be complex and require a deep knowledge of the problem. In the case of option 3) the drawback is that it is possible to lose prominent solutions, that with small changes can yield good solutions. Finally, in this research it is considered option 4) as the best, because it allows to evolve solutions that could have good features over the next generations.

3.2.2 Fitness

Fitness is a performance measurement of the individuals on the environment. Generally, it has positive value so it is necessary a transformation for negative objective functions. When the problem is a maximization, the fitness can be the same objective function or a normalization of it. On the other hand, for minimization problems a transformation of the objective functions is mandatory.

Transforming minimization objective functions can be done by inverting the sign of the function or by using approaches like (3.4) where $\phi(\chi_i)$ is the fitness of the solution χ_i, f_{max} is the global optimal value, $f(\chi_i(t))$ the value of the objective function for the χ_i solution at generation t, $f_{max}(t)$ the value of the objective function for the best solution at generation t, and $f_{min}(t)$ the value of the objective function for the worst solution at generation t.

$$\phi(\chi_i) = \begin{cases} f_{max} - f(\chi_i(t)) \\ f_{max}(t) - f(\chi_i(t)) \\ \frac{1}{1+f(\chi_i(t))-f_{min}(t)} \\ \frac{1}{1+f_{max}(t)-f(\chi_i(t))} \end{cases} \tag{3.4}$$

It is worth to notice that choosing a good fitness function and a correct codification (e.g., binary, real, permutation, etc.) in concordance to the decision space is very important, because it will influence the computational time and the performance of the algorithm (e.g., if a fitness solution is modeled as binary for real problems, the chromosome will be large and so the computational time). It is important to make a correct mathematical model of the problem, because it could lead to convex or not convex models.

3.2.3 Constraints handling

When the problem has restrictions, it is necessary to make a constraint handling. The typical approach is to penalize the fitness functions when some solutions are outside the feasible region. This penalization can be proportional to the grade of non-feasibility or simply by making the fitness null. The problem of making zero the fitness is that prominent solutions with small constraint violation are expelled from the population.

Constraint handling is very important to obtain solutions inside the feasible region and bring back solutions outside of the feasible region. The constraint handling for the problem in this research will be explained later.

3.2.4 Crossover

On classical GAs crossover is the most important operator, because, according to the evolutionary theory, individuals with more fitness will have more chance of recombining their genetic material producing new and better individuals. To generate a pair of descendents (sons) a pair of individuals with high fitness (parents) mix their features.

The most simple crossover than can be applied to almost all type of variables are the crossover of n points and the uniform crossover presented in Fig. 3.4.

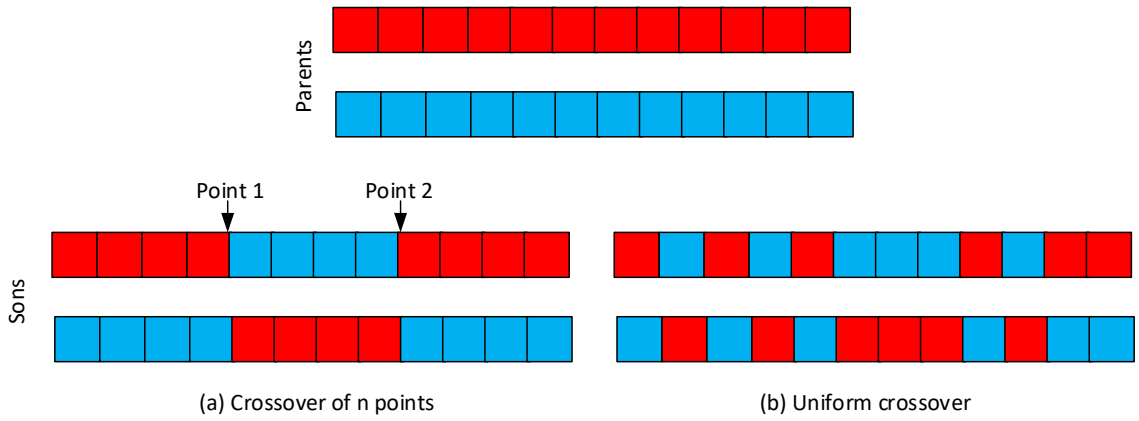

Figure 3.4 – (a) Crossover of n points. (b) Uniform crossover.

In crossover of n points, n points inside the chromosome are selected to share their genetic material. As can be seen in Fig. 3.4a the genes until the point 1 of the first son correspond to the first parent, meanwhile from point 1 to 2 to the second parent. The second son have the same behavior, but beginning with the gens of the second parent.

On the other hand, in the uniform crossover represented in Fig. 3.4b random gens of the sons are selected for belonging to the first parent, whereas the rest of the gens are filled with the gens of the second parent. Again the second son has the same pattern, but beginning with the genes of the second parent.

However, the recombination can occur in different ways depending on the codification adopted for the problem, i.e., there are different variations of crossover for variables such as binary, real, integer, permutation based space variables, trees and others.

3.2.4.1 Crossover for binary variables

The original codification used for genetic algorithms was binary variables. The most known crossover types for this type of variables are the Random Respectful Crossover (RRC), Masked Crossover (MX), and Homologous Crossover (HX). In this research the MX was used. Therefore, it is the only one that will be explained here.

3.2.4.1.1 Masked Crossover (MX):

In this crossover is created a copy of both progenitors. Then, two random binary masks are created. If a gene is 1 in mask 2 and 0 in mask 1 the gen of progenitor 2 in that position is copied to the first son. On the other hand, if a gene is 1 in mask 1 and 0 in mask 2 the gen of progenitor 1 in that position is copied to the second son. Example:

- Progenitor 1: 1 0 0 0 1 0 1 0 0 1
- Progenitor 2: 0 1 0 1 0 0 1 1 0 1
- Mask 1: 1 1 1 0 0 0 1 0 1 0
- Mask 2: 0 0 1 0 1 1 0 1 1 0
- Son 1: 1 0 0 0 0 0 1 1 0 1
- Son 2: 1 0 0 1 0 0 1 1 0 1

3.2.4.2 Crossover for real variables

Specific crossover operators for real variables are the intermediate crossover in (3.5), the arithmetic crossover in (3.6) and the heuristic crossover in (3.7). In former equations, x_i is the i gen of a son, x_a the first progenitor, x_b the second progenitor, $x_{a,i}$ the i gen of the first progenitor, $x_{b,i}$ the i gen of the second progenitor and α a random

variable from [0,1]. Note that those types of crossover use either math functions over the parents or linear combinations. In this research, the arithmetic crossover was used.

$$x_i = \frac{x_{a,i} + x_{b,i}}{2} \tag{3.5}$$

$$x_i = \begin{cases} \alpha x_a + (1-\alpha)x_b & \text{for the first son} \\ \alpha x_b + (1-\alpha)x_a & \text{for the second son} \end{cases} \tag{3.6}$$

$$x_i = \alpha(x_a - x_b) + x_b \quad \text{for } f(x_a) \geq f(x_b) \tag{3.7}$$

3.2.4.3 Crossover for integer variables

For integer variables normally it is chosen the uniform crossover or the crossover of n points. It could be used the operators for real variables, but the values must be approximated to the nearest integer. Accordingly, there are no presented specific operators for this type of variables.

3.2.4.4 Crossover for variables based on permutation spaces

When dealing with permutation based spaces it is necessary to ensure that the new individuals produced in the crossover are also permutations. Ensuring this characteristic is not a simple task. However, there are some algorithms like the Order Crossover (OX), Partially Mapped Crossover (PMX), Crossover of position, Maximal Preservation crossover (MPX), among others to solve this issue. In this research only the OX crossover was used. Therefore, only the procedure of the OX crossover is explained.

3.2.4.4.1 Order Crossover (OX):

It is one of the most simple crossover. Its procedure is described below:

1. Select the first progenitor.
2. Select randomly a part of chromosome (substring) of progenitor 1.
3. Produce a proto-child by copying the substring in the same position of progenitor 1.
4. Select the second progenitor.
5. Delete the progenitor 2 genes that are already in the substring
6. Add the remain genes of progenitor 2 to the child filling the empty gens in the same order that appear on the progenitor 2.

7. The second child is produced in the same form but the initial substring comes from progenitor 2.

Fig. 3.5 presents an example of one son produced with this crossover.

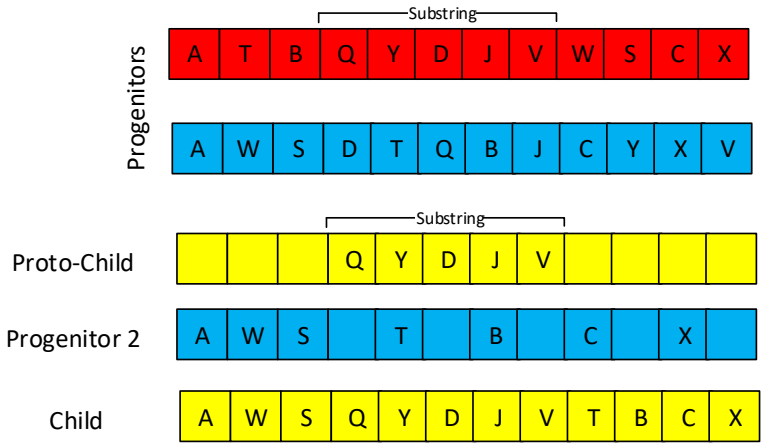

Figure 3.5 – Crossover OX example.

3.2.5 Mutation

Mutation is a natural random process that allows obtaining different individuals on the population. Mutation is important because it gives the possibility of exploring characteristics that do not exist in the current population. Sometimes, mutation can yield characteristics that are better than those seen in the population. However, in many cases mutation produces individuals with worst characteristics.

Regarding to optimization processes, a high mutation rate leads to a random search and can deteriorate the optimization process. However, as will be presented later, there are some techniques to lead the mutation towards points than can have good performance.

In evolutionary algorithms mutation occurs individuality in each gen of the chromosome according to a probability that in classical GAs is low (5%). However, it can affect one or several parts of the chromosome at the same time. Usually, the mutations only affect the sons. As can be seen in Fig. 3.6 two parents combined their genetic material through uniform crossover and then a random mutation appeared in the second son at gen x_6. Similar to the case of recombination, different mutation operators can be used according the type of variable.

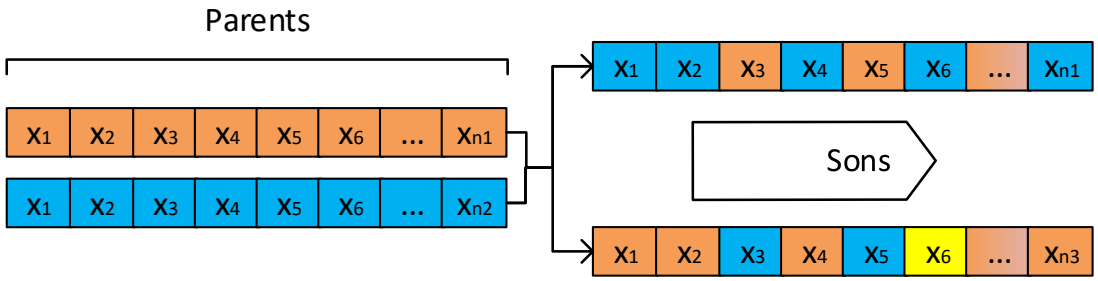

Figure 3.6 – Example of crossover and mutation.

3.2.5.1 Mutation for binary variables

Mutation of binary chains is a straightforward procedure. Basically, each one of the genes of the chromosomes has a probability p_m of mutation. When the mutation occurs the original value of the gene is changed (0 to 1, or 1 to 0). According to (FOGARTY, 1989) the probability of mutation in initial generations should be high and then decrease over the generations.

3.2.5.2 Mutation for real variables

Mutation for real variables can be expressed as $x' = m(x)$, where x is the original variable, x' the variable after mutation and $m()$ the mutation function. Normally, $m(x) = x + d$, being d a random variable usually defined by a flat or normal probability density function. In this research, this type of mutation was used, considering Gaussian distributions.

Other mutation functions depend on the generation in which the algorithm is. Thus, in the early generations the mutation is high in order to explore the whole solution space and in the end it is low to improve local solutions. In other words, these mutation functions try to explore the decision space and then intensify the quality of the solutions. An example of this type of function is (3.8) in which a is the lower limit of x, b the upper limit, p the grade of dependence to the generation (suggested $p = 5$), r a random number between [0,1], t the current generation and T the maximum number of generations.

$$m(x) = \begin{cases} x + (b - x)\left(1 - r^{(1-t/T)^p}\right) & \text{with 50\% of probability} \\ x + (x - a)\left(1 - r^{(1-t/T)^p}\right) & \text{with 50\% of probability} \end{cases} \tag{3.8}$$

More complex mutations use self-adaptation process. The self-adaption mutation originally was proposed for Evolutionary Strategies (ES), another evolutionary algorithm focused on mutation without crossover. The self mutation can occur in

three different ways: isotropic self-adaptation, non-isotropic self-adaptation or correlated self-adaptation (DEB *et al.*, 2002). These types of mutation will not be explained in this document.

3.2.5.3 Mutation for variables in permutation spaces

Mutation of variables in a permutation space is simpler than in the case of crossover. On the literature, the main mutation algorithms are inversion mutation, insertion mutation, displacement mutation, exchange mutation, and heuristic mutation. However, none of those algorithms were used. It is because the mutation of the permutation variables in this research can be easily obtained by random permutations of the sub-strings. Each sub-string will be comprised by the elements $[A, B, C]$. Therefore, the mutation will be a simple permutation of that sub-string. An example for double circuit lines can be done considering the initial string $[[A, B, C], [A, B, C]]$. If the mutation only occurs in the second sub-string, a possible result could be $[[A, B, C], [C, A, B]]$. As you can see, this type of mutation can be easily extended to more complex cases.

3.2.6 Natural Selection

Natural selection is the process that determines the solutions that will continue on the population for the next generation. According to the evolution theory the individuals with more fitness have more chances to survive. The problem with the natural selection is that according to their selective pressure the individual with higher fitness can dominate the population quickly transforming all the population equal or very similar. Thus, if the selective pressure is high the population will lose diversity quickly and the decision space will not be explored properly, leading to local optima. Some strategies to overcome this problem are presented in the section 3.2.7.

In this research the natural selection based on modified tournaments explained below was selected. However, different natural selection approaches are also explained, aiming to evidence the importance of the selection procedure and the selective pressure.

3.2.6.1 Roulette wheel:

It is the classical natural selection method to choose the N solutions that will continue in the next generation. It is proportional to the fitness of each n solution (f_n). Thus, the probability p_n of a n solution survival is given according to their normalized fitness in a range between [0,1]. It can be calculated by using eq. (3.9). Accordingly, the individuals are allocated in a roulette and then N darts are thrown one per time to choose

who is going to survive. Therefore, the same solution can be chosen several times.

$$p_n = \frac{f_n}{\sum_{j=1}^{N} f_j} \tag{3.9}$$

Fig. 3.7 shows an example of this algorithm. As can be seen the best solution have 70% of probability to survive whereas the rest 30% is for the other four solutions. However, since the dart can hit any part of the roulette it is still possible to lose the best solution.

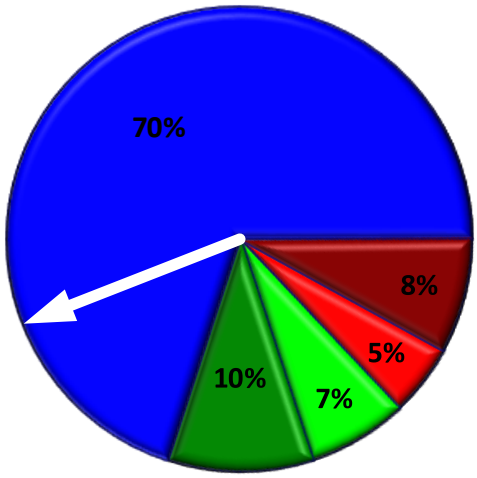

Figure 3.7 – Roulette wheel example.

3.2.6.2 Ranking:

In this approach the individuals are sorted according to their fitness. Then, using their position a rank is given and the probability of survival is calculated (can be linear or non-linear to the rank). A simple linear ranking can be obtained using (3.10) where $p(S_i)$ is the probability of a solution S_i being select, N the number of solutions on the population, $rank(S_i)$ the rank of the solution S_i, and $rank(S_j)$ the rank of the solution S_j.

$$p(S_i) = \frac{rank(S_i)}{\sum_{j=1}^{N} rank(S_j)} \tag{3.10}$$

In Fig. 3.8 it is presented the same example as the roulette wheel approach, but with ranked selection. Note that now the best solution has a chance of 31.25% of being selected, whereas the worst has a chance of 6.25%.

Because the probability of selection depends on the rank, the selective pressure always is maintained, even if the fitness of each solution is very close. However, still it is possible to lose the best solution.

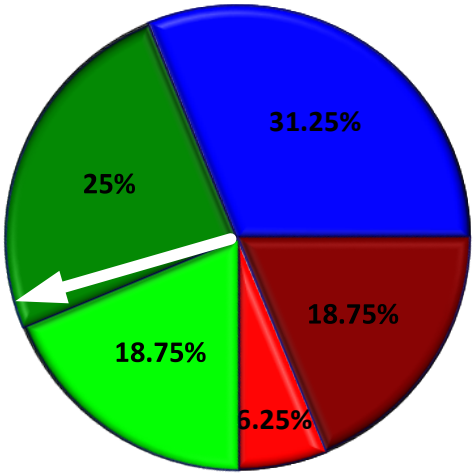

Figure 3.8 – Ranked selection example.

3.2.6.3 Tournament:

In this natural selection process the solutions will compete in N tournaments. Each tournament is composed of q random individuals. Then, the winner of each tournament will survive to the next generation. In this case the selective pressure can be adjusted according to the size q of the groups. Note that since the solutions participating on the tournaments are random, it is possible to lose the best individual if it is never selected to compete in the tournaments.

In the modified version of the tournaments, each individual participates in one tournament against q random individuals. Then, the number of victories are counted and the individuals with the larger quantities of victories are maintained for the next generation. With this approach, the survival of the best individual is ensured and the selective pressure is not strong.

3.2.6.4 Elitism:

This is one of the simplest methods. Basically, the best solutions are always maintained meanwhile the rest does not survive. The problem with this approach is that the selective pressure is very high.

3.2.7 Diversity preservation

Maintain a diversity on the population is important to ensure a correct exploration of the solutions space and prevent a fast attraction by a local optimum. Maintaining diversity is achieved by different approaches. The first one is to increase the size of the population. However, the larger the population, the higher the computational time. The second one is to increase the mutation rate. However, the more mutation rate, the more random is the search. Finally, there are diversity-preserving operators based on

the concept of crowding and niches. Thus, several sub-populations are created around locals optimal.

The crowding approach measures the similitude grade of the solutions and replaces the more similar by other similar. On the other hand, the niche solutions uses the sharing fitness concept. Thus, instead of replacing by a similar solution, the fitness of similar solutions is degraded. Because of the fitness degradation, niches surrounding different local optimal are created. The drawback with this approach is that it requires a deep knowledge of the problem to stabilize the niches. Trying to solve this problem Goldberg and Richardson (GOLDBERG; RICHARDSON, 1987) suggested an adaptive function to determine the quantity of solutions belonging to each optimum. This function is known as the sharing function, presented in (3.11) where d_{ij} is the distance between solutions i and j, σ_{share} the maximum distance to share the fitness, and α a parameter to determine the grade of degradation of the fitness (suggested $\sigma_{share} = 1$ for a linear degradation).

$$Sh(d) = \begin{cases} 1 - \left(\frac{d_{ij}}{\sigma_{share}}\right)^{\alpha} & \text{if } d \leq \sigma_{share} \\ 0 & \text{otherwise} \end{cases} \tag{3.11}$$

For each solution the number of niches nc_i is calculated by using (3.12)

$$nc_i = \sum_{j=1}^{N} Sh(d_{ij}) \tag{3.12}$$

Finally, for a solution i the degraded fitness (ϕ'_i) is calculated as $\phi'_i = \phi_i / nc_i$. The problem with this approach is that the user has to define the parameters α and σ_{share}. Additionally, the ranked and tournament selection operators have difficulties with this approach and only proportional fitness selection operators works well.

3.3 Multi-objective GAs

The study of multi-objective optimization with GAs began in the early 80s with the doctoral thesis of David Schafler in 1984 (SCHAFFER, 1984). He created an algorithm named vector-evaluated genetic algorithm (VEGA) by a simple modification of a single objective GA, achieving multiple trade-off solutions in few generations. Then, in 1989 David E. Goldberg suggested a multi-objective evolutionary algorithm (MOEA) (GOLDBERG, 1989) based on the concept of domination. This work was the base of following researches: the multi-objective GA (FONSECA; FLEMING, 1993), the non-dominated sorting GA (NSGA) (SRINIVAS; DEB, 1994), the Strength Pareto

Evolutionary Algorithm (SPEA) (ZITZLER; THIELE, 1999), the improved SPEA (SPEA2) (ZITZLER *et al.*, 2002), the Pareto-Archived Evolution Strategy (PAES) (KNOWLES; CORNE, 2000), the Pareto Envelope-based Selection Algorithm (PESA) (CORNE *et al.*, 2000), the Region-based Selection in Evolutionary multi-objective Optimization (PESA-II) (CORNE *et al.*, 2001), the Non-dominated Sorting Genetic Algorithm II (NSGA-II) (DEB *et al.*, 2002), the niched Pareto-GA (NPGA) (HORN *et al.*, 1994), the SMS-EMOA: Multi-objective selection based on dominated hyper-volume (BEUME *et al.*, 2007), among others. Basically, those algorithms differ on the way that the fitness is assigned. A good survey paper of multi-objective evolutionary algorithms is presented in (KONAK *et al.*, 2006).

A summary of the techniques used in multi-objective GAs is presented below.

3.3.1 Fitness function

3.3.1.1 Weighted sum approach

Transforming multiple objectives in a single one using this approach is done by the sum of the normalized objectives multiplied by a weight vector $\vec{w} = w_1, \ldots, w_m$ composed with the weights of the m objective functions, as seen in (3.13), where f is the new objective function, M is the total number of objectives and f'_m the normalized objective functions.

$$f = \sum_{m=1}^{M} f'_m w_m \tag{3.13}$$

This is a straightforward and computationally efficient strategy to solve multi-objective functions. However, the weights have to be given by the user. Additionally, it is possible to obtain only a single answer per run. Therefore, constructing a Pareto front requires multiple runs and depends on the weights. To solve this issue in (HAJELA; LIN, 1992) it is proposed to use different weights for each solution. Other approach in (MURATA; ISHIBUCHI, 1995) proposed to generate random weights for each solution at each generation.

3.3.1.2 Pseudo Pareto approach

This approach is similar to single GAs. However, the population of solutions is divided in M equal sized sub-populations. Then, the fitness of each sub-population is calculated according to the m objective functions. Finally, the selection is done in

conventional ways according to the fitness. Other approaches proposes changing the objective function at each generation.

The main advantage of this strategy is that it is simple. The main problem is that the solutions can be outside of the true Pareto front. Therefore, the answer is a pseudo Pareto front.

3.3.1.3 Pareto approach

In this category are the approaches that use the Pareto dominance concept to try to obtain the true Pareto front by solving multi-objective problems in their original formulation. The selection process is done according to the Pareto dominance of each solution and not according to their fitness. In this approach are created N Pareto fronts according to the dominance of the solutions. Solutions on the front 1 are better than the solutions in the other fronts.

Some of the most representative algorithms in this category are NSGA, NSGA-II, SPEA, SPEA-II, among others. Basically, all these algorithms classify the solutions according to their dominance, make a sorting and then select the better solutions. Usually these approaches also try to find a diverse and uniform Pareto front.

3.3.1.4 Hyper-volume approach

Algorithms based on this approach have similar ideas with the Pareto approach because dominated sorting is used as a ranking criterion. However, this kind of algorithms try to maximize the hyper-volume produced by the non-dominated solutions in the objective space. Thus, the selection operator depends on the maximization of that volume. The hyper-volume measure is a quality indicator to evaluate how well is the distribution of the solutions on the Pareto front. The volume is measured from a dominated point to the non-dominated solutions. According to (FLEISCHER, 2003) maximize the hyper-volume is equivalent to find the Pareto set.

As in the case of Pareto approaches, hyper-volume approaches produce a set of solutions to be used a posteriori. Therefore, the decision making process is performed in the end of the optimization after knowing the complete set of trade-off solutions.

Algorithms based on this approach like SMS-EMOA (BEUME *et al.*, 2007) have shown good results on multi-objective problems. However, the computational cost of computing the hyper-volumes is high.

3.3.2 Diversity conservation

Conservation of the diversity is important to explore solutions that can be promising after evolution. In approaches based on weighted sum the diversity conservation is performed in the same way as in conventional GAs by mutations or by niching. However, in pseudo-Pareto and Pareto approaches, maintaining the diversity aims to obtain solutions uniformly distributed on the Pareto front. In these types of approach niching is one of the techniques used. The difference is that the distance between each pair of solutions is often calculated in the objective space and not in the decision space. Eq. (3.14) shows the calculation of the distance $dz(i,j)$ for the $z_m(i)$ and $z_m(j)$ objective values of the solutions i and j for M objectives, their maximum objective value z_m^{max} and their minimal objective value z_m^{min}. Eq. (3.15) presents the niche count of all solutions i in the solutions space P. The final fitness calculation is performed the same way as in conventional GAs by dividing the original fitness $f(i)$ of a solution i by the niche count $nc(i)$.

$$dz(i,j) = \sqrt{\sum_{m=1}^{M} \left(\frac{z_m(i) - z_m(j)}{z_m^{max} - z_m^{min}} \right)^2} \tag{3.14}$$

$$nc(i) = \sum_{i,j \in P} \max \left(\frac{\sigma_{share} - dz(i,j)}{\sigma_{share}}, 0 \right) \tag{3.15}$$

The other types of diversity conservation techniques are based on the Pareto frontier ranking. Crowding distance was proposed in the NSGA-II algorithm (DEB *et al.*, 2002) and is one of the most known diversity conservation techniques. In crowding distance algorithm first the Pareto frontiers are identified and ranked. Then, in each one of the frontiers the solutions are sorted for each one of the M objectives in ascending order. The crowding distance of first and last solutions are set as ∞ whereas the others are set as 0. In a frontier with L solutions the crowding distance for each i solution is calculated using (3.16) for the solutions $i = 2$ to $i = L - 1$. Then the solutions are sorted according to their crowding distance in descending order. Therefore, the more crowding distance the better, because the solutions are more spaced on the Pareto frontiers. Although there is another approach based on *cell-based density* no explanation is done in this text because of its similarity with the fitness sharing approach. For further information the reader can refer to (CORNE *et al.*, 2000).

$$cd(i) = \sum_{m \in M} \frac{z_m(i+1) - z_m(i-1)}{z_m^{max} - z_m^{min}} \tag{3.16}$$

3.3.3 Selection

Selection in multi-objective GAs can be done applying the techniques used in single-objective GAs. However, most of the successful algorithms use an elitist selection. Basically, the best individuals on the solutions space are selected to survive in the next generation. The difference is that in pseudo-Pareto and Pareto approaches the selection is done according to the Pareto frontier and the crowding distance, or other diversity conservation operations. In the Weighted sum approach same operators as single GAs can be used without concern.

3.3.4 Constraint handling

Most of the real world problems are subjected to constraints. In multi-objective problems same solutions as in single-objective problems can be used, i.e, discard unfeasible solutions, repair unfeasible solutions, produce only feasible solutions by the crossover and mutation operators, or by penalizing the fitness. However, special care is necessary when penalizing the fitness in pseudo-Pareto and Pareto approaches, because the ranking is done according the Pareto front and not according the objective functions by itself. A straightforward strategy to penalize the fitness is to penalize each one of the objective function, so if a solutions is unfeasible their inner objective values are penalized and their rank on the Pareto frontier will be worst.

3.3.5 Execution time problems

Solving real life multi-objective problems requires substantial computer resources and may take a considerable time. The execution time can be drastically reduced through two techniques: 1) Optimizing the code and vectorizing most of the algorithms; 2) By using parallel computing. Parallel computing can be realized in CPU or GPU and considerably reduces the execution time of the algorithms. However, its implementation tends to be difficult and in some cases when using GPUs the performance is lower due to the data exchange between CPU and GPU. Therefore, although the following algorithms were implemented in CPU and GPU, better performance was obtained with parallel CPUs. Since parallel computing is not the main focus of this research, no additional theoretical information is given here.

4 Mathematical model of the problem

An optimal transmission line depends on the specified objectives. Commonly, there exist technical and economical objectives, that in most of the cases are in conflict between themselves. Thus, if a technical optimization is selected (i.e., increase the transmission line capacity or SIL) the cost will increase. On other hand, if an economical optimization is granted, the technical objectives will have poor values.

In this research three technical objectives and one economical objective were modeled. The technical objectives are: increase the SIL (f_1), reduce the ROW (f_3), and reduce the tower height (f_4), meanwhile the economical objective is to decrease the costs (f_2).

The problem to be solve in this research is modeled initially as the maximization problem presented in (4.1). Note that Eq. (4.1) presents four objective functions. The inner objectives in (4.1) are in conflict between them because improving one objective implies deteriorating another, e.g., augmenting the SIL requires more investment on conductors.

$$\max(f_1(x), -f_2(x), -f_3(x), -f_4(x)) \tag{4.1}$$

In the first approach presented in this research, the problem is transformed into the mono-objective problem in (4.2). Note that according to (4.3) to (4.6) f_1' can acquire values between $[-1, \infty)$, meanwhile f_2' to f_4' acquire values between $(-\infty, 1]$. Thus, f_1' is focused on the SIL increments whereas f_2' to f_4' in penalize the solutions that are worst than conventional lines in those objectives (costs, ROW and height).

$$\max f = f_1' + f_2' + f_3' + f_4' \tag{4.2}$$

With:

$$f_1' = SIL_{op}/SIL_o - 1 \tag{4.3}$$

$$f_2' = (Ct_o - Ct_{op})/Ct_o \tag{4.4}$$

$$f_3' = (ROW_o - ROW_{op})/ROW_o \tag{4.5}$$

$$f_4' = (Ht_o - Ht_{op})/Ht_o \tag{4.6}$$

Subjected to:

$$b_{sm_b} \leq b_{s_b} \leq B_{s_b} \tag{4.7}$$

$$d_{f\,ci} \geq \frac{20V_{l\,ci}}{10^{-3}\delta_{r_{ci}}\sqrt{3}} \tag{4.8}$$

$$S_{d\,ci} \geq 1.03\left(\frac{2.0 \cdot 1.1V_{l\,ci} \cdot \sqrt{2} \cdot 1.15}{600\sqrt{3}}\right)^{1.667} \tag{4.9}$$

$$D_{ci_1,ci_2} \geq \max\left(S_{d_{ci_1}} + S_{d_{ci_2}} + t_c,\ \max(d_{f\,ci_1}, d_{f\,ci_2})\right) \tag{4.10}$$

$$m_{V_{l_{ci}}} \leq n_{sc_{ci}} \leq M_{V_{l_{ci}}} \tag{4.11}$$

$$M_{Tx} = 0 \tag{4.12}$$

$$-5 \leq hv_{ci} \leq 5 \tag{4.13}$$

$$E_{soil} \leq 8.33 \tag{4.14}$$

$$E_{sup_k} < E_{crit_k} \tag{4.15}$$

$$b_{E_{ci}} \leq 10 \tag{4.16}$$

$$Pa_{tot} \leq 60 \tag{4.17}$$

$$I_k < A_k \tag{4.18}$$

Where:

CI, ci Set/Index of circuits

K, k Set/Index of sub-conductors

B, b Set/Index of bundles

SIL_o Sum of the surge impedance loading (SIL) of the CI conventional lines at their own voltage levels [MW]

SIL_{op} Sum of the SIL of the CI optimized lines at their own voltage levels [MW]

Ct_o Sum of the costs of the CI conventional lines at their own voltage levels

Ct_{op} Sum of the costs of the CI optimized lines at their own voltage levels

ROW_o Sum of the individual ROW of the CI conventional lines at their own voltage levels [m]

ROW_{op} Total ROW of the optimized tower [m]

Ht_o Sum of the individual height of the CI conventional lines at their own voltage levels [m]

Ht_{op} Total height of the optimized tower [m]

b_{s_b} Bundle size of bundle b [m]

b_{sm_b} Minimum bundle size of bundle b [m]

B_{s_b} Maximum bundle size of bundle b [m]

V_{lci} Line voltage at circuit ci [kV]

$d_{f\,ci}$ Clearance between phases of circuit ci [m]

$d_{f\,ci_1}$ Clearance between phases of circuit ci_1 [m]

$d_{f\,ci_2}$ Clearance between phases of circuit ci_2 [m]

D_{ci_1,ci_2} Clearance between phases of circuits ci_1 and ci_2 [m]

$S_{d_{ci}}$ Disruption distance of circuit ci [m]

$S_{d_{ci_1}}$ Disruption distance of circuit ci_1 [m]

$S_{d_{ci_2}}$ Disruption distance of circuit ci_2 [m]

tc Width of the tower column [m]

$n_{sc_{ci}}$ Wires per bundle at circuit ci

$m_{V_{l_{ci}}}$ Minimum quantity of sub-conductors per bundle at voltage V_{lci} (see Table 4.2)

$M_{V_{l_{ci}}}$ Maximum quantity of sub-conductors per bundle at voltage V_{lci} (see Table 4.2)

M_{Tx} X coordinate of the tower mass center [m]

hv_{ci} Horizontal or vertical distance between central phase and external phases at circuit ci [m]

E_{soil} Maximum electric field on the soil [kV/m]

E_{sup_k} Maximum electric field on the surface of k sub-conductor [kV/cm]

E_{crit_k} Critical electric field in the k sub-conductor [kV/cm]

$b_{E_{ci}}$ Difference on the electric field of the sub-conductors that belong to the same phase at circuit ci [%]

δ_r Air relativity density

Pa_{tot} Total audible noise power in [dB]

I_k Current flowing in the sub-conductor k

A_k Ampacity of sub-conductor k, calculated according the IEEE 738 standard (IEEE Standards association, 2013)

The following mind-map summarizes the optimization problem solved in this research. In green, you can see the objective functions, in orange the constraints, and in blue the optimization algorithms used to solve the problem. In this chapter, the objective functions and constraints are mathematically modeled, whereas the optimization algorithms are explained in chapter 5.

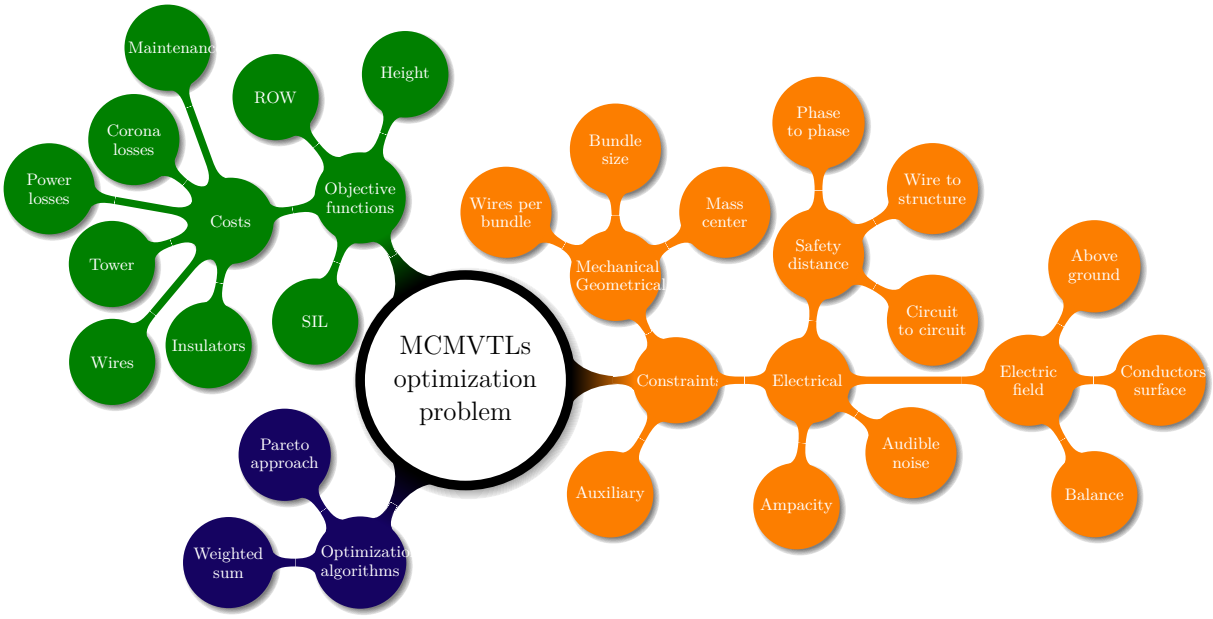

Figure 4.1 – Mind-map summarizing the optimization problem,

4.1 Objective functions

4.1.1 Surge Impedance Loading

The surge impedance loading is a reference for transmission line capacity. Although TLs may operate under heavy loading conditions, SIL is associated to TLs power capacity. When a TL transmits a power equal to its SIL, the self generated and consumed reactive power are the same, so the line has minimum reactive power exchange with the power system. At fundamental frequency (50 or 60 Hz) SIL is defined by the characteristic impedance of the line (z_c) and the line voltage (V_l), as presented in Eq. (4.19). At the same time z_c depends on the positive sequence series impedance ($\tilde{z}_1$) and positive sequence shunt

admittance per unity of length ($\widetilde{y}_1$), as presented in Eq. (4.20) (Electric Power Research Institute, 2005).

$$SIL = \frac{V_l^2}{z_c} \tag{4.19}$$

$$z_c = \sqrt{\frac{imaginary(\widetilde{z}_1)}{imaginary(\widetilde{y}_1)}} \tag{4.20}$$

To obtain the positive sequence parameters $\widetilde{z}_1$ and $\widetilde{y}_1$ it is necessary to find the primitive line matrices $\widetilde{\mathbf{Z}}$ and $\widetilde{\mathbf{Y}}$ (with dimensions of K by K, in which K is the total number of sub-conductors and shield wires) by using the image method represented in Fig. 4.2. Those matrices $\widetilde{\mathbf{Z}}$ and $\widetilde{\mathbf{Y}}$ are reduced to 3 by 3 by using the Kron reduction, incorporating earth wires effect (KRON, 1939). Finally, the positive sequence parameters $\widetilde{z}_1$ and $\widetilde{y}_1$ are obtained by using the Fortescue transformation (FORTESCUE, 1918), supposing that the transmission line is balanced.

In the image method represented in Fig. 4.2 the imaginary sub-conductors are drawn under the soil. When a return current is taken into account an imaginary soil at depth δ appears (DUBANTON, 1969; DERI *et al.*, 1981; TEVAN; DERI, 1984). In the case of $\widetilde{\mathbf{Z}}$ there is a return current on the soil and δ is calculated by the complex depth equation (4.21) where σ_c is the soil conductivity. For $\widetilde{\mathbf{Y}}$ at fundamental frequency analysis there is no return current on the soil, then $\delta = 0$.

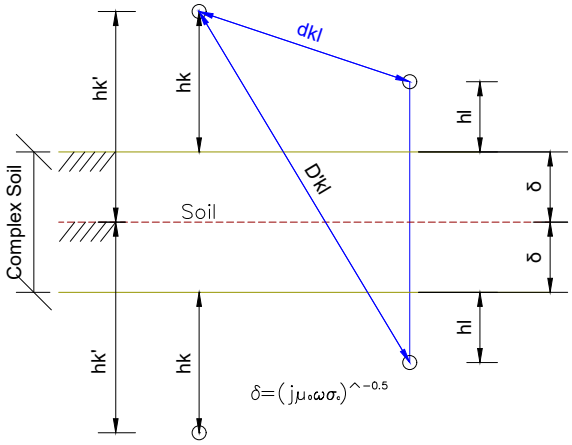

Figure 4.2 – Image method representation.

Each one of the elements of $\widetilde{\mathbf{Z}}$ and $\widetilde{\mathbf{Y}}$ can be calculated using Eqs. (4.22) and (4.23), respectively. Note that the self impedance of a k sub-conductor is denoted as $\widetilde{z}_{kk}$ meanwhile the mutual impedance between a sub-conductor k and l is denoted as $\widetilde{z}_{kl}$. On the other hand, the shunt admittance depends on the potential coefficients matrix $\mathbf{P}$,

composed by the self potential coefficient of the k sub-conductor (p_{kk}) and the mutual potential coefficients between the sub-conductor k and l (p_{kl}).

$$\delta = \frac{1}{\sqrt{j\omega\mu_0\sigma_c}} \tag{4.21}$$

$$\widetilde{z}_{kk} = \frac{j\omega\mu_0}{2\pi} Ln\left(\frac{2\widetilde{h'}_k}{R_k}\right) + r_{DC_k} \quad \widetilde{z}_{kl} = \frac{j\omega\mu_0}{2\pi} Ln\left(\frac{\widetilde{D'}_{kl}}{d_{kl}}\right) \tag{4.22}$$

$$\widetilde{\mathbf{Y}} = j\omega 2\pi\varepsilon_0[\mathbf{P}]^{-1} \quad p_{kk} = Ln\left(\frac{2h_k}{R_k}\right) \quad p_{kl} = Ln\left(\frac{D_{kl}}{d_{kl}}\right) \tag{4.23}$$

On the above equation r_{DC_k} is the internal DC resistance of the sub-conductor k for fundamental frequency. Since the internal reactance does not have high influence at fundamental frequency, it was not considered.

4.1.1.1 SIL calculation of multi-circuit transmission lines

Calculating SIL in multi-circuit TLs is slightly different from the case of single circuit TLs. Dimension of $\widetilde{\mathbf{Z}}$ and $\widetilde{\mathbf{Y}}$ matrices depends on the number of circuits (CI). Thus, the reduced $\widetilde{\mathbf{Z}}_{red}$ and $\widetilde{\mathbf{Y}}_{red}$ matrices are going to be squared with dimension of $3 \cdot CI$. Calculating the sequence component matrices $\widetilde{\mathbf{Z}}_{012}$ and $\widetilde{\mathbf{Y}}_{012}$ follows the next equations (DOMMEL, 1986):

$$\widetilde{\mathbf{T}} = \begin{bmatrix} 1 & 1 & 1 \\ 1 & e^{j\frac{4\pi}{3}} & e^{j\frac{2\pi}{3}} \\ 1 & e^{j\frac{2\pi}{3}} & e^{j\frac{4\pi}{3}} \end{bmatrix} \tag{4.24}$$

$$\mathbf{T}_m = \begin{bmatrix} 0 & 0 & 0 \\ 0 & 0 & 0 \\ 0 & 0 & 0 \end{bmatrix} \tag{4.25}$$

$$\widetilde{\mathbf{T}}_2 = \begin{bmatrix} \widetilde{\mathbf{T}} & \mathbf{T}_m & \cdots & \mathbf{T}_m \\ \mathbf{T}_m & \ddots & \ddots & \vdots \\ \vdots & \ddots & \ddots & \mathbf{T}_m \\ \mathbf{T}_m & \cdots & \mathbf{T}_m & \widetilde{\mathbf{T}} \end{bmatrix} \tag{4.26}$$

$$\widetilde{\mathbf{Z}}_{012} = \widetilde{\mathbf{T}}_2^{-1} \cdot \widetilde{\mathbf{Z}}_{red} \cdot \widetilde{\mathbf{T}}_2 \tag{4.27}$$

$$\widetilde{\mathbf{Y}}_{012} = \widetilde{\mathbf{T}}_2^{-1} \cdot \widetilde{\mathbf{Y}}_{red} \cdot \widetilde{\mathbf{T}}_2 \tag{4.28}$$

Note that $\widetilde{\mathbf{T}}_2$ in equation (4.26) is a squared matrix with dimension of $3 \cdot CI$. The total SIL will be the sum of the SIL of each circuit.

4.1.2 Costs

When designing a transmission line project is highly desired to minimize the costs. Determining these costs with precision is complex because each change on the design affects the costs. Therefore, in this research the most significant costs have been taken into account, trying to have a good reproduction of real costs. However, this will not compromise the comparison between the conventional lines and the optimized lines, because both kind of transmission lines are evaluated with the same calculations, so the degree of cost optimization is fairly calculated.

The total cost C_t (4.43), related to the proposed TLs, involves the cost of: insulators I_{tc} (4.29); phase wires and shielding wires W_{tc} (4.30); support elements for shielding wires S_{tc} (4.31); conductor laying Cl_{tc} (4.32); foundations F_{tc} (4.33); tower re-positioning Rp_{tc} (4.34); commissioning Co_{tc} (4.35); steel and assembling of towers To_{tc} (4.36); power losses $P_{l_{tc}}$ (4.39); corona losses $P_{c_{tc}}$ (4.41); and maintenance of elements M_{tc} (4.42) (ACOSTA; TAVARES, 2017). Note that all the costs are given in [USD].

4.1.2.1 Insulator costs

The costs related to insulators in this research are only the acquisition costs. Maintenance cost are considered as a percentage of the total cost of materials as presented later in (4.42). To calculate the cost of the insulators it is necessary to know the number of standard insulators used per phase.

Table 4.1, adapted from (Electric Power Research Institute, 2005), shows the IEEE recommendation of the number of standard insulators according the voltage level and pollution level. The minimum creepage distance in [mm/kV] according to the IEC 60815 considering the pollution level is 16 for light, 20 for medium, 25 for heavy, and 31 for very heavy contaminated environments.

Table 4.1 – Recommended number of standard insulators according IEEE.

Voltage	Standard units for contamination level (string I/V)			
[kV]	Very Light	Light	Moderate	Heavy
138	6/6	8/7	9/7	11/8
161	7/7	10/8	11/9	13/10
230	11/10	14/12	16/13	19/15
345	16/15	21/17	24/19	29/22
500	25/22	32/27	37/29	44/33
765	36/22	47/39	53/42	64/48

The total cost of insulators can be calculated using (4.29) that in its inner terms takes into account the number of insulators units by means of the insulator leakage distance.

$$I_{tc} = 1.1 \cdot I_c Q_t \sum_{ci=1}^{CI} \frac{3V_{l_{ci}} l_d}{L_d} \tag{4.29}$$

Where:

I_{tc} Total cost of insulators [USD]

I_c Insulator disk cost (21 [USD])

Q_t Quantity of towers per km (3)

CI Total quantity of circuits in the tower

$V_{l_{ci}}$ Line voltage of circuit ci [kV]

L_d Minimal insulator leakage distance of each insulator (445 [mm])

l_d Insulator leakage distance (20 [mm/kV])

4.1.2.2 Wires and Shielding wires costs

The cost of the wires and shielding wires are related to their acquisition (4.30), necessary support elements (4.31) and cost of conductor laying (4.32). These equations were proposed in this research. The constant values were taken from data of electrical companies at the moment in which this document was written. Therefore, they can change at any moment and for each particular project.

$$W_{tc} = 1.1 \sum_{k=1}^{K} L_l M_k C_w \tag{4.30}$$

$$S_{tc} = 120 \cdot Q_t N_{sw} \tag{4.31}$$

$$Cl_{tc} = (6000K + 3500N_{sw}) L_l \tag{4.32}$$

Where:

W_{tc} Total cost of wires and shielding wires [USD]

K Total quantity of sub-conductors in the tower

L_l Line length [km]

M_k Mass per kilometer of the k sub-conductor [kg/km]

C_w Wire cost (4000 [USD/ton] for phase wires and 2000 [USD/ton] for shielding wires)

S_{tc} Total cost of support elements for shielding wires [USD]

Q_t Quantity of towers per km (3)

N_{sw} Total quantity of shielding wires

Cl_{tc} Total cost of conductor laying [USD]

4.1.2.3 Tower costs

Address the cost of the towers requires evaluating the cost of foundations (4.33), re-positioning of tower foundations after field studies (4.34), system commissioning (4.35), and material (4.36) (in this case: steel) considering suspension type towers. Since there are no equations on the literature for foundations F_{tc}, tower re-positioning $R_{p_{tc}}$ and commissioning $C_{o_{tc}}$, they are consider as constants[1] multiplied by the number of towers. On the other hand, Eqs. (4.37) and (4.38) are take from the Bonneville Power Administration (BPA) formula in (MARJERRISON, 1969).

$$F_{tc} = 7200 \cdot Q_t \tag{4.33}$$

$$Rp_{tc} = 500 \cdot Q_t \tag{4.34}$$

$$Co_{tc} = 1000 \cdot Q_t \tag{4.35}$$

$$To_{tc} = \frac{1.1 \cdot C_t To_w}{1000} \tag{4.36}$$

$$To_w = \sum_{k=1}^{K} 0.043 \cdot K_t y_k \left(L_k^{2/3} + T_k^{2/3} + \frac{\sqrt{V_k}}{1.141} \right) \tag{4.37}$$

$$K_t = \sqrt{2.89 + \frac{(3.28 + DF)^2}{400}} \tag{4.38}$$

Where:

F_{tc} Total cost of foundations [USD]

[1] The values were taken from data of electrical companies at the moment in which this document was written.

Rp_{tc} Total cost of reallocation of towers [USD]

Co_{tc} Total cost of commissioning [USD]

To_{tc} Total cost of tower [USD]

To_w Weight of the tower [ton]

C_t Steel cost (7000 [USD/ton])

K Total quantity of sub-conductors in the tower

K_t Auxiliary variable for suspension type towers

y_k Height of k sub-conductor [m]

L_k Longitudinal loads at sub-conductor k [daN]

T_k Transverse loads at sub-conductor k [daN]

V_k Vertical loads at sub-conductor k [daN]

DF Maximum horizontal distance between phases [m]

4.1.2.4 Resistance losses and corona losses costs

All transmission line projects present losses due to the resistance of the cables and occasionally by the corona effect. The resistance losses (4.40) depend on the positive resistance of each transmission line ($r_{+_{ci}}$), meanwhile corona losses (4.41) depend on the sub-conductor diameter and the electric field in the sub-conductor surface (Electric Power Research Institute, 2005). Note that since the projects are designed for a specific life-cycle, the power losses vary along years. For sake of simplicity the corona losses cost is evaluated in normal environmental conditions without rain.

$$P_{l_{tc}} = 8760 \cdot P_l L_f C_{pl} \left(\frac{(1+I_r)^Y - 1}{I_r (1+I_r)^Y} \right) \tag{4.39}$$

$$P_l = \sum_{ci=1}^{CI} r_{+_{ci}} \left[\frac{1}{V_{l_{ci}}} \left(SIL_{ci} + r_{+_{ci}} \left(\frac{SIL_{ci}}{V_{l_{ci}}} \right)^2 \right) \right]^2 \tag{4.40}$$

$$P_{c_{tc}} = 1e^{-3} \cdot 8760 \cdot C_{pl} \sum_{ph=1}^{3ci} \left[P_0 R_{ph}^{1.8} (n_{sc_{ph}} + 6)^2 \cdot 10^{7\left(\frac{E_{sup_{ph}}}{E_{crit_{ph}}} - 0.7 \right)} \right] \tag{4.41}$$

Where:

$P_{l_{tc}}$ Total cost of resistance losses [USD/km] per year

P_l Resistance losses [MWh]

L_f Load factor (0.8)

C_{pl} Power losses cost (36.10 [USD/MWh])

Y Expected life time

I_r Interest rate (8 [%])

CI Total quantity of circuits in the tower

$r_{+_{ci}}$ Positive sequence resistance of each circuit ci $[\Omega/km]$

$V_{l_{ci}}$ Line voltage of circuit ci [kV]

SIL_{ci} SIL of circuit ci [MW]

$P_{c_{tc}}$ Total cost of corona losses per year [USD/km]

P_0 $1.5e^{-2}$ for contaminated and new conductors, or $1.5e^{-3}$ for clean and aged conductors.

$E_{sup_{ph}}$ Maximum electric field at the surface of sub-conductors in phase ph [kV/cm]

$E_{crit_{ph}}$ Critical electric field of sub-conductors in phase ph [kV/cm]

R_{ph} External radius of sub-conductors in phase ph [cm]

$n_{sc_{ph}}$ Number of sub-conductors at phase ph

4.1.2.5 Total costs

The total cost of the project C_t in (4.43) involves the costs explained in the previous sections and the maintenance costs. As seen in (4.42) it was assumed that the maintenance cost M_{tc} is 20% of the total cost of the materials.

$$M_{tc} = 0.2 \cdot [(4.29) + (4.30) + (4.31) + (4.32) + (4.33) + (4.34) + (4.35) + (4.36)] \quad (4.42)$$

$$C_t = (4.29) + (4.30) + (4.31) + (4.32) + (4.33) + (4.34) + (4.35) + (4.36) + (4.39) + (4.41) + (4.42) \quad (4.43)$$

4.1.3 Right of Way

The Right of Way (ROW) or transmission corridor is a set of land used to maintain, repair operate and construct the transmission lines. ROW also serves to

maintain the safety clearances. It varies according to the voltage level and the type of use of near land. The ROW is composed by a wire zone (previously called tower width) that is under the wires plus their maximum swing due to wind, and a border zone that is set for safety clearances.

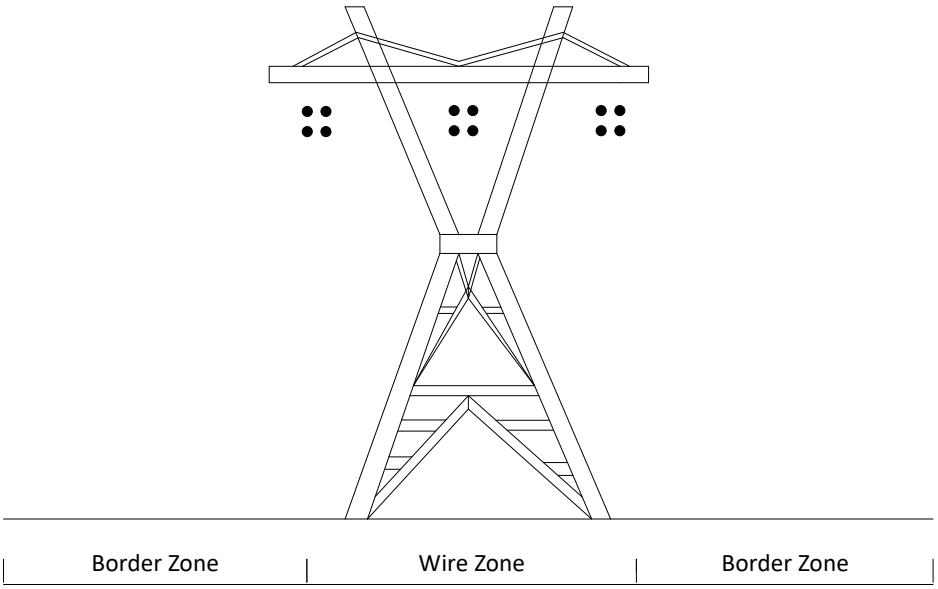

Figure 4.3 – Right of way of a transmission line.

ROW also can be obtained by using the EPRI criteria (Electric Power Research Institute, 2005) related to the audible noise. In 500 kV TLs and above audible noise is an important matter. Normally, it is produced under corona effects and it is measured at the edge of the ROW (Electric Power Research Institute, 2005). Therefore, since we are assuming a maximum electric field of 8.33 kV/m at 1.5 m above the soil, the corresponding ROW is twice the distance from the tower center to where the electric field at 1.5 m above the soil is constantly equal/lower to 1.67 kV/m.

Audible noise can be calculated for different weather conditions. However, since heavy rain condition is one of the most critical operation point, the current research assumes this weather, using Eqs. (4.44) to (4.46) (Electric Power Research Institute, 2005).

if $n_b < 3$:

$$Pa_b = 20\log n_b + 44\log d_b - \frac{665}{E_{max_b}} + k_{n_b} + 75.2 - 10\log D_b - 0.02D_b \quad (4.44)$$

if $n_b \geq 3$:

$$Pa_b = 20\log n_b + 44\log d_b - \frac{665}{E_{max_b}} + \frac{22.9(n_b-1)d_b}{b_{s_b}} + 67.9 - 10\log D_b - 0.02D_b \quad (4.45)$$

$$Pa_{tot} = 10\log \sum_{b\in B} 10^{Pa_b/10} \quad (4.46)$$

Where:

n_b Number of sub-conductors in bundle b

Pa_b Audible noise power at bundle b in [dB]

d_b Diameter of sub-conductors at bundle b in [cm]

D_b Distance from bundle b to measured point in [m]

E_{max_b} Maximum electric field of at bundle b in [kV/cm]

k_{n_b} Auxiliary constant. If $n_b = 1$, then $k_{n_b} = 7.5$, but if $n_b = 2$, then $k_{n_b} = 2.6$

Pa_{tot} Total audible noise power in [dB]

4.1.4 Tower Height

The tower height is defined in such way that the minimal height has to be equal or higher than the mid-span clearance dictated by the 2002 NESC (IEEE, 2001). It has to ensure that electric field at 1.5 m above the ground (E_{soil}) is lower than the maximum allowable values. According to Brazilian standards the maximum E_{soil} is 4.5 kV/m for occasional transit of people and 8.3 kV/m for trained workers.

This objective was created trying to avoid trivial solutions in which all the circuits are allocated one on top of the other with phases in vertical arrangement produced trying to reduce the ROW. Finally, the tower height is calculated as the maximum absolute value of y component of all k sub-conductors.

4.2 Constraints

Real transmission line projects are subjected to several constraints. Most of them are continuous and linear. However, there are also integer and non-linear constraints. The harder constraints to address are the non-linear, i.e., the electric field on the sub-conductors and on the ground. This section shows and models mathematically the constraints used in this research.

4.2.1 Bundle size

The minimal separation of the sub-conductors belonging to the same phase is 45.7 cm according to United States standards and 40 cm according to European standards. However, no upper limits are given. Thus, in theory it is possible to have bundles of high dimensions as in (SALARI, 1993), (MACIEL, 2013), (PORTELA; GOMES, 1998), among

others. However, bundles with those dimensions, i.e., almost 8 m, are very big and there are no mechanical studies to ensure that the towers support those bundles and the loads produced by the wind over them. Therefore, in this research the maximum bundle size was set as 1.5 m, aiming to reduce a possible high mechanical stresses. Lines of 1000 kV naturally have bundles of almost 1.2 m, so this limit is near to actual transmission lines.

4.2.2 Clearance distances

4.2.2.1 Mid-span height

The minimal mid-span height intends to ensure that the personnel and buildings are in a safety distance, not being affected by the electromagnetic field of the transmission lines. Therefore, the minimal height of the tower has to be in agreement to the NESC 2002 (IEEE, 2001). The minimal mid-span clearance (MS) in [m] can be calculated using (4.47).

$$MS = MS_{22kV} + 0.01(V_{LG} - 22) \tag{4.47}$$

Where:

MS_{22kV} Mid-span clearance for lines with maximum rms line-ground voltage between 750 V to 22 kV (5.6 [m])

V_{LG} Maximum rms operating voltage of the line in [kV]

The NSCE 2002 allows the alternative method in (4.48) to calculate the minimal mid-span clearance when the maximum switching-surge factor is known for line to ground voltages higher than 98 kV. This method must be used for line to line voltage higher than 814 kV. However, for a line with operational voltage lower than 169 kV, the mid-span clearance calculated with the alternative approach shall not be less than the calculated in the primary approach in (4.47).

$$MS = 1.03 \cdot c \left[\frac{1.15 \cdot V \cdot PU}{500 \cdot 1.15}\right]^{1.667} \tag{4.48}$$

Where:

V Maximum peak line-ground voltage of the line in [kV].

PU Maximum switching-surge factor of the line-ground voltage of the line in [pu].

c Margin of safety: 1.2 for vertical clearances and 1.0 for horizontal clearances.

Finally, the minimum tower height has to be such as the mid-span height is higher than MS.

4.2.2.2 Distance between phases (air clearance)

The design of air clearances have to be done to avoid flashover and back-flashover on the transmission lines. It depends on the contamination of the zone, because it modifies the creepage distance per kV of line-to-ground voltage and the insulators' power frequency voltage strength. According to the IEC 60815 the minimum creepage distance in [mm/kV] according to the pollution level is 16 for light, 20 for medium, 25 for heavy, and 31 for very heavy contamination. Hence, using the IEC 71-1 and 71-2 the minimal distance $d_{f_{ci}}$ in [m] between phases of each ci circuit can be calculated with Eqs. (4.49) to (4.51).

$$d_{f_{ci}} = \frac{c_d V_{LG_{ci}}}{\delta_{r_{ci}} 10^{-3}} \tag{4.49}$$

$$\delta_{ci} = \frac{3.9210 \cdot p_{b_{ci}}}{273 + T_e} \tag{4.50}$$

$$p_{b_{ci}} = 10^{\log(76) - y_{ci}/18336} \tag{4.51}$$

Where:

c_d Creepage distance [mm/kV].

$V_{LG_{ci}}$ Maximum line-ground over-voltage in circuit ci [kV].

$\delta_{r_{ci}}$ Relative density of the air in circuit ci.

T_e Environmental temperature in [°C].

p_{ci} Barometric pressure in circuit ci position.

y_k Maximum height of sub-conductors in circuit ci [m].

4.2.2.3 Distance to metallic structures (Strike distances)

To avoid back-flashovers the sub-conductors have to be separated by a certain distance from metallic structures and support elements. In a similar way than the mid-span clearance, NESC provides two forms to calculate the tower strike distance S_d. The primary approach in (4.52) is used for lines operating with voltages above 50 kV.

$$S_d = 0.280 + 0.005(V_l - 50) \tag{4.52}$$

Where V_l is the phase-phase voltage in [kV].

The NSCE 2002 allows the alternative method in (4.53) to calculate the minimal tower strike distance when the maximum switching-surge factor is known for line-ground voltages higher than 98 kV. This method must be used for phase-phase voltage higher than 814 kV. However, if calculated for a line with phase-phase voltage lower than 169 kV, the mid-span clearance calculated with the alternative approach shall not be less than the calculated with the primary approach in (4.52).

$$S_d = 1.03 \left[\frac{1.15V \cdot PU}{600}\right]^{1.667} \tag{4.53}$$

Where:

V Maximum peak line-ground voltage of the line in [kV].

PU Maximum switching-surge factor of the line-ground voltage of the line in [pu].

When working with multi-circuit lines, the circuits can be separated in such way that a metallic structure or a support element can be located in the middle of them. Fig. 4.4 illustrate this situation in which a column tower with width tc is located in the middle of two circuits. In this case the distance D_{ci_1,ci_2} between circuits ci_1 and ci_2 have to be (4.54).

$$D_{ci_1,ci_2} \geq \max\left(S_{d_{ci_1}} + S_{d_{ci_2}} + t_c,\ \max(d_{f_{ci_1}}, d_{f_{ci_2}})\right) \tag{4.54}$$

Where:

$S_{d_{ci_1}}$ Strike distance of circuit ci_1 [m].

$S_{d_{ci_2}}$ Strike distance of circuit ci_2 [m].

tc Width of the tower column [m].

$d_{f_{ci_1}}$ Clearance between phases of circuit ci_1 [m]

$d_{f_{ci_2}}$ Clearance between phases of circuit ci_2 [m]

Also it is possible to assume that there is no support elements or towers in the middle of the circuits. In this case D_{ci_1,ci_2} have to be $\geq \max(d_{f_{ci_1}}, d_{f_{ci_2}})$ where $d_{f_{ci_1}}$ is the distance between phases of circuit ci_1 and $d_{f_{ci_2}}$ the distance between phases of circuit $ci2$.

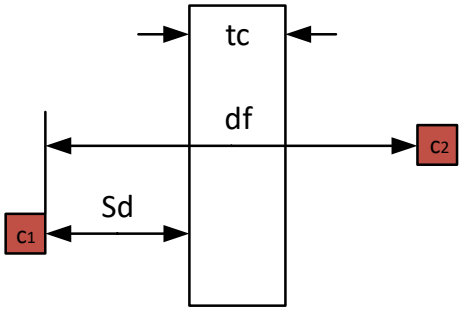

Figure 4.4 – Distance of conductors to tower.

4.2.3 Number of sub-conductors

The quantity of sub-conductors allowed per bundle varies according the operating voltage level as presented in table 4.2. This number of sub-conductors is not standardized, they correspond to the limits proposed in this research, considering regular transmission lines in operation.

Table 4.2 – Allowed number of sub-conductors according to the voltage level.

Voltage [kV]	69/138	230	345	440/500/550	750/765	1000	1150
min n_{sc}	1	2	2	3	4	8	10
max n_{sc}	2	3	4	6	8	10	12

4.2.4 Electric Field

When working with transmission lines in HV/EHV/UHV it is desired to avoid power losses due to Corona effect and avoid overcome the maximum electric field at soil level. According to researches made by (STARR *et al.*, 1927) and (MILLER, 1957) the Corona effect is produced when the electric field on the surface of the sub-conductors overcome the maximum electric field value (E_{crit}). E_{crit} depends on the sub-conductor radius and the environmental conditions and in most of the cases has a value near to 20 kV/cm. On the other hand, according to the Brazilian law nº 11.934/200 of ANEEL (*Brazilian Electrical Agency*) the maximum electric field allowed at 1.5 m above the soil is 8.33 kV/m (60 Hz). To calculate the electric field at any point p it is used the image method presented in Figure 4.5 and the equations (4.55) to (4.57). This method can be extended to any quantity of sub-conductors and voltage level. Thus, for the case of multi-circuit transmission lines the most significant change will be given by the superficial charge on each sub-conductor ($\widetilde{q}_k$) that depends on the voltage of each k sub-conductor and the capacitance matrix ($\widetilde{\mathbf{Q}} = \mathbf{C} \cdot \widetilde{\mathbf{V}}$) (Electric Power Research Institute, 2005).

In this research, we are considering $\widetilde{\mathbf{Q}} = \mathbf{C} \cdot 1.1 \cdot \widetilde{\mathbf{V}}$ when calculating E_{sup_k} at mid-span and for Corona effect calculation. This is to ensure that the electric field has an

adequate value in most of the situations.

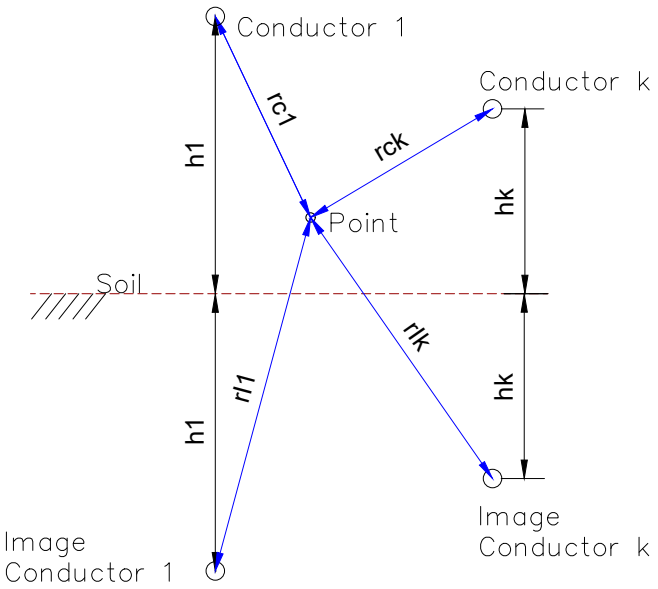

Figure 4.5 – Images method representation for electric field calculation.

$$\widetilde{E}_x = \sum_{k=1}^{K} \frac{q_k}{2\pi\varepsilon_0} \left(\frac{x_p - x_k}{r_c^2} - \frac{x_p - x_k}{r_I^2} \right) = E_{rx} + jE_{ix} \tag{4.55}$$

$$\widetilde{E}_y = \sum_{k=1}^{K} \frac{q_k}{2\pi\varepsilon_0} \left(\frac{y_p - y_k}{r_c^2} - \frac{y_p + y_k}{r_I^2} \right) = E_{ry} + jE_{iy} \tag{4.56}$$

$$E_p = \sqrt{E_{rx}^2 + E_{ix}^2 + E_{ry}^2 + E_{iy}^2} \tag{4.57}$$

Where:

$$r_c^2 = (x_p - x_k)^2 + (y_p - y_k)^2 \tag{4.58}$$

$$r_I^2 = (x_p - x_k)^2 + (y_p + y_k)^2 \tag{4.59}$$

In the above equations ε_0 is the vacuum permittivity; x_p and y_p the coordinates of the analyzed point p; x_k and z_k the coordinates of the k sub-conductor; $\widetilde{E}_x$ the total electric field on the point p in the x axis; $\widetilde{E}_y$ the total electric field on the point p in the y axis; E_p the effective electric field on the point p; and the sub-index r and i denote the real and imaginary part of the corresponding complex variables.

For the calculation of the electric field at the surface of the sub-conductors we are considering 20 points at the sub-conductor's surface. The total electric field at each one of the points in the sub-conductor's surface will be the contribution of each charge and their images, as illustrated in Fig. 4.6. Also, it is important to note that we are using

the real distance from each sub-conductor to another, and not the equivalent geometric mean radius (GMR) value.

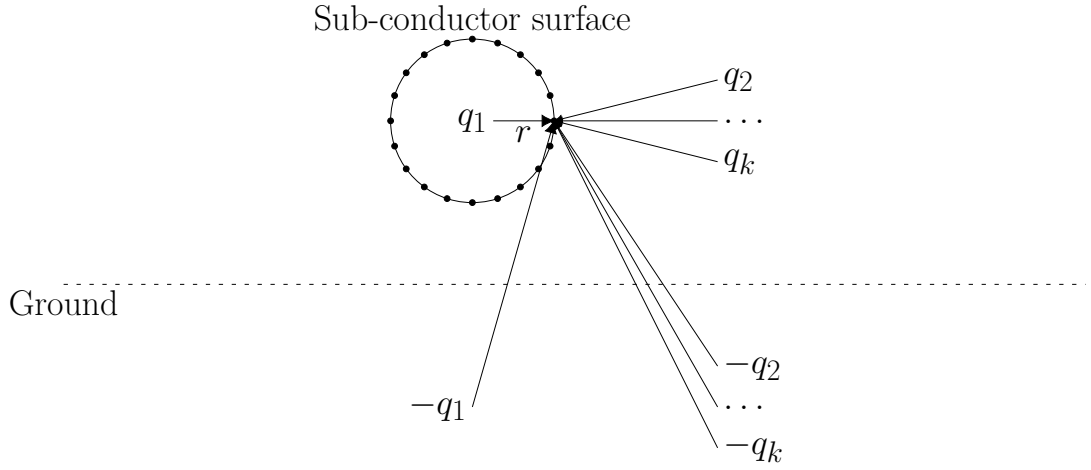

Figure 4.6 – Electric charge contribution at sub-conductors' surface.

4.2.5 Electric field balance

A correct balance on the electric field on the sub-conductors of the same phase is important to avoid overheating one sub-conductor or to reduce losses. Therefore, in this research was established that the maximum difference on the superficial electric field of the sub-conductors can not be higher than 10% of the average superficial electric field of that phase. However, any other value could be selected. It will depend on the designer since this item has no standard.

4.2.6 Ampacity

The ampacity is defined as the maximum allowable current to maintain the sub-conductors under a certain temperature. It can be calculated following the IEEE standard 738 (IEEE Standards association, 2013). At distribution levels, the ampacity is an important limit. However, at transmission levels the ampacity is considerable above the current when transmitting the natural power of the line. Additionally, since the transmission lines have several sub-conductors per bundle, the current in the individual sub-conductors will produce low temperatures. Therefore, although the ampacity was considered in the restrictions, the impact on the solutions is almost null.

4.2.7 Auxiliary constraints

An additional constraint hv_{ci} was created to control the vertical or horizontal distance between the central phase and the axis created by the external phases of the

same circuit. Thus, hv_{ci} does not allow the central phase to be more than 5 m away from that axis. In circuits with phases in delta hv_{ci} works slightly different, controlling the movement of the central phase in a straight line limited by the coordinates of the external phases.

4.2.8 Constraints handling

In order to explore prominent solutions, even if some of them are outside of the feasible region, the objective function has to be penalized when a constraint has been overcome. Therefore, the penalization function presented in (4.60) is proposed. Thus, when the value Cv_c of a constraint $c \in C$ overcomes the limit Cl_c of that constraint, the inner sum in (4.60) is negative (e.g., if E_{crit_k} (Cl_9) is 20 and E_{sup_k} (Cv_9) is 50, the inner sum of (4.60) yields to -1.5). Note that the set C of constraints is composed by the ten proposed constraints presented in (4.7) to (4.16).

$$P = \sum_{c \in C} \begin{cases} \left(\frac{Cl_c - Cv_c}{Cl_c}\right) & \text{if } Cv_c > Cl_c \\ 0 & \text{otherwise} \end{cases} \tag{4.60}$$

Note that the inner term of the sum in (4.60) is negative if some constraint is overcome, and otherwise it is 0. With this model, even solutions outside the feasible region are explored. Therefore, after several generations, solutions outside the feasible region can be improved and migrate to the feasible region.

4.2.9 Final Model

Accordingly, the mathematical model using the weighted sum approach, introducing all the restrictions and the penalization function, is presented in (4.61).

$$\max \quad f'_1 + f'_2 + f'_3 + f'_4 + P \tag{4.61}$$

subject to:

(4.7), (4.8), (4.9), (4.10), (4.11), (4.12) (4.13), (4.14), (4.15), (4.16), (4.17), and (4.18).

Note that the final model has restrictions of type integer, real, complex, linear and non-linear. Therefore, the problem to be solved is a Mixed-integer non-linear programming model (MINLP).

5 Optimization method

In this chapter, two approaches to solve the optimization problem defined in the previous chapter are presented. The first approach is the Weighted sum method which transforms the multi-objective problem into a mono-objective problem. The advantage of this method is the high speed. However, to obtain a Pareto Front is required to do many simulations. On the other hand, the second approach solves the multi-objective problem without any transformation. This approach requires more computational effort, but allows getting a Pareto front in each generation.

5.1 First approach: Weighted sum method

The MINLP problem in (4.61) is solved using a GA. Thus, a set of N possible solutions compounds a population $\mathbf{P_o}$ as shown in (5.1). Each one of the $\vec{S}_n$ candidates solution ($\forall n \in N$) is represented by a chromosome comprised by the variables shown in (5.2).

$$\mathbf{P_o} = \left\{\vec{S}_1, ..., \vec{S}_N\right\}^T \tag{5.1}$$

$$\vec{S}_n = \left\{T_{ty}, \vec{ht}, \vec{Cx}, \vec{Cy}, \vec{c}_{ty}, \vec{n}_{sc}, \vec{D}, \vec{hv}, \vec{co}_{ty}, \vec{r}_x, \vec{r}_y, \vec{r}_{xc}, \vec{r}_{yc}\right\} \tag{5.2}$$

Where:

T_{ty} Base tower type

$\vec{ht}$ Vector formed by the height of each ci circuit (ht_{ic})

$\vec{Cx}$ Vector formed by the X center of each ci circuit (Cx_{ic})

$\vec{Cy}$ Vector formed by the Y center of each ci circuit (Cy_{ic})

$\vec{c}_{ty}$ Base topology of each ci circuit

$\vec{n}_{sc}$ Vector formed by the number of wires at each ci circuit ($n_{sc_{ic}}$)

$\vec{D}$ Vector formed by the D_{ci} value of each ci circuit

$\vec{hv}$ Vector formed by the hv_{ci} value of each ci circuit

$\vec{co}_{ty}$ Vector formed by the conductor type of each ci circuit ($co_{ty_{ic}}$). The 100 ACSR conductor types were numbered from 1 to 100 (ACOSTA; TAVARES, 2017).

$\vec{r}_x$ Vector formed by the $\vec{r}_{x_{ic}}$ component of each ci circuit

$\vec{r}_y$ Vector formed by the $\vec{r}_{y_{ic}}$ component of each ci circuit

$\vec{r}_{xc}$ Vector formed by the $\vec{r}_{xc_{ic}}$ component of each ci circuit

$\vec{r}_{yc}$ Vector formed by the $\vec{r}_{yc_{ic}}$ component of each ci circuit

The general procedure used to optimize (4.61) follows the pseudo code presented in Algorithm 1. Note that since the optimization problem has a large number of constraints, it is necessary to ensure that the initial population is inside the feasible region. From former knowledge of the problem it is known that circular geometries with small bundles usually meet all constraints (ACOSTA; TAVARES, 2017). This is because circular bundles maintain a better electric field balance on the surface of the sub-conductors than other geometries, and smaller bundles have lower superficial electric field than larger bundles. Thus, to generate feasible individuals, it is often sufficient to make all internal elements of $\vec{r}_x$, $\vec{r}_y$, $\vec{r}_{xc}$, and $\vec{r}_{yc}$ equal (it does not imply that $\vec{r}_x = \vec{r}_y = \vec{r}_{xc} = \vec{r}_{yc}$).

Thus, as shown in Algorithm 1, the initial population $\mathbf{P_o}$ is composed by N random solutions generated inside the feasible region. Then, the algorithm begins the main optimization process, composed by the stages of solutions evaluation, insertion of new random solutions, natural selection, crossover and mutation. The stages are executed until the maximum number of generations stabilized is obtained. Then, the final $\mathbf{P_o}$ is evaluated and the natural selection process is performed.

Algorithm 1 Multi-circuit transmission line optimization

```
Initialize parameters and limits
P_o ← N random solutions inside the feasible region
it ← 1
while it < max(generations) do
    Evaluate all solutions in P_o
    P_a ← N/10 random solutions in the feasible region
    P_o ← P_o ∪ P_a
    P_o ← Natural selection of P_o
    S_o ← Crossover of P_o with 90% of probability
    S_o ← Mutation of S_o with 5% of probability
    P_o ← P_o ∪ S_o
    if it = max(generations) then
        Evaluate all solutions in P_o
        P_o ← Natural selection of P_o
    it ← it + 1
```

When working with GAs it is desired to explore the space solutions as much as possible. However, at each iteration the solutions become more similar between themselves, making it more difficult to explore new solutions. To overcome this issue,

there are different strategies like increasing the initial population, choosing a natural selection procedure with low selective pressure, or even introducing new random solutions to the population in each generation. Thus, algorithm 1 introduces in $\mathbf{P_o}$ a population $\mathbf{P_a}$ with 10% of new random solutions at each generation, and uses a natural selection process with a slow selection pressure.

Inside the main optimization processes, at each generation, the first stage computes the value of (4.61) for each one of the solutions in $\mathbf{P_o}$. Then, $N/10$ new random solutions are added to the population $\mathbf{P_o}$. The new $\mathbf{P_o}$ experiment a natural selection process and $\mathbf{P_o}$ is reduced to N solutions. The natural selection is performed through a tournament in which each solution faces $0.4N$ random solutions in $\mathbf{P_o}$. The number of wins of each solution is counted and ranked, and the N solutions with more wins remain on $\mathbf{P_o}$ whereas the others are eliminated. When the natural selection ends, a uniform crossover is performed over $\mathbf{P_o}$ (parents), i.e., a random pair of parents produces with a probability of 90% two sons with combined genetic material. Thus, N sons are produced comprising the population $\mathbf{S_o}$. As happens in nature, a genetic mutation can occur with low probability in any generation. Therefore, the population $\mathbf{S_o}$ can suffer a mutation with a probability of 5%. The mutation of each variable is controlled by gaussians with standard deviation of 0.1 for continuous variables $\left(\vec{ht}, \vec{Cx}, \vec{Cy}, \vec{D}, \vec{hv}, \vec{r}_x, \vec{r}_y, \vec{r}_{xc}, \vec{r}_{yc}\right)$ and 1 for integer variables $(T_{ty}, \vec{c}_{ty}, \vec{n}_{sc}, \vec{co}_{ty})$. After mutation, the new $\mathbf{P_o}$ will be composed by the union of the previous generation $\mathbf{P_o}$ (parents) plus the population $\mathbf{S_o}$ (sons). At this point, the population $\mathbf{P_o}$ has a size of $2N$ that will be reduced to N in the next natural selection stage. That happens in the next generation or immediately (in the same generation) if the algorithm has reached the maximum generation number. At the end, almost all the solutions in $\mathbf{P_o}$ will be very similar and optimized.

5.2 Second approach: Pareto approximation method

Optimization using a Pareto approach does not require to transform the objective function because it is not necessary to get a fitness with only one objective. Therefore, the problem to be solved is initially represented as (5.3) and then as (5.4) by adding the penalization (4.60).

$$\max(f_1'(x), f_2'(x), f_3'(x), f_4'(x)) \tag{5.3}$$

$$\max \quad (5.3) + (4.60) \tag{5.4}$$

subject to:

(4.7), (4.8), (4.9), (4.10), (4.11), (4.12) (4.13), (4.14), (4.15), and (4.16).

NSGA-II was chosen to solve the multi-objective problem by the Pareto approach since it is one of the most representative and consistent algorithms. NSGA-II was modified as presented in algorithm 2 in order to introduce diversity to the population by adding random solutions.

Algorithm 2 Optimization using a modified NSGA-II

```
1: Initialize parameters and limits
2: P_o ← N random solutions inside the feasible region
3: it ← 1
4: while it < max(generations) do
5:     P_a ← N/10 random solutions in the feasible region
6:     P_o ← P_o ∪ P_a
7:     P_o ← Ranking P_o according their Pareto dominance
8:     P_o ← Selection of P_o according their crowding distance
9:     S_o ← Crossover of P_o with 90% of probability
10:    S_o ← Mutation of S_o with 5% of probability
11:    P_o ← P_o ∪ S_o
12:    if it = max(generations) then
13:        P_o ← Ranking P_o according their Pareto dominance
14:        P_o ← Selection of P_o according their crowding distance
15:    it ← it + 1
```

The main difference with Algorithm 1 is that in Algorithm 2 it is used a selection process based on the Pareto frontiers and the crowding distance. Fig. 5.1 graphically describes the process followed by NSGA-II after crossover and mutation. Note that from a population composed by an initial population of parents and a population of sons it is applied the Pareto ranking. Then, the whole population is sorted according to the Pareto frontier in which they belong. The final population begins to be filled by adding all the elements in a Pareto frontier if the size of the new population is lower than the population limit. The process is repeated until a frontier does not fit on the final population. In this case, a selection based on the crowding distance is applied only to the elements of the frontier that does not fit the final population. Then, the best elements according to the crowding distance will join the population and the rest will be deleted. In Fig. 5.1 the population $P + S$ is ranked in five frontiers. The frontier 1 to 3 enter directly to the final population, but since the elements on the frontier 4 do not fit on the final population, a selection based on the crowding distance is performed on them. Then, only the best elements on frontier 4 will be part to the final population.

The main advantage of this Pareto approach is that in a single run it is possible to find several solutions well distributed on the Pareto frontier. However, the complexity

of the algorithm is incremented and so the computational time. For further explanation of NSGA-II it is suggested to consult the original algorithm in (DEB *et al.*, 2002).

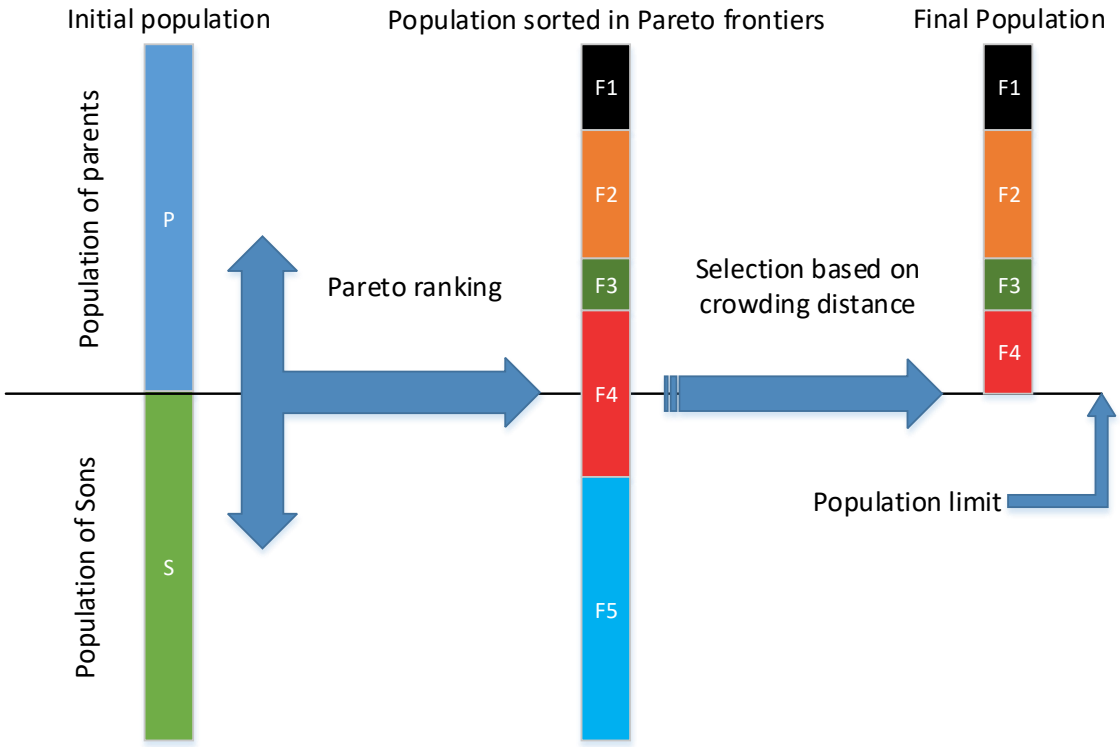

Figure 5.1 – NSGA-II process.

5.3 Techniques used to solve the optimization problem

In the following sections are explained in detail some features used in both approximations to solve the specific problem of this research.

5.3.1 Initial population

Commonly, the GAs initialize the population randomly with normalized values. This allows to explore the whole search space in better form. However, since the problem solved in this research has several restrictions, most of the solutions randomly created are outside the feasible region. Therefore, the initial population is created randomly, but inside the limits imposed by the restrictions. Thus, in the generation of the initial population only feasible solutions are produced.

5.3.2 Geometry generation

To help to solve the problem in (4.2) the sub-conductors' positions of each circuit were mathematically represented. For the sake of simplicity the notation is done

assuming a single circuit. Four possible base circuit types were modeled: vertical in (5.5), horizontal in (5.6), delta in (5.7) and inverted delta in (5.8), where $D = D + d_f$. The variables $(\vec{X}_a, \vec{Y}_a, \vec{X}_b, \vec{Y}_b, \vec{X}_c, \vec{Y}_c)$ denote the (x, y) positions of the sub-conductors in each phase.

The mathematical model of circuits with horizontal configuration is presented in (5.5).

$$\begin{array}{cc} \vec{X}_a = \vec{X}_1 - D & \vec{Y}_a = \vec{Y}_1 \\ \vec{X}_b = \vec{X}_2 & \vec{Y}_b = \vec{Y}_2 + hv \\ \vec{X}_c = -\vec{X}_a & \vec{Y}_c = \vec{Y}_a \end{array} \tag{5.5}$$

The mathematical model of circuits with vertical configuration is presented in (5.6).

$$\begin{array}{cc} \vec{X}_a = \vec{X}_1 & \vec{Y}_a = \vec{Y}_1 - D \\ \vec{X}_b = \vec{X}_2 + hv & \vec{Y}_b = \vec{Y}_2 \\ \vec{X}_c = \vec{X}_a & \vec{Y}_c = \vec{Y}_1 + D \end{array} \tag{5.6}$$

The mathematical model of circuits with delta configuration is presented in (5.7).

$$\begin{array}{cc} \vec{X}_a = \vec{X}_1 - D/2 & \vec{Y}_a = \vec{Y}_1 \\ \vec{X}_b = \vec{X}_2 + hv \cdot D/10 & \vec{Y}_b = \vec{Y}_2 + \sqrt{D^2 + \left(\frac{D}{2}\right)^2} \\ \vec{X}_c = -\vec{X}_a & \vec{Y}_c = \vec{Y}_a \end{array} \tag{5.7}$$

The mathematical model of circuits with delta inverted configuration is presented in (5.8).

$$\begin{array}{cc} \vec{X}_a = \vec{X}_1 - D/2 & \vec{Y}_a = \vec{Y}_1 + \sqrt{D^2 + \left(\frac{D}{2}\right)^2} \\ \vec{X}_b = \vec{X}_2 + hv \cdot D/10 & \vec{Y}_b = \vec{Y}_2 \\ \vec{X}_c = -\vec{X}_a & \vec{Y}_c = \vec{Y}_1 \end{array} \tag{5.8}$$

Where:

$$\begin{array}{cc} \vec{X}_1 = \vec{r}_x cos(\vec{\theta} - \phi_1) & \vec{Y}_1 = \vec{r}_y sin(\vec{\theta} - \phi_1) \\ \vec{X}_2 = \vec{r}_x cos(\vec{\theta} - \phi_2) & \vec{Y}_2 = \vec{r}_y sin(\vec{\theta} - \phi_2) \end{array} \tag{5.9}$$

$$\phi_1 = k_2\pi/n_{sc} \qquad \phi_2 = k_2\pi/n_{sc} + \pi(1 - k_2)/2 \tag{5.10}$$

Eq. (5.9) and (5.10) are used to help to maintain the sub-conductors in the bundles uniformly spaced at the beginning, aiming to obtain a small electric field unbalance on the wires. Furthermore, if n_{sc} is odd $k_2 = 1$, otherwise $k_2 = 0$. It is important to clarify that $\vec{r}_x$, $\vec{r}_y$, $\vec{r}_{xc}$, $\vec{r}_{yc}$, and θ are vectors with dimension of n_{sc}. Additionally, while $\vec{r}_x$, $\vec{r}_y$, $\vec{r}_{xc}$, and $\vec{r}_{yc}$ may accept any continuous value, $\vec{\theta}$ is a vector with equally spaced angles from 0 to 360°. It should be noted that the outer phases have been formulated to be symmetrical. Additionally, the variable D helps to ensure the restriction (4.8). In the case of multi-circuit lines, all the variables from Eqs. (5.5) to (5.8) will have a sub-index ci indicating that belong to the $i-th$ circuit.

Since Eqs. (5.5) to (5.8) produce circuits with the bundle of the lower phase centered in $(0, 0)$, it is necessary to move the circuits to their position in the tower. The variables Cx_{ci} and Cy_{ci} are the displacement of each circuit center in a direction (x, y). However, since the problem has many constraints it is necessary to generate base topologies for the towers, helping to allocate the solutions in the feasible region. As shown in Fig. 5.2 two tower configurations were proposed for double circuit lines (in blue rectangle), four for triple circuit lines (in green rectangle) and six for quadruple circuit lines (in red rectangle).

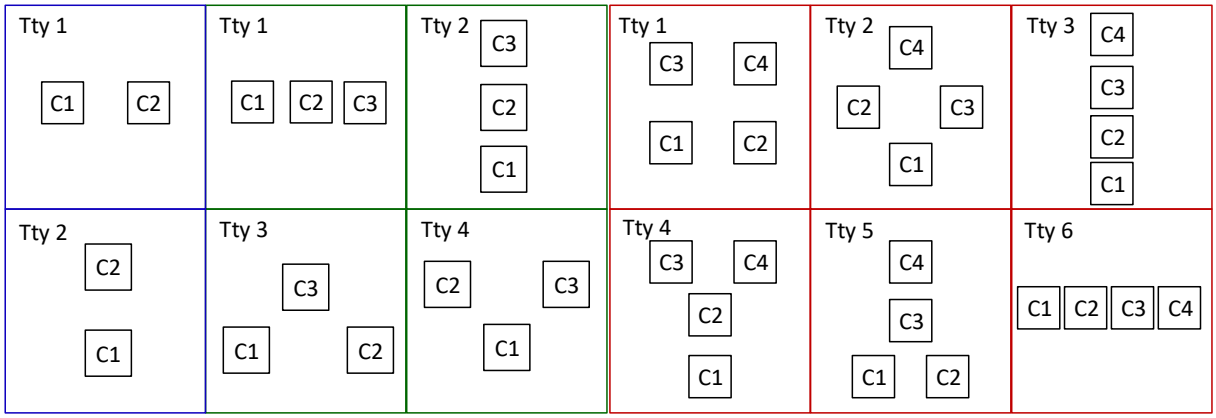

Figure 5.2 – Proposed tower configuration according to the number of circuits.

The mathematical model of each tower configuration was proposed taking into account the restrictions (4.9), (4.10), and (4.14). The specific model for each tower type T_{ty} is presented below by using the center Cx_{ci} and Cy_{ci} of the circuits.

The mathematical model of horizontal geometries for any number of circuits is presented in (5.11) and (5.12). The geometries that correspond to this description are T_{ty_1} in the blue and green box, and T_{ty_6} in the red box.

$$Cx_{ci} = \max(x_{ci-1}) + D_{ci,ci-1} + \frac{|\max(x_{ci}) - \min(x_{ci})|}{2} \tag{5.11}$$

$$Cy_{ci} = Cy_{ci+1} = Cy_{CI} \tag{5.12}$$

Vertical geometries with any number of circuits are modeled with (5.14) and (5.13). The geometries that correspond to this description are T_{ty_2} in blue and green box, and T_{ty_3} in red box.

$$Cy_{ci} = \max(y_{ci-1}) + D_{ci,ci-1} + \frac{|\max(y_{ci}) - \min(y_{ci})|}{2} \tag{5.13}$$

$$Cx_{ci} = Cx_{ci+1} = Cx_{CI} \tag{5.14}$$

The mathematical model of geometry type 3 for the three circuit-line is presented in (5.15) and (5.16).

$$Cx_{ci} = \begin{cases} \max(x_{ci-1}) + D_{ci,ci-1} + \frac{|\max(x_{ci}) - \min(x_{ci})|}{2} & ci = 2 \\ Cx_{ci-2} + \frac{|Cx_{ci-2} - Cx_{ci-1}|}{2} & ci = 3 \end{cases} \tag{5.15}$$

$$Cy_{ci} = \begin{cases} Cy_{ci} = Cy_{ci-1} & ci = 2 \\ \max(y_{ci-1}) + D_{ci,ci-1} + \frac{|\max(y_{ci}) - \min(y_{ci})|}{2} & ci = 3 \end{cases} \tag{5.16}$$

The mathematical model of geometry type 4 for the three circuit-line is presented in (5.17) and (5.18).

$$Cx_{ci} = \begin{cases} \max(x_{ci-1}) + D_{ci,ci-1} + \frac{|\max(x_{ci}) - \min(x_{ci})|}{2} & ci = 2 \\ Cx_{ci-2} + \frac{|Cx_{ci-2} - Cx_{ci-1}|}{2} & ci = 3 \end{cases} \tag{5.17}$$

$$Cy_{ci} = \begin{cases} Cx_{ci} = Cx_{ci-1} & ci = 2 \\ \min(y_{ci-1}) - D_{ci,ci-1} - \frac{|\max(y_{ci}) - \min(y_{ci})|}{2} & ci = 3 \end{cases} \tag{5.18}$$

The mathematical model of geometry type 1 for the four circuit-line is presented in (5.19) and (5.20).

$$Cx_{ci} = \begin{cases} \max(x_{ci-1}) + D_{ci,ci-1} + \frac{|\max(x_{ci}) - \min(x_{ci})|}{2} & ci = 2, 4 \\ Cx_{ci} = Cx_{ci-2} & ci = 3 \end{cases} \tag{5.19}$$

$$Cy_{ci} = \begin{cases} Cy_{ci} = Cy_{ci-1} & ci = 2 \\ \max(y_{ci-1}) + D_{ci,ci-1} + \frac{|\max(y_{ci}) - \min(y_{ci})|}{2} & ci = 3, 4 \end{cases} \tag{5.20}$$

The mathematical model of geometry type 2 for the four circuit-line is presented in (5.21) and (5.22).

$$Cx_{ci} = \begin{cases} \max(x_{ci-1}) + D_{ci,ci-1} + \frac{|\max(x_{ci}) - \min(x_{ci})|}{2} & ci = 2 \\ Cx_{ci-2} + \frac{|Cx_{ci-2} - Cx_{ci-1}|}{2} & ci = 3, 4 \end{cases} \tag{5.21}$$

$$Cy_{ci} = \begin{cases} Cy_{ci} = Cy_{ci-1} & ci = 2 \\ \max(y_{ci-1}) + D_{ci,ci-1} + \frac{|\max(y_{ci}) - \min(y_{ci})|}{2} & ci = 3 \\ \min(y_{ci-2}) - D_{ci,ci-2} - \frac{|\max(y_{ci}) - \min(y_{ci})|}{2} & ci = 4 \end{cases} \tag{5.22}$$

The mathematical model of geometry type 4 for the four circuit-line is presented in (5.23) and (5.24).

$$Cx_{ci} = \begin{cases} \max(x_{ci-1}) + D_{ci,ci-1} + \frac{|\max(x_{ci}) - \min(x_{ci})|}{2} & ci = 2 \\ Cx_{ci-2} + \frac{|Cx_{ci-2} - Cx_{ci-1}|}{2} & ci = 3 \\ Cx_{ci} = Cx_{ci-1} & ci = 4 \end{cases} \tag{5.23}$$

$$Cy_{ci} = \begin{cases} Cy_{ci} = Cy_{ci-1} & ci = 2 \\ \min(y_{ci-1}) - D_{ci,ci-1} - \frac{|\max(y_{ci}) - \min(y_{ci})|}{2} & ci = 3, 4 \end{cases} \tag{5.24}$$

Finally, the mathematical model of the geometry type 5 for the four circuit-line is presented in 5.25 and 5.26.

$$Cx_{ci} = \begin{cases} \max(x_{ci-1}) + D_{ci,ci-1} + \frac{|\max(x_{ci}) - \min(x_{ci})|}{2} & ci = 2 \\ Cx_{ci-2} + \frac{|Cx_{ci-2} - Cx_{ci-1}|}{2} & ci = 3 \\ Cy_{ci} = Cy_{ci-1} & ci = 4 \end{cases} \tag{5.25}$$

$$Cy_{ci} = \begin{cases} Cy_{ci} = Cy_{ci-1} & ci = 2 \\ \max(y_{ci-1}) + D_{ci,ci-1} + \frac{|\max(y_{ci}) - \min(y_{ci})|}{2} & ci = 3, 4 \end{cases} \tag{5.26}$$

5.3.3 Handling the size of solutions

The problem solved in this research optimizes multi-circuit transmission lines with circuits at different voltages on the same tower. Since constraint (4.11) limits the number of sub-conductors per circuit $n_{sc_{ci}}$, according to table 4.2, the variables $\vec{r}_x, \vec{r}_y, \vec{r}_{xc}, \vec{r}_{yc}$ have different dimension depending on $n_{sc_{ci}}$. The problem of dealing with different dimensions is that in order to have the operators of crossover and mutation working properly and being vectorized, the solutions should have the same dimensions. To solve this problem a special process was applied to those variables. The method is described in the next pseudo-code:

Algorithm 3 Handling of variable dimension

1: Identify the higher $n_{sc_{ci}}$
2: Add random numbers to the initial $\vec{r}_x, \vec{r}_y, \vec{r}_{xc}, \vec{r}_{yc}$ until complete a dimension equal to $\max(n_{sc_{ci}})$
3: When applying crossover and mutation use the new $\vec{r}_x, \vec{r}_y, \vec{r}_{xc}, \vec{r}_{yc}$ with dimension given by $\max(n_{sc_{ci}})$
4: When evaluating the fitness use $\vec{r}_x, \vec{r}_y, \vec{r}_{xc}, \vec{r}_{yc}$ with their original dimension given by $n_{sc_{ci}}$

Accordingly, crossover and mutation are performed in solutions with same dimension, composed by the original elements of $\vec{r}_x, \vec{r}_y, \vec{r}_{xc}, \vec{r}_{yc}$ and random elements added to complete the desired dimension. Thus, elements that do no have a contribution to the problem are added. However, the fitness calculation is performed correctly by only taking into account the original dimension of $\vec{r}_x, \vec{r}_y, \vec{r}_{xc}, \vec{r}_{yc}$.

By this simple approach, crossover and mutation can be vectorized improving the computation time.

5.3.4 Algorithm optimization

Since evaluating the objective functions requires complex calculus that can not be vectorized, the execution time is high. Therefore, trying to reduce the computation time, the Matlab tool *profile viewer* was used. With *profile viewer* the functions and calculations with higher time consumption were identified. Then, critical functions were vectorized and the equation systems to be solved were calculated with the Newton's method instead of using the Matlab function *solve()*.

Another approach to reduce the computational time was to calculate the constants just once, save them in external files and load them when needed, e.g., the calculus of the sag was performed just once for each conductor type and then the sag value of a specific conductor was loaded when needed.

Finally, parallel computing was used in the fitness calculus. Therefore, instead of evaluating sequentially the fitness of each solution, several solutions were evaluated in parallel. The number of solutions to be addressed at the same time depends on the number of CPUs or the number of cores in the GPUs in cases with simple operations.

After the aforementioned changes, a reduction of 144 times in the execution time was achieved, compared with the approach without these techniques.

6 Optimized transmission lines

In this chapter are presented some of the transmission lines optimized with the proposed mathematical model. All simulations were performed in a notebook with 8 Gb of RAM, a quad-core i7 7700HQ operating at 2.8 GHz with all the processors running in parallel for the (4.61) and (5.4) computation. To show the efficiency and scalability of the proposed model and algorithm, single, double, triple and quadruple transmission lines with $B_s = 1.5$ m (4.7) were optimized.

Although the algorithm does not limit the voltage of the circuits, only standard voltages were simulated. Additionally, the circuits with higher voltage levels were positioned on top of the circuits with lower voltage levels. This was assumed because the algorithm does not optimize the location of the circuits according to the voltage level. Also, in practical circumstances, it is not reasonable to design circuits with higher voltage at the bottom.

The simulations are divided in two parts: simulations with the Weighted sum method and simulations with a Pareto approach, based on the NSGA-II. Before presenting the optimization results, the execution time with different methods, parameters and using serial or parallel computing is analyzed.

6.1 Execution time

Aiming to determine the parameters that influence the most the computational time used by the algorithms, several parameters were analyzed. The influence of the number of circuits, voltage level, number of generations, population size, serial and parallel execution was investigated. Fig. 6.1 and 6.2 show the influence of the former variables on the computational time used by the algorithm based on the weighted sum approach.

Figs. 6.1a and 6.1b set a fixed number of maximal generations equal to 50 meanwhile it is varied the population size. In 6.1a the voltage level is also modified. Meanwhile, in 6.1b the number of circuits is also modified. On the other hand Fig. 6.1c and 6.1d set a fixed population size equal to 50 meanwhile it is modified the number of maximum generations. Again, in 6.1c the voltage level is also modified and in 6.1d the number of circuits is modified. Accordingly, from Fig. 6.1 it is possible to observe that more generations, circuits and populations imply in higher computational time. No important correlation was observed when varying the population size and the number of generations regarding the computational time. However, the more generations, the more

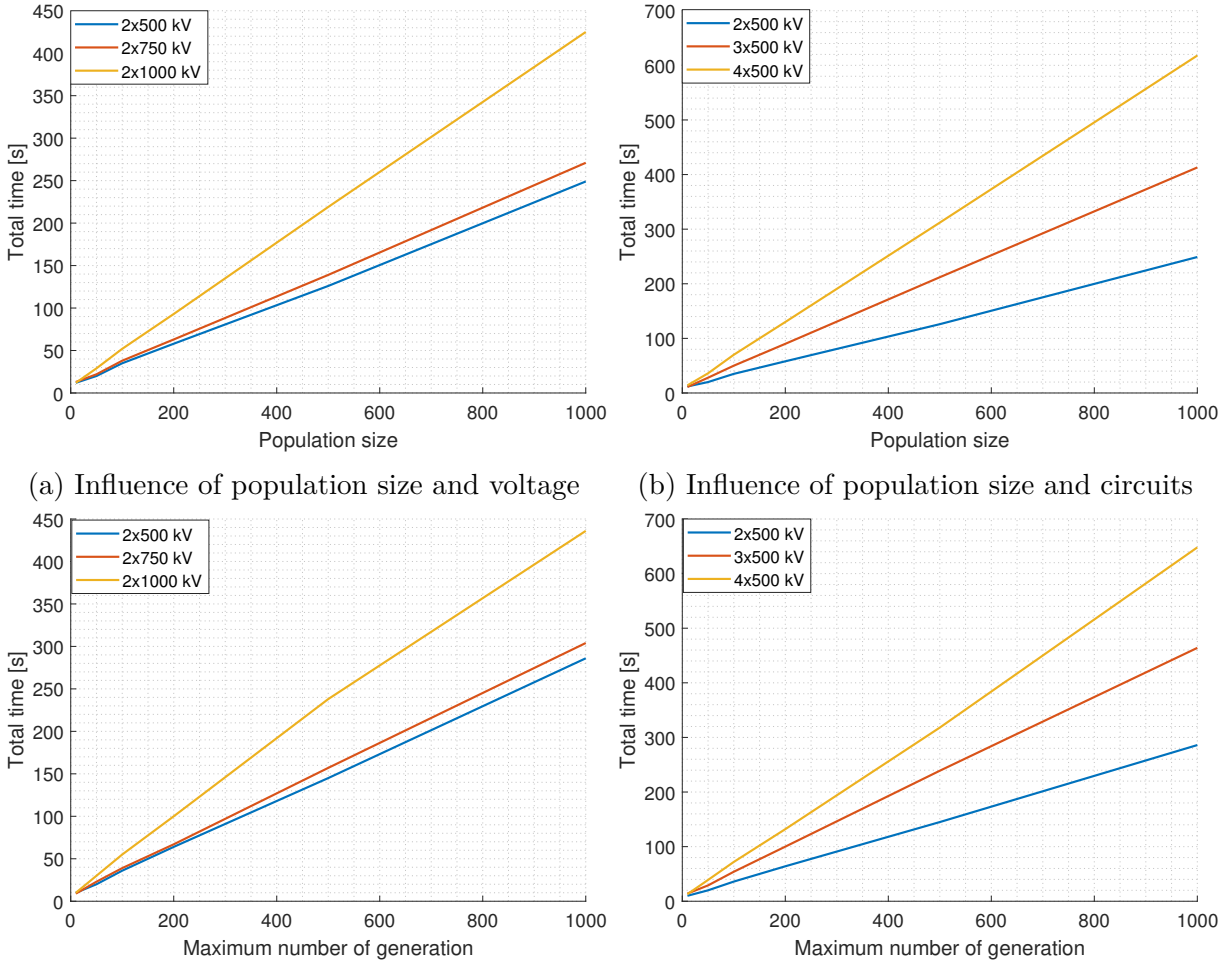

(a) Influence of population size and voltage

(b) Influence of population size and circuits

(c) Influence of generations and voltage

(d) Influence of generations and circuits

Figure 6.1 – Computational time for different situations

opportunity has the population to evolve and improve. Therefore, it is necessary to find an equilibrium between population size and generations to produce good solutions. In section 6.2 it is shown that the fitness can be highly influenced by the population size and number of generations.

In Fig. 6.2 it is shown a comparison between solving the optimization with serial and parallel computing. Note that solving the problem with parallel computing is 2.96 times faster than with serial computing under the same simulation conditions. However, it is possible to conclude that the more generations and circuits, the higher is the time difference between serial and parallel computing.

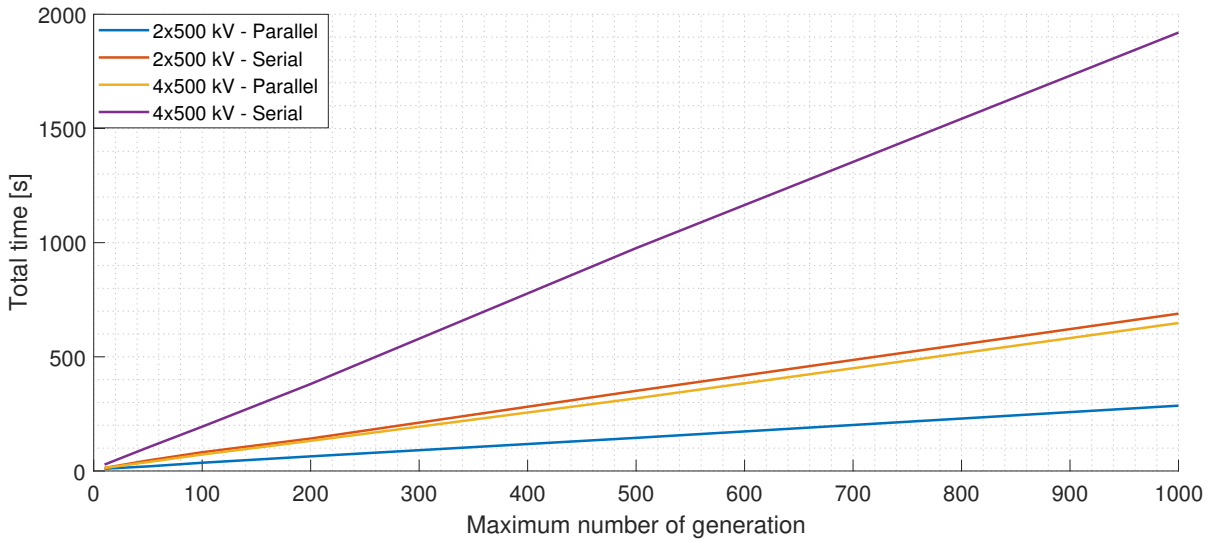

Figure 6.2 – Computational time using serial and parallel computing.

6.2 Influence of simulation parameters on the fitness

Similar analysis was performed to analyze the variations of the fitness according to the population size, number of generations, number of circuits and serial or parallel execution. Fig. 6.3 and 6.4 shows the results obtained when those parameters were varied. Important conclusions can be summarized. 1) It is always observed an evolution on the fitness when increasing the population size and the maximum number of generations. 2) Higher fitness is obtained when the number of circuits is increased. This is because the ROW is better used, having more circuits in a single ROW. 3) Lower fitness increments are obtained when increasing the voltage level. This is derived from two facts. First, higher voltage transmission lines use higher number of sub-conductors, then their natural bundle is higher than lower voltage lines. Therefore, their initial bundle is near to $B_s = 1.5$ m, which is the bundle size limit, making SIL increments harder because it is highly dependent on the bundle size. Second, the electric field on the surface of the sub-conductors increases with the voltage, so it is difficult to increase the SIL because of the electric field restriction. 4) The more generations, the more opportunities to improve the solutions.

Comparing Fig. 6.3a and 6.3c it is possible to observe that when optimizing two multi-circuits transmission lines at 1000 kV the two figures began with negative fitness. However, when increasing the number of generations as in 6.3c the solutions were improved and the fitness became positive over generations, whereas when increasing the population size, although the fitness was improved, no positive values on the fitness were obtained. This is an evidence that even bad solutions can become good solutions with enough time.

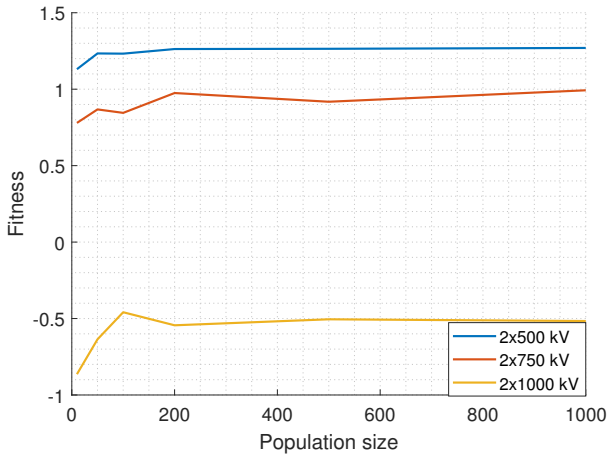

(a) Influence of population size and voltage

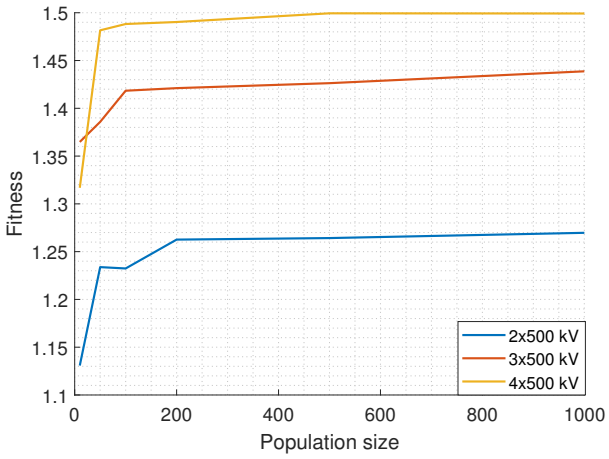

(b) Influence of population size and circuits

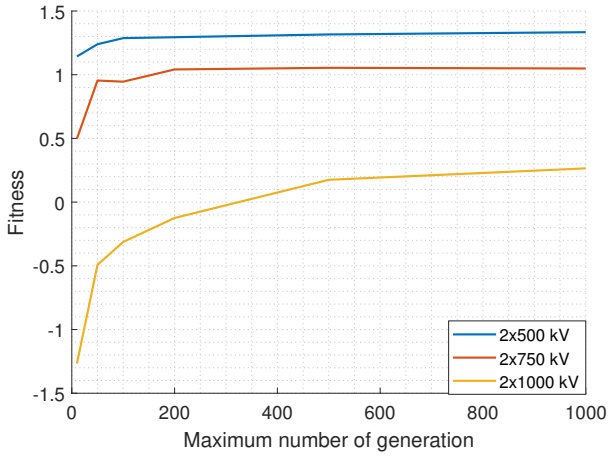

(c) Influence of generations and voltage

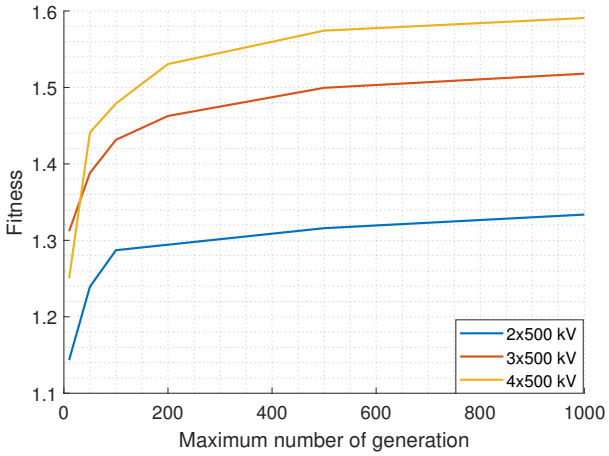

(d) Influence of generations and circuits

Figure 6.3 – Fitness result in pu for different situations

Regarding the serial or parallel execution, Fig. 6.4 shows that no important differences are evidenced when fitness is analyzed. Thus, both approaches achieve almost the same fitness value.

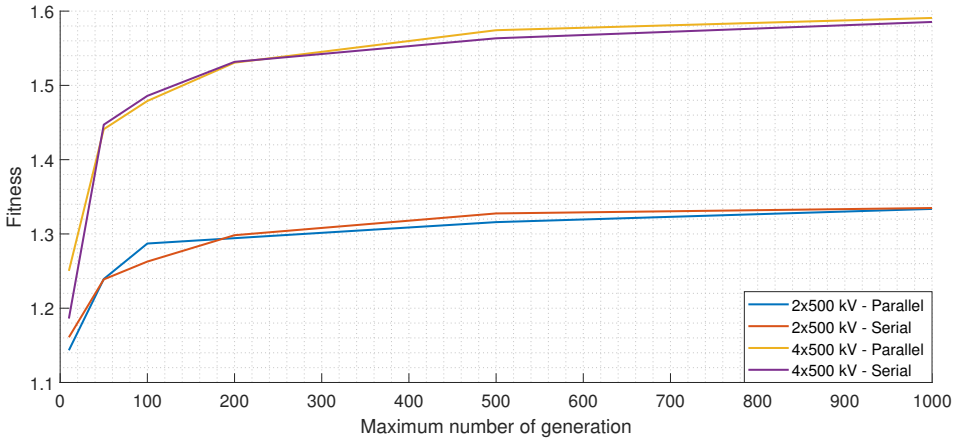

Figure 6.4 – Fitness in in pu and computational time using serial and parallel computing.

6.3 Comparison of Weighted sum approach and Pareto approach

In this section the results using the Weighted sum approach and the Pareto approach based on the NSGA-II are presented. In Fig. 6.5 is shown the time and fitness response when varying the population size, number of maximum iterations, and number of objectives to be addressed on the NSGA-II approach. When refereed to two objectives it means that SIL and $Costs$ are optimized; when refereed to three objectives, SIL, $Costs$ and ROW are optimized; and when refereed to four objectives, SIL, $Costs$, ROW and $Height$ are optimized. For comparison purposes, since the Weighted sum approach only optimizes one objective (4.61), when evaluating the NSGA-II approach the four inner objectives in (5.4) were summed, even if not all of them were used during the optimization.

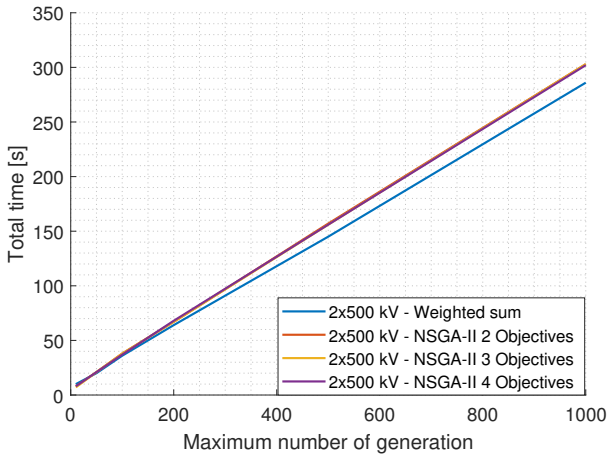

(a) Influence of generations on the time

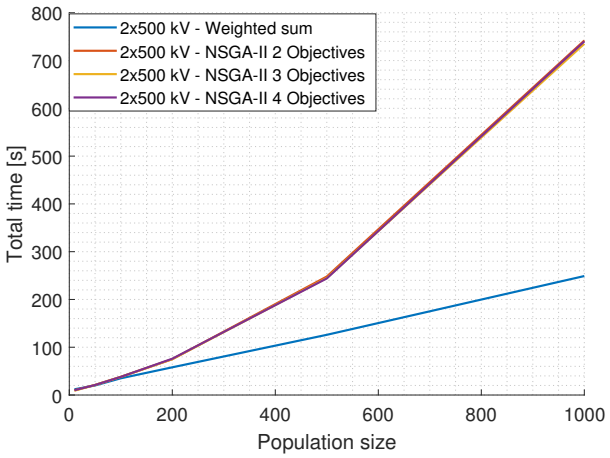

(b) Influence of population on the time

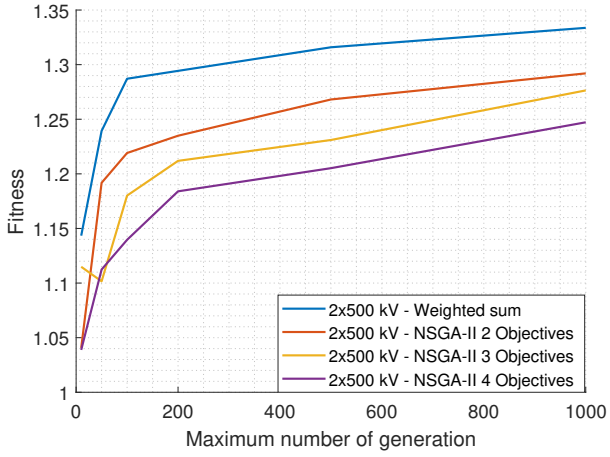

(c) Influence of generations on the fitness

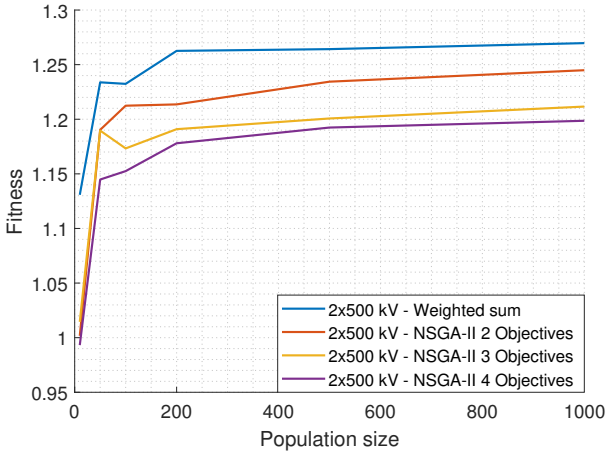

(d) Influence of population on the fitness

Figure 6.5 – Comparison between Weighted sum and NSGA-II. Fitness in pu.

Note in Fig. 6.5 that increasing the population size has a high influence on the time in the NSGA-II approach. The time grows at a fast rate with the population because the dominance ranking depends on the population size and it is computationally expensive. Additionally, the increment is not compensated by savings on the fitness, on

the contrary, the fitness is worst than in the case when the generations are increased. Therefore, the best option is to increase the number of generations rather than the population size. Note that when using NSGA-II the maximum fitness value, calculated as the sum of all inner objectives, was lower than in the case of the Weighted sum approach. That is because NSGA-II creates a Pareto frontier in each iteration, so for obtaining more similar results NSGA-II needs a higher population/generation size. However, as presented in Fig. 6.5 the larger population/generation size, the more time to obtain a solution.

Since the computational time of regular NSGA-II is very high compared with the Weighted sum approach, NSGA-II was modified in order to vectorize the calculus of the Pareto frontiers ranking and the subsequent crowding distance calculation. Additionally, the ranking and the crowding distance was modified to be computed in a single run-time just at the moment in which no more frontiers fit on the final population.

The results of vectorizing the NSGA-II are presented in Fig. 6.6. Note that when vectorized NSGA-II the computational time was greatly reduced. In Fig. 6.6 is presented a comparison for different situations between the Weighted sum approach and NSGA-II vectorized. Compared with Fig. 6.5, now the computational time between the two approaches is very similar even when the population is increased. In the case of the fitness no important changes were observed, so Weighted sum approach is still better when considered the sum of all objectives. However, the NSGA-II vectorized approach becomes better than Weighted sum because the Pareto frontier is obtained in a single execution.

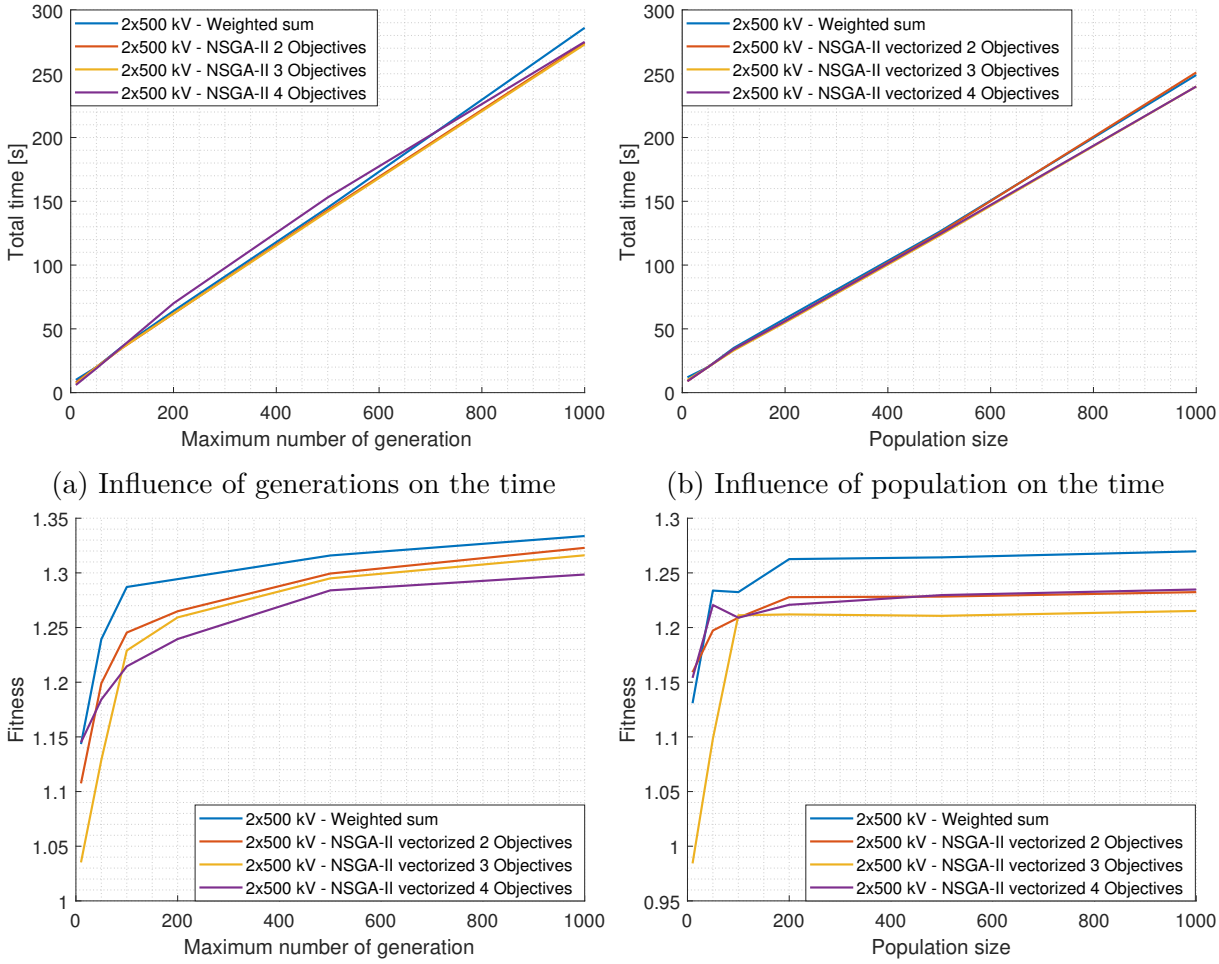

(a) Influence of generations on the time

(b) Influence of population on the time

(c) Influence of generations on the fitness

(d) Influence of population on the fitness

Figure 6.6 – Comparison between Weighted sum and NSGA-II vectorized. Fitness in pu.

6.4 Optimization results with the Weighted sum approach

In this section are presented some solutions obtained with the Weighted sum approach. Many circuits' combinations could be performed and optimized. However, only some selected geometries are presented. The solutions considered different voltage, population size Ni and maximum number of generations g. The characteristics of the chosen optimized lines are shown in Tables 6.1 and 6.2, whereas the geometries are presented in Figs. 6.7 to 6.10. From Table 6.1 it is possible to observe that increasing the SIL always requires more investment. However, the ROW and height in most of the cases will be lower. Only in the single-circuit line case the height was higher because the algorithm chose a delta circuit to increase the SIL. Note that, in overall, the transmission lines of the examples were improved in ranges between 51% to 147%. Any combination of circuits will produce significant increments, even more if the number of circuits increases. Therefore, with more circuits on the same tower more improvement is obtained. However, note that if the circuits have higher voltage levels (e.g., 2x750 - 1x1000 kV transmission

line), it is more difficult to increase the SIL, but still better solutions than conventional lines will be produced.

Table 6.1 – Simulation settings and objective function values - Weighted sum approach

Line [kV]	Ni	g	time [s]	f_1'[%]	f_2'[%]	f_3'[%]	f_4[%]	f[%]
500	300	500	382.49	27.01	-7.36	48.88	-16.91	51.62
2x500	300	500	525.71	24.61	1.04	51.09	35.56	112.30
2x750 - 1x1000	300	500	1001.3	18.97	-7.92	59.51	37.88	108.44
2x230 - 2x500	300	500	773.79	30.78	-7.56	63.49	60.28	147.17

Table 6.2 – Characteristics of the example optimized transmission lines - Weighted sum approach

Line	$n_{sc_{ci}}$	Sub-conductor type	b_s [m]
500 kV	4	Tern	0.94
2x500 kV	4/4	Coot/Coot	1.10
2x750 - 1x1000 kV	4/4/8	Bobolink/Tanager/Coot	1.38
2x230 - 2x500 kV	2/2/4/4	Swift/Swift/Coot/Coot	1.33

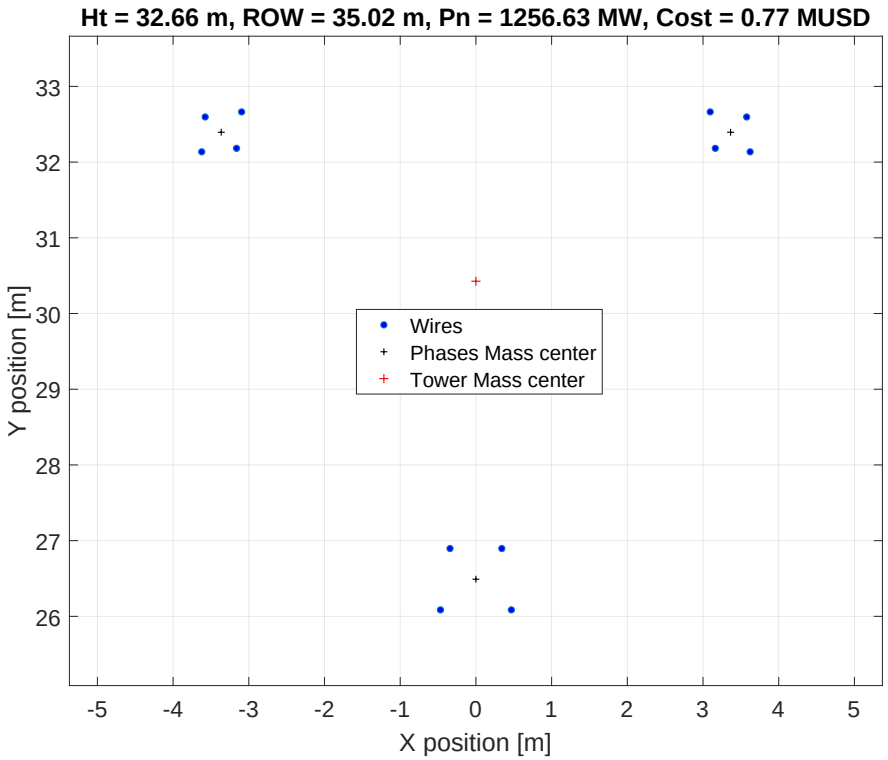

Figure 6.7 – Optimized single-circuit transmission line at 500 kV with weighted sum approach.

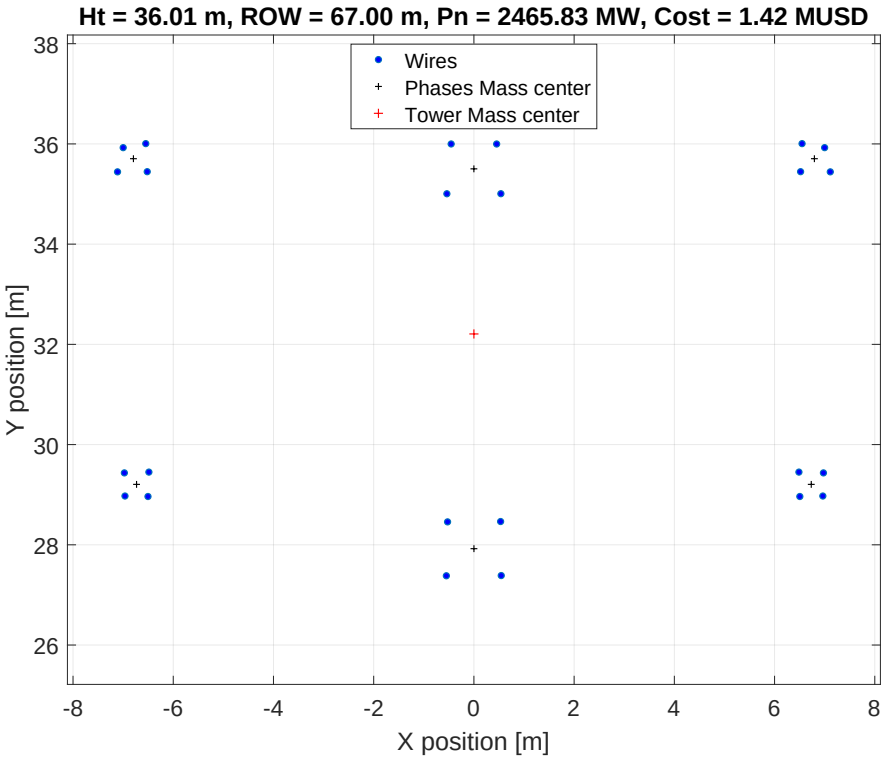

Figure 6.8 – Optimized double-circuit 500 kV transmission line with weighted sum approach.

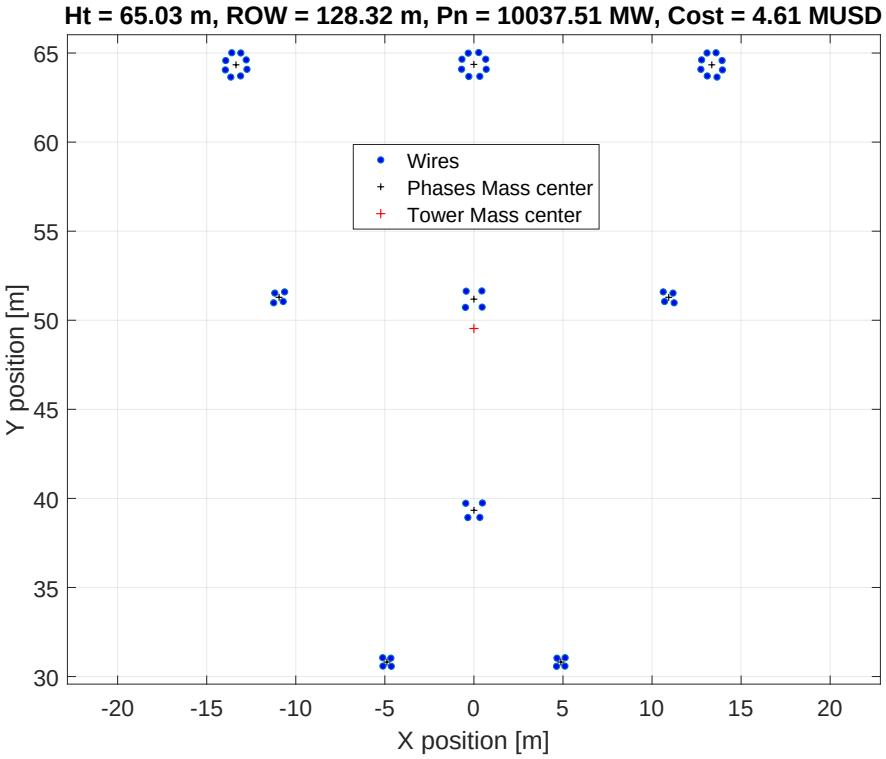

Figure 6.9 – Optimized triple-circuit transmission line at 2x750 kV and 1x1000 kV with weighted sum approach.

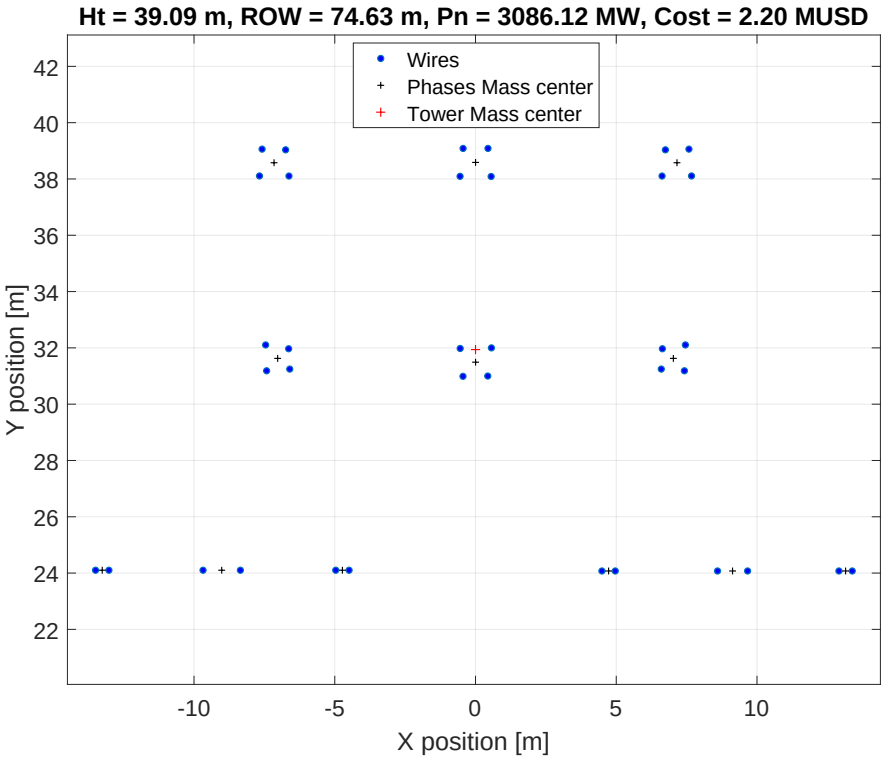

Figure 6.10 – Optimized quadruple-circuit transmission line at 2x230 kV and 2x500 kV with weighted sum approach.

Note that the major advantage of the optimized multi-circuit transmission lines is the ROW reduction (f_3'), obtaining reductions up to 64%, with a good height reduction (f_4'), that in the best case was 60%. At the same time it was possible to obtain high SIL increments (f_1') up to 31%, using bundles smaller than 1.5 m. However, in almost all cases it was necessary to make a higher initial investment because of the use of higher bundles, more quantity of sub-conductors, larger sub-conductors, and more steel in the towers. The highest initial investment was 8% higher than conventional lines. It is also very interesting to observe that different conductor types were proposed for the same voltage level circuit. This is not a predictable result.

Additionally, no matter the quantity and voltage level of the circuits in the tower, the algorithm is always going to optimize all the circuits. Thus, the objective function of a circuit will not be deteriorated by the optimization of other circuit. Therefore the proposed solutions are worth even for towers with circuits belonging to different owners.

6.5 Optimization with Pareto approach

Same quantity of circuits and voltage level than in the previous case was used for the optimization with the NSGA-II based algorithm. Only the vectorized version of

NSGA-II was used. Additionally, since NSGA-II is a Pareto approach, the Pareto frontier when optimizing two and three objectives are presented. However, when optimizing four objectives the Pareto frontier is presented only in two dimensions, since it is not possible to observe a Pareto frontier in more than three dimensions.

Tables 6.3 and 6.4 show the characteristics and results of the simulations performed.

Table 6.3 – Simulation settings and objective function values - Pareto approach

Line [kV]	Ni	g	time [s]	f_1'[%]	f_2'[%]	f_3'[%]	f_4'[%]	f[%]
500	300	500	370.75	29.47	4.83	46.21	-13.17	67.33
2x500	300	500	527.34	44.13	-16.34	57.39	39.41	124.32
2x750 - 1x1000	300	500	997.27	34.93	-2.82	65.97	34.29	132.12
2x230 - 2x500	300	500	833.09	30.19	-5.78	58.91	71.48	152.45

Table 6.4 – Characteristics of the example optimized transmission lines - Pareto approach

Line	$n_{sc_{ci}}$	Sub-conductor type	b_s [m]
500 kV	4	Flamingo	0.72
2x500 kV	5/5	Flamingo/Flamingo	1.20
2x750 - 1x1000 kV	6/6/8	Flamingo/Flamingo/Flamingo	1.37
2x230 - 2x500 kV	2/2/4/4	Rook/Flamingo/Flamingo/Flamingo	1.00

From Tables 6.3 and 6.4 it is possible to observe that the results are slightly better than in the case of Weighted sum approach. Improvements between 67% and 152% were achieved. Again, the highest improvement on the objectives was in the ROW, corresponding to 71%. On the other hand, the lowest improvement was in the $Costs$, showing that it is very hard to increase the other objectives without making higher investments.

Aiming to observe the behavior of NSGA-II when optimizing different quantity of objectives at the same time, the following simulations are presented:

- NSGA-II Optimizing all the objectives and showing a Pareto front of only two objectives: SIL and $Costs$.
- NSGA-II Optimizing three objectives: SIL, $Costs$ and ROW, and showing a three dimensional Pareto front with those objectives.
- NSGA-II Optimizing two objectives: SIL and $Costs$, and showing a two dimensional Pareto front with those objectives.

The selected geometries in Fig. 6.11 to 6.31 correspond to the solution of the Pareto front with higher (4.61), no matter if not all the objectives were optimized.

6.5.1 Optimizing the four objectives at the same time

In this section are presented the results when optimizing (5.4) for the same cases than in the previous approach. Figs. 6.11, 6.14, 6.16 and 6.18 shows the geometries on the Pareto front with higher (4.61). Whereas in Fig. 6.12 is presented the Pareto front of an optimized single-circuit line. Note that trying to represent a four dimensional Pareto front in two dimensions leads to a non-defined Pareto front, so it is not possible to see a direct relation between the objectives. For this reason, only one Pareto front aiming to observe the dispersion of the solutions is presented in this section. However, although is not possible to see the Pareto front, all the solutions correspond to non-dominated solutions.

Nevertheless, there are another forms to observe the behaviour of all objectives. One of them is the *Value Path Method* that presents the normalized value of the objectives for each solution. Note that the value is normalized according to the available values of the objectives in the Pareto front. Therefore, a value of 1 in one objective does not mean that it was improved by 100%, but means that it has the maximum value of the population in that objective. Thus, *Value Path Method* allows to see the trade-off between the objectives, e.g., in Fig. 6.13 the best solution in objective 1 is 80% worst than the best solution of objective 2. In other words, the solution with highest SIL is also the solution with highest $Costs$. Graphs with solutions dispersed on the black bars indicate that the algorithm is good in finding diverse solutions. In 6.13, 6.15, 6.17 and 6.19 the Value Path Graph of each optimization is presented.

Finally, since the results in this section correspond to those presented in Tables 6.3 and 6.4, no further analyzes are done.

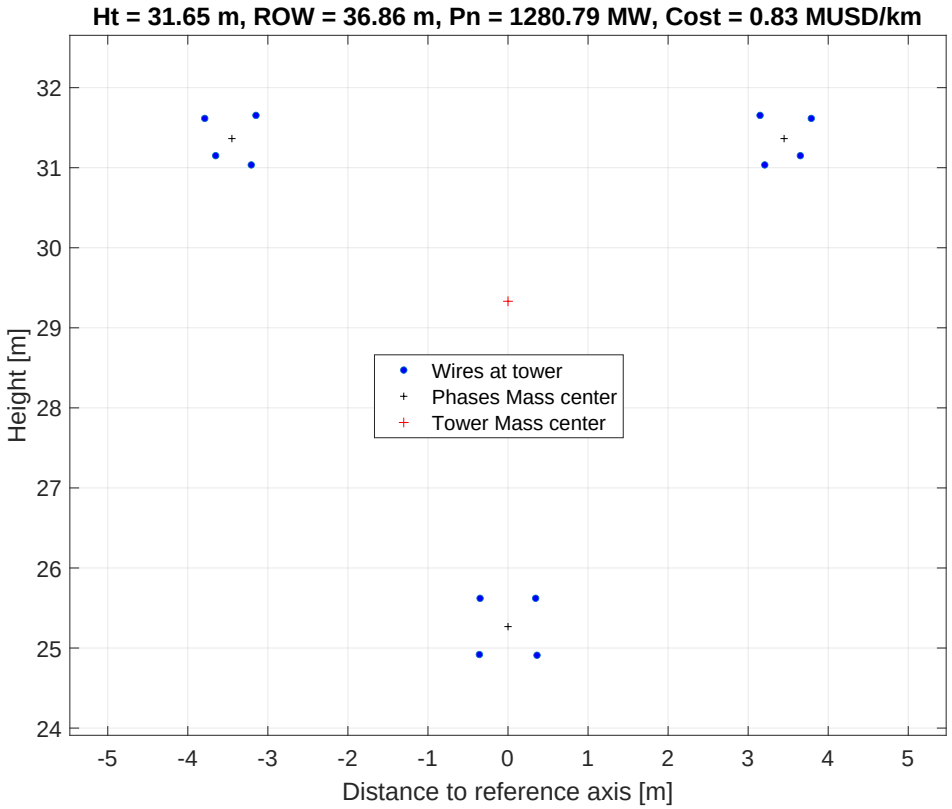

Figure 6.11 – Optimized single-circuit transmission line at 1x500 kV with NSGA-II approach optimizing the four objectives.

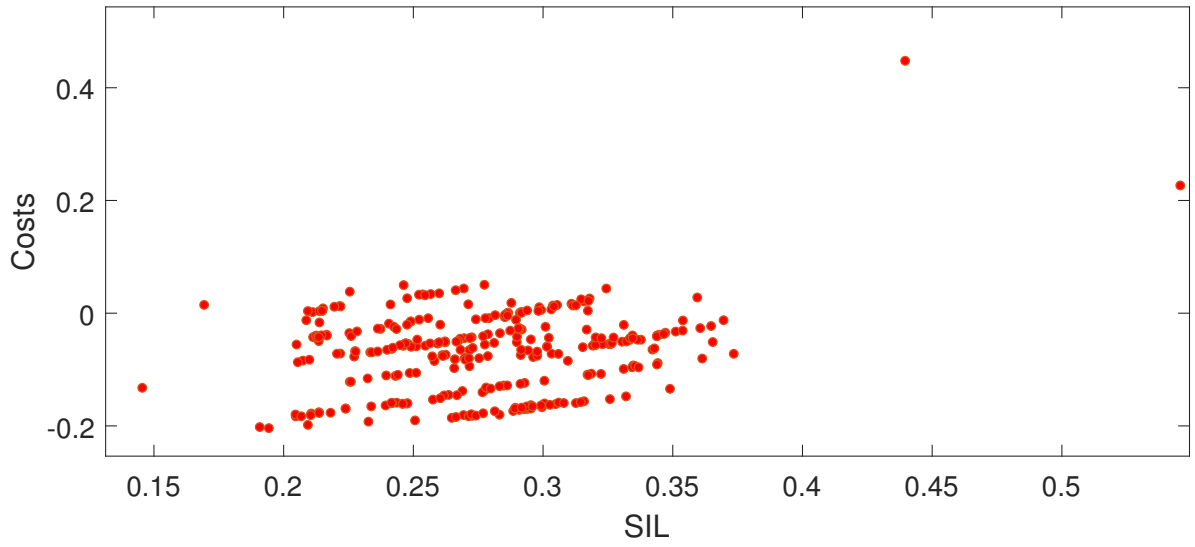

Figure 6.12 – Pareto front for an optimized single-circuit transmission line at 1x500 kV with NSGA-II approach optimizing the four objectives. Values in pu.

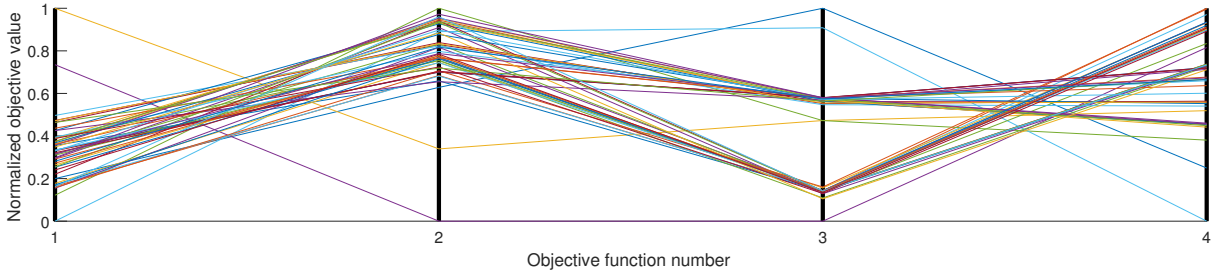

Figure 6.13 – Vale Path Graph for an optimized single-circuit transmission line at 1x500 kV with NSGA-II approach optimizing the four objectives.

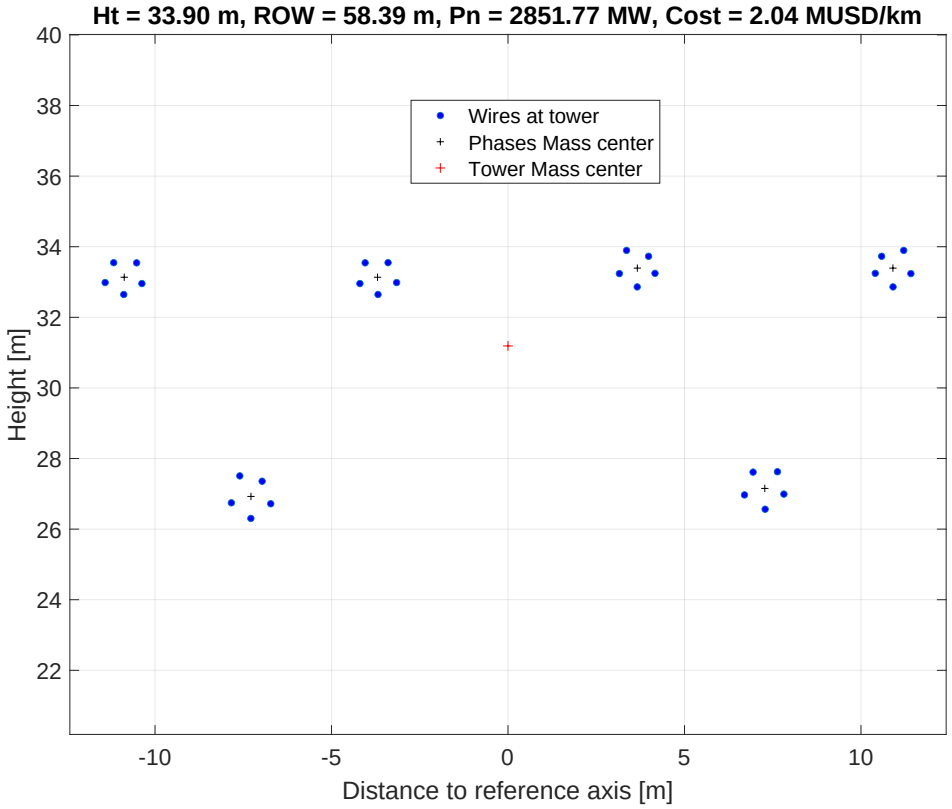

Figure 6.14 – Optimized double-circuit transmission line at 2x500 kV with NSGA-II approach optimizing the four objectives.

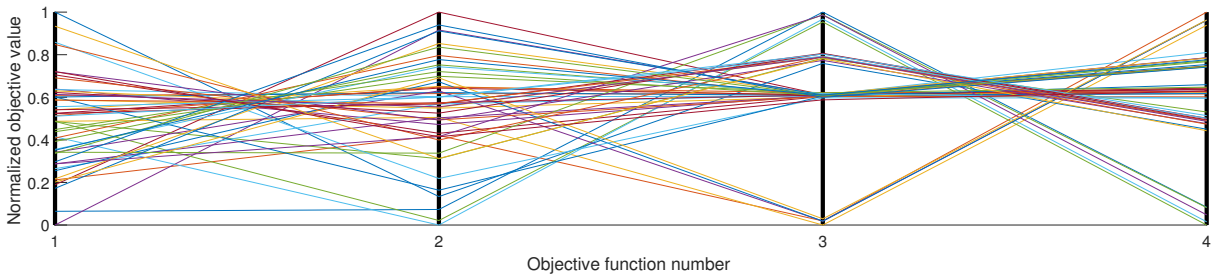

Figure 6.15 – Vale Path Graph for an optimized double-circuit transmission line at 2x500 kV with NSGA-II approach optimizing the four objectives.

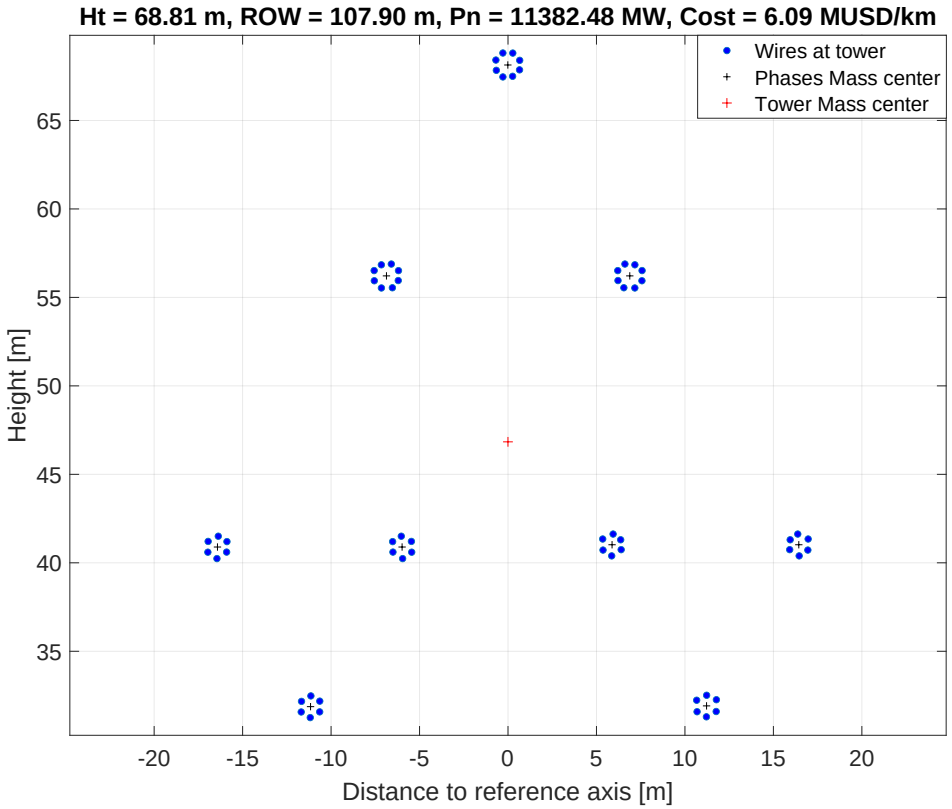

Figure 6.16 – Optimized triple-circuit transmission line at 2x750 kV and 1x1000 kV with NSGA-II approach optimizing the four objectives.

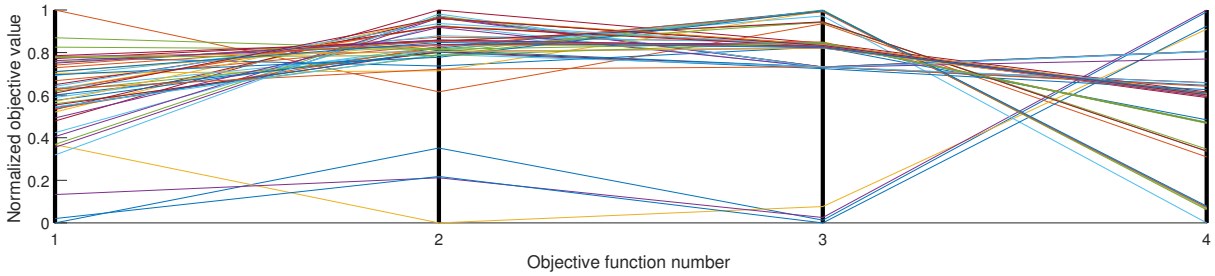

Figure 6.17 – Vale Path Graph for an optimized triple-circuit transmission line at 2x750 kV and 1x1000 kV with NSGA-II approach optimizing the four objectives.

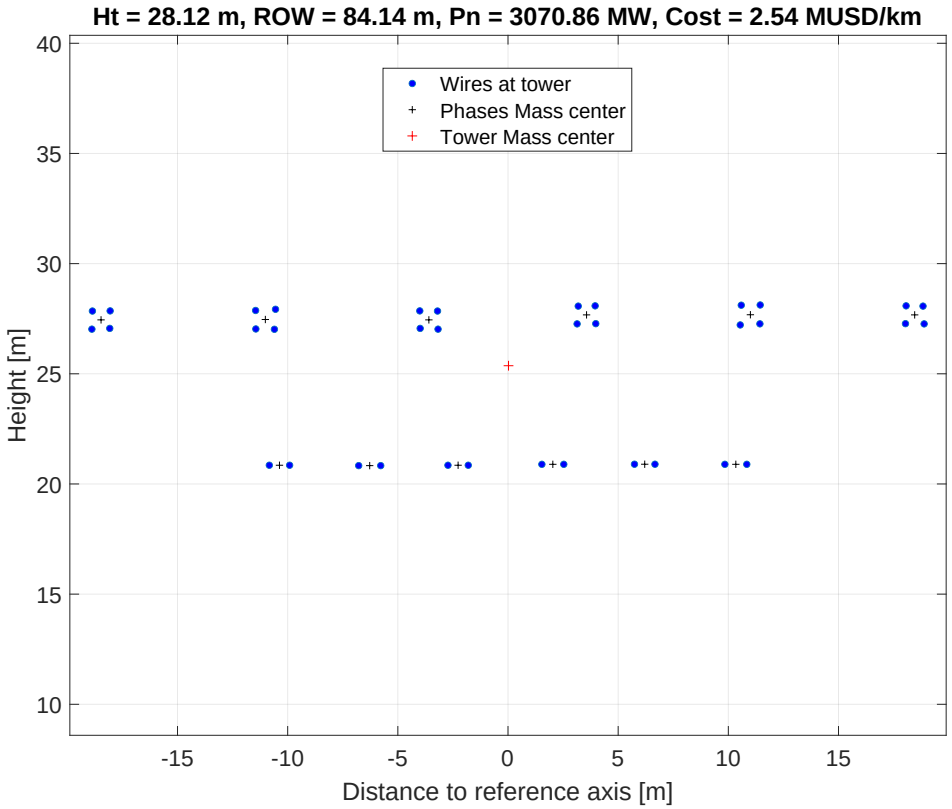

Figure 6.18 – Optimized quadruple-circuit transmission line at 2x230 kV and 2x500 kV with NSGA-II approach optimizing the four objectives.

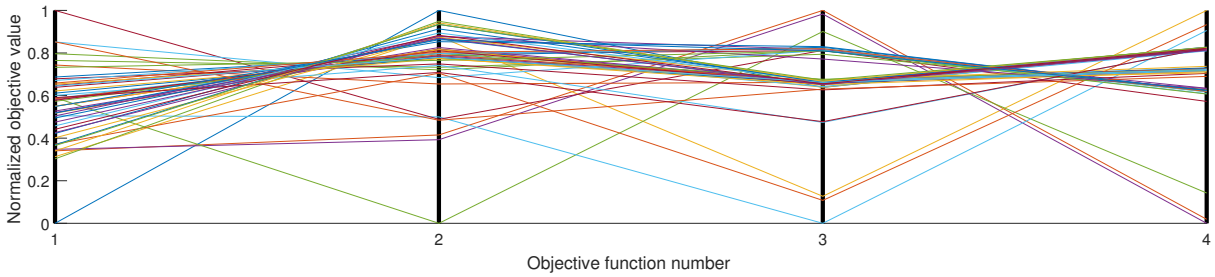

Figure 6.19 – Vale Path Graph for an optimized triple-circuit transmission line at 2x230 kV and 2x500 kV with NSGA-II approach optimizing the four objectives.

6.5.2 Optimizing only three objectives at the same time

In this section, the original problem in (5.4) is changed to the problem in (6.1) and (6.2). Therefore, since only three objectives are being addressed it is possible to construct a three dimensional Pareto front. Figs. 6.20, 6.22 and 6.24 shows the geometries on the Pareto front with higher (4.61). Whereas in Figs. 6.21, 6.23 and 6.25 are presented the Pareto fronts of each optimization.

$$\max(f_1'(x), f_2'(x), f_3'(x)) \tag{6.1}$$

$$\max \quad (6.1) + (4.60) \tag{6.2}$$

subject to:

(4.7), (4.8), (4.9), (4.10), (4.11), (4.12) (4.13), (4.14), (4.15), and (4.16).

From the Pareto fronts it is possible to see that the frontier is not continuous. In a continuous Pareto front all solutions should be near to the lower right corner of the cuboid because the goal is to increase SIL while reducing $Costs$ and ROW. Despite of not being continuous, it is possible to see the relationship between the three objectives. Note that there are some small blue points. They correspond to the solutions dominated by the non-dominated solutions, i.e., the big red circles. The red solutions produce an hyper-plane in which all non-dominated solutions are present.

Regarding the geometries, no important differences were observed compared with the previous case. That is because of two facts: 1) the selected geometries are the geometries with higher (4.61), so it is expected to have similar geometries; 2) Despite of not evaluating the $Height$, the $Costs$ objective function tries to limit the height of the tower. However, in some cases like in Fig. 6.23 it is possible to obtain geometries different than when the four objectives are optimized. In this case, the reason was that the SIL increment was higher than the $Costs$ increments caused by the higher height. Occasionally, since the problem is not convex and the solution method is a genetic algorithm, it is possible to have similar solutions for each run, but not exactly the same.

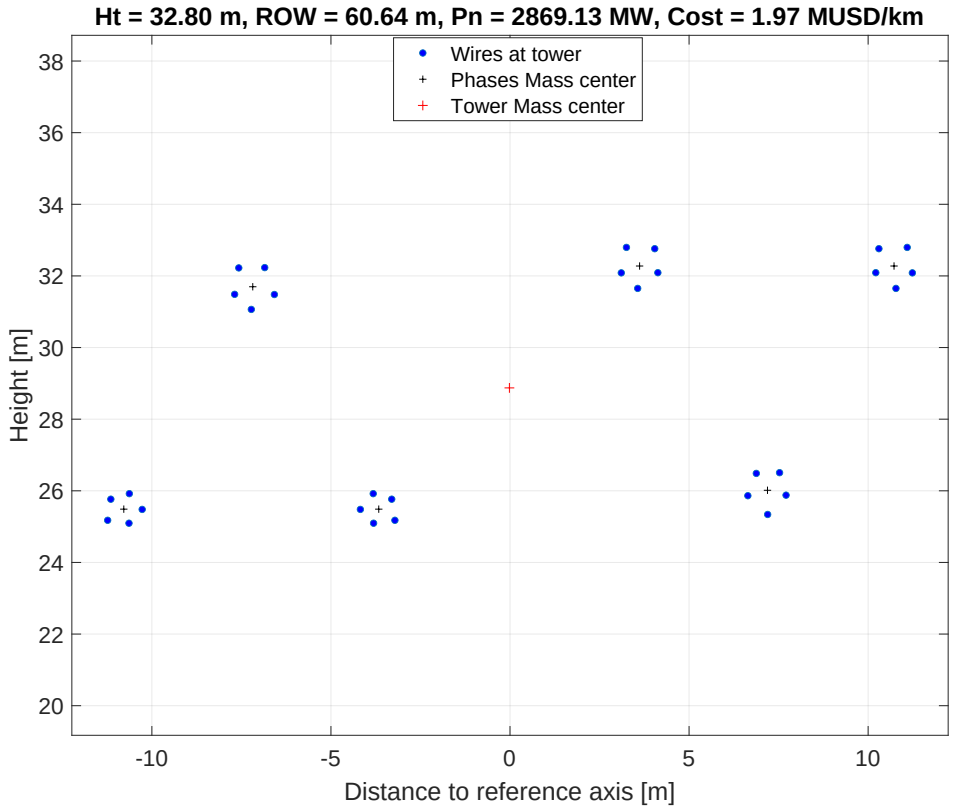

Figure 6.20 – Optimized double-circuit transmission line at 2x500 kV with NSGA-II approach optimizing three objectives.

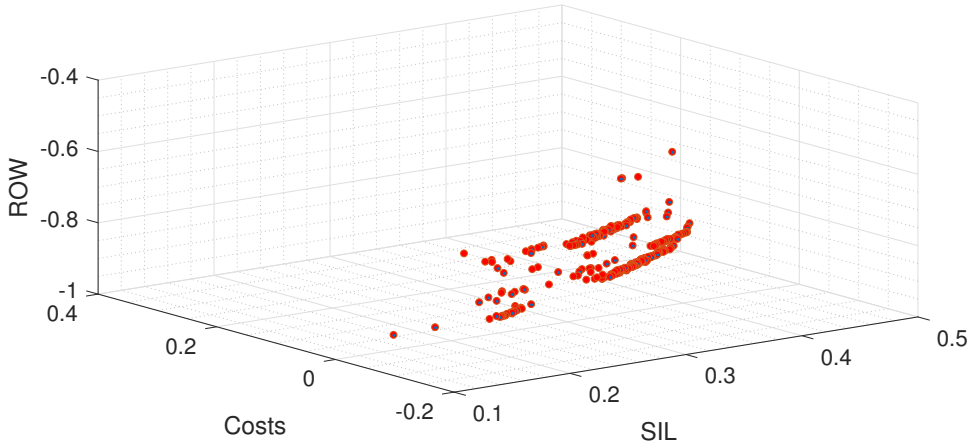

Figure 6.21 – Pareto front for an optimized double-circuit transmission line at 2x500 kV with NSGA-II approach optimizing three objectives. Values in pu.

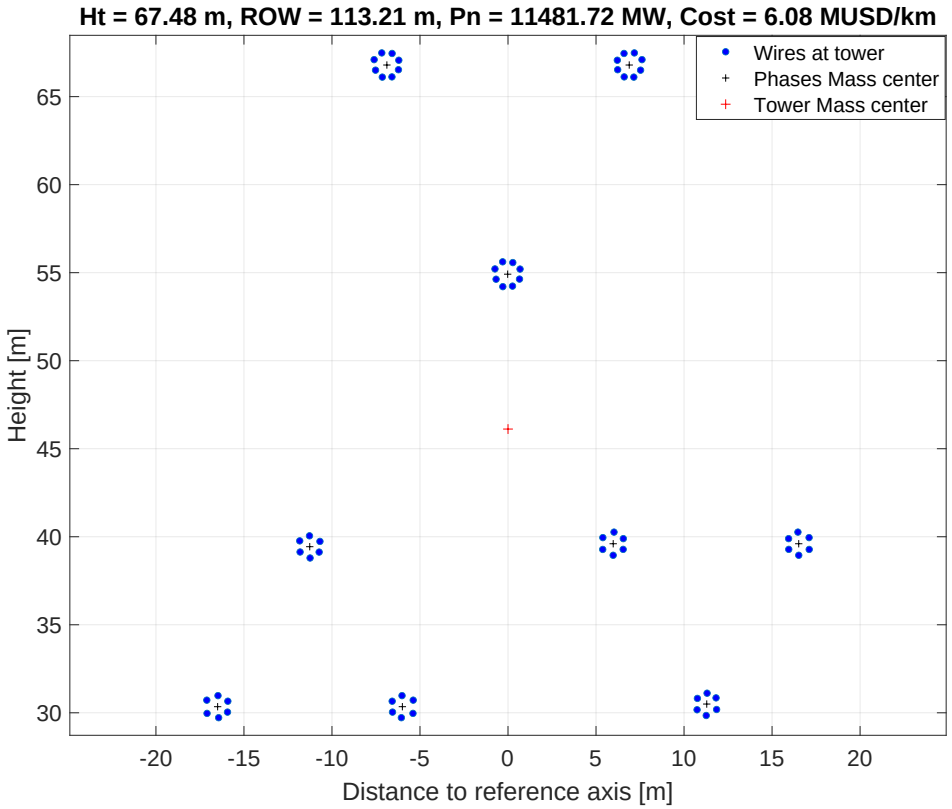

Figure 6.22 – Optimized triple-circuit transmission line at 2x750 kV and 1x1000 kV with NSGA-II approach optimizing three objectives.

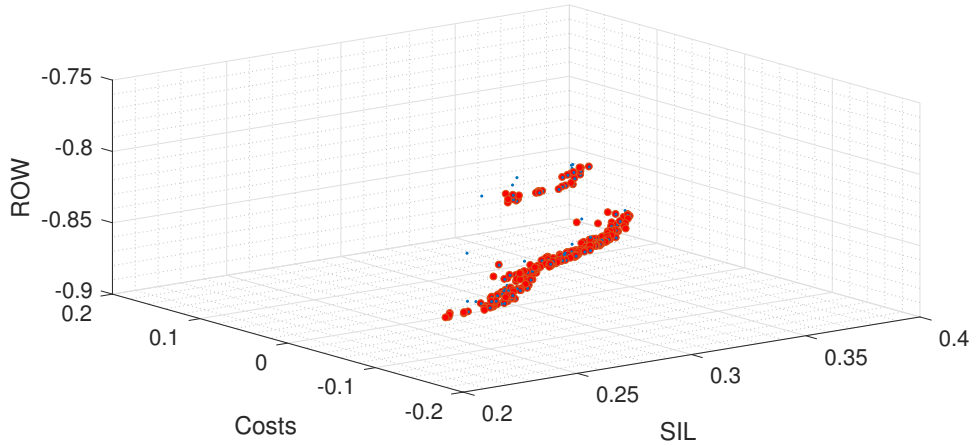

Figure 6.23 – Pareto front for an optimized triple-circuit transmission line at 2x750 kV and 1x1000 kV with NSGA-II approach optimizing three objectives. Values in pu.

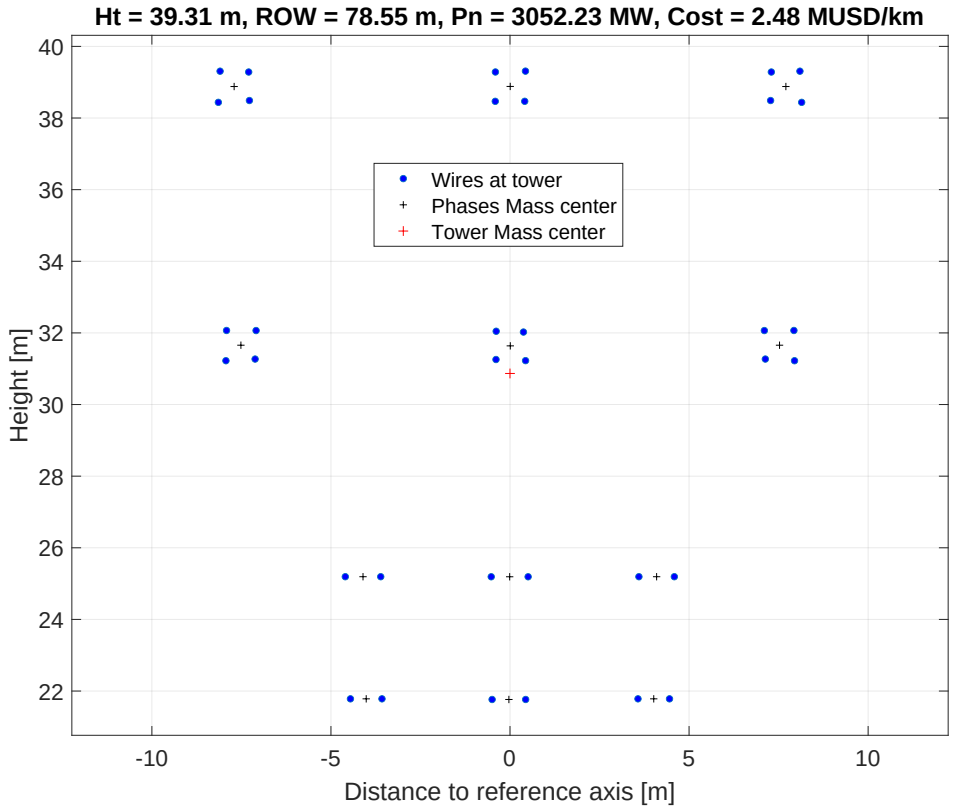

Figure 6.24 – Optimized quadruple-circuit transmission line at 2x230 kV and 2x500 kV with NSGA-II approach optimizing three objectives.

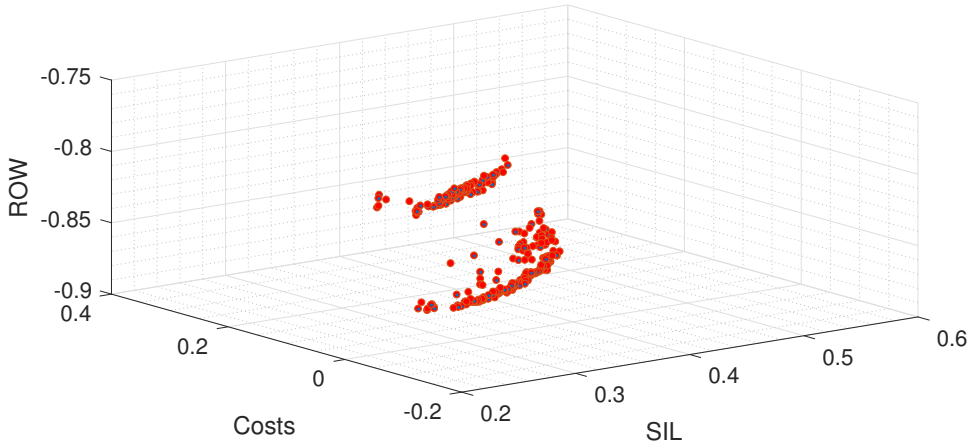

Figure 6.25 – Pareto front for an optimized quadruple-circuit transmission line at 2x230 kV and 2x500 kV with NSGA-II approach optimizing three objectives. Values in pu.

6.5.3 Optimizing only two objectives at the same time

The final test regarding to NSGA-II consider only two objectives for optimizing: SIL and $Costs$. Therefore, the problem to solve is presented in Eqs. (6.3)

and (6.4).

$$\max(f_1'(x), f_2'(x)) \tag{6.3}$$

$$\max \quad (6.3) + (4.60) \tag{6.4}$$

subject to:

(4.7), (4.8), (4.9), (4.10), (4.11), (4.12) (4.13), (4.14), (4.15), and (4.16).

Since only two objectives are being optimized, it is possible to construct a classical two dimensional Pareto front. Figs. 6.26, 6.28 and 6.30 shows the geometries on the Pareto front with higher (4.61). Whereas in Figs. 6.27, 6.29 and 6.31 are presented the Pareto fronts of each optimization.

Note that in all the cases an almost continuous Pareto front was obtained. Here it is clear that there is a trade-off between SIL and $Costs$. Thus, by using the Pareto front the designers can choose the geometries accordingly to their specific needs.

Again, when the geometries are analyzed, no remarkable differences with the two previous cases were observed. The reason is the same as in the previous case.

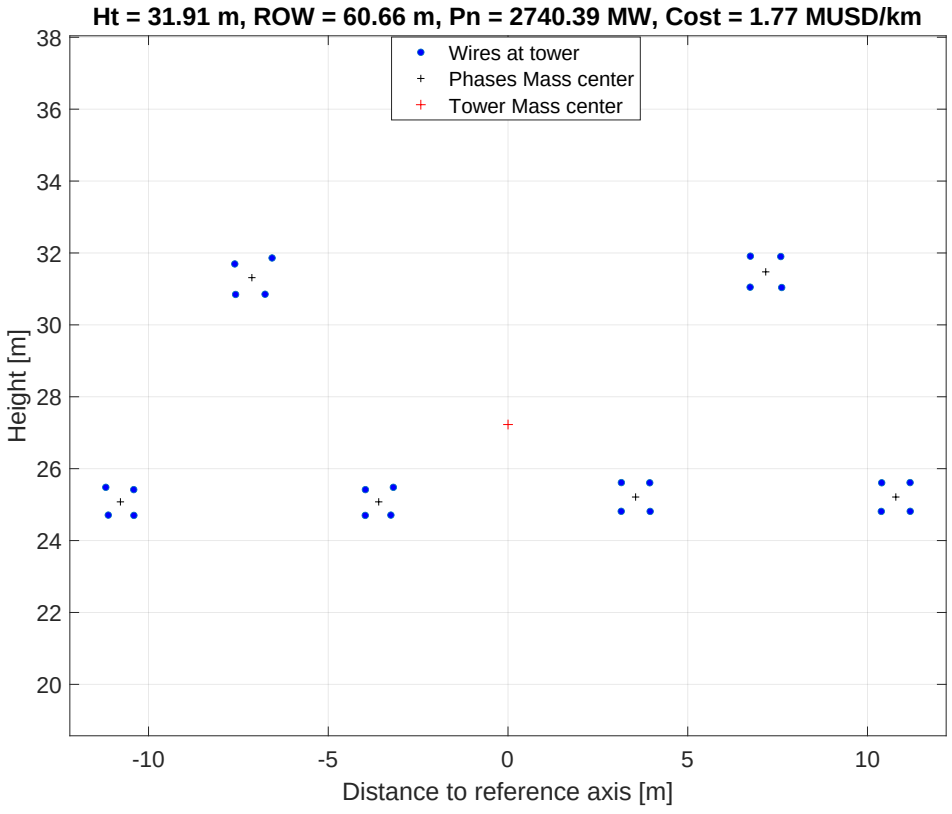

Figure 6.26 – Optimized double-circuit transmission line at 2x500 kV with NSGA-II approach optimizing two objectives.

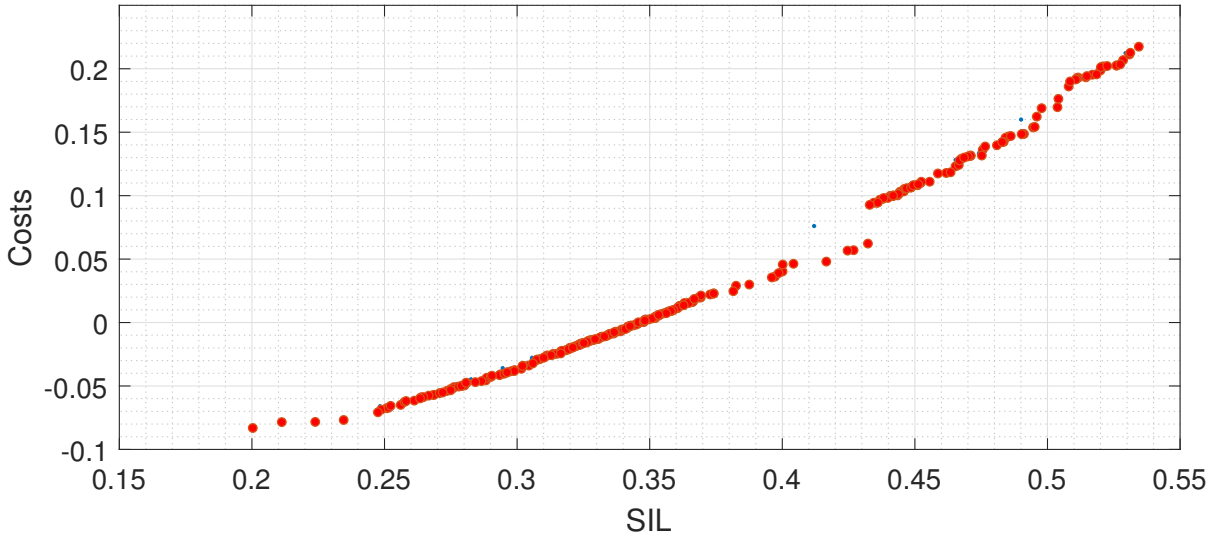

Figure 6.27 – Pareto front for an optimized double-circuit transmission line at 2x500 kV and 2x500 kV with NSGA-II approach optimizing two objectives. Values in pu.

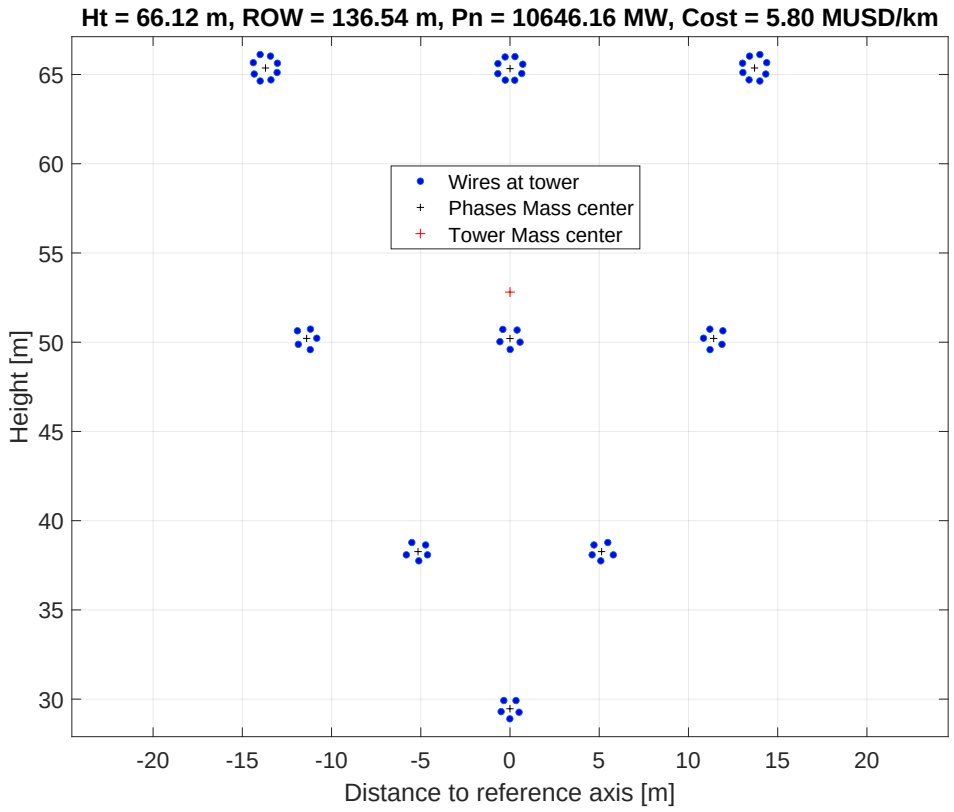

Figure 6.28 – Optimized triple-circuit transmission line at 2x750 kV and 1x1000 kV with NSGA-II approach optimizing two objectives.

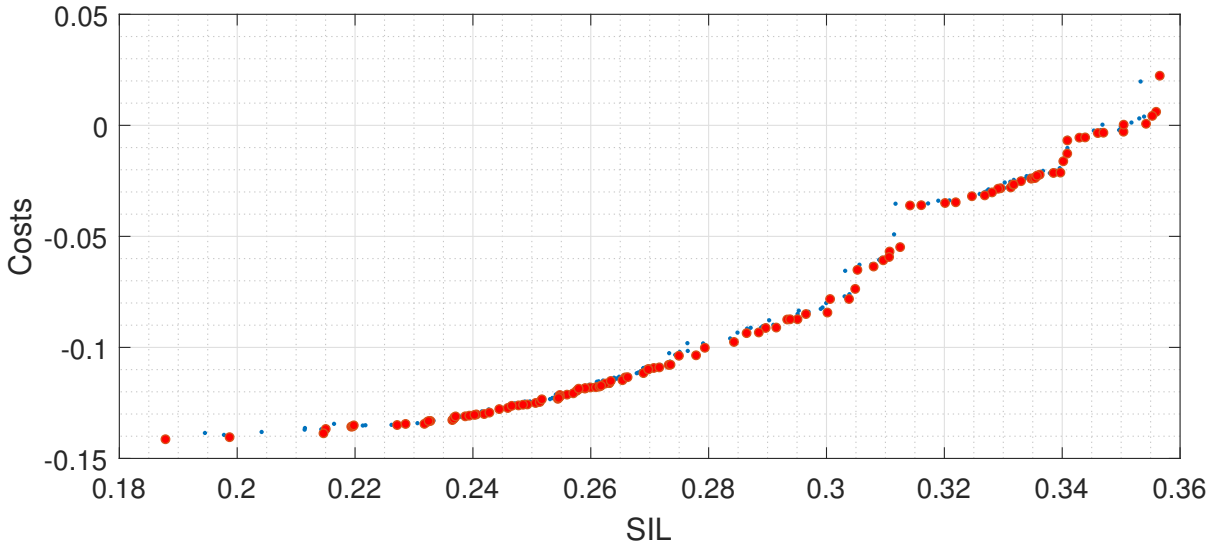

Figure 6.29 – Pareto front for an optimized triple-circuit transmission line at 2x750 kV and 1x1000 kV with NSGA-II approach optimizing two objectives. Values in pu.

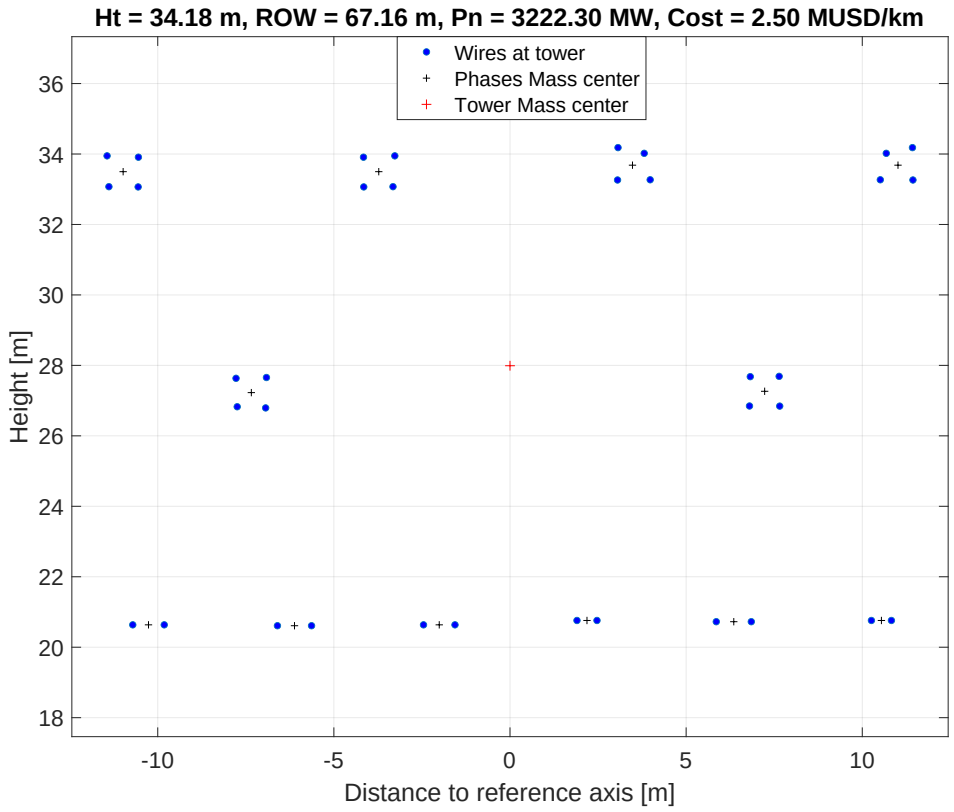

Figure 6.30 – Optimized quadruple-circuit transmission line at 2x230 kV and 2x500 kV with NSGA-II approach optimizing two objectives.

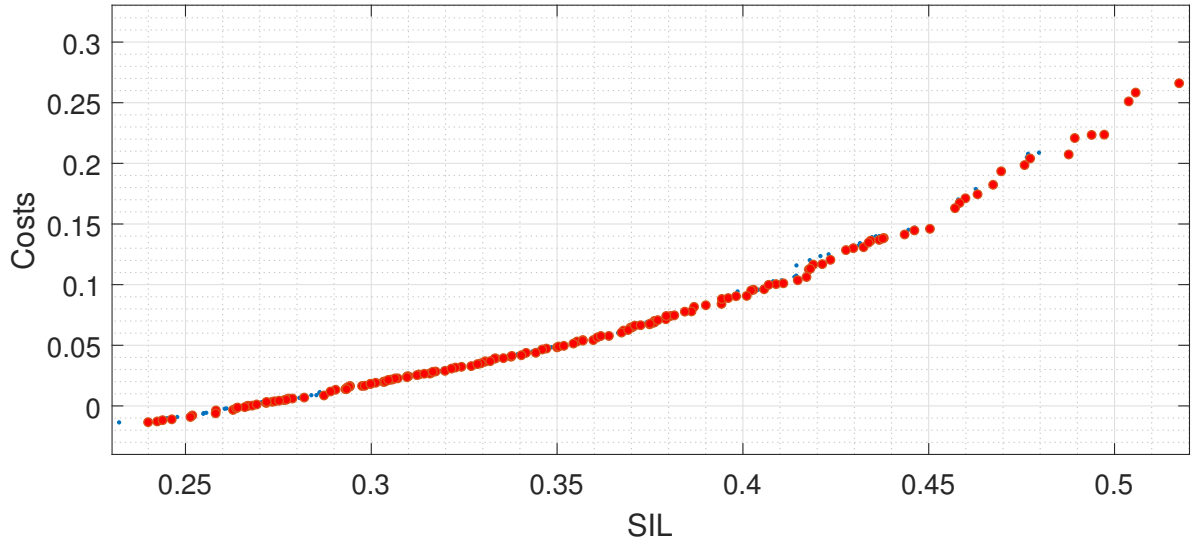

Figure 6.31 – Pareto front for an optimized quadruple-circuit transmission line at 2x230 kV and 2x500 kV with NSGA-II approach optimizing two objectives. Values in pu.

6.5.4 Behavior of the algorithm over the simulations

Since GAs use random variables on the process, the results are not the same over the simulations. To show that the number of generations and population size leads to Pareto frontiers near to the optimal, 10 runs on the NSGA-II algorithm were performed and the value of each objective function of each solution was saved. To show the results a box plot with the value of all four objective was used, specifically SIL, Cost, ROW, and height. Fig. 6.32 shows the box plot when optimizing single-, double-, triple- and quadruple-circuits transmission lines. The figure was generated using the whole Pareto front obtained in each simulation. Therefore, it is possible to observe the behavior of the final population. Note that with this kind of graphic it is evidenced the range in which all the objectives are allocated. Thus, red line indicates the median whereas the bottom and top edges of the box indicate the 25^{th} and 75^{th} percentiles, respectively. The black limits extend to the most extreme data points not considered atypical values. The atypical values are plotted individually using the '+' symbol.

Accordingly, it is possible to observe that the average SIL improvement in the population in all cases is in the range of to 30-40% with investments between -10 to 10%, using ROWs 70-80% lowers and towers 30-50% lowers. The only case in which the towers were higher was in the single-circuit case, because the selected geometry was a delta and not a flat tower, as the conventional case.

Finally, there are several outliers. That is an evidence that the Pareto front is highly distributed, i.e., the diversity is high. In the case of weighted sum approach it is not

possible to observe this behavior, because in the final population all solutions are almost the same. The box-plot of AGs only shows the median values, so almost no diversity is found.

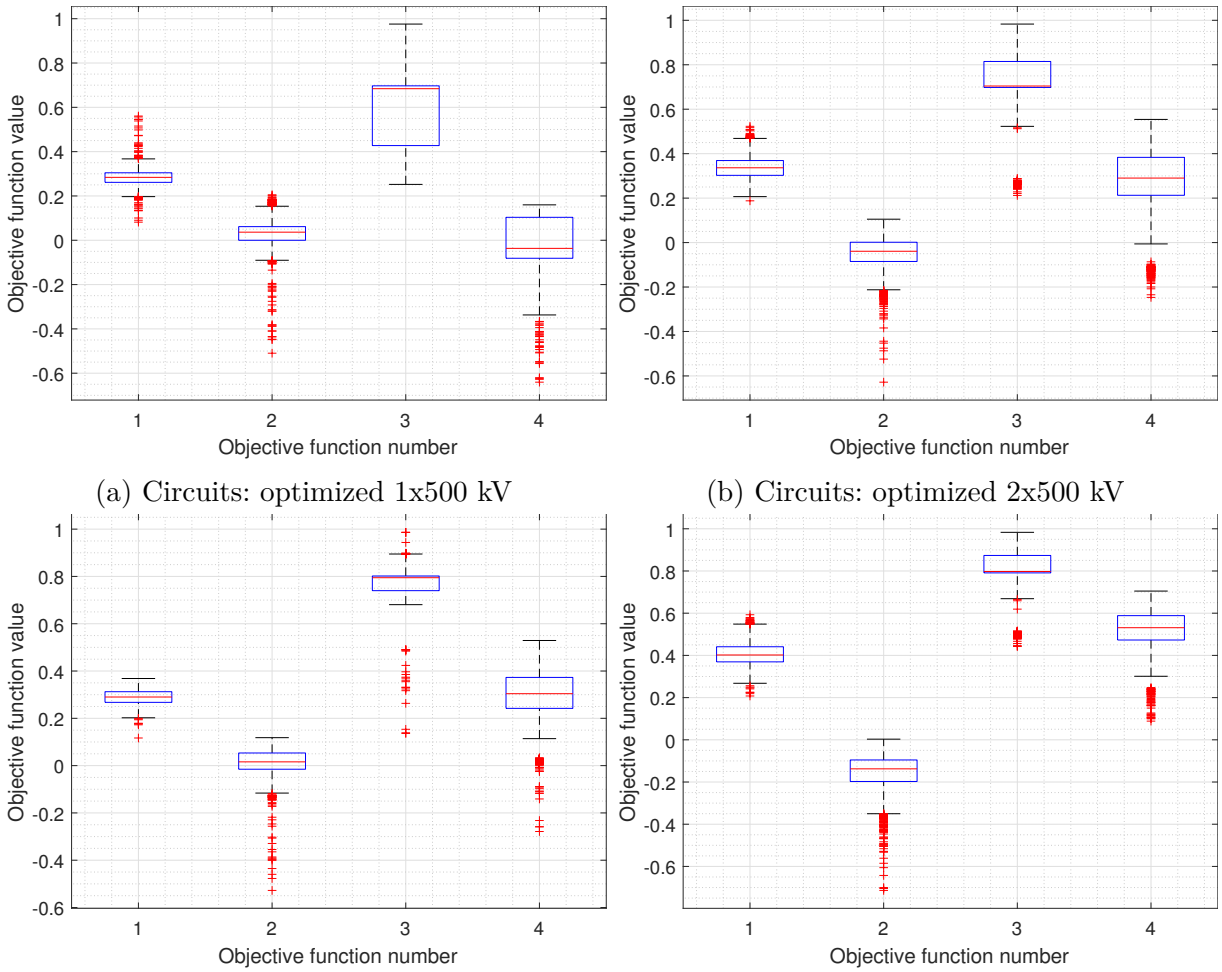

(a) Circuits: optimized 1x500 kV

(b) Circuits: optimized 2x500 kV

(c) Circuits: optimized 2x750 and 1x1000 kV

(d) Circuits: optimized 2x230 and 2x500 kV

Figure 6.32 – Box plots showing the dispersion over ten Pareto fronts using different circuits.

7 Electric field and potential behavior

The optimized lines presented in the previous sections attended all the proposed restrictions. However it is interesting to observe some facts about their electric field behavior. To optimize the lines, the electric field behavior was modeled in *Matlab*. However, to observe the electric field and potential of the lines, Python was used. The advantage of using Python is that there are packages like *MeshPy* available to easily calculate a mesh like the one in Fig. 7.1, required to evaluate the electrical environment around the transmission lines.

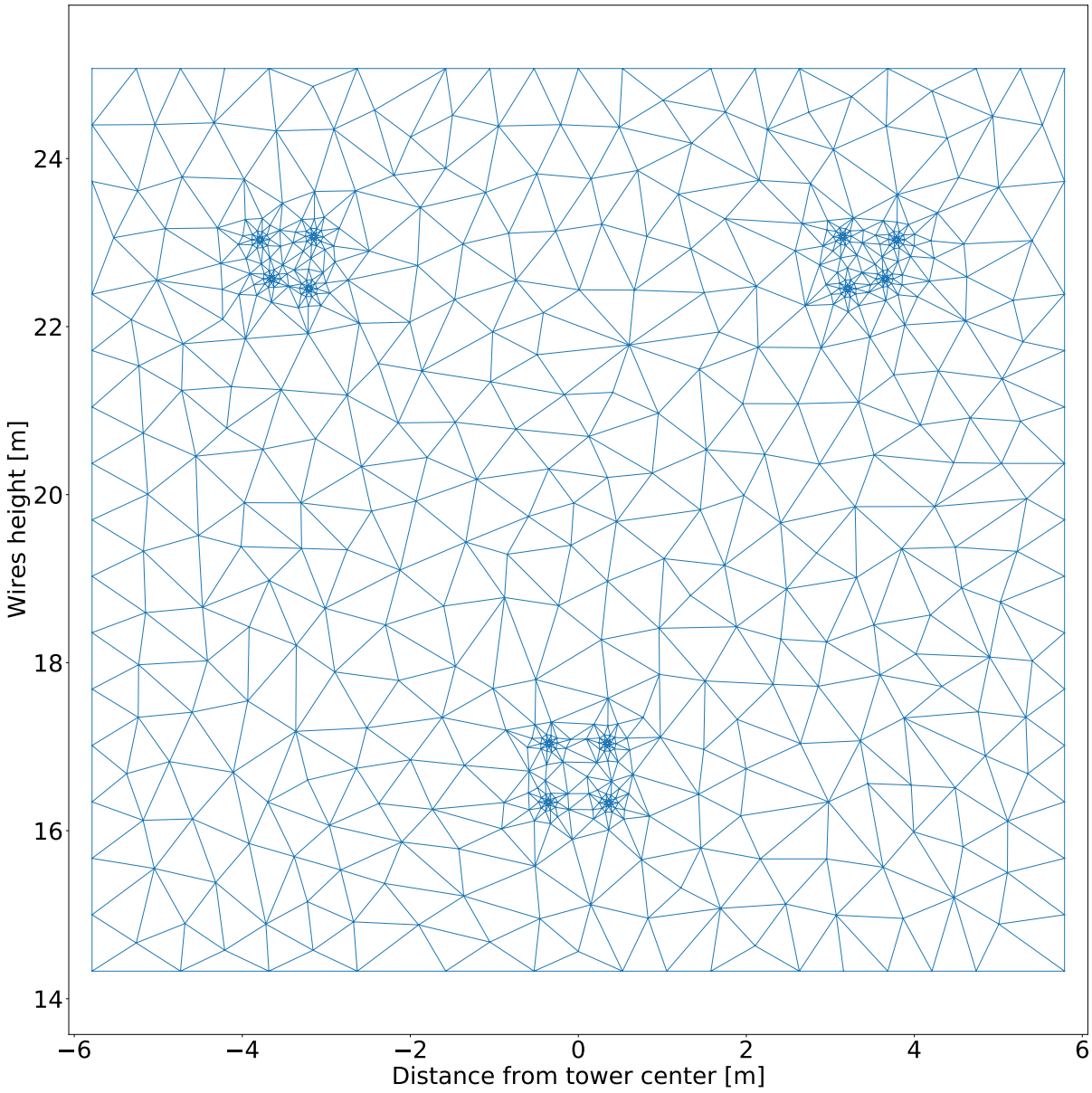

Figure 7.1 – Sample mesh of a single-circuit transmission line.

The RMS electric potential V_p in each point p due to the electric charges q_k of each k sub-conductor was calculated using the image method following (7.1)[1](Electric Power Research Institute, 2005), considering the (x, y) position of the point and each sub-conductor. The electric field was calculated with the equations presented in section 4.2.4.

$$V_p = \left| \sum_{k=1}^{K} \frac{q_k}{2\pi\epsilon_0} \ln \frac{\sqrt{(x_p - x_k)^2 + (y_k - yp)^2}}{\sqrt{(x_p - x_k)^2 + (y_k + y_p)^2}} \right| \tag{7.1}$$

Figs. 7.2 to 7.5 show the electric potential (surface graph) and the electric field around the sub-conductors (contour graph) for different geometries. The geometries correspond to some of those obtained with the NSGA-II based approach optimizing the four objectives. Fig. 7.2 is a geometry for a single 500 kV transmission line; Fig. 7.3 a double 2x500 kV transmission line; Fig. 7.4 a triple 2x750 1x1000 kV transmission line; and Fig. 7.5 a quadruple 2x230 2x500 kV transmission line.

Figs. 7.2 to 7.5 show that the electric field lines in all cases are symmetrically distributed along the Y axis. This is because of the symmetry of the geometry. Also, the figures evidence that higher electrical fields are located in sub-conductors that are close to the sub-conductors in other phases. However, the electric field in all cases is lower than the critical values. Conversely, the electric potential reduces faster in the middle of the phases. Finally, as expected, the more circuits, the more complex is the electric field interaction.

[1] $\epsilon_0 = 8.854187\text{e-}12$ [C/m]

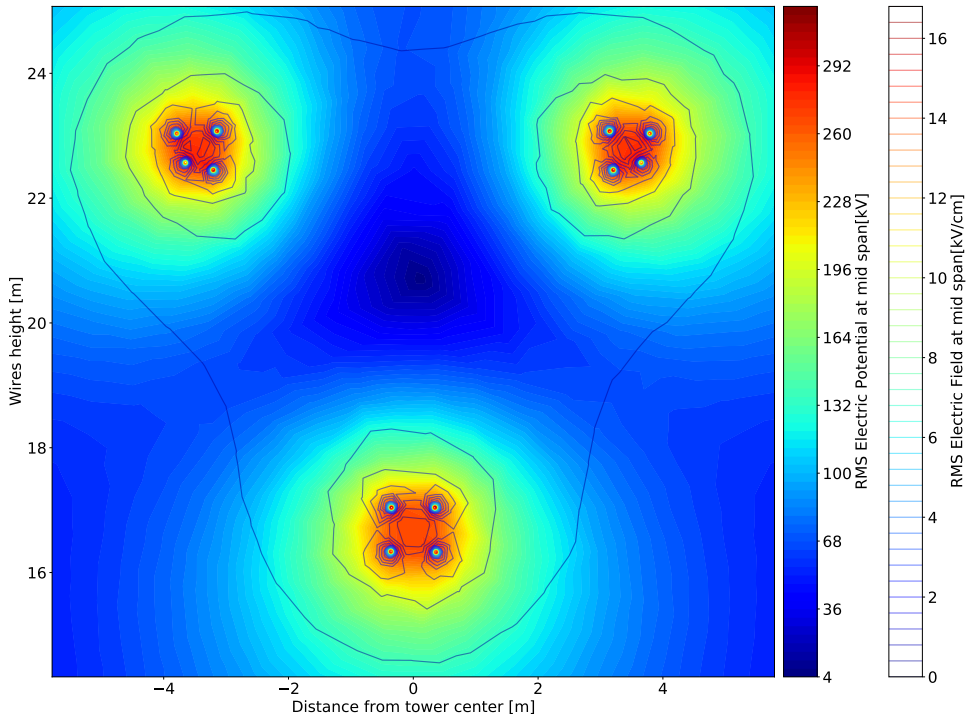

Figure 7.2 – Electric field and potential for an optimized single-circuit transmission line at 1x500 kV with NSGA-II approach optimizing four objectives.

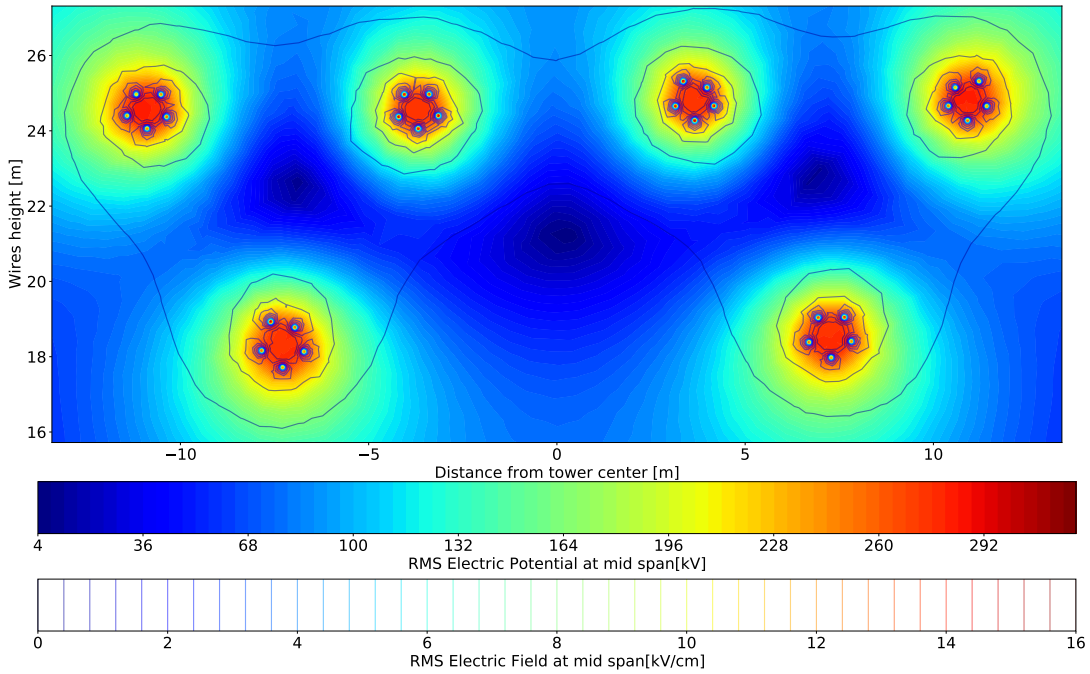

Figure 7.3 – Electric field and potential for an optimized double-circuit transmission line at 2x500 kV with NSGA-II approach optimizing four objectives.

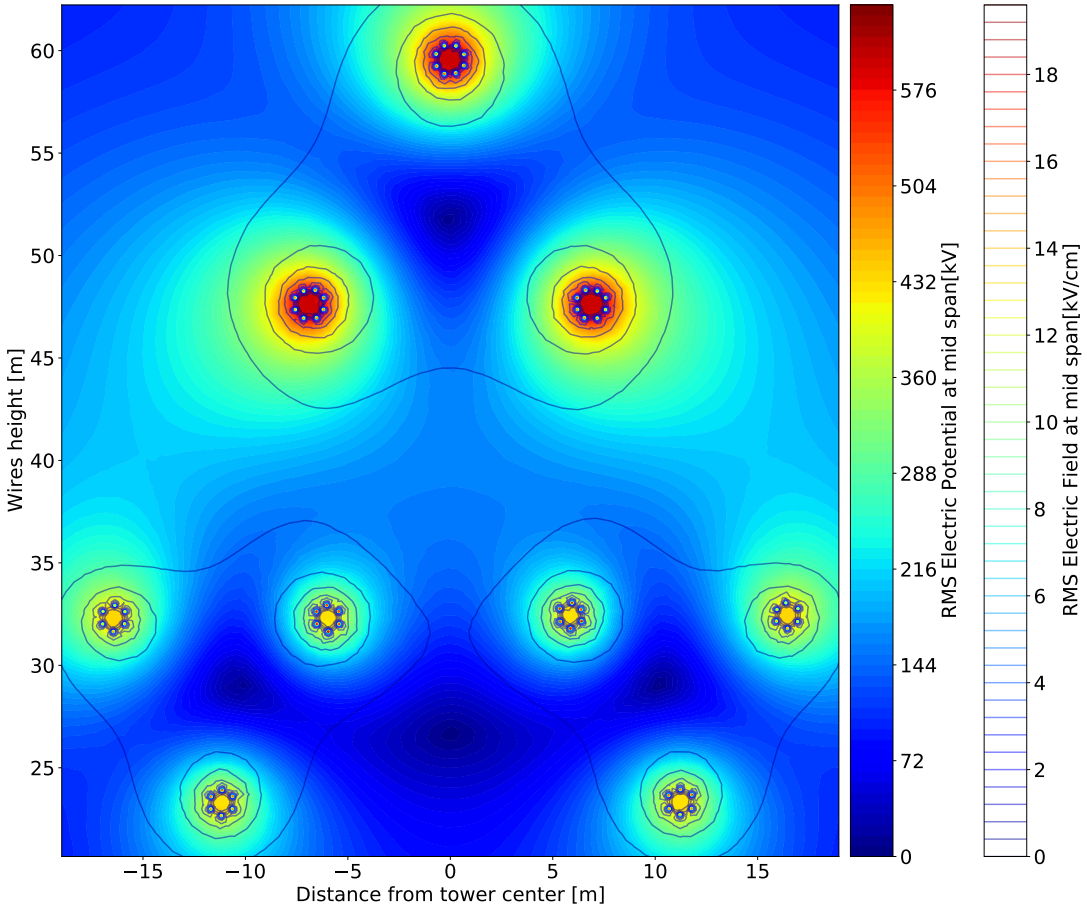

Figure 7.4 – Electric field and potential for an optimized triple-circuit transmission line at 2x750 kV and 1x1000 kV with NSGA-II approach optimizing four objectives.

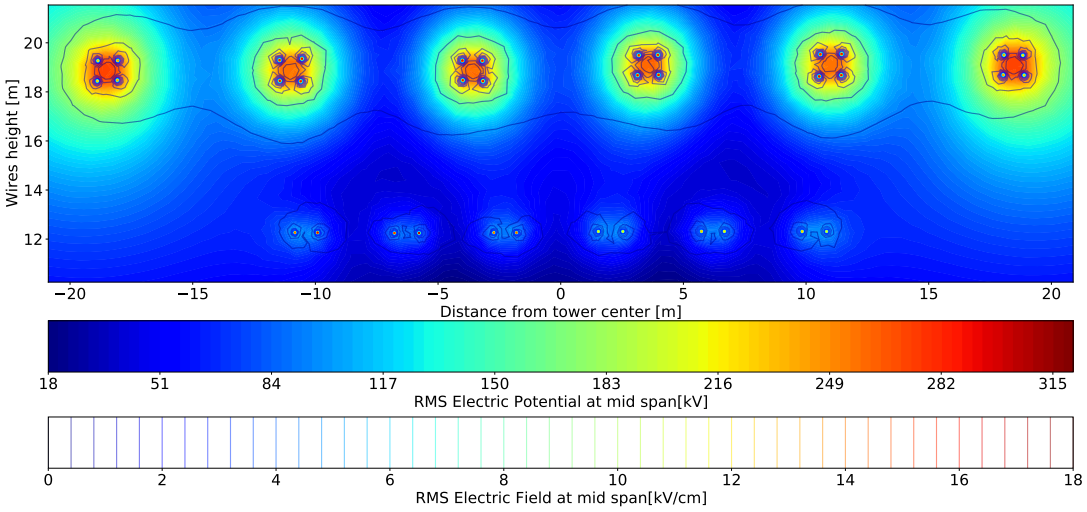

Figure 7.5 – Electric field and potential for an optimized quadruple-circuit transmission line at 2x230 kV and 2x500 kV with NSGA-II approach optimizing four objectives.

Other important aspect to analyze, that has not been optimized so far in this

research, is the influence of the phase sequence. To see the influence, consider the optimized four circuit transmission line in Fig. 6.24. It corresponds to a four-circuit transmission line with the two bottom circuits operating at 230 kV and the two top circuits operating at 500 kV. If a conventional phase sequence ABC (left to right) is used in all circuits, the electric potential (surface) and electric field (contour) in Fig. 7.6a is obtained. On the other hand, if the phase sequence is ABC-BCA-CAB-ABC, the electric potential and electric field in Fig. 7.6b is obtained. Whereas, the electric field under the transmission line for both cases is illustrated in Figs. 7.6c and 7.6d, respectively.

Observe that using the regular ABC sequence, the maximum electrical field around the sub-conductors was lower than when using the alternative phase sequence. However, the electric field under the transmission line was more than 2 times higher when using the ABC sequence. Nonetheless, with the alternative phase sequence a non-symmetrical electric field under the line was produced. Therefore, the phase sequence influences the electric field around the sub-conductors and under the line, allowing to modify the height and right-of-way of the tower. However, finding the optimal phase sequence is not simple and requires solving a huge combinatorial problem.

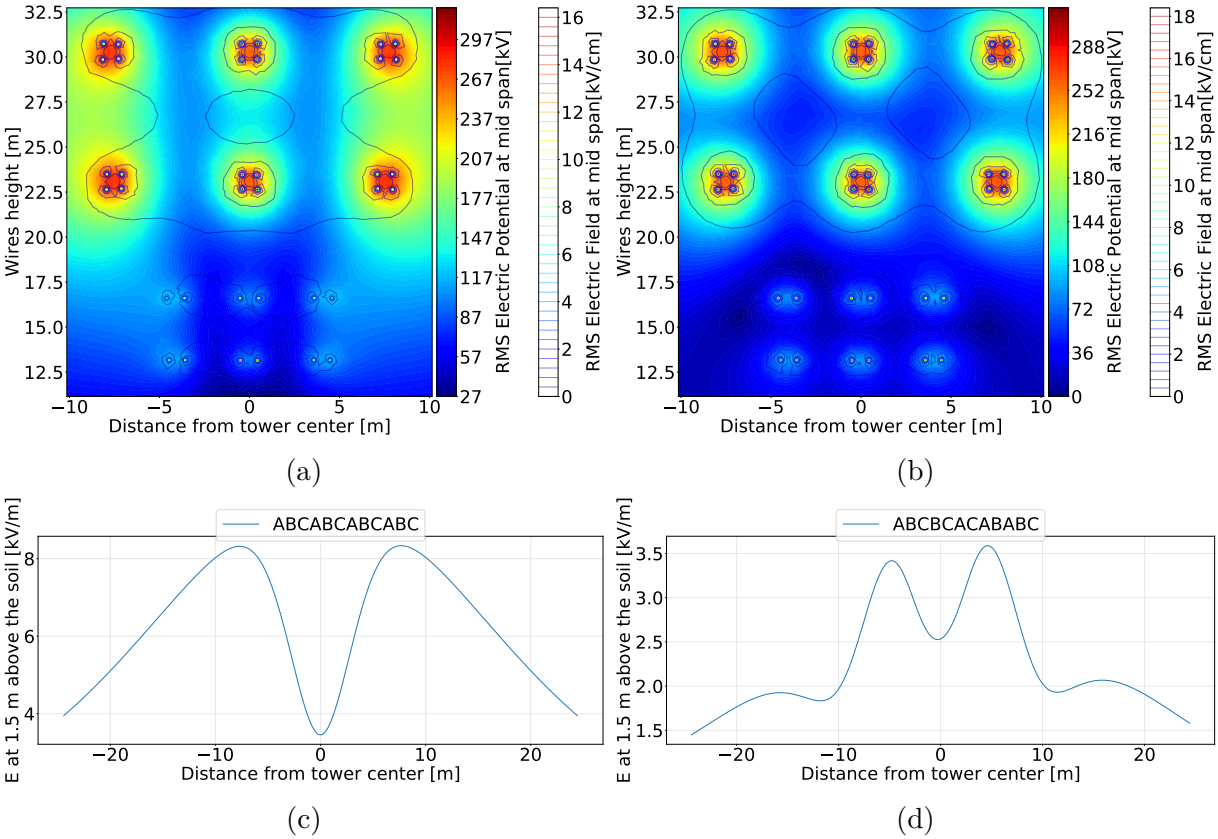

Figure 7.6 – Influence of the phase sequence on the RMS electric potential (V_E), E_{sup} and E_{soil}. a) V_E and E_{sup} for a phase sequence ABC-ABC-ABC-ABC. b) V_E and E_{sup} for a phase sequence ABC-BCA-CAB-ABC. c) E_{soil} at 1.5 m for a phase sequence ABC-ABC-ABC-ABC. d) E_{soil} at 1.5 m for a phase sequence ABC-BCA-CAB-ABC.

A common alternative to select the phase sequence in double-circuit transmission lines is to alternate between direct and reverse sequence (i.e., ABC-CBA). The disposition ABC-ABC is known as *superbundle* and produce the highest electric field under the line, but the lowest electric field on the sub-conductors. On the other hand, the disposition ABC-CBA is known as *low-reactance* and produce the lowest electric field on ground, but the highest electric field on the sub-conductors and, consequently, the highest corona effects (Electric Power Research Institute, 2005). However, for lines with more circuits the behavior changes and cannot be easily predicted.

If we test a random phase sequence like ABC-CBA-ABC-CBA in the transmission line of Fig. 6.24, the electric potential and electric field of Fig. 7.7 is obtained. Whereas the electric field under the transmission line, represented in Fig. 7.8, is obtained. Note that contrary of what happens in double-circuit lines, the phase arrangement does not produces the lowest electric field under the transmission line.

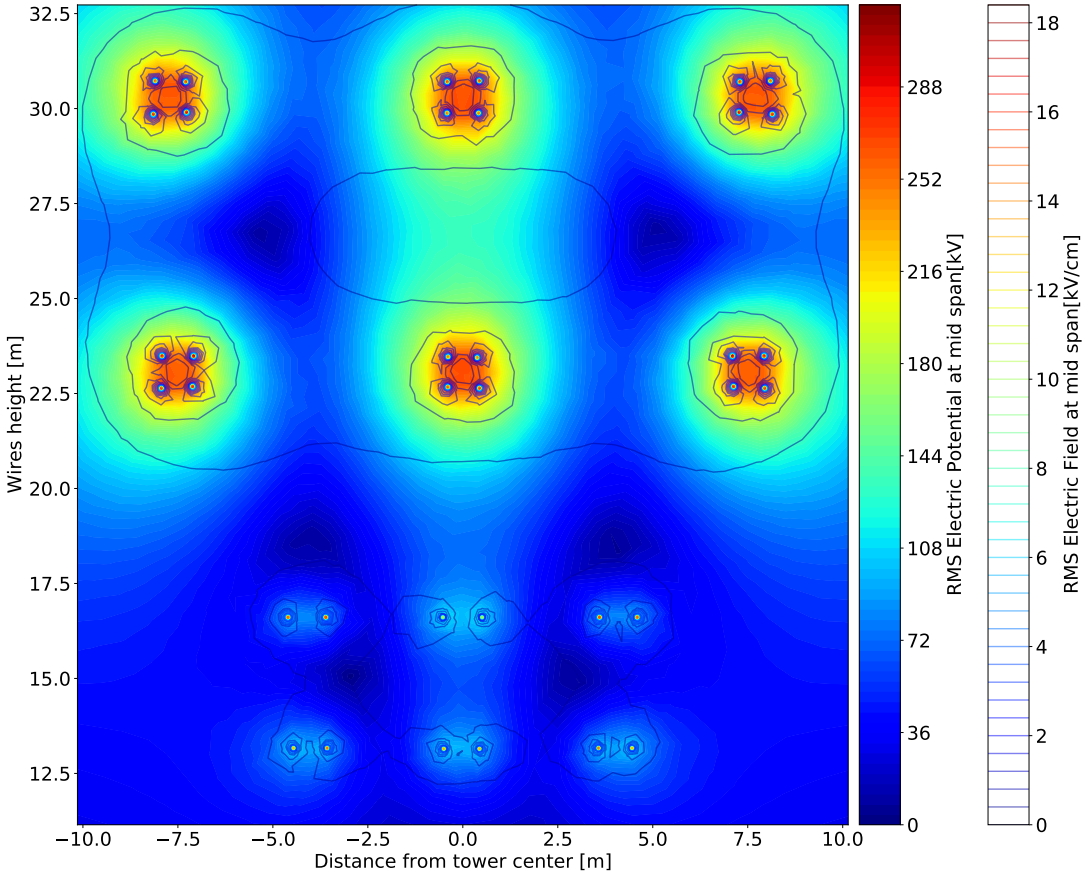

Figure 7.7 – V_E and E_{sup} for a phase sequence ABC-CBA-ABC-CBA.

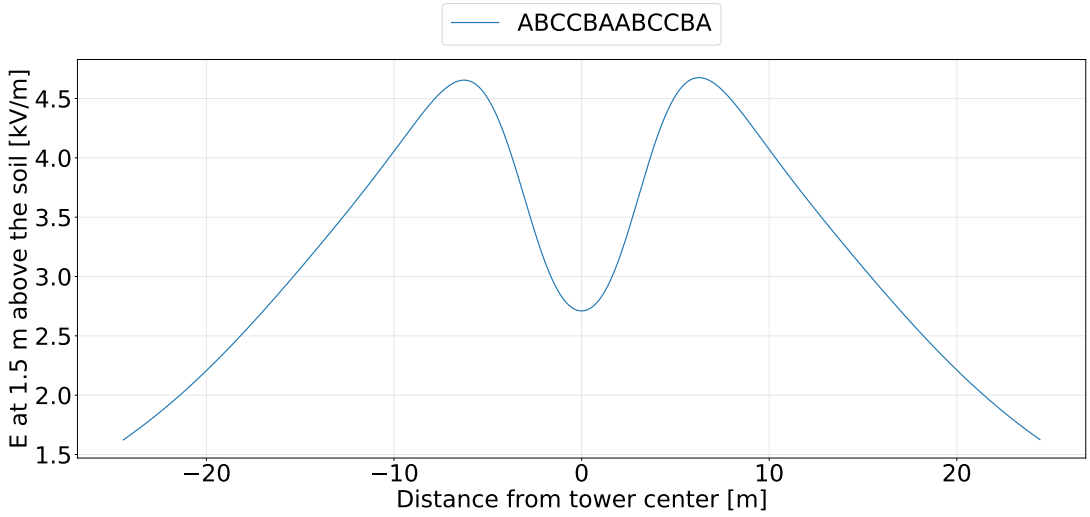

Figure 7.8 – E_{soil} for a phase sequence ABC-CBA-ABC-CBA.

As you can see, the electromagnetic environment is strongly influenced by the phase sequence, which complicates finding the optimal phase sequence. The problem is even more complex considering that the electromagnetic environment will also be affected by the disposition of the sub-conductors in the tower.

To show the influence of the sequence phase and the geometry, the transmission lines of Fig. 6.18 and 6.24 were considered. Then, the same twelve random phase arrangements were applied in each one of the geometries, and the electric field under the transmission lines at a height of 1.5 m was calculated. The results are presented in Fig. 7.9c and 7.9d. Note that the electric field is different for each phase sequence and tower geometry. In some cases, a phase sequence can be the best for a specific geometry, but terrible for another geometry. Since the electric field is influenced by the phase sequence and the tower geometry, it is hard to determine which is the best phase sequence for all cases. Therefore, the most conservative option commonly adopted is to use an ABC sequence for all circuits. However, finding an optimal phase sequence is ideal to modify the electric field, ROW and height of the transmission lines.

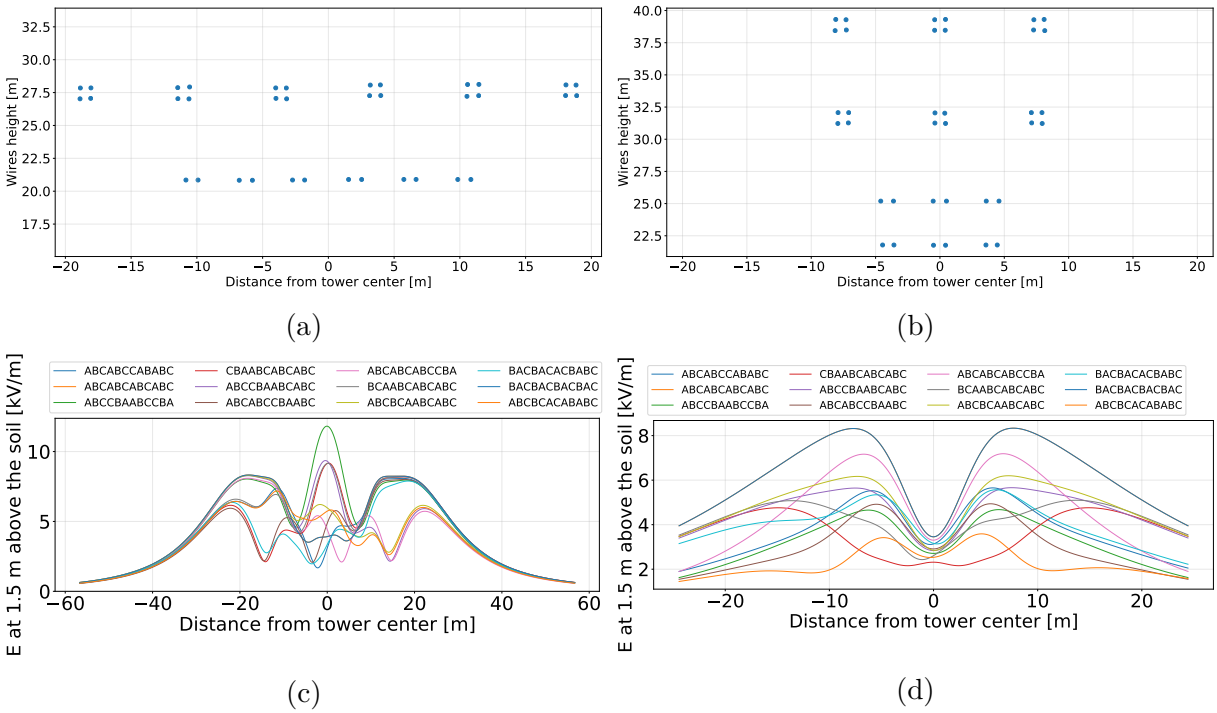

Figure 7.9 – Influence of the tower geometry type and phase sequence. a) Optimized tower of Fig. 6.18. b) Optimized tower of Fig. 6.24. c) Electric field for random phase arrangements in the optimized tower of Fig. 6.18. d) Electric field for random phase arrangements in the optimized tower of Fig. 6.24.

The results presented in this chapter were validated with COMSOL. The maximum error found in the superficial electric field calculation was 3%. On the other hand, the maximum error in the calculation of the electric field under the transmission lines was 0.5%.

8 Optimization of phase sequence

In the previous chapter it was evidenced that the phase sequence plays an important role in the transmission line behaviour. Therefore, it was decided to include the phase sequence in the optimization process[1]. Accordingly, the problem became more complex and constrained to a permutation space. Since the phase sequence is modeled as a permutation, fixing the sequence of one circuit meanwhile varying the others, 6 possibilities are obtained for two circuits, 720 possibilities for three circuits and 362,880 for four circuits. As can be foreseen, this analysis highly increases the problem complexity.

To include the phase sequence on the optimization model it is necessary to solve the problem in (5.4), but adding the phase sequence constraint (8.1).

$$\vec{P}_{s_{ci}} \rightarrow \text{is in a permutation based space} \tag{8.1}$$

Where:

$\vec{P}_{s_{ci}}$ Vector containing the phase sequence of each circuit ci.

As consequence, the problem to solve now is:

$$\max \quad (5.4) \tag{8.2}$$

subject to:

(4.7), (4.8), (4.9), (4.10), (4.11), (4.12) (4.13), (4.14), (4.15), (4.16), and (8.1).

With the addition of the phase sequence as a decision variable, the form of the individuals in the population must be modified. Therefore, the chromosome (5.2) of each solution is transformed as follow:

$$\vec{S}_n = \left\{T_{ty}, \vec{c}_{ty}, \vec{n}_{sc}, \vec{co}_{ty}, \vec{P}_s, \vec{ht}, \vec{Cx}, \vec{Cy}, \vec{D}, \vec{hv}, \vec{r}_x, \vec{r}_y, \vec{r}_{xc}, \vec{r}_{yc}\right\} \tag{8.3}$$

Where:

T_{ty} Base tower type

[1] This section is outside of the chapter of optimization method because it was not included on the initial objectives or plans of the research.

$\vec{c}_{ty}$ Base topology of each *ci* circuit

$\vec{n}_{sc}$ Vector formed by the number of wires at each *ci* circuit ($n_{sc_{ic}}$)

$\vec{co}_{ty}$ Vector formed by the sub-conductor type of each *ci* circuit ($co_{ty_{ic}}$). The 100 ACSR conductor types were numbered from 1 to 100 (ACOSTA; TAVARES, 2017)

$\vec{P}_s$ Vector formed by the phase sequence of each *ci* circuit ($\vec{P}_{s_{ci}}$)

$\vec{ht}$ Vector formed by the height of each *ci* circuit (ht_{ic})

$\vec{Cx}$ Vector formed by the X center of each *ci* circuit (Cx_{ic})

$\vec{Cy}$ Vector formed by the Y center of each *ci* circuit (Cy_{ic})

$\vec{D}$ Vector formed by the D_{ci} value of each *ci* circuit

$\vec{hv}$ Vector formed by the hv_{ci} value of each *ci* circuit

$\vec{r}_x$ Vector formed by the $\vec{r}_{x_{ci}}$ component of each *ci* circuit

$\vec{r}_y$ Vector formed by the $\vec{r}_{y_{ci}}$ component of each *ci* circuit

$\vec{r}_{xc}$ Vector formed by the $\vec{r}_{xc_{ci}}$ component of each *ci* circuit

$\vec{r}_{yc}$ Vector formed by the $\vec{r}_{yc_{ci}}$ component of each *ci* circuit

Note that the variables of the chromosome in (8.3) are in a different order than in the chromosome in (5.2). It was done to split the variables according to their types and then to apply more easily their specifics operators. Thus, in (8.3) the first four variables are integer, the next variable is in a permutation based space variable, and finally, the remaining variables are real. For integer variables it was used an uniform crossover, for real variables it was used an arithmetic crossover, and for the phase sequence an OX crossover. In the case of mutation it was used a random mutation for integer variables, the same Gaussian mutation as in previous chapters for real variables, and an exchange mutation for the permutation based space variable. It is worth to highlight that those operators were chosen because they show good response for each type of variable.

With the model ready to use, the same cases as in chapter 6 were optimized. As a result, Figs. 8.1 to 8.4 show the geometries obtained after 10 runs when optimizing transmission lines with 1 to 4 circuits in the same tower using NSGA-II including the phase sequence optimization. The results summarized in Tables 8.1 and 8.2 show that the obtained geometries do not differ drastically from those presented before without phase sequence optimization. However, in certain cases the fitness obtained is better than when the phase sequence is not taken into account. The main advantage of optimizing the phase sequence of each circuit is that the electric field under the line is reduced, so the ROW and

tower height are also reduced. Note also that in most of the cases the SIL was higher and the costs were reduced. Therefore, the phase sequence optimization produces significant improvements regarding to the objectives. This is a very important result that, to the best of our knowledge, was not observed before. Additionally, in the next sections it will be shown that the phase sequence also produces important advantages regarding to the transient behaviour.

Table 8.1 – Simulation settings and objective function values - Including phase sequence

Line [kV]	N	g	time [s]	f_1'[%]	f_2'[%]	f_3'[%]	f_4'[%]	f[%]
500	300	500	371	31.4	3.9	43.7	-12.5	66.5
2x500	300	500	527	31.6	-1.6	64.8	41.8	136.2
2x750 - 1x1000	300	500	997	26.1	9.6	82.6	45.8	164.0
2x230 - 2x500	300	500	833	32.7	-0.5	87.6	62.1	181.8

Table 8.2 – Characteristics of the selected optimized TLs - Including phase sequence

Line	$n_{sc_{ci}}$	Sub-conductor type	b_s [m]	Phase Sequence
500 kV	4	Flamingo	0.76	ABC
2x500 kV	5/5	Duck	1.12	ABCCBA
2x750 - 1x1000 kV	5/6/8	Flamingo	1.43	ACBBACCBA
2x230 - 2x500 kV	2/2/4/4	Flamingo	1.09	ABCBCACABABC

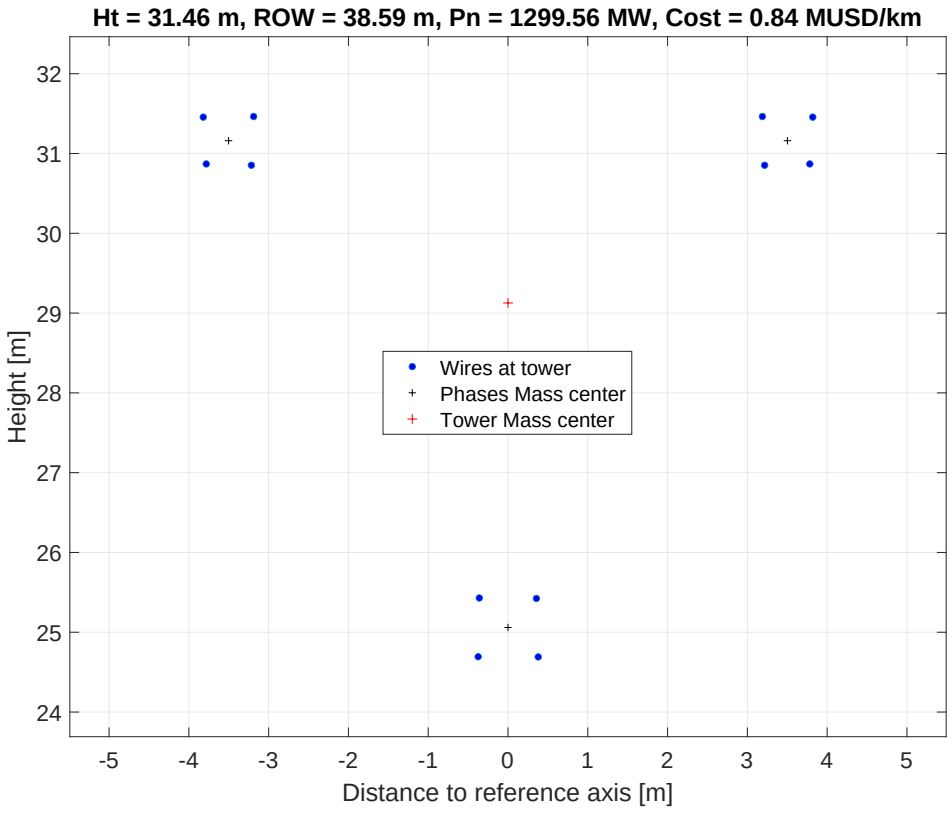

Figure 8.1 – Single-circuit transmission line.

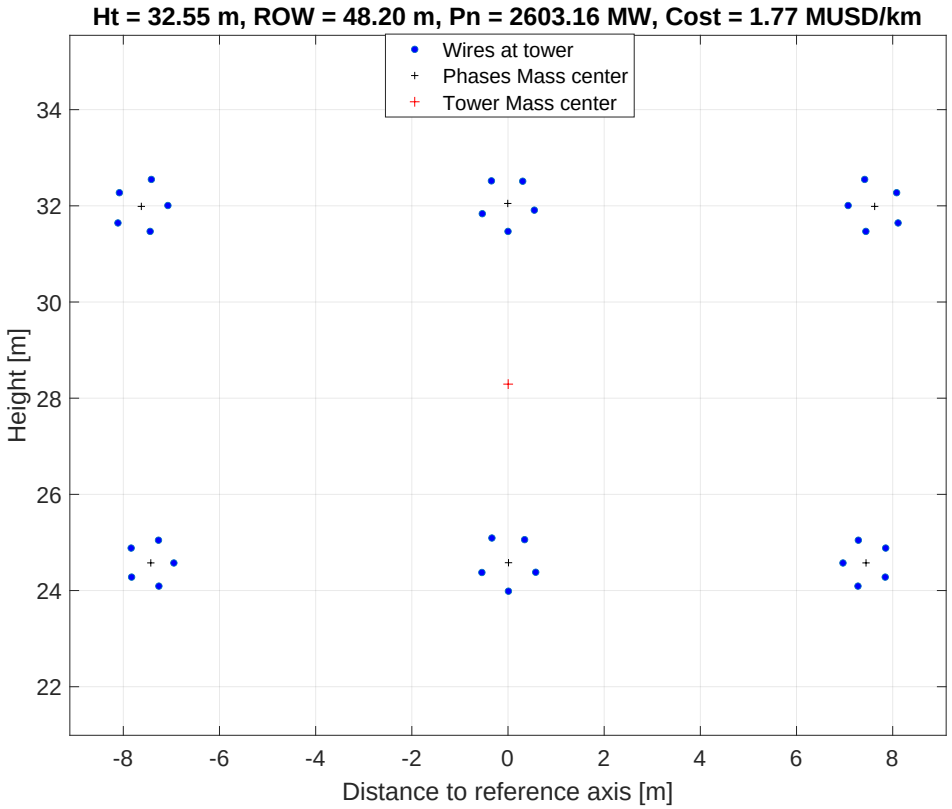

Figure 8.2 – Double-circuit transmission line.

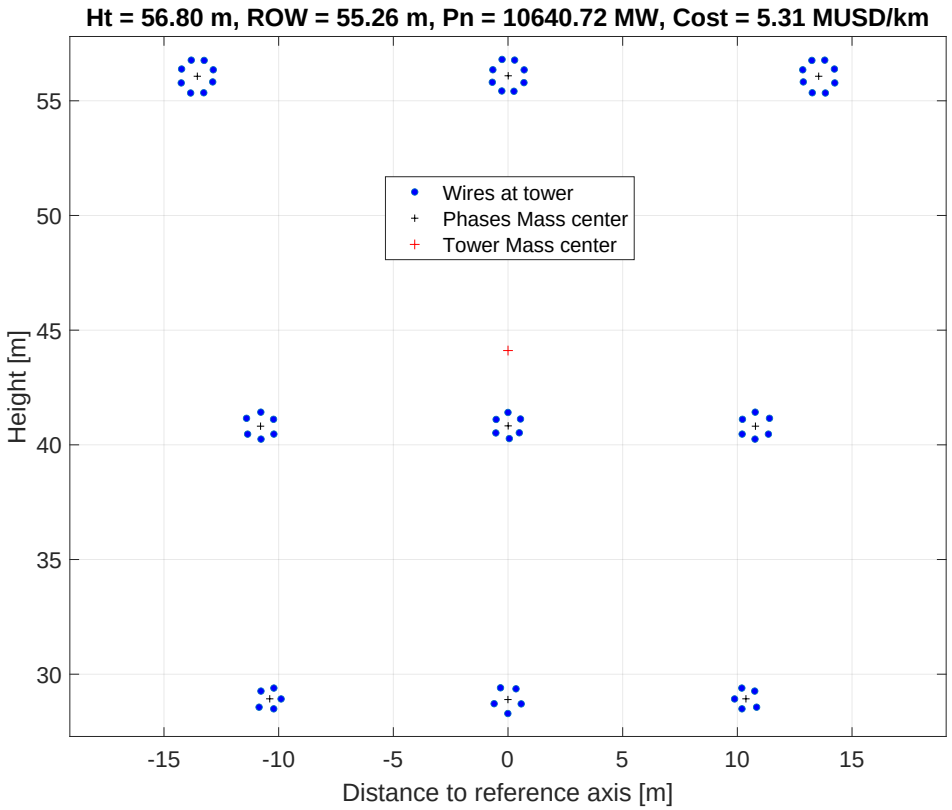

Figure 8.3 – Triple-circuit transmission line.

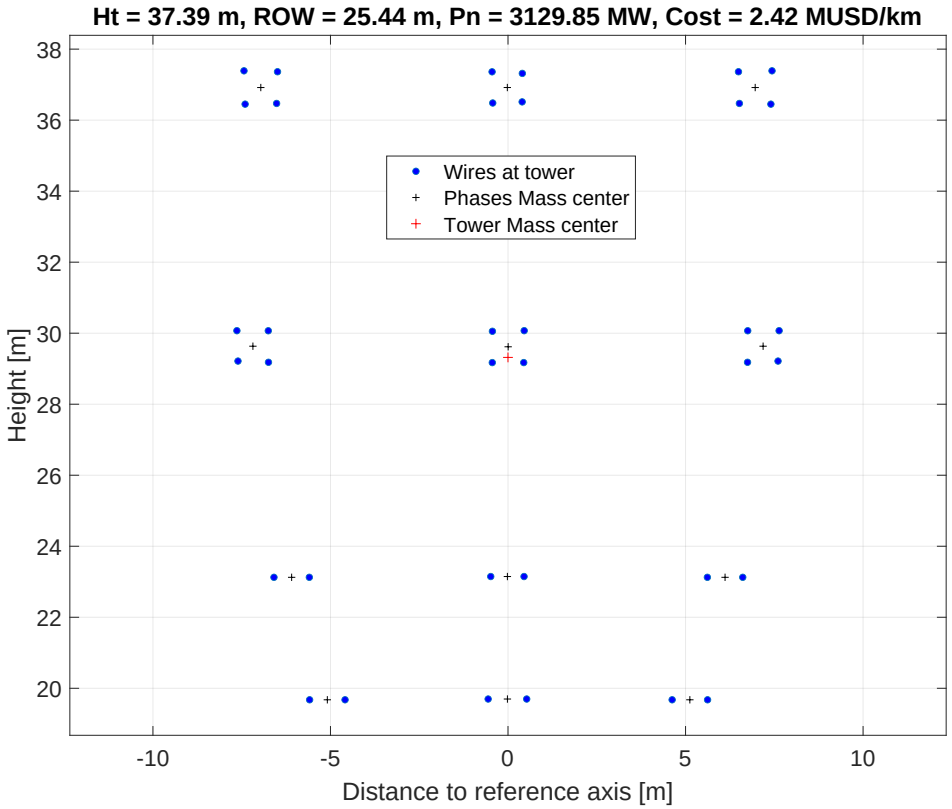

Figure 8.4 – Quadruple-circuit transmission line.

As in the previous cases, it is possible to observe the behaviour of all objectives at the same time and their relationship using parallel coordinate plots with the normalized value of the objective functions for each solution. In this case the value is normalized according to the available values of the objectives in the population. Again, a value of 1 in one objective does not mean that it was improved by 100%, but means that it has the maximum value of the population in a specific objective. Thus, the parallel coordinate plot allows to see the trade-off between the objectives, e.g., in Fig. 8.5 the worst solution for objective 1 is the best solution for objective 2. In other words, the solution with the lowest SIL is also the solution with the lowest $Costs$. Same analysis can be done with other objectives, e.g., in Fig. 8.5 the solution with the lowest ROW is also the solution with highest $height$. With this the trade-off between objectives and the existent conflict is highlighted. Graphs with solutions dispersed on the black bars indicate that the algorithm is good finding diverse solutions.

It is possible to create also a parallel coordinate plot of the actual values of f_1' to f_4' and see the real enhancement of all objectives. Fig. 8.6 shows the parallel coordinate plot in this circumstance when optimizing TLs with 1 to 4 circuits on the same tower. With this graph it is possible to see the behaviour of the objectives according to the number of circuits. Accordingly, it is possible to see that single-circuit lines present the worst value of ROW and height, meanwhile the four-circuit TLs have the best values in those objectives.

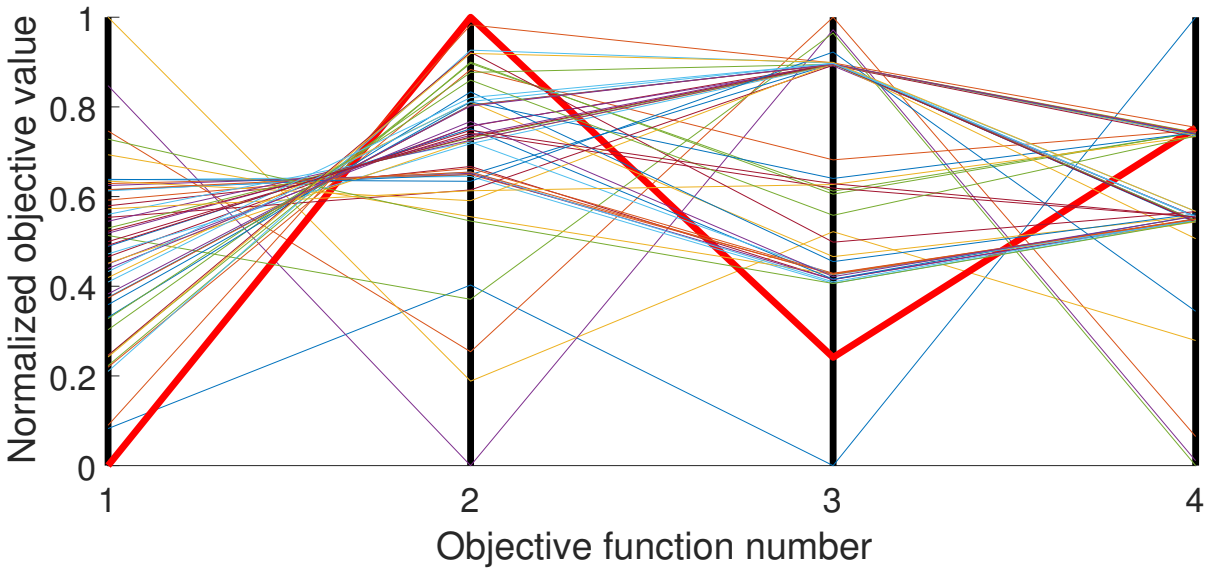

Figure 8.5 – Parallel coordinate plot for an optimized four circuit-transmission line at 2x230 kV and 2x500 kV with NSGA-II taking into account the phase sequence optimization.

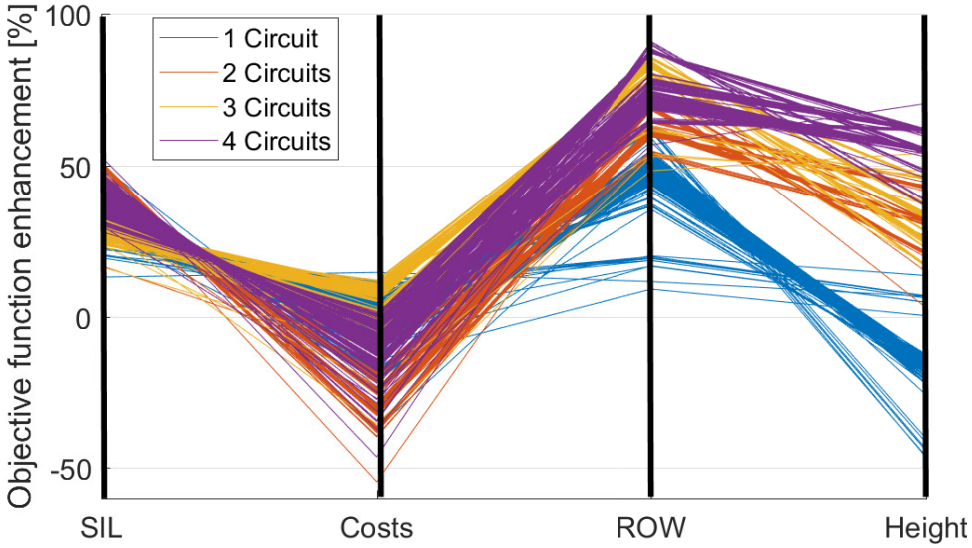

Figure 8.6 – Parallel coordinate plot when optimizing 1 to 4 circuits taking into account the phase sequence optimization.

Regarding the other objectives, the solutions have similar values. However, according to the number of circuits, they are more concentrated in a specific zone, e.g., regarding to costs, the solutions when using three-circuits are concentrated in better values than with other quantity of circuits. However, it is not possible to conclude that the behavior will be always the same, because it depends on the voltage level of the circuits. Therefore, if the voltage level changes it is necessary to generate new graph for the analysis process.

As stated in chapter 7, phase sequence is an important element for the electromagnetic behaviour. Therefore, after the phase sequence was included in the

optimization process, the electromagnetic profile under the transmission lines changes. Figs. 8.7 to 8.10 show the phase sequence influence on the electromagnetic behaviour of the transmission lines presented in Figs. 8.1 to 8.4. It is possible to note that the phase sequence plays an important role for transmission lines with several circuits in the same tower. Consequently, the electric field profile is not affected by the phase sequence in single circuit transmission lines (Fig. 8.7), whereas in multi-circuit transmission lines (Figs. 8.8 to 8.10) it is severely affected.

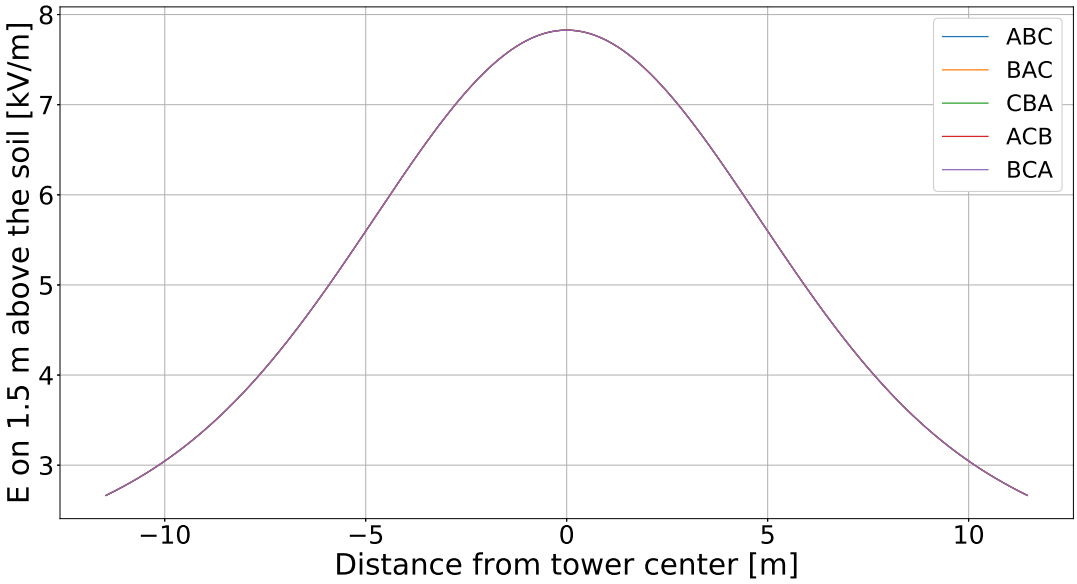

Figure 8.7 – E_{soil} in the 1 circuit transmission line with different phase sequence.

Note that the electromagnetic profile under the transmission lines for the optimal phase sequence (in blue) and different phase sequences is represented in Figs. 8.7 to 8.10. Therefore, it is possible to observe that the optimal phase sequence produces the lowest ROW in all cases, remembering that the ROW is assumed as twice the distance from the tower center to the point where the electric field under the transmission line is lower than 1.67 kV/m. Additionally, in most of the cases, except in the three-circuit transmission line in Fig. 8.9, the maximum electric field under the transmission lines is the lowest for the optimized phase sequence. Therefore, it is possible to conclude that the algorithm selected a specific phase sequence because it reduces the ROW and the tower height at the same time.

This behaviour is basically caused by the changing on the capacitive coupling between circuits, remembering that the capacitance depends on the charge density and the voltage level. Therefore, the capacitance, the charge density, and the electric field are directly linked to the voltage phasor of each phase.

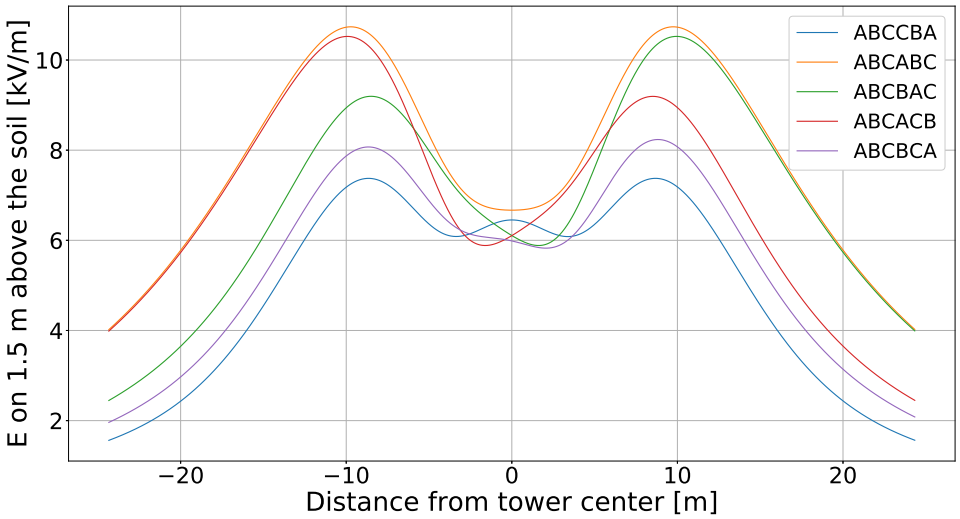

Figure 8.8 – E_{soil} in the two-circuit transmission line with different phase sequence.

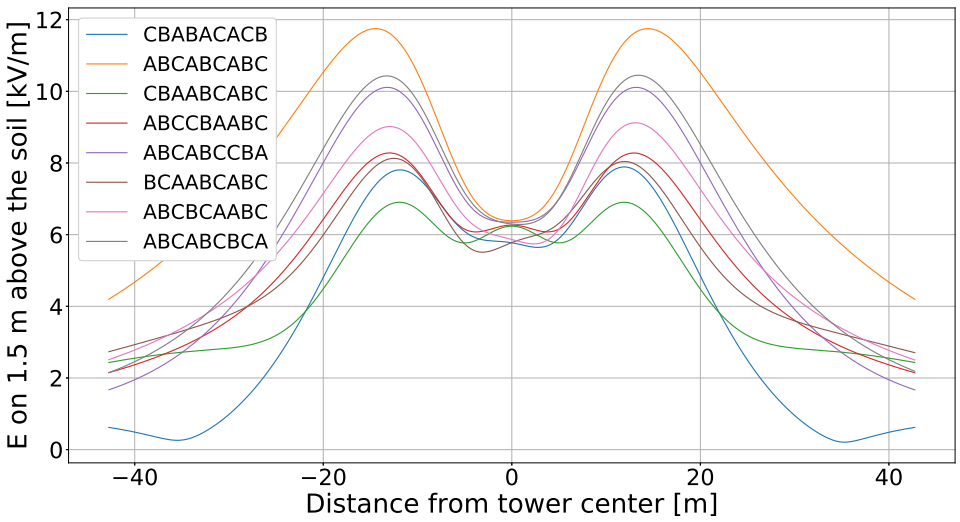

Figure 8.9 – E_{soil} in the three-circuit transmission line with different phase sequence.

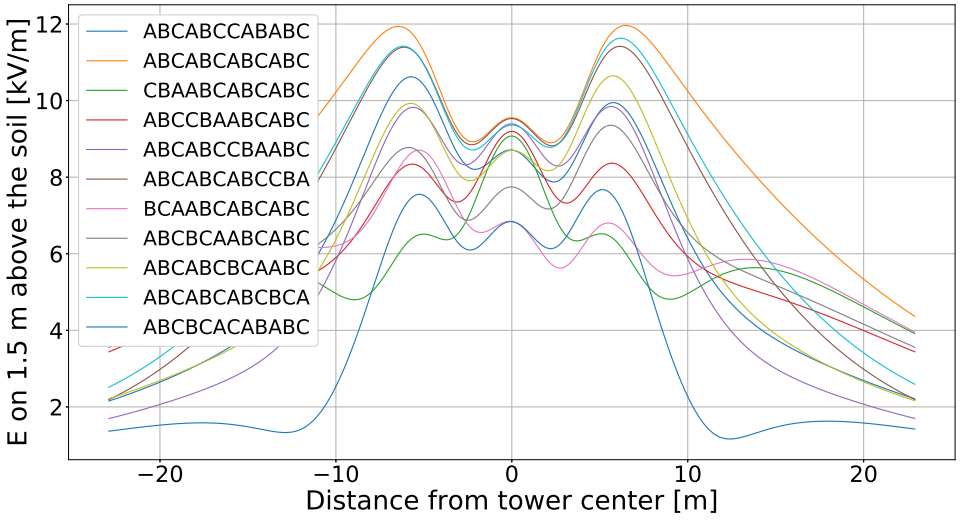

Figure 8.10 – E_{soil} in the four-circuit transmission line with different phase sequence.

As can be seen in Figs. 8.7 to 8.10 the electric field under the transmission lines changes according to the phase sequence and the number of circuits. However, it is important to remember that it is also influenced by the tower geometry. Therefore, the optimal phase sequence presented will not be the same for another type of geometry. Also, it is important to highlight and remember that the Pareto approach produces a set of solutions, so the optimal phase sequence could be different according the preferences on the objective functions.

Additional implications of the phase sequence optimization focused in the transient behavior will be discussed in the next chapter.

9 Transient behavior

Transient response of multi-circuit multi-voltage transmission lines (MCMVTL) is an important topic because adjacent circuits have influence on the others. To perform the transient study the optimized transmission lines presented in previous section in Figs. 8.1 to 8.4 were chosen, assuming a length of 350 km for each line. The transmission lines were modeled in PSCAD with the frequency dependent phase domain model into a system composed by CI circuits, each one with its own source, shunt compensation (with a compensation level of 70% for all voltage levels), circuit-breakers and fault blocks. The basic approach is that all transmission circuits have the same length and are connected at terminals' substations to equivalent systems of different short-circuit ratio (SCR).

Fig. 9.1 shows a preview of a 4 circuit system modeled in PSCAD. However, as will be detailed below, the actual system is more complex and takes into account the actual transposition of the transmission lines and the fault point according to the transposition.

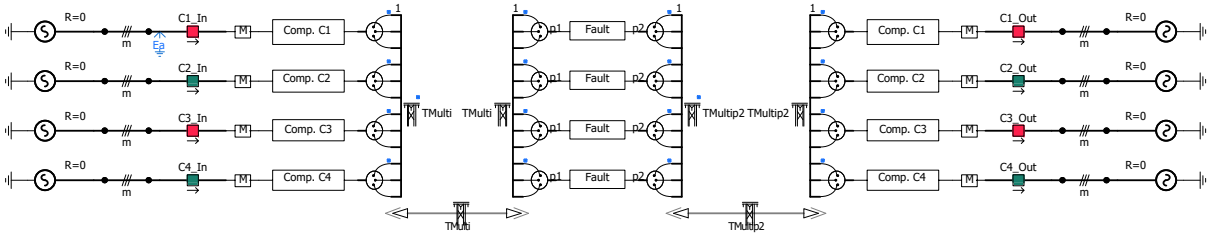

Figure 9.1 – Electrical system for transient behavior analyzes in PSCAD using four-circuits at the same tower.

The multi-circuits lines were modeled with real transposition cycles (1/6, 1/3, 1/3, 1/6). All circuits were transposed at the same location (tower), resulting in coincident transposition cycles. Although this approach is not the regular one, it is necessary to keep the correct phase sequence in all circuits along the entire system.

It is worth mentioning that because of the real transposition, when a single-line-to-ground (SLG) fault is applied at an specific phase, the position of the faulted phase in the tower will vary according to the fault location. As an example, if the fault is applied in phase A at 90% of the line length, phase A will be located in the original place. However, if the fault is applied in phase A at 65% of the line length phase A will be located in the original place of phase C. Fig. 9.2 represents the situation described before. As will be seen later, this characteristic will modify the response of the SLG faults with

and without single-pole auto-reclosing (SPAR) along the line.

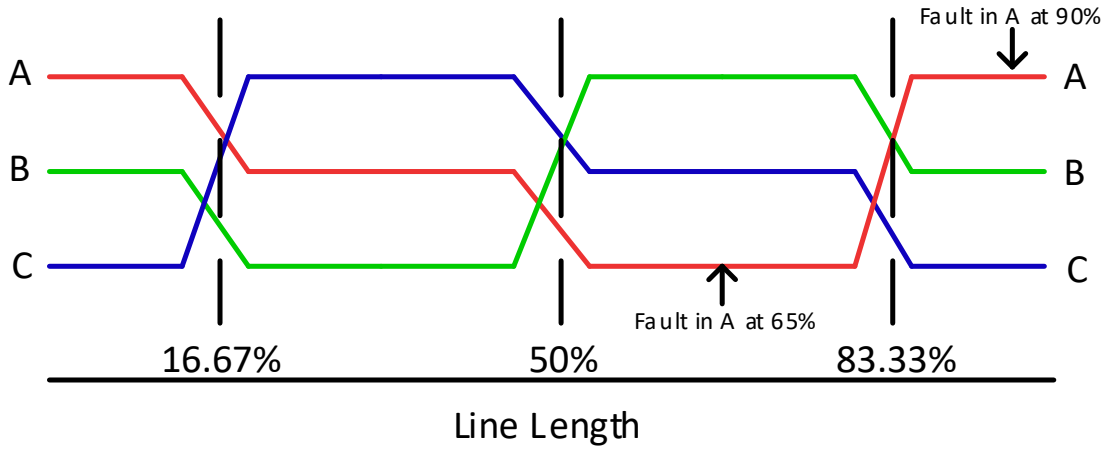

Figure 9.2 – Single-line-to-ground fault scheme in a circuit with real transposition.

As said before the transient response of the four systems was analyzed. In system one, the single-circuit line in Fig. 8.1 was used; in system two the double-circuit transmission line in Fig. 8.2 with phase sequence ABC CBA was used; in system three the triple-circuit transmission line in Fig. 8.3 with phase sequence CBA BAC ACB was used; finally, in fourth system the quadruple-circuit transmission line in Fig. 8.4 was used. The general equivalent system is shown in Fig. 9.3.

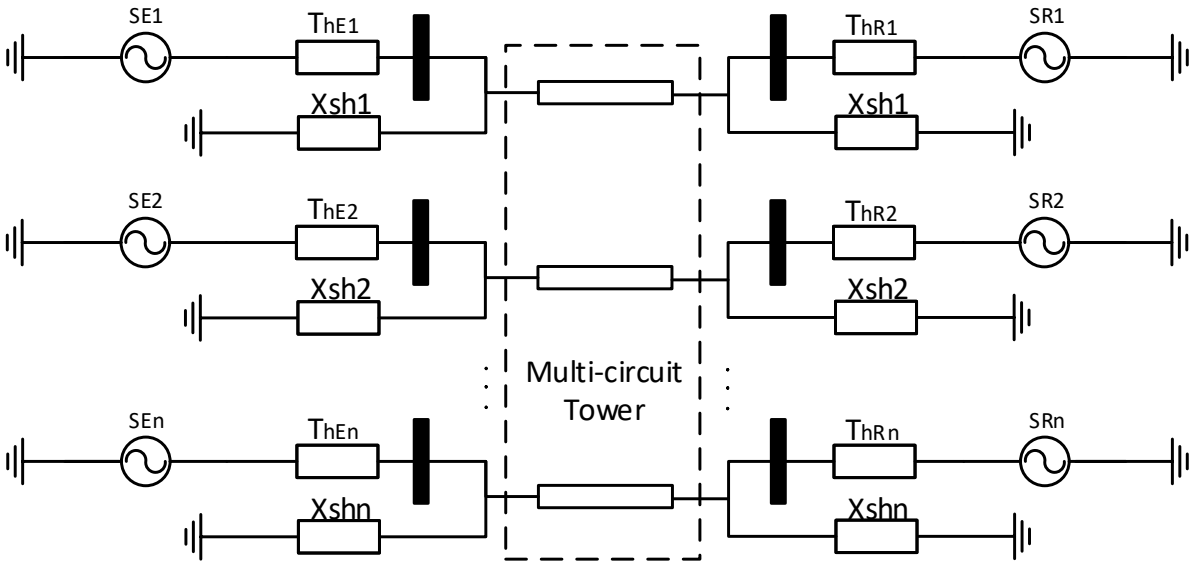

Figure 9.3 – Equivalent system for n circuits.

The parameters of each system were calculated using the two-port networks theory considering a loading condition of 90% of the SIL of each circuit (SIL_{ci}), and a SCR of 10 kA in all the reception equivalents, a SCR of 20 kA in the sending equivalent of 230 kV systems and a SCR of 40 kA in 500 kV systems and above.

The voltage phasor of the sending source $\widetilde{V}_{f1_{ci}}$ can be calculated using Eq. (9.1).

$$\widetilde{\mathbf{VI}}_{1_{ci}} = \begin{bmatrix} \widetilde{V}_{f1_{ci}} \\ \widetilde{I}_{f1_{ci}} \end{bmatrix} = \widetilde{\mathbf{Q}}_{f1_{ci}} \cdot \widetilde{\mathbf{Q}}_{c_{ci}} \cdot \widetilde{\mathbf{Q}}_{l_{ci}} \cdot \widetilde{\mathbf{Q}}_{c_{ci}} \cdot \widetilde{\mathbf{VI}}_{2_{ci}} \tag{9.1}$$

Where:

$\widetilde{\mathbf{I}}_{f1_{ci}}$ Current phasor of sending source of circuit *ci*

$\widetilde{\mathbf{VI}}_{1_{ci}}$ Voltage and current column vector of the sending source of circuit *ci*

$\widetilde{\mathbf{VI}}_{2_{ci}}$ Voltage and current column vector of the reception source of circuit *ci*

$\widetilde{\mathbf{Q}}_{f1_{ci}}$ Two-port network of the impedance of the sending source of circuit *ci*

$\widetilde{\mathbf{Q}}_{c_{ci}}$ Two-port network of line compensation of circuit *ci*

$\widetilde{\mathbf{Q}}_{l_{ci}}$ Two-port network of transmission line of circuit *ci*

The e.m.f (voltage phasor) of the reception source $\widetilde{V}_{f2_{ci}}$ can be calculated by knowing the load at reception terminal and assuming nominal voltage, as follows:

$$\widetilde{V}_{2_{ci}} = V_{l_{ci}} \tag{9.2}$$

$$\widetilde{S}_{t_{ci}} = SIL_{ci} \cdot L_{\%_{ci}}(pf_{ci} - jsin\theta_{ci}) \tag{9.3}$$

$$\theta_{ci} = tan^{-1}(pf_{ci}) \tag{9.4}$$

$$\widetilde{V}_{f2_{ci}} = \widetilde{V}_{2_{ci}} - S_{t_{ci}} \frac{\widetilde{Z}_{f2_{ci}}}{\widetilde{V}_{2_{ci}}} \tag{9.5}$$

$$\widetilde{I}_{2_{ci}} = \frac{\widetilde{V}_{2_{ci}} - \widetilde{V}_{f2_{ci}}}{\widetilde{Z}_{f2_{ci}}} \tag{9.6}$$

$$\widetilde{\mathbf{VI}}_{2_{ci}} = \begin{bmatrix} \widetilde{V}_{2_{ci}} \\ \widetilde{I}_{2_{ci}} \end{bmatrix} \tag{9.7}$$

Where:

$\widetilde{V}_{2_{ci}}$ Voltage at load point of circuit *ci*

$\widetilde{I}_{2_{ci}}$ Current at load point of circuit *ci*

$\widetilde{S}_{t_{ci}}$ Power at load point of circuit *ci*

$L_{\%_{ci}}$ % of the SIL of circuit *ci*

pf_{ci} Power factor of circuit *ci*

$\widetilde{V}_{f2_{ci}}$ Voltage phasor of reception source of circuit *ci*

$\widetilde{Z}_{f2_{ci}}$ Impedance of reception source of circuit *ci*

$\widetilde{\mathbf{VI}}_{2_{ci}}$ Voltage and current column vector of the reception source of circuit *ci*

The two-port network of the impedance of the receiver equivalent source is:

$$\widetilde{\mathbf{Q}}_{f2_{ci}} = \begin{bmatrix} 1 & \widetilde{Z}_{f2_{ci}} \\ 0 & 1 \end{bmatrix} \tag{9.8}$$

The two-port network of the line is calculating using (9.9) to (9.14).

$$\widetilde{\mathbf{Q}}_{l_{ci}} = \begin{bmatrix} \widetilde{\mathbf{A}}_{ci} & \widetilde{\mathbf{B}}_{ci} \\ \widetilde{\mathbf{C}}_{ci} & \widetilde{\mathbf{D}}_{ci} \end{bmatrix} \tag{9.9}$$

$$\widetilde{\mathbf{A}}_{ci} = cosh(\gamma_{+_{ci}} L) \tag{9.10}$$

$$\widetilde{\mathbf{B}}_{ci} = Z_{c+_{ci}} sinh(\gamma_{+_{ci}} L) \tag{9.11}$$

$$\widetilde{\mathbf{C}}_{ci} = \frac{sinh(\gamma_{+_{ci}} L)}{Z_{c+_{ci}}} \tag{9.12}$$

$$\widetilde{\mathbf{D}}_{ci} = \widetilde{\mathbf{A}}_{ci} \tag{9.13}$$

$$\gamma_{+_{ci}} = \sqrt{z_{+_{ci}} y_{+_{ci}}} \tag{9.14}$$

Where:

$\gamma_{+_{ci}}$ Positive sequence propagation constant of transmission line of circuit *ci*

L Line length of transmission line of circuit *ci* in [km].

$Z_{c+_{ci}}$ Positive sequence characteristic impedance of transmission line of circuit *ci*

$z_{+_{ci}}$ Positive sequence impedance per unit of length of transmission line of circuit *ci*

$y_{+_{ci}}$ Positive sequence admittance per unit of length of transmission line of circuit ci

The two-port network of the line compensation is calculated using (9.15) and (9.16).

$$\widetilde{\mathbf{Q}}_{c_{ci}} = \begin{bmatrix} 1 & 0 \\ \widetilde{Y}_{c_{ci}} & 1 \end{bmatrix} \tag{9.15}$$

$$\widetilde{Y}_{c_{ci}} = -\%_{c_{ci}} \frac{Y_{+_{ci}} \cdot L}{2} \cdot \frac{tanh(0.5\gamma_{+_{ci}} L)}{0.5\gamma_{+_{ci}} L} \tag{9.16}$$

Where:

$\widetilde{Y}_{c_{ci}}$ Compensation admittance of transmission line of circuit ci in $[\Omega]$

$\%_{c_{ci}}$ Percentage of compensation for transmission line of circuit ci

Normally, a fourth reactor called neutral reactor is added between the neutral point of the reactor bank and the ground. This reactor aims to eliminate or minimize the capacitive coupling between line phases. This coupling is the main power source for secondary arc in the lines when single- or three-phase tripping is implemented (ZEVALLOS, 2013). Fig. 9.4 shows the reactive compensation scheme, known as four-legged reactor: line reactor + neutral reactor.

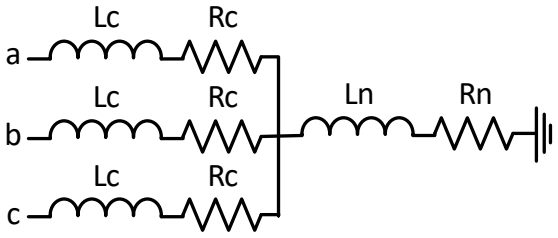

Figure 9.4 – Neutral reactor scheme.

Eqs. (9.17) to (9.19) show how to obtain the values for the neutral reactor according to line reactors. Typical reactor quality factors were considered, according to common practice in Brazilian power system.

$$R_{c_{ci}} = \frac{X_{c_{ci}}}{400} \tag{9.17}$$

$$X_{n_{ci}} = \frac{r_0 \cdot X_{c_{ci}} - 1}{3} \tag{9.18}$$

$$R_{n_{ci}} = \frac{X_{n_{ci}}}{40} \tag{9.19}$$

Where:

$X_{c_{ci}}$ Compensation reactance of transmission line of circuit ci ($\frac{1}{Y_{c_{ci}}}$) in $[\Omega]$.

$R_{c_{ci}}$ Resistance associated to phase reactor of circuit ci in $[\Omega]$.

$X_{n_{ci}}$ Neutral reactor reactance of transmission line of circuit ci in $[\Omega]$.

$R_{n_{ci}}$ Resistance associated to neutral reactor of circuit ci in $[\Omega]$.

r_0 X_0/X_1 ratio of reactor zero and positive sequence components assumed as 1.5 (ZEVALLOS, 2013).

The parameters obtained for the systems presented in Figs. 8.1 to 8.4 that were used in transient studies are presented in Table 9.1. Additionally, the parameters of each transmission line in each system are shown in Table 9.2.

Table 9.1 – Parameters of the systems.

	SE		*SR*		Compensation		Neutral React.	
Circuit	V [kV]	angle [°]	V [kV]	angle [°]	$R_c[\Omega]$	$X_c[\Omega]$	$R_n[\Omega]$	$X_n[\Omega]$
Single-circuit line								
1	545.16	22.92	493.43	-7.72	3.03	1210.96	15.13	605.14
Double-circuit line								
1	543.69	23.29	493.44	-7.68	2.99	1197.99	14.97	598.66
2	544.77	23.41	493.40	-7.80	2.93	1171.94	14.64	585.64
Triple-circuit line								
1	815.83	23.92	739.97	-10.69	3.25	1300.39	16.14	645.57
2	814.73	24.12	740.17	-11.29	3.08	1230.86	15.38	615.10
3	1088.70	24.93	991.42	-15.23	3.06	1222.82	15.27	611.08
Quadruple-circuit line								
1	255.29	22.69	228.34	-2.96	3.49	1394.52	17.42	696.93
2	254.79	22.79	228.39	-2.83	3.63	1450.26	18.12	724.79
3	546.54	23.43	493.38	-7.89	2.89	1154.59	14.42	576.96
4	547.21	23.39	493.36	-7.98	2.86	1143.31	14.28	571.32

Table 9.2 – Line parameters calculated for 60 Hz.

Circuit	$R_{l_0}[\Omega/km]$	$X_{l_0}[\Omega/km]$	$Y_{l_0}[\mu S/km]$	$R_{l_{1,2}}[\Omega/km]$	$X_{l_{1,2}}[\Omega/km]$	$Y_{l_{1,2}}[\mu S/km]$
Single-circuit line						
1	0.48	1.59	2.87	0.022	0.24	6.62
Double-circuit line						
1	0.43	1.56	4.18	0.019	0.25	6.73
2	0.47	1.53	4.11	0.019	0.25	6.73
Triple-circuit line						
1	0.35	1.53	3.92	0.017	0.27	6.20
2	0.37	1.50	4.18	0.015	0.25	6.53
3	0.41	1.43	3.84	0.011	0.25	6.54
Quadruple-circuit line						
1	0.41	1.70	4.02	0.043	0.29	5.78
2	0.42	1.67	4.39	0.043	0.31	5.54
3	0.43	1.56	4.83	0.022	0.24	6.96
4	0.48	1.54	4.07	0.022	0.24	6.93

Notes

$_0$: zero sequence

$_{1,2}$: positive, negative sequence

Aiming to characterize the transient behaviour of the proposed MCMVTLs, a typical transient study was performed, considering specifically the following cases: single-line-to-ground fault (SLG) applied always in phase A with three-phase and single-phase reclosing, three-phase fault and load rejection. The actual transposition cycles were modeled and a soil resistivity of 4000 Ω.m was used, considering that this is a high, but still frequent value in Brazil.

The faults were applied individually at 90% of the line length of each circuit. No simultaneous faults in different circuits were considered.

The sequence used for fault studies is the following: 1) A fault with a resistance of 10 Ω is applied during 300 ms near to the maximum voltage value of one phase; 2) The nearest breaker opens after 100 ms of fault occurrence; 3) The remote breaker opens 20 ms after nearest breaker operation; 4) After 500 ms of dead-time the line reclosing is performed.

For fault extinction it was considered either the imposed fault duration or a self fault extinction for fault currents lower than 30 A in 230 kV systems; 50 A in 500 kV and 750 kV systems, and 80 A in 1000 kV systems.

In the case of load rejection there is no fault, only the breaker at reception substation opens and there is no reclosing.

In all cases a statistical breaker operation was considered with 100 cases. The

master pole operation time varies uniformly over one fundamental cycle, and remainder slaves poles operation times consider Gaussian distributions with standard deviation of 2 ms related to master pole.

In this section only the graphical response of the quadruple-circuit transmission line for a LG fault applied in the fourth circuit with single-phase auto-reclosing is presented. However, the response of the other cases/systems were summarized in Tables 9.3 to 9.6.

Figs. 9.5 to 9.7 show the voltage response at both line terminals and fault point in the 4-circuit line for a LG fault in circuit 4 with single-phase tripping. Note that during the fault in c_4 the voltages at the sending terminal of the healthy circuits present a small disturbance that disappears after protection actuation. Also, it is possible to observe another disturbance in the sound circuits when the reclosing is performed. On the other hand, higher disturbances are experienced at receiving terminal at the same instants. This is derived both due to fault proximity and weaker remote equivalent. The strongest coupling is sensed at the fault location, where higher coupling overvoltages were produced in the others circuits.

It is interesting to observe the strong coupling between circuits 1 and 4 that have the same phase sequence (ABC BCA CAB ABC). Thus, circuit 1 overvoltage is higher than the ones in circuits that are closer to the faulted circuit, the 4^{th} one.

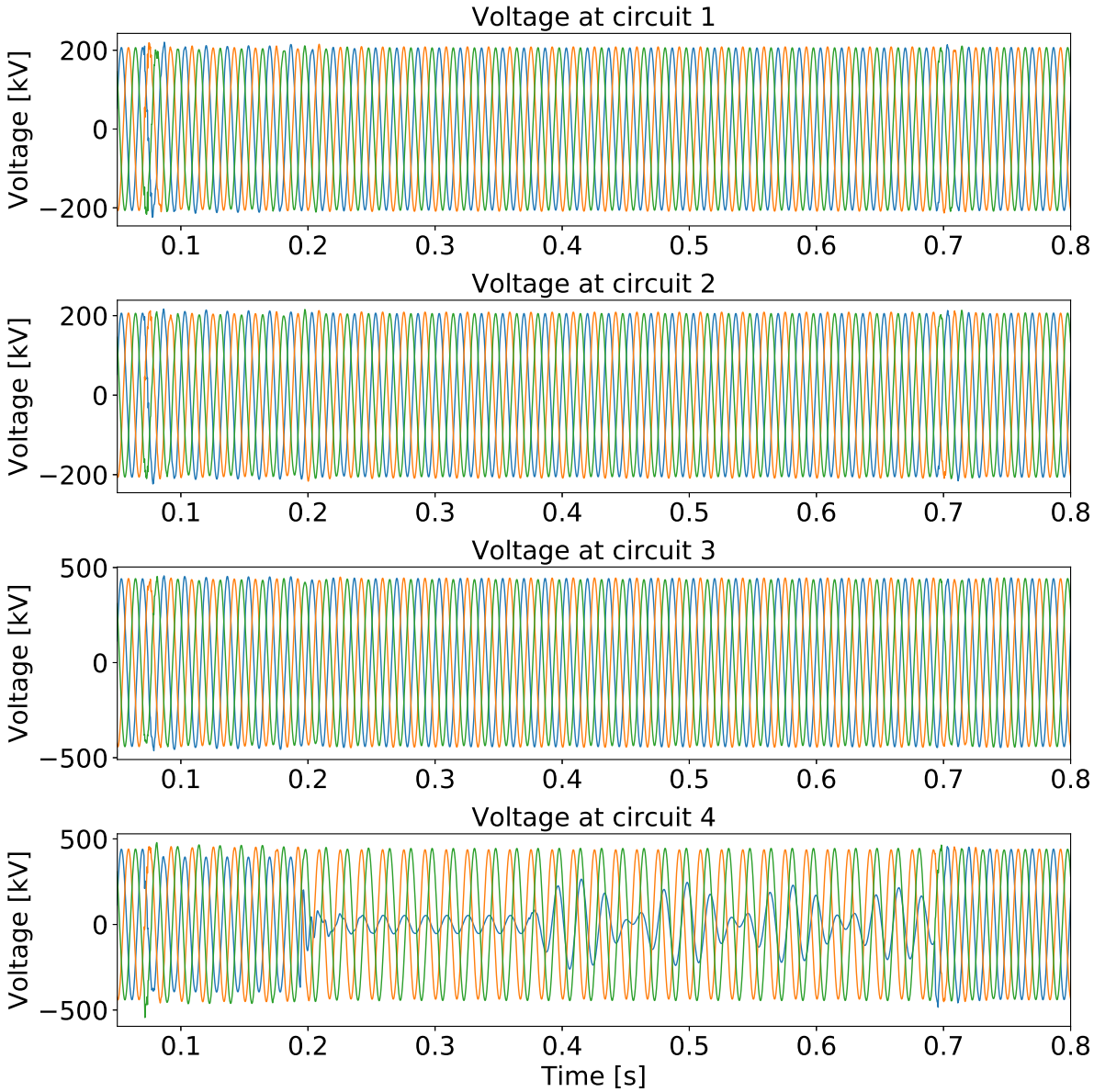

Figure 9.5 – Voltage at sending terminal for a SLG fault at circuit 4 with single-phase reclosing in the quadruple-circuit line.

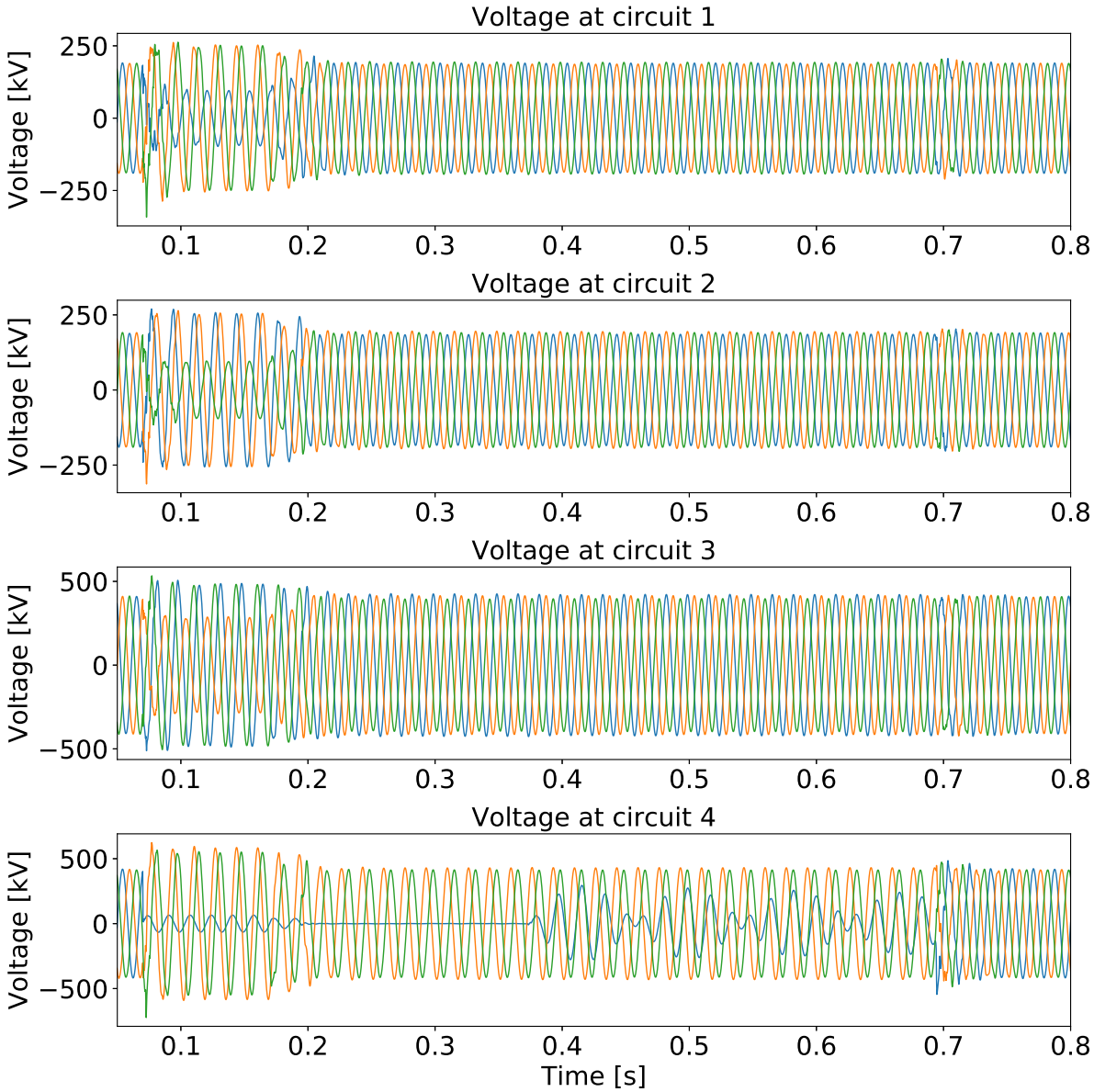

Figure 9.6 – Voltage at fault point for a SLG fault at circuit 4 with single-phase reclosing in the quadruple-circuit line.

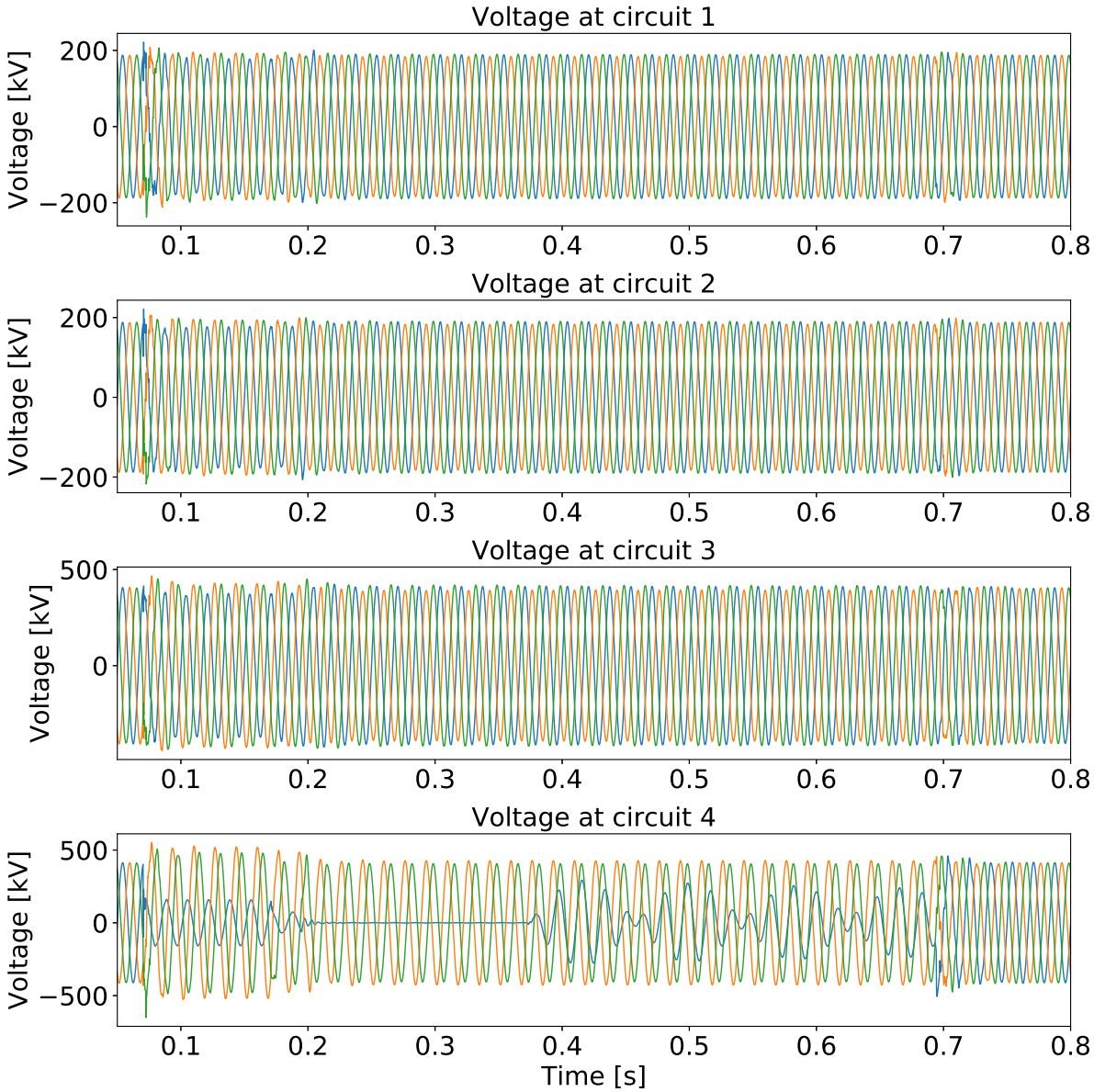

Figure 9.7 – Voltage at receiving terminal for a SLG fault at circuit 4 with single-phase reclosing in the quadruple-circuit line.

At the top of Fig. 9.8 it is shown the current at the fault point. The events of fault occurrence, breaker operation, secondary arc extinction and reclosing are marked. It is possible to observe that the fault was removed after 300 ms of fault occurrence (defined maximum fault duration - premise). This occurred because the secondary arc current was higher than the imposed limits for self-extinction. A zoom of the secondary arc current of the related case can be seen at the bottom of Fig. 9.8. To have a self-extinction during a dead time of 500 ms it is necessary to design the appropriate neutral reactor for each case or high-speed grounding switches. However, this has not been considered in this chapter.

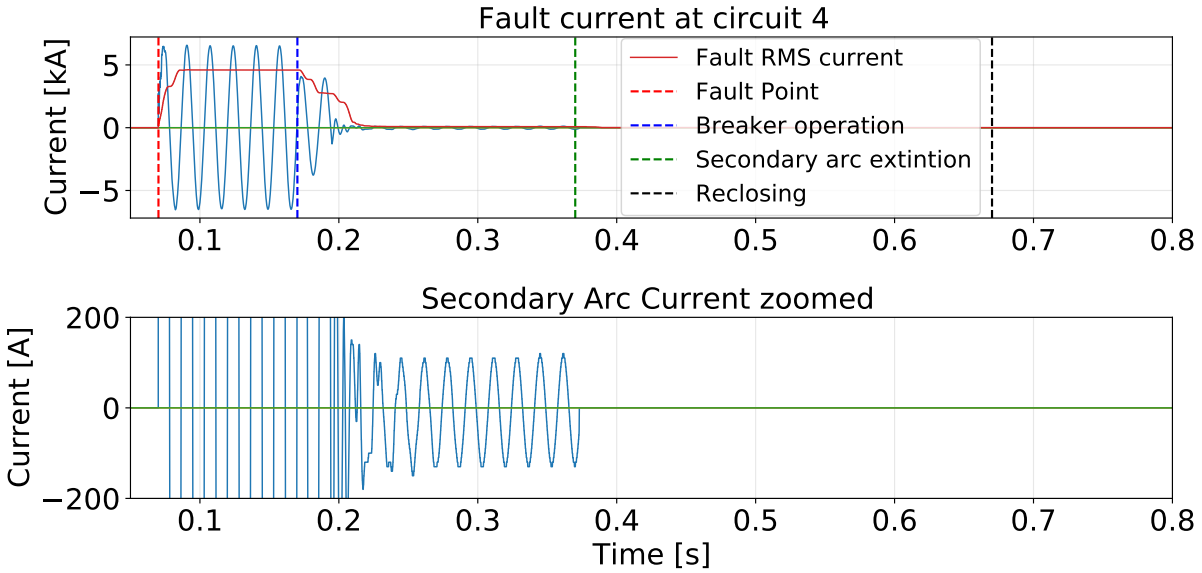

Figure 9.8 – (Top) Current at fault point for a SLG fault at circuit 4 with single-phase reclosing in the quadruple-circuit line. (Bottom) Secondary arc current zoomed at fault point for a SLG fault at circuit 4 with single-phase reclosing in the quadruple-circuit line.

Although secondary arc current minimization was not focused in the present study, a regular neutral reactor optimal relationship of $X_0/X_1 = 1.5$ (ZEVALLOS, 2013) was adopted, considering each circuit stand-alone. A more complete study is necessary to mitigate circuit coupling, and high-speed grounding switches may be an interesting alternative.

It was observed that, as a consequence of the electric field produced by each circuit, the phase sequence plays an important role in secondary arc current minimization. Thus, with the conventional ABC sequence in the quadruple-circuit transmission line, a secondary arc current of 120 A is obtained for a fault in c_4, meanwhile with the proposed phase sequence the value is only 85 A. Additionally, when neutral reactors are not installed, the secondary arc current grows to 185 A in the conventional phase sequence case and to 140 A in the optimal phase sequence case. This shows the importance of the phase sequence design and optimal neutral reactors use to reduce secondary arc currents.

Figs. 9.9 to 9.10 show the current wave-forms at both line terminals. Note that although the voltage of health circuits were not severely affected by the fault, the current sensed it most. This is because in the tested system the voltage is imposed by the terminal equivalents, whereas the current is not. Thus, when a fault occurs in one circuit, overcurrents will be coupled in near circuits. Because of this, the protection scheme has to be properly designed to cope with multi-circuit lines.

Again, a very important result is the influence of phase sequence. Thus, the strongest coupling is observed between circuits 1 and 4. Therefore, circuit 1 suffers a

strong unbalance throughout the single-phase opening period, that is even higher than the one experienced by the 3^{rd} circuit. This is not an expected result, but it is produced because phases A in 1^{st} and 4^{th} circuit are in phase, whereas phases A in 1^{st} and 3^{rd} circuit are not (ABC BCA CAB ABC). This result puts in evidence that the phase sequence also plays an important role reducing the induction caused by the nearest circuits.

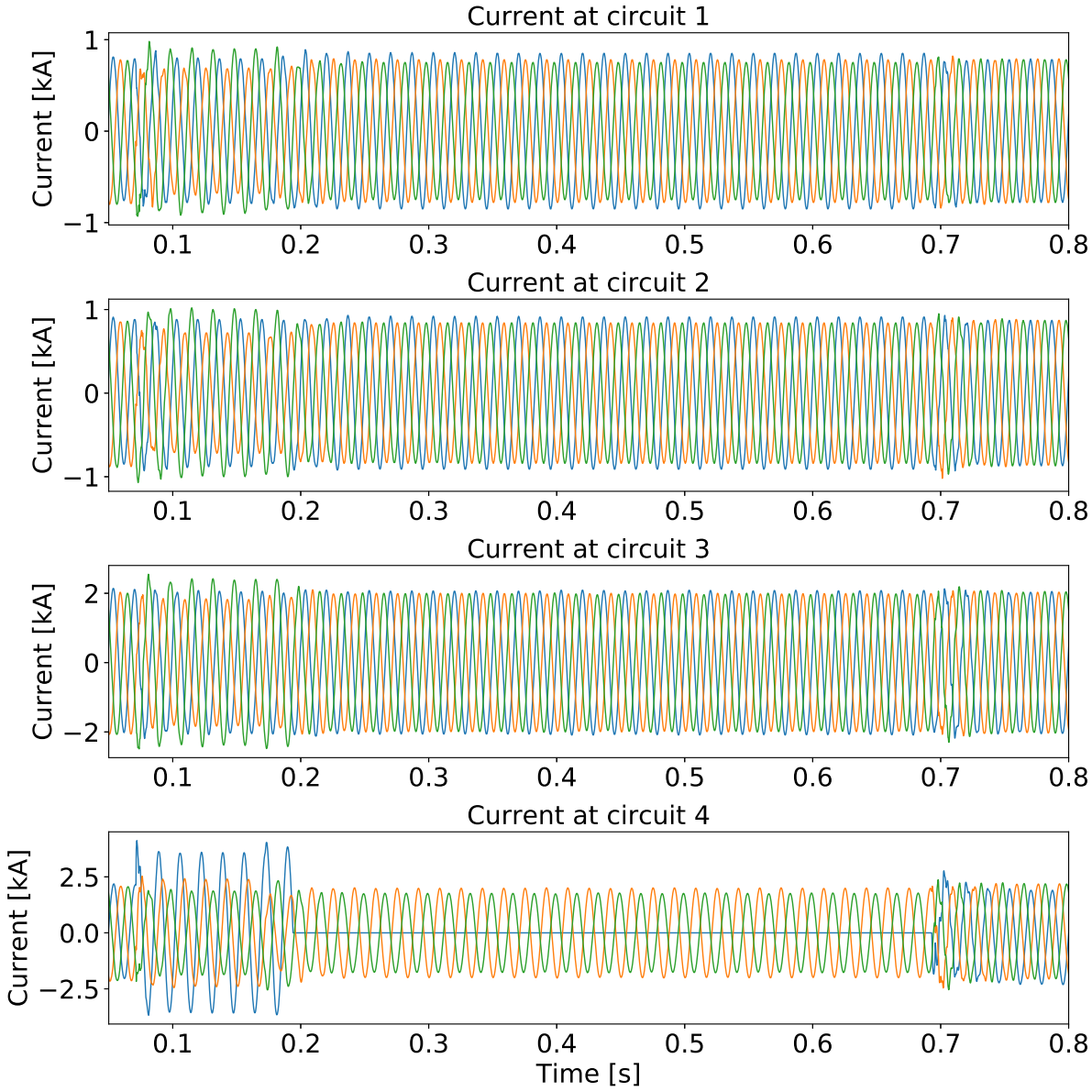

Figure 9.9 – Current at sending terminal circuit-breaker for a SLG fault at circuit 4 with single-phase reclosing in the quadruple-circuit line.

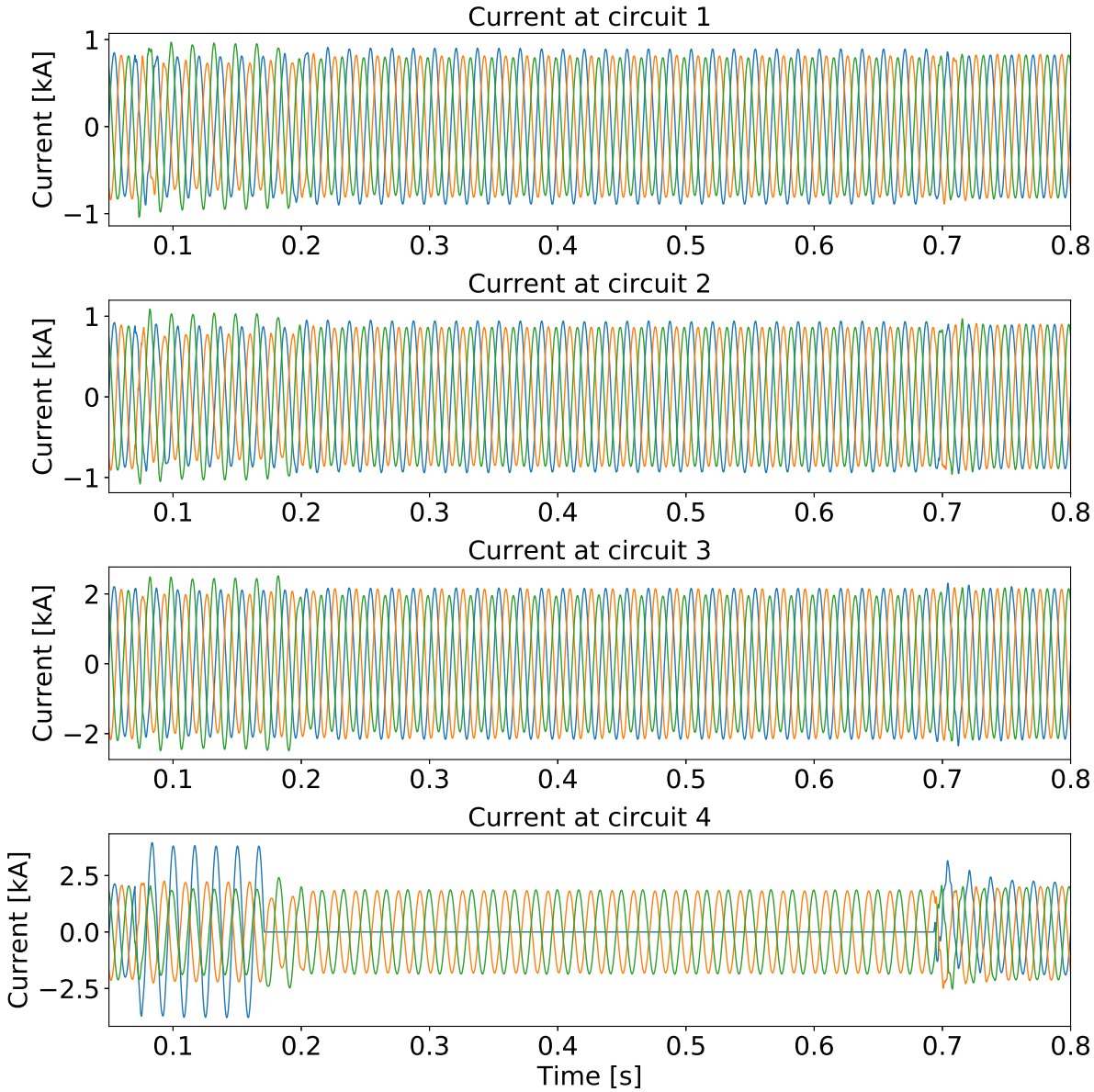

Figure 9.10 – Current at receiving terminal circuit-breaker for a SLG fault at circuit 4 with single-phase reclosing in the quadruple-circuit line.

The other tested systems behave in a similar way as in the quadruple-circuit line, inducing oververvoltages and overcurrents in near circuits during disturbances.

Tables 9.3 to 9.6 summarize the overvoltages presented in circuit one at 90% of line length when a disturbance occurs in the others c_i circuits. The system with a single-circuit transmission line was simulated in order to compare with multi-circuit transmission lines. It is important to highlight that the results were selected to be presented in the fault location in order to reduce the terminal equivalent interference.

Note that the highest overvoltages occur generally in the case of a SLG fault with three-phase reclosing. Although the highest overvoltage is observed in the circuit where the fault occurred, the coupling overvoltage varies as analyzed above.

Table 9.3 – Overvoltage for events in a single-circuit transmission line at 90% of line length.

Voltage in [pu]	Single-line-to-ground fault with		Three-phase fault	Load rejection
	Three-phase reclosing	Single-phase reclosing		
Min.:	1.98	1.45	1.93	1.78
Max.:	2.33	2.17	2.16	1.80
Mean:	2.14	1.71	2.06	1.79

From Tables 9.4 to 9.6 it is possible to note that when a fault occurs in one circuit, the other circuits suffer important disturbances on their own voltage waveform. The strength of the disturbance depends on factors such as fault type, phase sequence and circuit proximity.

Table 9.4 – Overvoltage in circuit 1 for events at circuit c_i in a double-circuit transmission line at 90% of line length.

Voltage [pu]	Single-line-to-ground fault at circuit with			
	Three-phase reclosing		Single-phase reclosing	
	c_1	c_2	c_1	c_2
Min.:	1.97	1.27	1.50	1.27
Max.:	3.25	1.42	1.85	1.42
Mean:	2.47	1.32	1.76	1.32
Voltage [pu]	Three-phase fault at circuit		Load rejection at circuit	
	c_1	c_2	c_1	c_2
Min.:	1.94	1.34	1.70	1.09
Max.:	2.81	1.54	1.83	1.09
Mean:	2.25	1.47	1.75	1.09

Table 9.5 – Overvoltage in circuit 1 for events at circuits c_i in a triple-circuit transmission line at 90% of line length.

Voltage [pu]	Single-line-to-ground fault at circuit with					
	Three-phase reclosing			Single-phase reclosing		
	c_1	c_2	c_3	c_1	c_2	c_3
Min.:	2.22	1.22	1.30	1.44	1.22	1.30
Max.:	3.16	1.36	1.44	1.87	1.35	1.44
Mean:	2.61	1.27	1.39	1.62	1.26	1.39
Voltage [pu]	Three-phase fault at circuit			Load rejection at circuit		
	c_1	c_2	c_3	c_1	c_2	c_3
Min.:	2.21	1.39	1.36	1.74	1.10	1.08
Max.:	2.75	1.44	1.46	1.85	1.11	1.10
Mean:	2.48	1.42	1.40	1.78	1.11	1.08

Table 9.6 – Overvoltage in circuit 1 for events at circuit c_i in a quadruple-circuit transmission line at 90% of line length.

	Single-line-to-ground fault at circuit with							
Voltage	Three-phase reclosing				Single-phase reclosing			
[pu]	c_1	c_2	c_3	c_4	c_1	c_2	c_3	c_4
Min.:	2.30	1.27	1.49	1.50	1.46	1.27	1.49	1.50
Max.:	3.54	1.32	1.66	**1.83**	2.21	1.32	1.65	**1.83**
Mean:	2.72	1.29	1.58	1.73	1.75	1.29	1.58	1.74
	Three-phase				Load rejection			
Voltage	fault at circuit				at circuit			
[pu]	c_1	c_2	c_3	c_4	c_1	c_2	c_3	c_4
Min.:	2.14	1.31	1.39	1.32	1.74	1.12	1.13	1.12
Max.:	2.54	1.40	1.49	1.38	1.79	1.13	1.13	1.13
Mean:	2.29	1.33	1.43	1.35	1.77	1.12	1.13	1.12

When analyzing the fault type it is possible to note that the coupled overvoltages produced by SLG faults with single-pole and three-pole tripping are practically the same, no matter the quantity of circuits. However, when the faults are applied and measured in their own circuit there is a difference on the overvoltage caused by single-pole and three-pole tripping. In this case, the overvoltage caused by the three-pole tripping is higher, and corresponds to the most significant overvoltages observed in the different events.

As expected, higher overvoltages were produced for faults in their own circuits, obtaining important overvoltages near to 3.5 pu in some cases. Note that no surge arrester was modeled in order to obtain the maximum overvoltages.

Also, note that the switching with lowest influence on the other circuits was load rejection, in which the highest induced overvoltage was only 1.13 pu. Additionally, load rejection was the only maneuver that did not suffered a significant change when the switching was performed in its own circuit, no matter the number of circuits in the tower. Therefore, we can conclude that load rejection is strongly linked to the SCR of the system and weakly connected to the phase sequence. In almost all cases the value was near to 1.8 pu.

If we sort the fault types according to the produced overvoltage on their own circuits, we can obtain the next order: SLG fault with three-pole tripping, three-phase fault, SLG fault with single-pole tripping and finally load rejection. However, if we sort the fault types according to the induced overvoltage on the other circuits, in most of the cases we obtain a different order: three-phase fault, SLG fault with three-pole/single-pole tripping, and finally load rejection. Surprisingly, depending on the phase sequence, the order of fault severity can change and be equal to the case of faults applied and measured in

their own circuits. The former case can be seen in Table 9.6, highlighting other important characteristic of the lines with non-conventional phase sequence. Therefore, the fault types severity degree, when induced overvoltages is focused, is also determined by the fault sequence.

As stated before, the phase sequence has an influence on the overvoltage level. Thus, an important point to highlight is that in some cases the most remote circuits have higher influence on circuit one than the closest circuits. This behaviour can be seen more clearly in Table 9.6 where the higher overvoltage was caused by the fault in circuit 4. One could expect that the closest circuit with higher voltage (i.e. circuit 3 in the quadruple line) would cause the highest induced overvoltage due to the stronger coupling. However, since a non-conventional phase sequence (e.g., ABC BCA CAB ABC in the quadruple line) was used, in the fault instant phase A of circuit 1 and 4 are in phase, meanwhile phase A of circuit 3 is delayed. Therefore, a higher overvoltage is induced by the circuit 4 and not by the third circuit. Note in Table 9.5 that the circuit 3 also induces higher overvoltage than circuit 2. However, in this case the higher value is caused by the higher nominal voltage in circuit three (1000 kV) and not by the fault sequence, because the phase under fault in circuit 3 is not in phase with circuit 1 (CBA BAC ACB). Therefore, the overvoltage caused by circuit 3 in circuit 1 was not so severe.

One last thing to note from Tables 9.4 to 9.6 is that comparing system 1 and 2 (both with 500 kV lines and similar SIL) the overvoltages for faults in their own circuits in the double-circuit transmission lines were higher. Therefore, having a closer circuit will increase overvoltages even when the fault occurs in their own circuit. Because of this, in order to ensure proper system operation and safety, future researches should be focused on the protection scheme and overvoltage mitigation in multi-circuit transmission lines.

10 Secondary arc mitigation

The large majority of the faults that occur in transmission lines are single-line to ground (SLG) faults. In the case of the Brazilian Interconnected System (SIN) 80.6% of the faults in 500 kV lines are SLG faults, meanwhile in 750 kV lines the occurrences of SLG faults increase to 88.2% (DIAS; TAVARES, 2016). In this sense, it is worth to use maneuvers that only involve the faulted phase.

Single phase/pole auto reclosing (SPAR) is a useful technique to maintain the power supply in the sound phases during a SLG fault. In (KIMBARK, 1964) it is shown that in single-circuit lines it is possible to maintain 54% of the total power, whereas in double-circuit lines the value increases to 75%. SPAR for a SLG fault trips only the faulted phase while maintaining the operation of the sound phases. Under this condition, the system will operate in unbalance state. After a certain dead-time, in an attempt for reestablishing the power flow, the faulty phase is reclosed. However, if in that instant the fault current and transient recovery voltage (TRV) are high enough, SPAR will fail. With SPAR failure, three-phase tripping must be performed, interrupting the entire power flow.

During a SPAR maneuver there exist two main faulty currents, the primary arc current and the secondary arc current. The primary arc current normally has a magnitude of dozens of kA and lasts from the moment of fault inception, to the moment when the single-pole tripping is performed. After the single-pole tripping, there is a residual secondary arc current (SAC), that normally range between tens to hundreds of amps. It is mainly maintained by the capacitive coupling between the sound phases and the faulted phase (KNUDSEN, 1962). Fig.10.1 illustrates this situation.

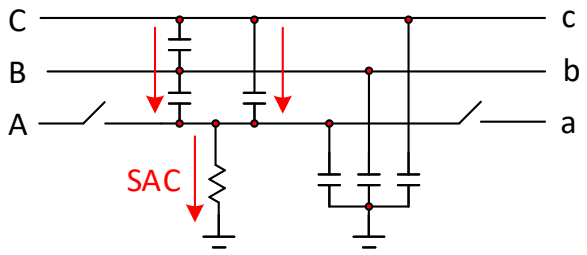

Figure 10.1 – Mutual coupling in a single-pole tripping situation.

Figs. 10.2 and 10.3 show an example of the arc current and voltage obtained in an optimized single-circuit transmission line. The arc extinction will occur when certain conditions are met. However, if the TRV, which is the first voltage peak after the arc extinction, is high enough, a re-ignition of the arc will occur. Some arc models have been

developed by different researchers. They will be discussed later.

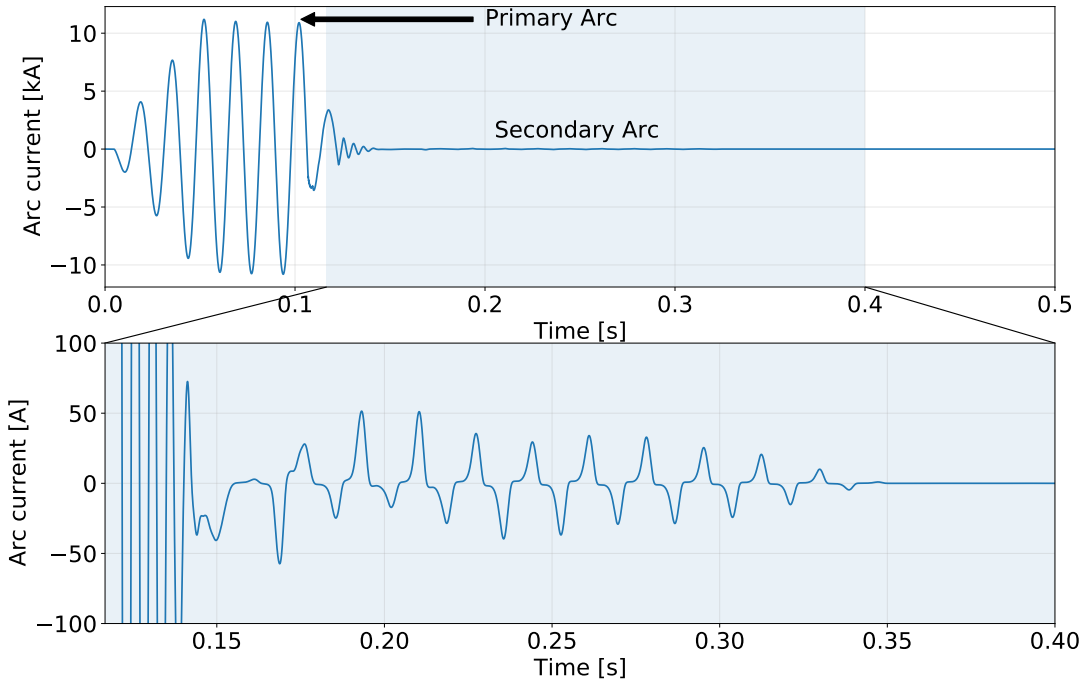

Figure 10.2 – Arc current (top) and secondary arc current (zoomed, bottom) for a fault applied on 95% of one optimized single-circuit line.

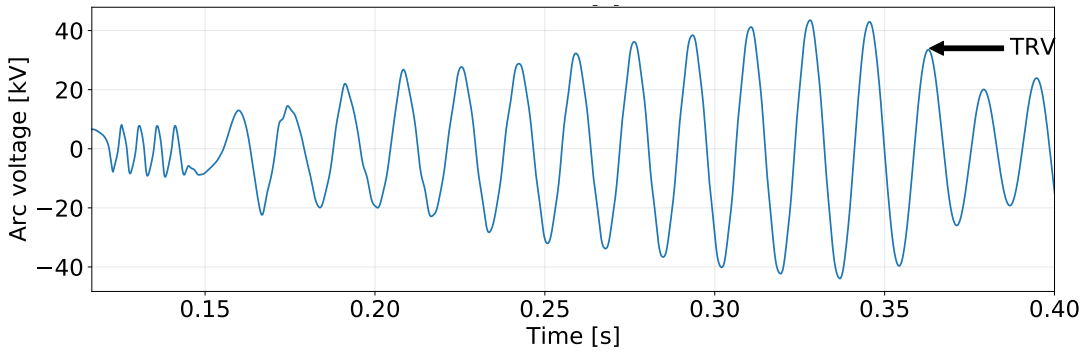

Figure 10.3 – Arc voltage for a fault applied on 95% of one optimized single-circuit line.

According to (BALOSSI *et al.*, 1966), SPAR under a dead time of 500 ms has a high probability of success in 500 kV transmission lines if the SAC and TRV steady state values are within the limits shown in Fig. 10.4. However, since there are not similar curves for other voltages levels, we are using the extrapolated SAC limits (SAC_{limit}) and TRV limits (TRV_{limit}) in Table 10.1 to determine the probability of successful SPAR.

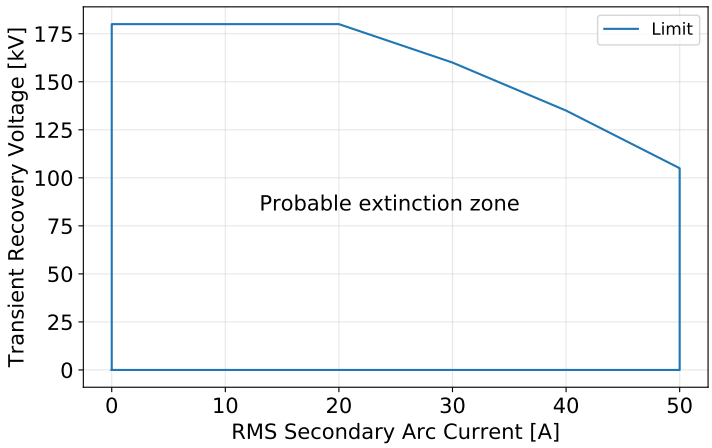

Figure 10.4 – Zone with high SPAR probability.

Table 10.1 – SAC_{limit} and TRV_{limit} according the line voltage V_l.

V_l [kV]	138 to 345	440 to 500	750 to 1150
SAC_{limit} [A]	30	50	80
TRV_{limit} [kV]	60	100	160

The typical approach to reduce the SAC is the use of the four-legged reactor as presented in Fig. 10.5.

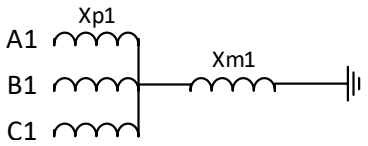

Figure 10.5 – Ideal conventional Four-legged reactor scheme: Phase reactors (X_{p_1}) + neutral reactor (X_{m_1}).

The four-legged reactor must be designed to reduce the Ferranti effect and reduce the SAC (KNUDSEN, 1962; KIMBARK, 1964). To address the first objective, the positive sequence susceptance of the four-legged reactor must equal the positive sequence susceptance of the line (b_1) multipled by a compensation factor ξ as in (10.1). Normally, this factor varies between 0.7-0.9 in long transmission lines.

$$x_{p_1} = 1/\xi b_1 \tag{10.1}$$

For SAC reduction, the coupling between line phases must be equal to the mutual susceptance of the shunt reactor. The neutral reactor x_{m_1} is then calculated as in (10.2), considering the zero and positive susceptance of the line (b_0 and b_1).

$$x_{m_1} = -\frac{b_0 - b_1}{3b_1\xi(b_0 - b_1 + b_1\xi)} \tag{10.2}$$

10.1 Secondary arc current in O-MCMVTLs

Although O-MCMVTLs have optimized phase sequence that contribute positively to reduce the secondary arc current, the current magnitudes are very high in many cases. This is caused by the high capacitive coupling between phases and circuits. This could yield a failure in the SPAR. Fig. 10.6 shows the complex capacitive coupling in a 4-circuit transmission line. As you may guess, the SAC and TRV behavior will be complex. Therefore, the design of the reactor compensation becomes extremely difficult.

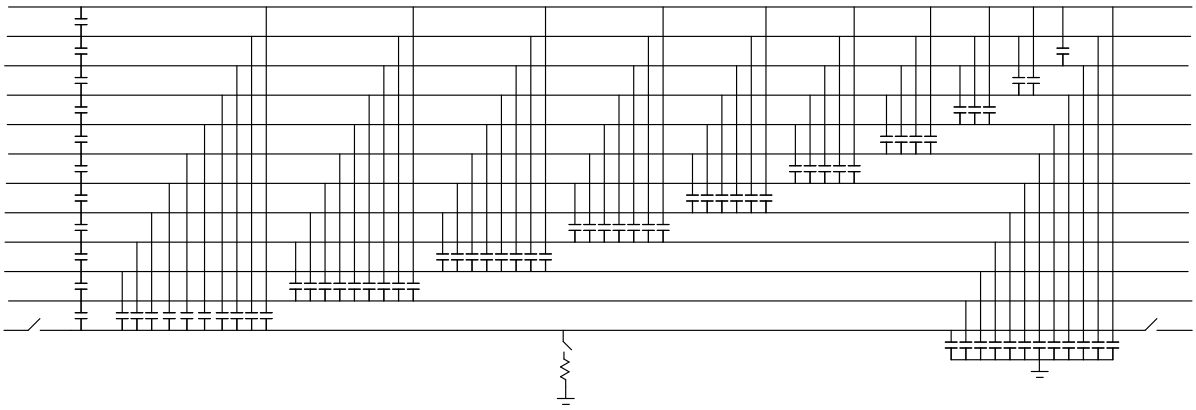

Figure 10.6 – Mutual coupling in a single-pole tripping situation.

To observe the behavior of the SAC and TRV in O-MCMVTLs PSCAD was used. The same transmission lines as in the previous section, presented in Fig. 10.7 to 10.10, were selected. However, the system equivalents were slightly changed. The lines were set to 350 km with real transposition (1/3, 1/6, 1/6, 1/3). They were connected to four-legged reactors at both sides. Also, to a strong system with short circuit ratio (SCR) = 25 at the sending end (different from previous chapter), and to a weak system of SCR = 15 at the receiving end. The base for the SCR is the current when transmitting their line surge impedance loading (SIL). The system equivalents were calculated using the following relationships: $x_1/r1 = 10$, $x_0/r0 = 5$ and $x_0/x1 = 5$. The fonts were set to transmit 90% of the line SIL. The adopted compensation level in each circuit was $\xi = 0.7$. The neutral reactors were obtained using (10.2). Table 10.2 presents the resulting values of the systems.[1]

[1] In practical situations it is possible to have a phase shift between the circuits, yielding a different behavior of the line. Therefore, this scenario should be studied in future researches.

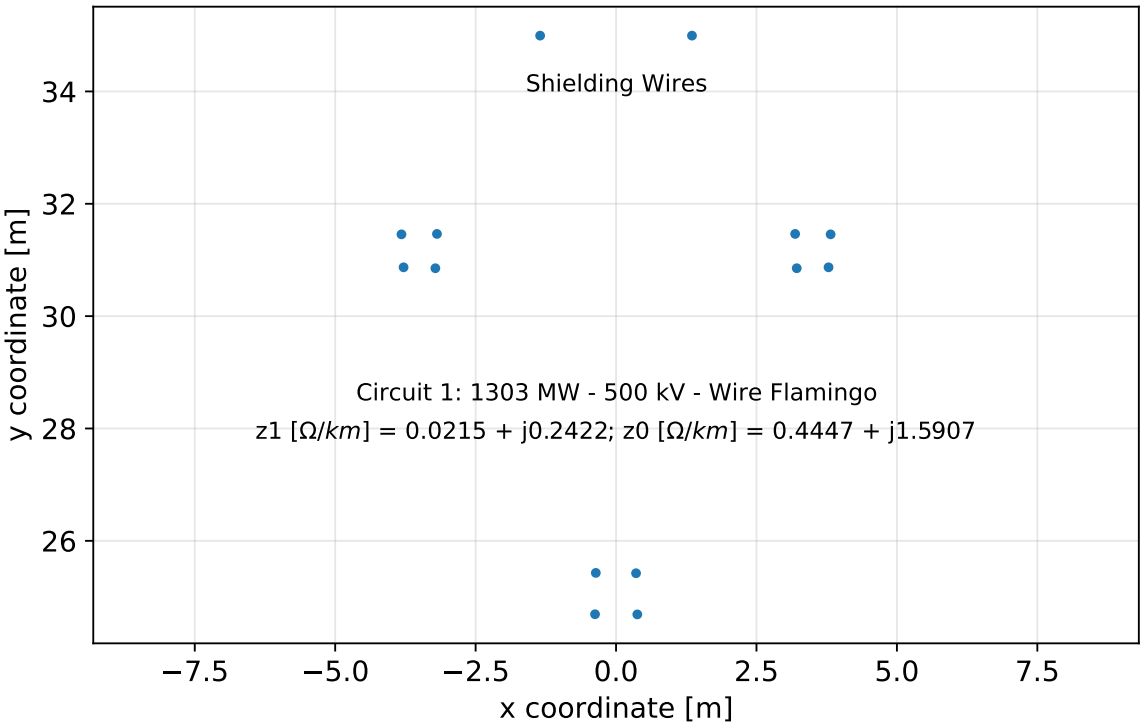

Figure 10.7 – Single-circuit transmission line for SAC study.

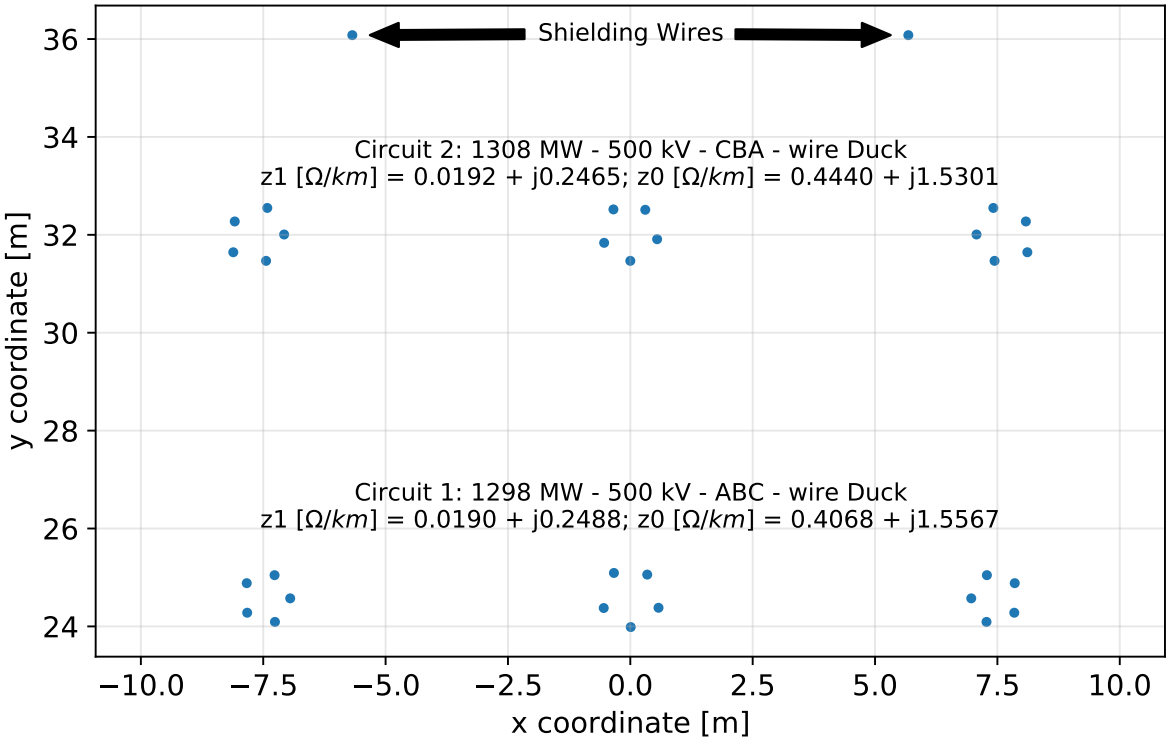

Figure 10.8 – Double-circuit transmission line for SAC study.

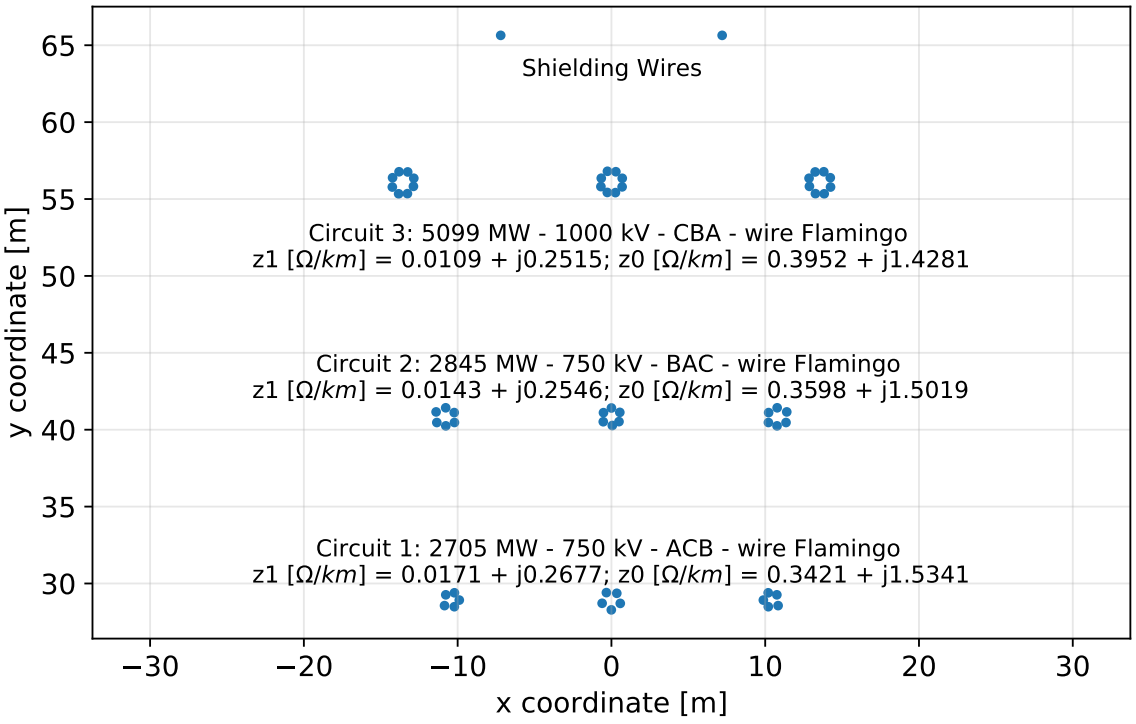

Figure 10.9 – Triple-circuit transmission line for SAC study.

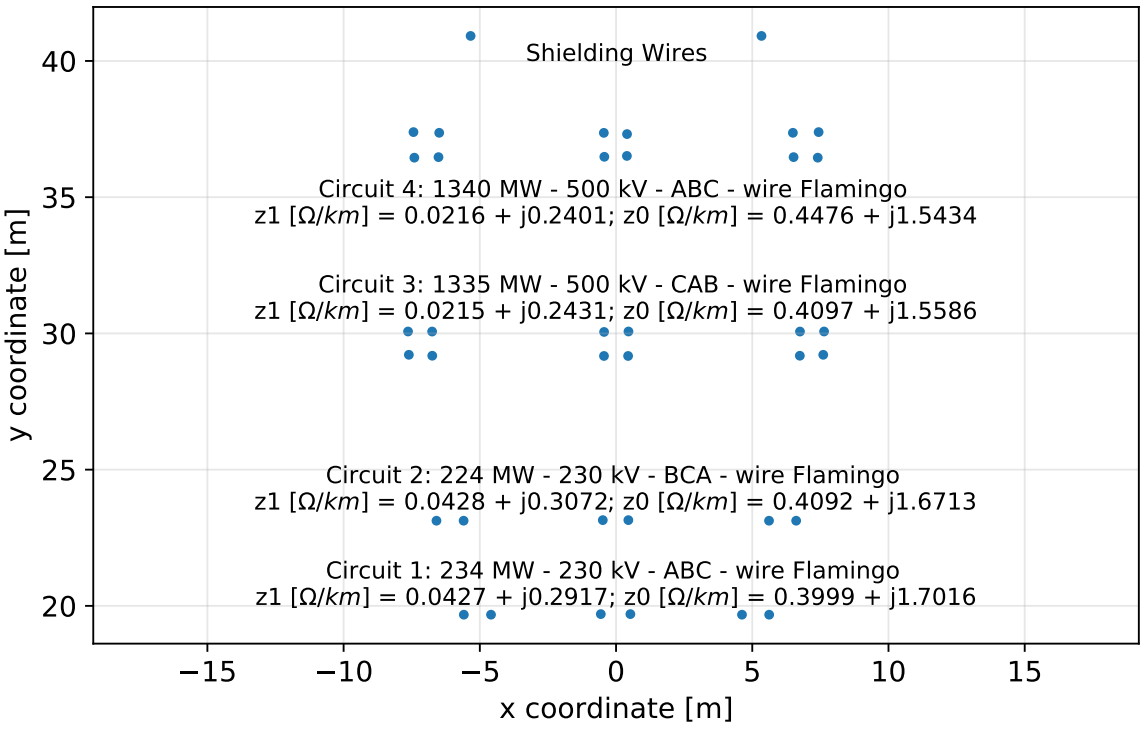

Figure 10.10 – Quadruple-circuit transmission line for SAC study.

Table 10.2 – Characteristics of the systems.

	Sending source [kV]			
Line	$V_{le_{ci_1}}$	$V_{le_{ci_2}}$	$V_{le_{ci_3}}$	$V_{le_{ci_4}}$
Single	$544.56\angle 23.07^o$	-	-	-
Double	$543.13\angle 23.46^o$	$544.11\angle 23.55^o$	-	-
Triple	$811.09\angle 23.47^o$	$809.19\angle 23.56^o$	$1074.21\angle 23.56^o$	-
Quadruple	$255.68\angle 23.20^o$	$255.28\angle 23.35^o$	$545.80\angle 23.55^o$	$546.40\angle 23.50^o$
	Receiving source [kV]			
Line	$V_{lr_{ci_1}}$	$V_{lr_{ci_2}}$	$V_{lr_{ci_3}}$	$V_{lr_{ci_4}}$
Single	$497.91\angle$-3.44^o	-	-	-
Double	$497.91\angle$-3.44^o	$497.91\angle$-3.44^o	-	-
Triple	$746.87\angle$-3.44^o	$746.87\angle$-3.44^o	$995.82\angle$-3.44^o	-
Quadruple	$229.04\angle$-3.44^o	$229.04\angle$-3.44^o	$497.91\angle$-3.44^o	$497.91\angle$-3.44^o
	Positive sequence sending equivalents [Ω]			
Line	$z_{e1_{ci_1}}$	$z_{e1_{ci_2}}$	$z_{e1_{ci_3}}$	$z_{e1_{ci_4}}$
Single	0.77 + j7.70	-	-	-
Double	0.77 + j7.73	0.76 + j7.62	-	-
Triple	0.84 + j8.36	0.79 + j7.92	0.78 + j7.83	-
Quadruple	0.92 + j9.16	0.96 + j9.57	0.75 + j7.53	0.74 + j7.45
	Zero sequence sending equivalents [Ω]			
Line	$z_{e0_{ci_1}}$	$z_{e0_{ci_2}}$	$z_{e0_{ci_3}}$	$z_{e0_{ci_4}}$
Single	7.70 + j38.48	-	-	-
Double	7.73 + j38.67	7.62 + j38.08	-	-
Triple	8.36 + j41.78	7.92 + j39.61	7.83 + j39.16	-
Quadruple	9.16 + j45.78	9.57 + j47.85	7.53 + j37.66	7.45 + j37.25
	Positive sequence receiving equivalents [Ω]			
Line	$z_{r1_{ci_1}}$	$z1_{r1_{ci_2}}$	$z_{r_{ci_3}}$	$z_{r1_{ci_4}}$
Single	1.28 + j12.83	-	-	-
Double	1.29 + j12.89	1.27 + j12.69	-	-
Triple	1.39 + j13.93	1.32 + j13.20	1.31 + j13.05	-
Quadruple	1.53 + j15.26	1.59 + j15.95	1.26 + j12.55	1.24 + j12.42
	Zero sequence receiving equivalents [Ω]			
Line	$z_{r0_{ci_1}}$	$z_{r0_{ci_2}}$	$z_{r0_{ci_3}}$	$z_{r0_{ci_4}}$
Single	12.83 + j64.13	-	-	-
Double	12.89 + j64.46	12.69 + j63.46	-	-
Triple	13.93 + j69.64	13.20 + j66.01	13.05 + j65.27	-
Quadruple	15.26 + j76.29	15.95 + j79.74	12.55 + j62.77	12.42 + j62.08
	Phase reactors [Ω]			
Line	$x_{p_{ci_1}}$	$x_{p_{ci_2}}$	$x_{p_{ci_3}}$	$x_{p_{ci_4}}$
Single	1210.97	-	-	-
Double	1198.0	1171.95	-	-
Triple	1300.4	1230.87	1222.83	-
Quadruple	1394.55	1450.28	1154.61	1143.33
	Neutral reactors [Ω]			
Line	$x_{m_{ci_1}}$	$x_{m_{ci_2}}$	$x_{m_{ci_3}}$	$x_{m_{ci_4}}$
Single	1363.39	-	-	-
Double	494.94	354.94	-	-
Triple	505.95	368.15	462.65	-
Quadruple	361.85	149.84	232.8	375.54

Figs. 10.11 to 10.18 shows the SAC and TRV obtained for SLG faults along the line. The faults were applied in each phase. The results for the single circuit line show that the highest SAC and TRV are located at the line ends, with higher values close to the strong system. Note that the SAC and TRV is not the same in all phases. The observed unbalance is because the lines have real transposition. Finally, note that the reactor compensation effectively maintained the SAC under the limit for successful SPAR.

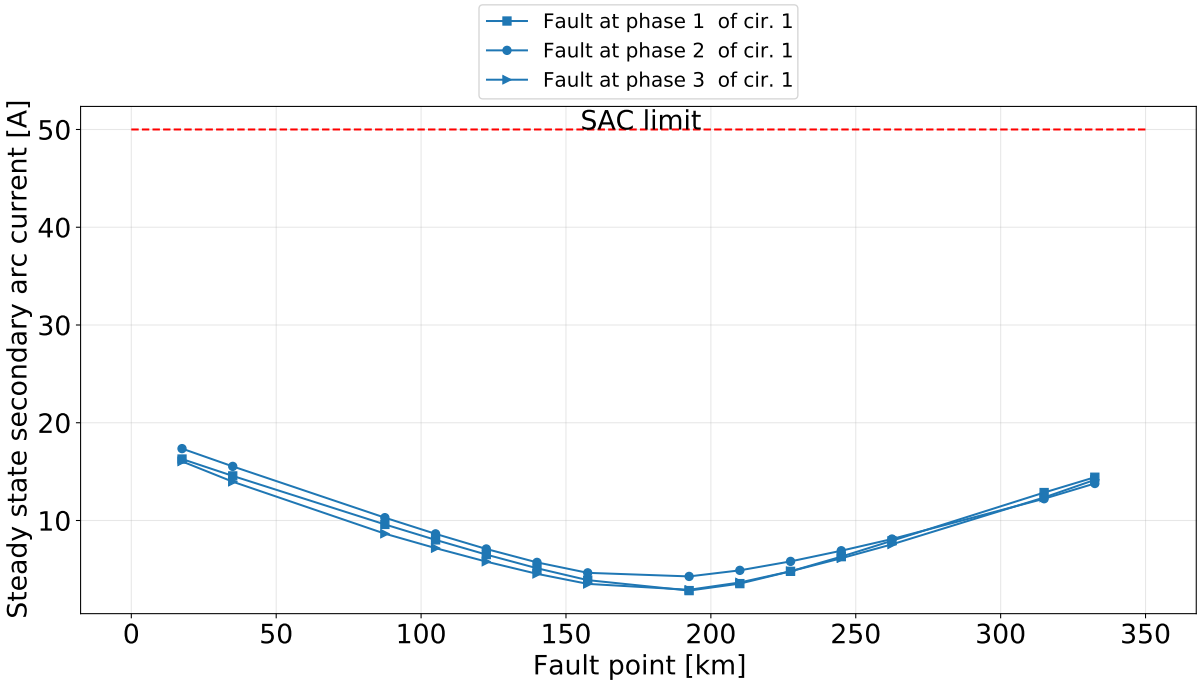

Figure 10.11 – Secondary arc current along the selected single circuit line.

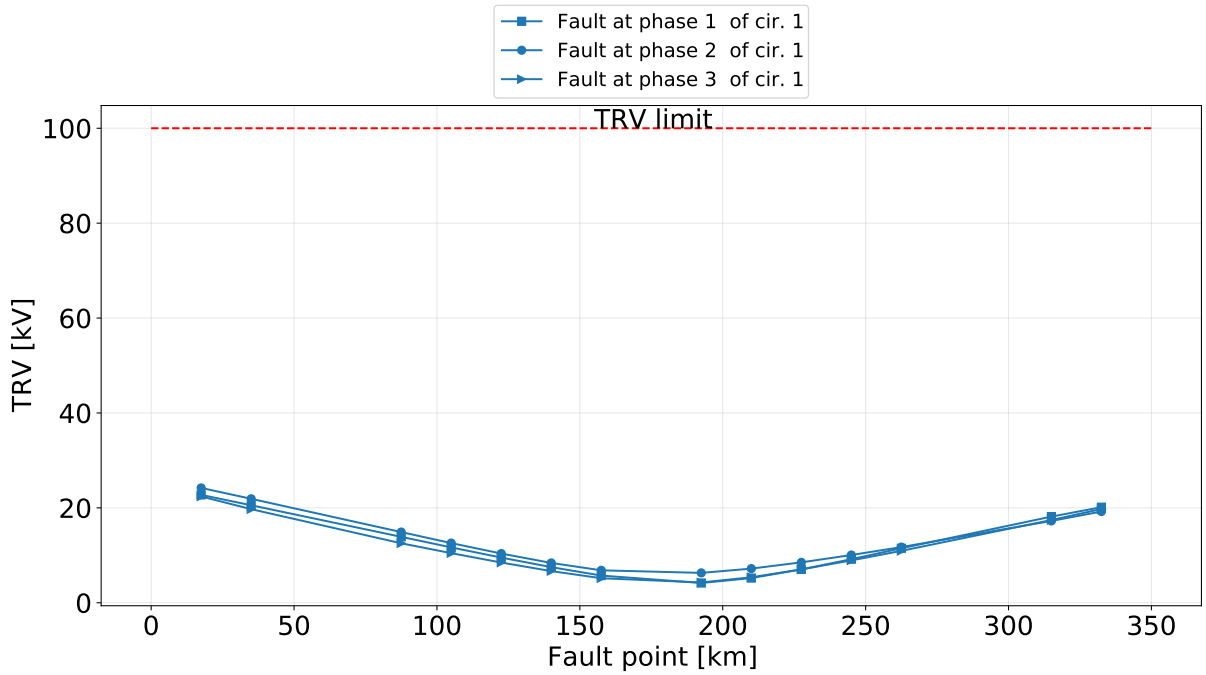

Figure 10.12 – TRV along the selected single circuit line.

The results for the double circuit line show different behavior. The effect of the mutual coupling is evident. Now, you can see that in all cases the SAC and TRV surpassed the limits. This suggest that the SPAR is not feasible in a dead time of 500 ms. Additionally, the effects of the real transposition and phase sequence yield different profiles for faults in different phases and locations. Remembering, the selected transmission line has an ABC - CBA. If the phase sequence changes, the profiles will be completely different.

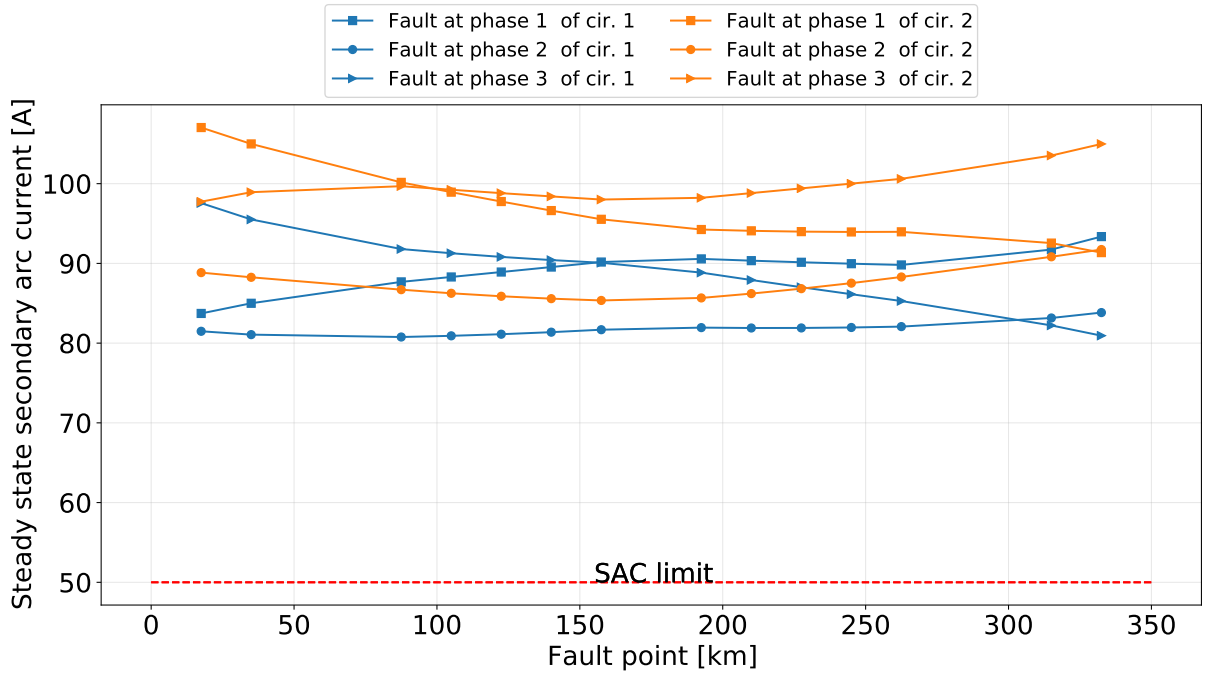

Figure 10.13 – Secondary arc current along the selected double circuit line.

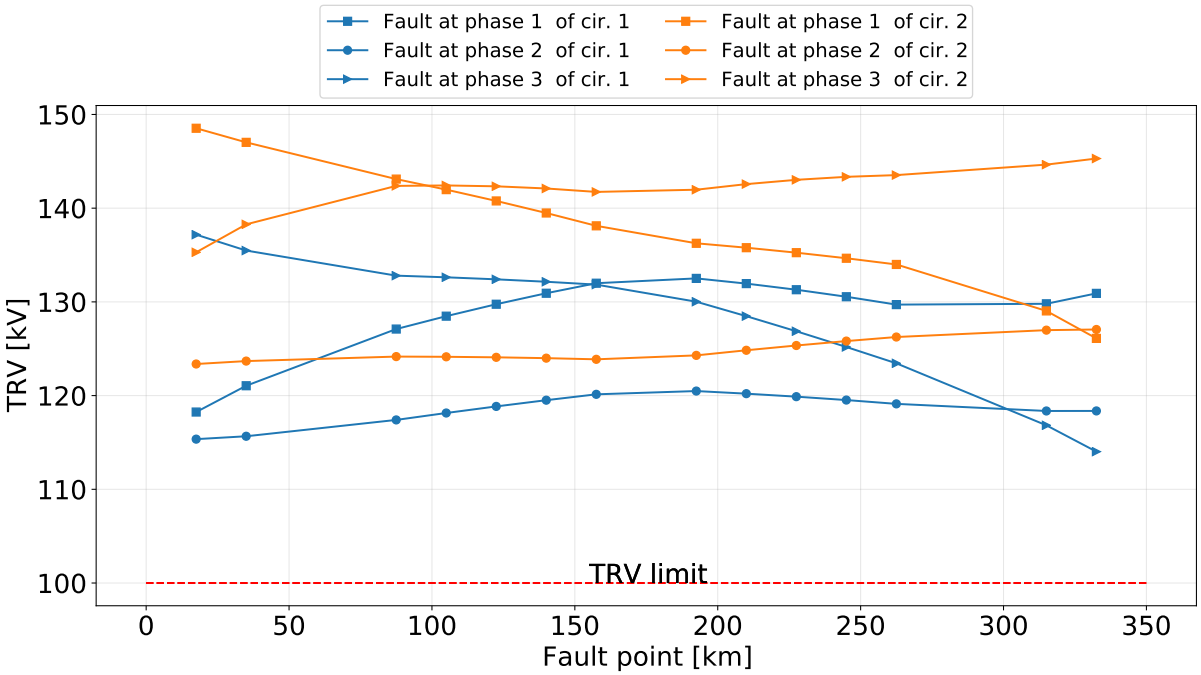

Figure 10.14 – TRV along the selected double circuit line.

The behaviour observed for the triple-circuit line is similar to the one observed in the double-circuit line. The SAC and TRV were surpassed in almost all phases and fault points. Additionally, we can see that in some cases the circuits have almost opposed SAC and TRV profiles, e.g., the first and third circuit. Also, note that the worst SAC and TRV for faults in the second phase of the second circuit is located in the middle of the line. Once more, the profile will change according to the phase sequence.

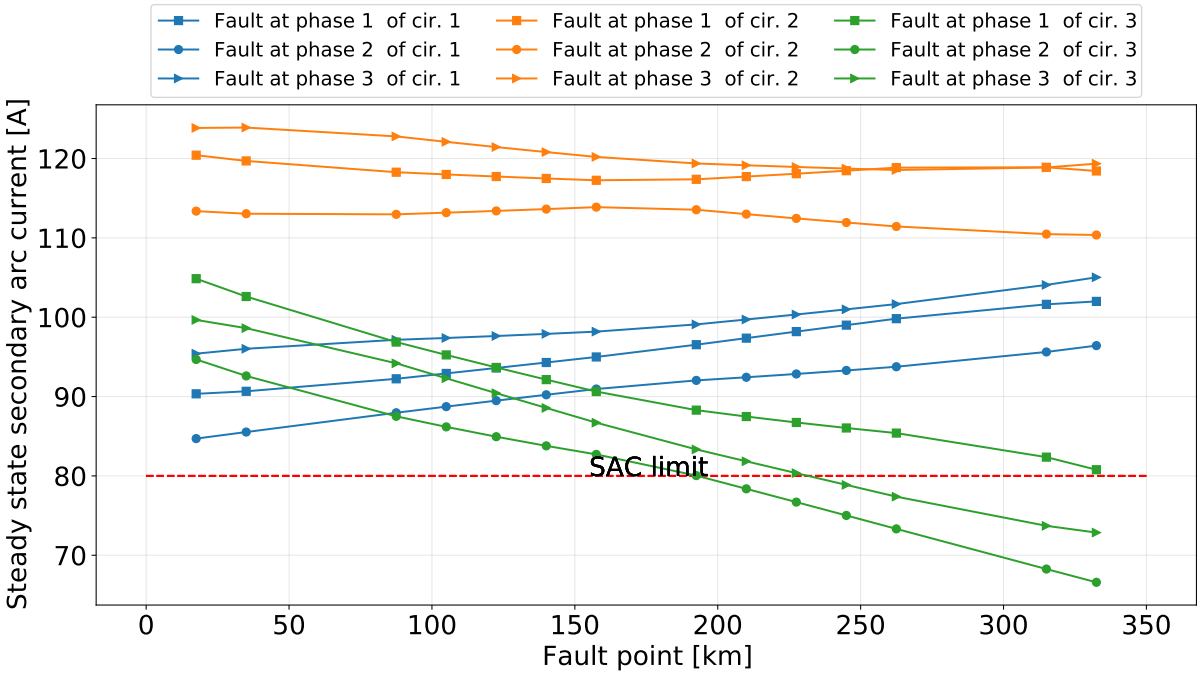

Figure 10.15 – Secondary arc current along the selected triple circuit line.

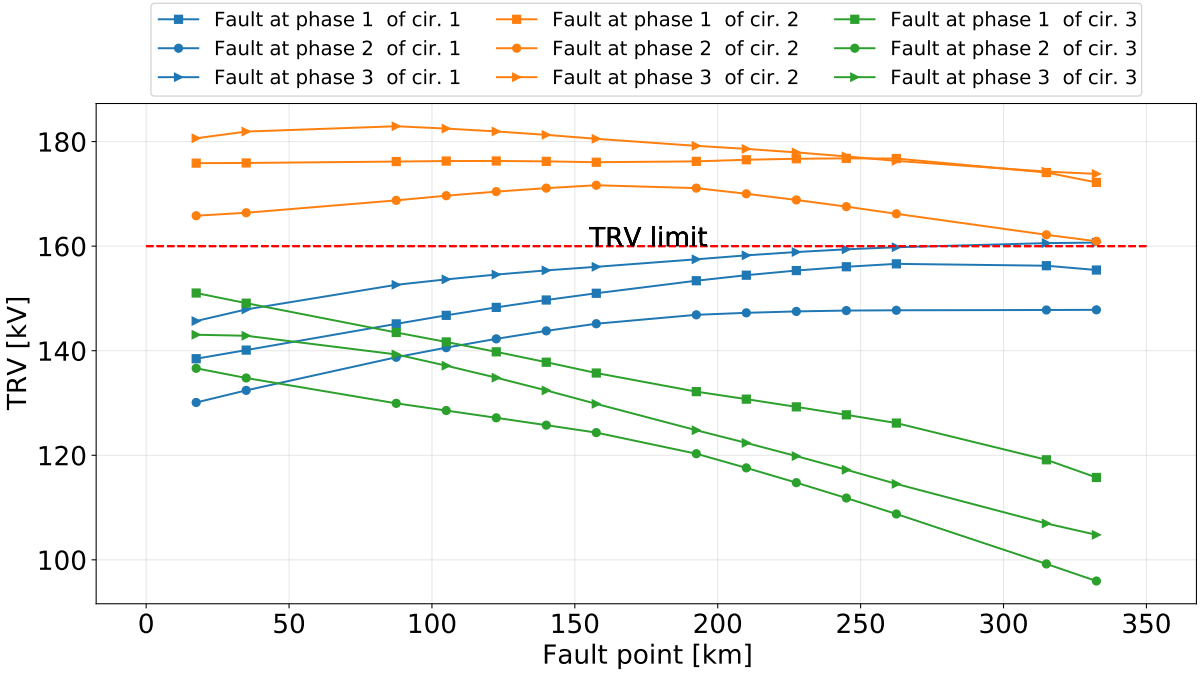

Figure 10.16 – TRV along the selected triple circuit line.

The last case, which corresponds to the quadruple-circuit line, have a similar behavior compared with the previous line. Note that two different SAC limits were marked, one for the 230 kV circuits, and another for the 500 kV circuits.

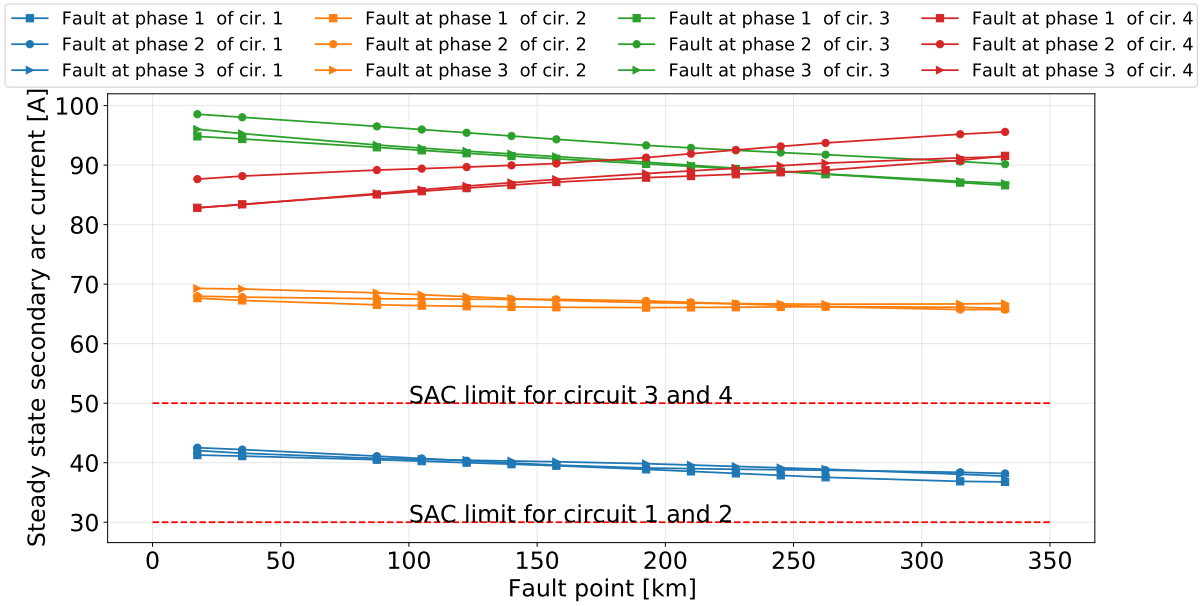

Figure 10.17 – Secondary arc current along the selected quadruple circuit line.

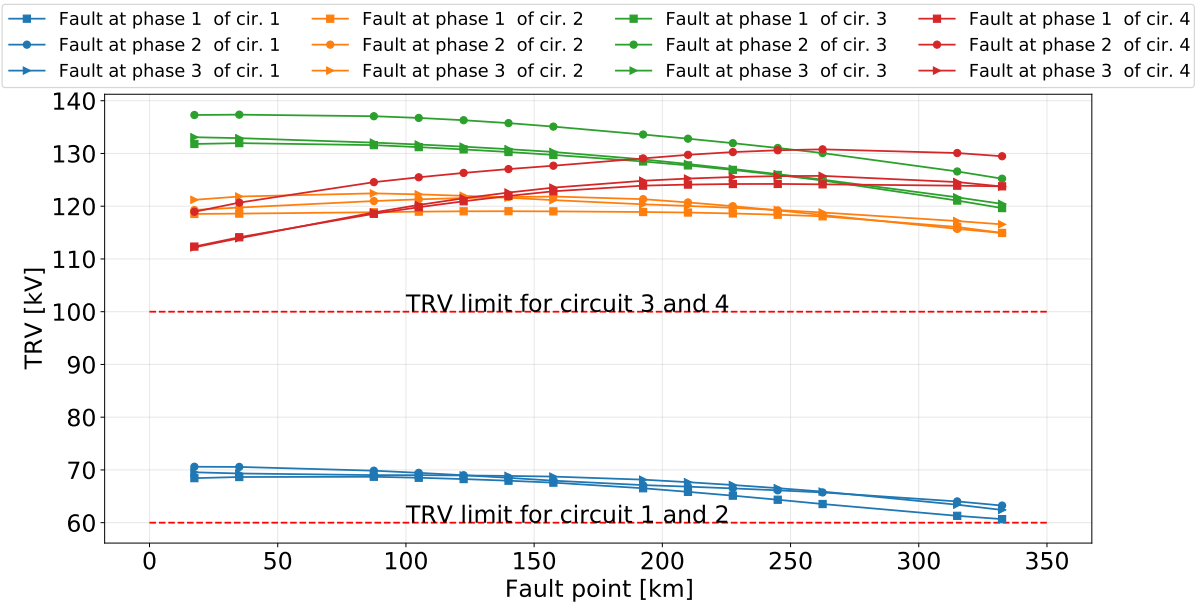

Figure 10.18 – TRV along the selected quadruple circuit line.

The behavior observed in the previous figures let us conclude the following:

1. The four-legged reactor effectively reduces the SAC and TRV in single-circuit transmission lines. However, it is not as effective in multi-circuit transmission lines due to the coupling between circuits.

2. The SAC and TRV are strongly influenced by the phase sequence and transposition.

3. The SAC and TRV are correlated, they present similar behavior in the same transmission line. Therefore, mitigating SAC will also mitigate the TRV.

4. The SAC and TRV must be observed in at least three points: both line ends and in the middle of the line.

10.2 Neutral reactor structures

As seen in the previous section, the four-legged reactor in Fig. 10.5 effectively reduces the SAC in single-circuit lines. However, the arc current values are still too high in multi-circuit transmission lines.

The problem with the formulation presented in (10.2) is that it is derived for single-circuits, so the mutual capacitance between circuits has not been taken into account. In multi-circuit transmission lines the susceptance matrix assumes the form as in (10.3), considering N circuits and an ideal transposition in each circuit. In (10.3) $b_{g_{ci}}$ is

the susceptance to ground in circuit ci, $b_{ch_{ci}}$ the mutual susceptance between the phases in the circuit, and $b_{m_{ci_1,ci_2}}$ the mutual susceptances between the circuits.

$$\begin{bmatrix} 2b_{ch_1} + b_{g_1} + 3b_{m_{12}} + \cdots + 3b_{m_{1n}} & & \\ -b_{ch_1} & \ddots & \\ \vdots & \ddots & \\ -b_{m_{n1}} & & 2b_{ch_n} + b_{g_n} + 3b_{m_{n1}} + \cdots + 3b_{m_{n,n-1}} \end{bmatrix} \tag{10.3}$$

The susceptance matrix for N circuits in sequence components is presented in (10.4). Note that in the off-diagonal there are some components related to the mutual susceptance between circuits.

$$\begin{bmatrix} b_{g_1} + 3b_{m_{12}} + \cdots + 3b_{m_{1n}} & 0 & \dots & -3b_{m_{1n}} & \dots \\ 0 & b_{g_1} + 3b_{ch_1} + 3b_{m_{12}} + \cdots + 3b_{m_{1n}} & \dots & 0 & \dots \\ \vdots & \vdots & \vdots & \vdots & \vdots \\ -3b_{m_{n1}} & 0 & \dots & b_{g_n} + 3b_{m_{n1}} + \cdots + 3b_{m_{n,n-1}} & 0 \\ 0 & 0 & \dots & 0 & b_{g_n} + 3b_{ch_n} + 3b_{m_{n1}} + \cdots + 3b_{m_{n,n-1}} \end{bmatrix} \tag{10.4}$$

To exemplify, (10.5) and (10.6) show the susceptance in a double-circuit line in phase and sequence components.

$$\begin{bmatrix} 2b_{ch_1} + 3b_{m_{12}} + b_{g_1} & -b_{ch_1} & -b_{ch_1} & -b_{m_{12}} & -b_{m_{12}} & -b_{m_{12}} \\ -b_{ch_1} & 2b_{ch_1} + 3b_{m_{12}} + b_{g_1} & -b_{ch_1} & -b_{m_{12}} & -b_{m_{12}} & -b_{m_{12}} \\ -b_{ch_1} & -b_{ch_1} & 2b_{ch_1} + 3b_{m_{12}} + b_{g_1} & -b_{m_{12}} & -b_{m_{12}} & -b_{m_{12}} \\ -b_{m_{12}} & -b_{m_{12}} & -b_{m_{12}} & 2b_{ch_2} + 3b_{m_{12}} + b_{g_2} & -b_{ch_2} & -b_{ch_2} \\ -b_{m_{12}} & -b_{m_{12}} & -b_{m_{12}} & -b_{ch_2} & 2b_{ch_2} + 3b_{m_{12}} + b_{g_2} & -b_{ch_2} \\ -b_{m_{12}} & -b_{m_{12}} & -b_{m_{12}} & -b_{ch_2} & -b_{ch_2} & 2b_{ch_2} + 3b_{m_{12}} + b_{g_2} \end{bmatrix} \tag{10.5}$$

$$\begin{bmatrix} b_{g_1} + 3b_{m_{12}} & 0 & 0 & -3b_{m_{12}} & 0 & 0 \\ 0 & b_{g_1} + 3b_{ch_1} + 3b_{m_{12}} & 0 & 0 & 0 & 0 \\ 0 & 0 & b_{g_1} + 3b_{ch_1} + 3b_{m_{12}} & 0 & 0 & 0 \\ -3b_{m_{12}} & 0 & 0 & b_{g_2} + 3b_{m_{12}} & 0 & 0 \\ 0 & 0 & 0 & 0 & b_{g_2} + 3b_{ch_2} + 3b_{m_{12}} & 0 \\ 0 & 0 & 0 & 0 & 0 & b_{g_2} + 3b_{ch_2} + 3b_{m_{12}} \end{bmatrix} \tag{10.6}$$

As you may guess, obtaining the compensation values analytically is not straightforward and the mathematical development is not the main focus of this research. Instead, some neutral reactor structures are considered and their values are obtained through optimization process.

10.2.1 Neutral reactor structures for double-circuit lines

To reduce the mutual coupling in double-circuit lines different compensation schemes could be used. In this research two different options, presented in Figs 10.19 and

10.20, are considered. Option 1 corresponds to conventional four-legged reactors connected to each circuit. Option 2 is a fully connected neutral reactor which aims to mitigate the mutual coupling between circuits through x_{n_1}.

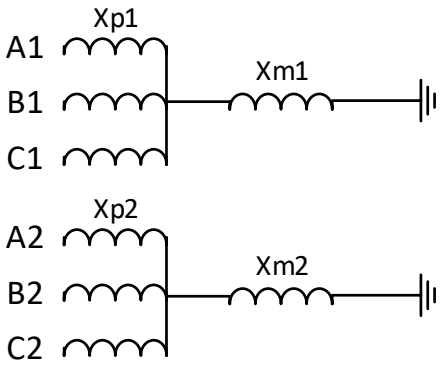

Figure 10.19 – Option 1 of compensation scheme for double-circuit lines.

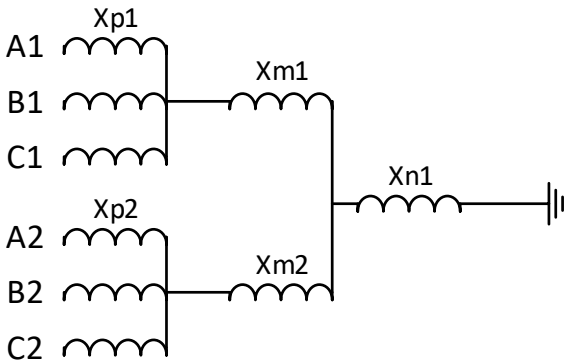

Figure 10.20 – Option 2 of compensation scheme for double-circuit lines.

The reactors in Option 1 are easily calculated with the formulation in (KIMBARK, 1964). However, obtaining the reactors for option 2 is difficult. They will be obtained later through an optimization procedure.

10.2.2 Neutral reactor structures for triple-circuit lines

To reduce the mutual coupling in triple-circuit lines, three different compensation schemes, presented in Figs 10.21, 10.22 and 10.23, are considered. Option 1 is the conventional four-legged reactor connected in each circuit. Option 2 and 3 are reactor schemes proposed in this research. The reactor in option 2 aims to mitigate the coupling between circuit 1 and circuit 2, while allows some coupling with circuit 3. Circuit 3 was not connected to circuit 1 and 2 through the neutral reactor because circuit 3 is operating in a different voltage level.

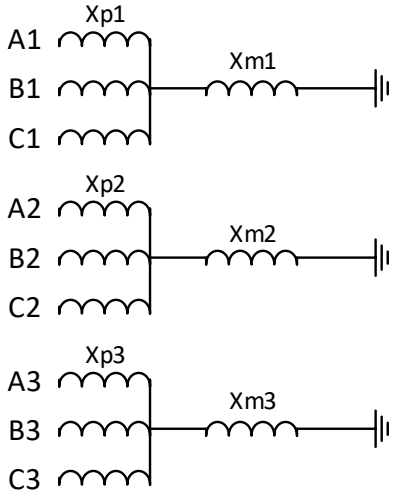

Figure 10.21 – Option 1 of compensation scheme for triple-circuit lines.

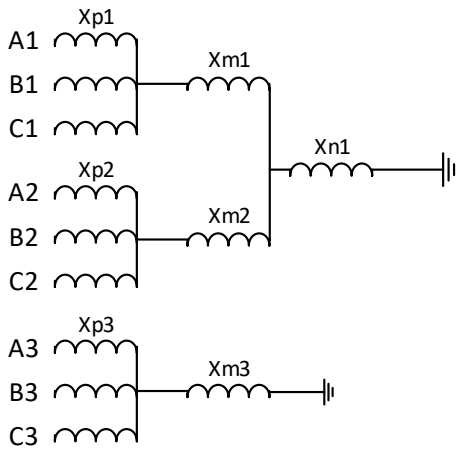

Figure 10.22 – Option 2 of compensation scheme for triple-circuit lines.

The final option presents a fully connected neutral reactor scheme. In this case, the aim is to reduce the coupling between all the circuits. As in the previous case, because of the voltage level difference between circuit 3 and the others, x_{m_3} was not connected in the same way as x_{m_1} and x_{m_2}. The problem with this kind of configuration is that under fault conditions overvoltages will be induced in the connection points of the other reactors. Therefore, the voltage at neutral points will be no longer nil. However, the advantage is that the required basic insulation level of each reactor will be lower.

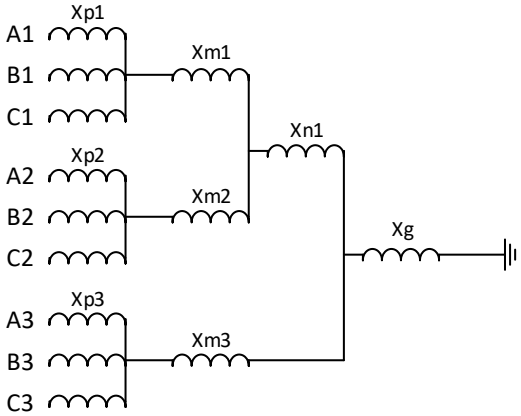

Figure 10.23 – Option 3 of compensation scheme for triple-circuit lines.

10.2.3 Neutral reactor structures for quadruple-circuit lines

Four reactor schemes to reduce the SAC in quadruple circuit transmission lines are considered in this research. They are presented in Figs. 10.24 to 10.27. Once again, the first option corresponds to the conventional four-legged reactor.

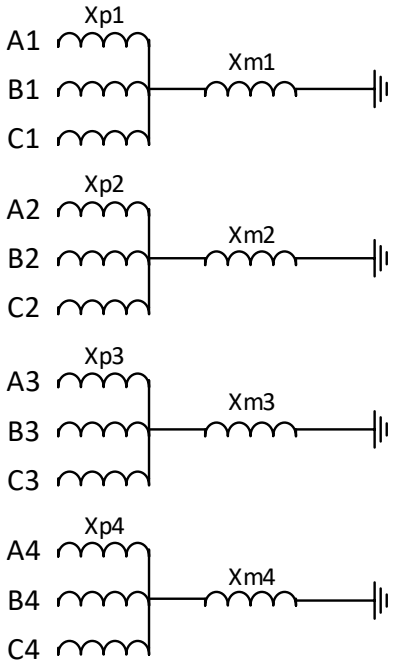

Figure 10.24 – Option 1 of compensation scheme for quadruple-circuit lines.

The remaining options follow the logic of the previous sections. In option 2, since circuit 1 and circuit 2 have the same voltage level, only the reactor of those circuits are interconnected. In option 3, the circuits 3 and 4 which have the same voltage level, are also interconnected. The final option, is a fully connected neutral reactor scheme.

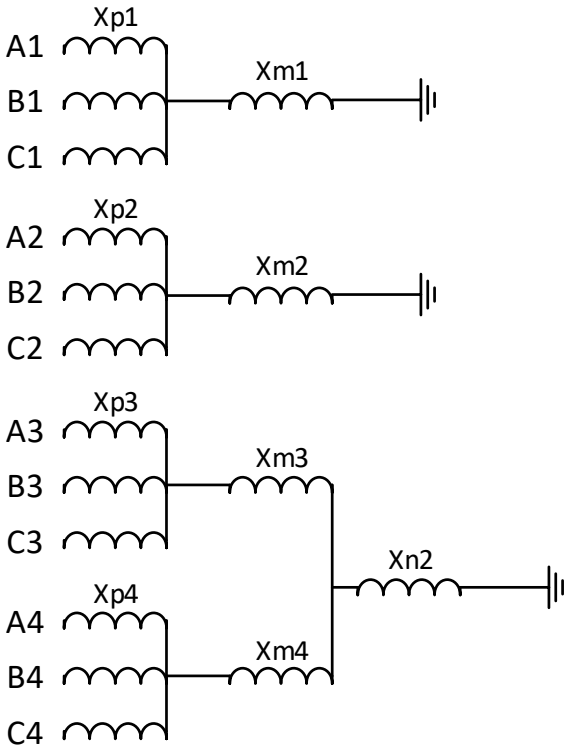

Figure 10.25 – Option 2 of compensation scheme for quadruple-circuit lines.

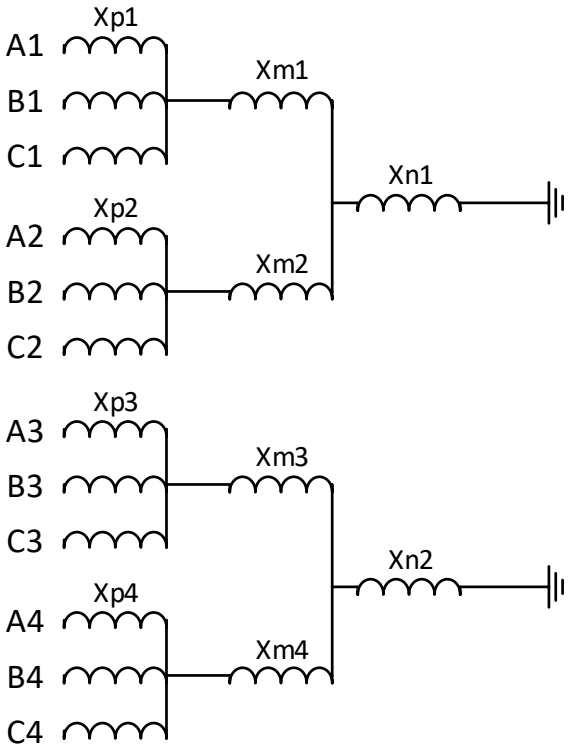

Figure 10.26 – Option 3 of compensation scheme for quadruple-circuit lines.

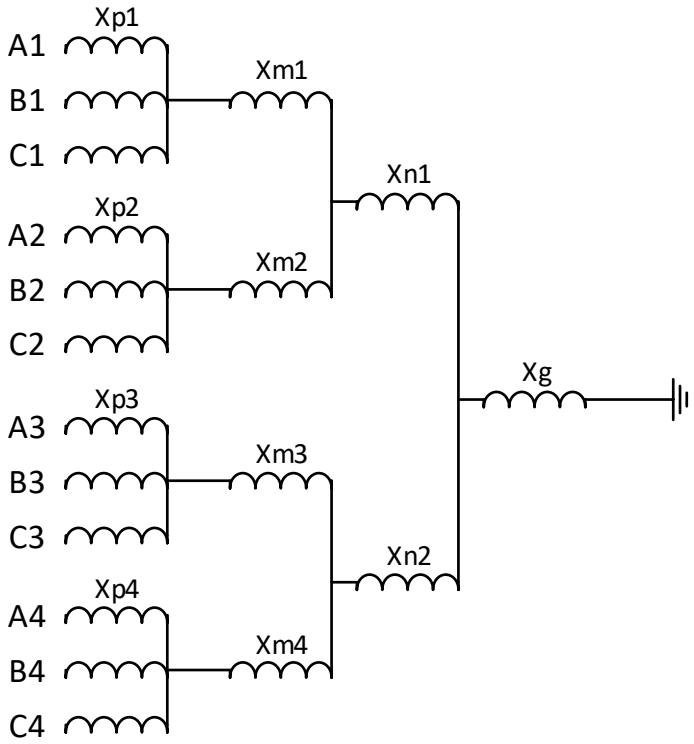

Figure 10.27 – Option 4 of compensation scheme for quadruple-circuit lines.

Now that the different neutral reactor alternatives were presented, the following section will show the procedure for obtaining their parameters.

10.3 Optimal neutral reactor parameters

The optimal neutral reactor parameters of the schemes presented in the previous section were obtained by solving the generalized multi-objective problem in (10.7). The problem was stated as multi-objective because the mutual coupling makes that reducing the SAC in one circuit may increase the SAC in another circuit. However, in single-circuit lines the problem is reduced to a mono-objective problem.

$$\begin{gathered}\text{argmin}_{\chi}\ f(\chi) = (SAC_{ci_1}, SAC_{ci_2}, SAC_{ci_3}, SAC_{ci_4}) \\ \chi = \{x_{m_1}, x_{m_2}, x_{m_3}, x_{m_4}, x_{n_1}, x_{n_2}, x_g\}\end{gathered} \tag{10.7}$$

Subjected to:

$$3000 \geq x_{m1}, x_{m2}, x_{m3}, x_{m4}, x_{n1}, x_{n2}, x_g \geq 0 \tag{10.8}$$

The limit of reactors of 3000 Ω was imposed to force the solution not to be very far from conventional reactor values. In Brazil, 500 kV transmission lines have a typical reactor value of 800 Ω.

To have an accurate answer, the SAC in each circuit was obtained through PSCAD simulations. Single-line to ground faults were applied in each phase at 5, 50, and 95% of the line length. The set of simulations were automated with the PSCAD Python automation library, and the optimization procedure was implemented in Python. Same as in the optimization of the multi-circuit multi-voltage transmission lines, the NSGA-II was selected as optimization algorithm.

Since using NSGA-II with PSCAD is very time consuming, parallel simulations in PSCAD were executed. PSCAD has two main possibilities to perform parallel simulations. The first one relies on the delay of the waveform caused by transmission lines, allowing to split the system into different subsystems separated by transmission lines. This approach is very useful when dealing with large systems with many transmission lines, however that is not the case of this research. The second approach, called volley simulation, perfectly suits the objectives of this research, because it consists of parallel simulations of the same system, but with different parameters. When dealing with volley simulations there are two options. The approach suggested in the PSCAD manual, using *master* and *slave* files, and the approach implemented in this research, that only uses one file. Both approaches are described in A.1 and A.2, respectively.

Similar to the MCMVTL optimization some steps are performed. Fist, N random solutions are created in Python and sent to PSCAD. PSCAD runs in parallel as many simulations as the number of cores (n_{cores}) in the machine. When the simulations in PSCAD finish, n_{cores} files are created. These files are processed in Python and the objective function values of each solution are extracted. After getting the objective function values, the Pareto frontiers are obtained, and the selection based on Crowding distance is performed. With the selected population new solutions are created through Crossover and Mutation operators. Then, the new solutions are sent again to PSCAD, repeating the whole process until reaching a stop criteria.

The neutral reactor schemes presented in the previous section were optimized with NSGA-II as described before. The simulations were performed using parallel computing in a workstation at the University of Manitoba, Winnipeg, Canada at the professor's Aniruddha Gole laboratory. The workstation has 64 Gb of ram and 4 AMD Opteron processors operating at 2.1 GHz. Each processor has 4 cores and each core 4 threads, counting a total of 32 cores and 64 logical processors. As a reminder, the simulations were performed in a systems like the one in Fig. 10.28 using the values in Table 10.2.

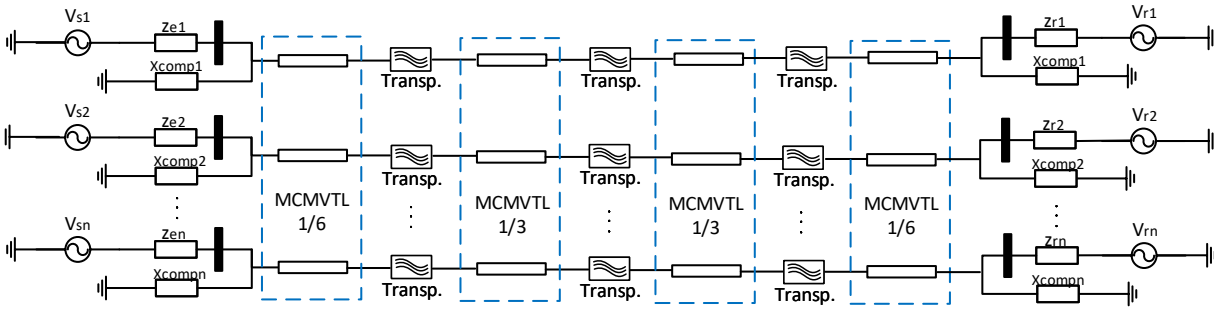

Figure 10.28 – Scheme of the test systems.

Parallel computing significantly speeds up the simulation time. Table 10.3 compares the simulation time required to optimize a neutral reactor in the single and quadruple-circuit line, using a population of 60 individuals evolving during 20 generations. The advantages of using parallel computing to solve EMT optimization problems are clearly evidenced. The simulation time was reduced from around 6 days 23 h and 27 min to almost 10 h and 42 min when 64 cores were used to simulate the system with the quadruple transmission line. Meanwhile, the simulation time was reduced from 8 h 12 min to 1 h 31 min when optimized the single-circuit line. Therefore, it is clear that the more complex systems will get more benefits from parallel computing.

Table 10.3 – Neutral reactor optimization time using different quantities of cores, with 60 solutions evolving during 20 generations.

Cores	1 circuit Line		4 circuit Line	
	Time [HH:MM:SS]	Speed-up [factor]	Time [HH:MM:SS]	Speed-up [factor]
1	08:12:09	-	6 days 23:26:51	-
4	02:15:27	3.63	1 day 21:00:18	3.72
8	01:44:06	4.73	1 day 02:05:42	6.42
16	01:27:36	5.62	17:25:21	9.61
32	01:24:54	5.80	14:27:45	11.58
64	01:31:03	5.41	10:41:51	15.62

Fig. 10.29 shows a log-log plot of the speedup factor as a function of the number of cores. The speedup is linear up to about 8 cores, but there is a diminishing increase for a larger number of cores. From Fig. 10.29 it is clear that the more complex the system, the more significant is the speedup. However, the cost of mapping the task on the processors and threads make the speedup saturate after a certain number of cores are harnessed. The additional pipeline observed during the simulations is that every time that a new set of simulations is given to PSCAD, the systems are compiled again. This situation is maintained even when no changes in breakers, faults or transmission lines are performed. The compilation process takes a considerable amount of time during the simulation.

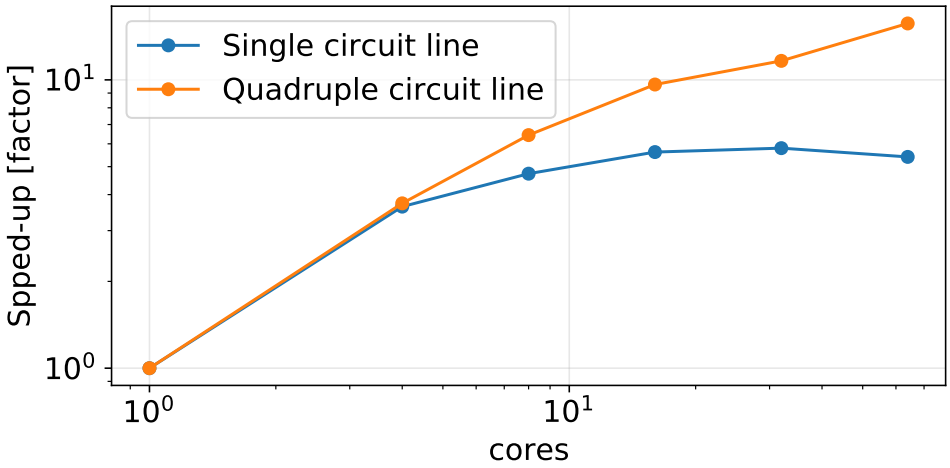

Figure 10.29 – Log–log plot of the speed-up for the single and quadruple transmission line SAC optimization according to the number of cores.

The following results of neutral reactor parameters were obtained with parallel computing using the numbers of cores until speedup saturation.

Since NSGA-II produces Pareto optimal solutions, it is convenient to show the results with Pareto curves or parallel coordinated plots, except for the single-circuit line case that only has one objective.

10.3.1 Single-circuit reactors

The optimization of neutral reactors in single-circuit lines is very simple to achieve. Since there is only one objective, and there is no influence of other circuits, the optimization can be performed in less than 10 generations. Fig. 10.30 shows the behavior of the SAC as function of the neutral reactor x_{m_1}. As you can see, the optimal point ($x_{m_1} = 1587.1$) uses a neutral reactor slightly higher than the calculated using the formulation in (KIMBARK, 1964) ($x_{m_1} = 1363.38j$). The small difference is because in the optimization process the full EMTP simulation is performed, so the influences of all elements and transpositions are considered. Nevertheless, the reactor calculated with (KIMBARK, 1964) has a very good response. Therefore, in the single-circuit line case, no optimization will be required.

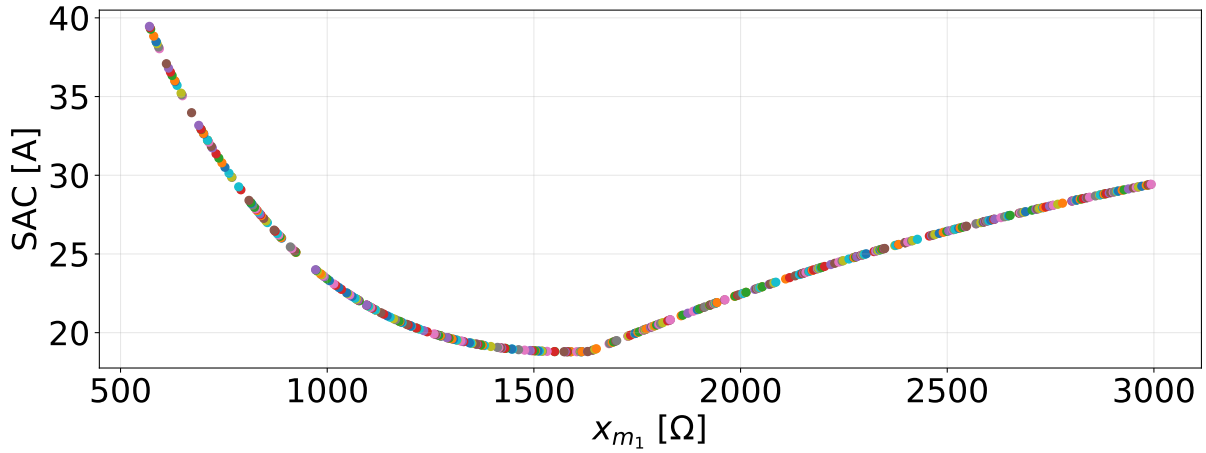

Figure 10.30 – SAC in a single-circuit line as function of the neutral reactor value.

Fig. 10.31 and 10.32 presents the SAC and TRV for the optimal reactor as a function of the fault point. You can see that the response is very similar to the one observed with the reactor calculated with (10.2). The SAC and TRV are in adequate levels for a successful SPAR.

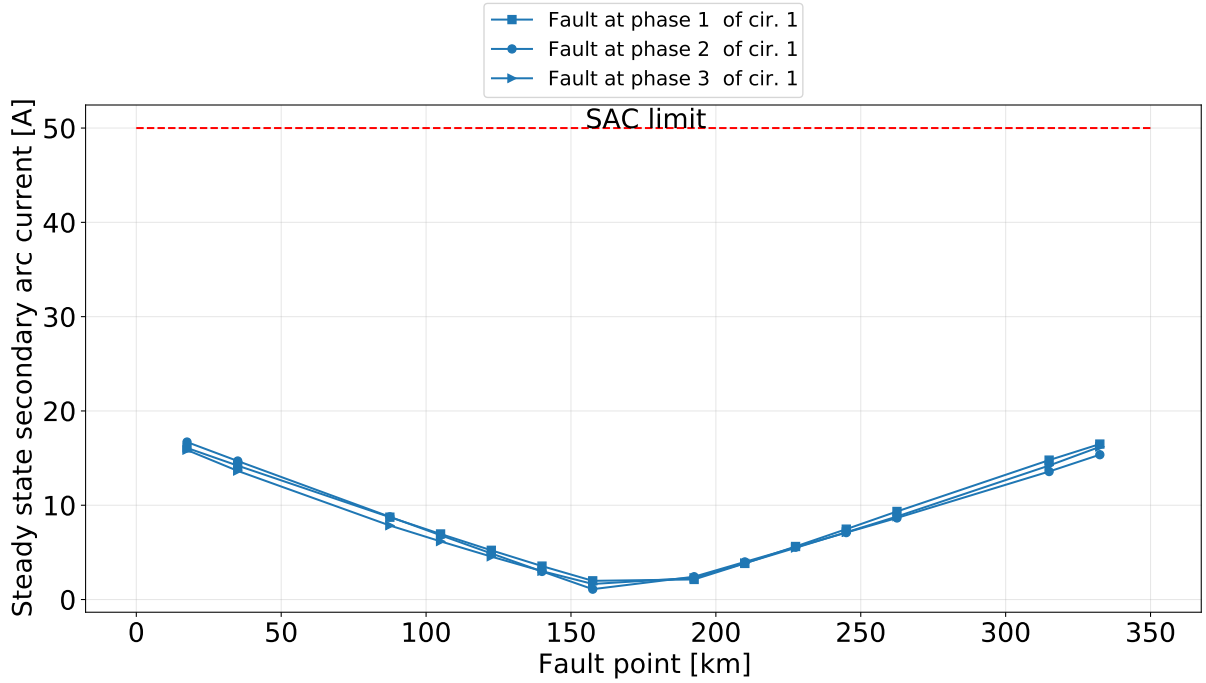

Figure 10.31 – SAC in a single-circuit line as function of the fault point, using a four-legged reactor with optimized parameters.

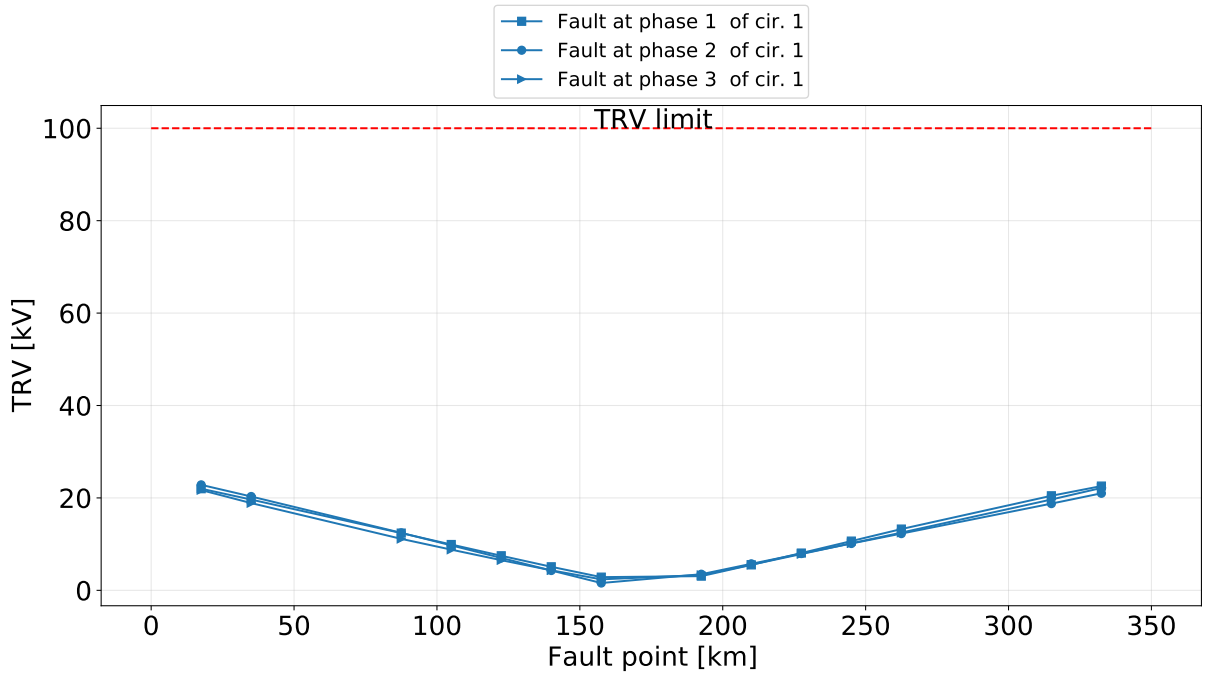

Figure 10.32 – TRV in a single-circuit line as function of the fault point, using a four-legged reactor with optimized parameters.

10.3.2 Double-circuit reactors

Fig. 10.33 presents the Pareto front obtained with the neutral reactor scheme option 1 for double-circuit transmission lines. It corresponds to conventional four-legged reactors schemes connected to each circuit. Note in Fig. 10.33 that there is almost no change in the secondary arc current at circuit 1 regarding to the secondary arc current in circuit 2. This behavior is because the neutral reactors in option 1 are not directly connected to each other, so a mono-objective optimization could be performed.

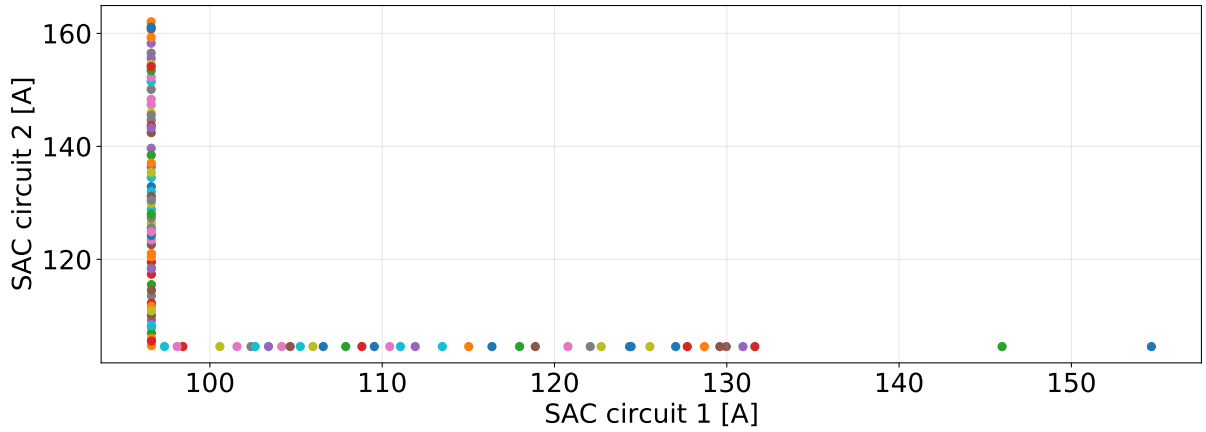

Figure 10.33 – Parallel coordinated plot of the neutral reactor scheme Option 1 for the double-circuit line.

Since no trade-off is observed for this option, it is possible to generate curves

of the SACs as function of the neutral reactor values. Figs. 10.34 shows the influences of the neutral reactors in their own circuits. The optimized neutral reactor parameters values are different from those calculated analytically. However, the SAC and TRV are similar. A conclusion and a summary of the results are presented after the results of the optimization with the reactor alternative option 2.

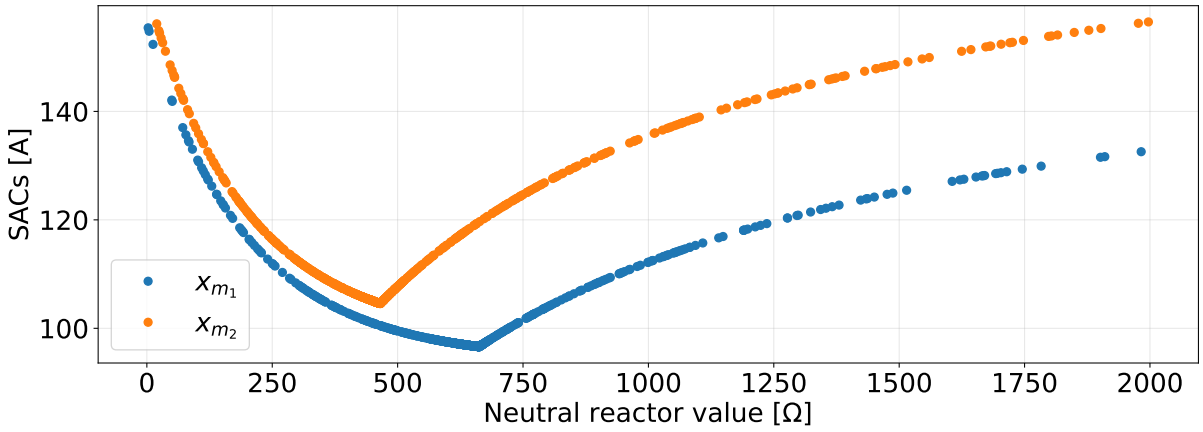

Figure 10.34 – Variation of the SAC in a double-circuit line as function of the neutral reactor value.

Figs.10.35 and 10.36 show SAC and TRV response for faults along the line using the optimized neutral reactor parameters. Note that in spite of the optimization it was not possible to reduce the SAC and TRV to adequate levels.

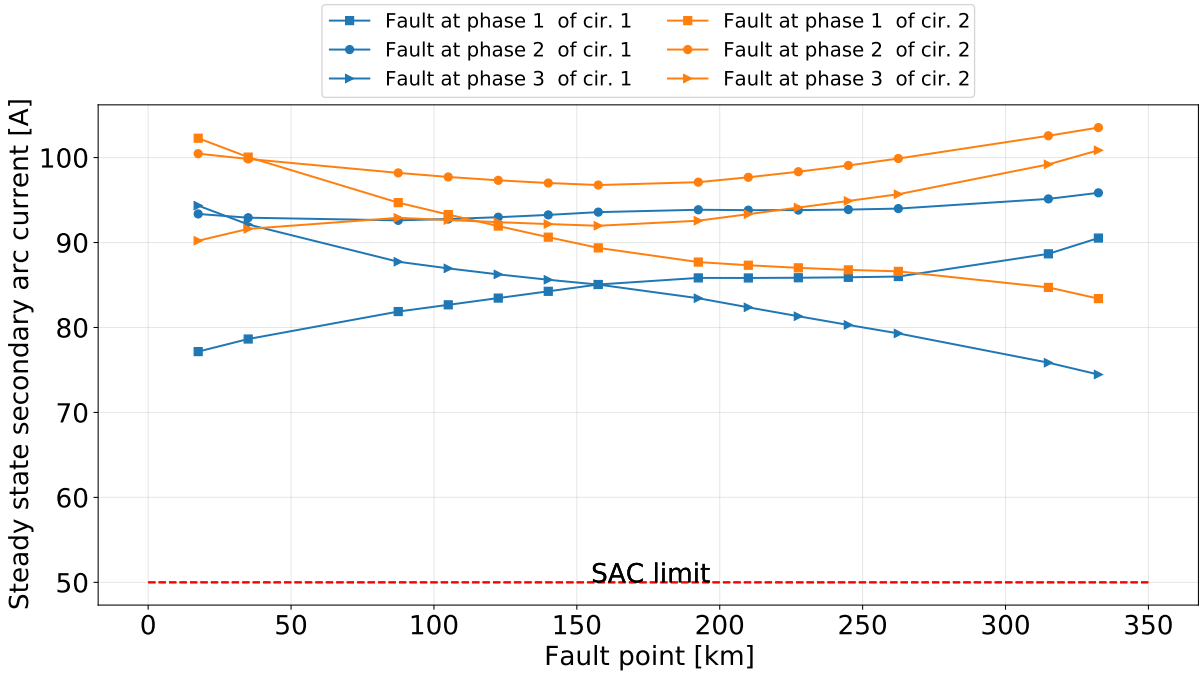

Figure 10.35 – SAC in a double-circuit line as function of the of the fault point, using optimized reactors for the scheme option 1.

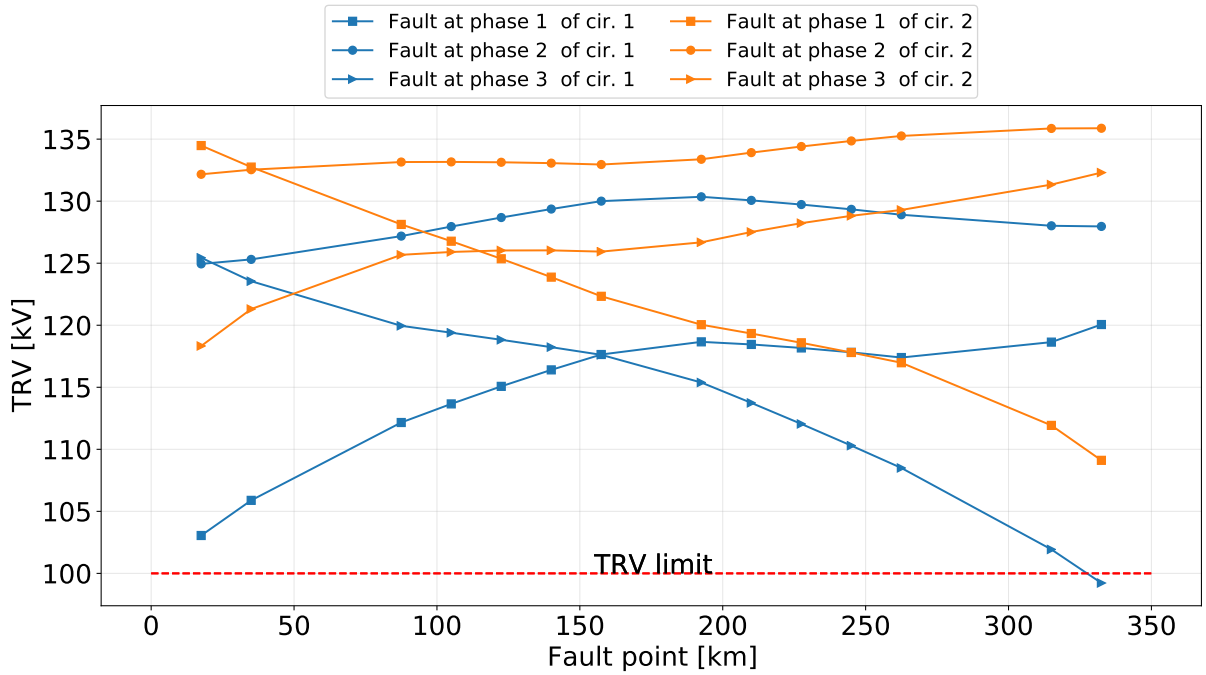

Figure 10.36 – TRV in a double-circuit line as function of the fault point, using optimized reactors for the scheme option 1.

Contrary to the case of conventional four-legged reactors, the neutral reactors in the Option 2 are linked, so the real Pareto front in Fig. 10.37 is obtained. One can clearly see that there is a trade-off between the SAC at circuit 1 and circuit 2. In this case, small variations on the SAC of circuit 1 produced important variations on the SAC of circuit 2.

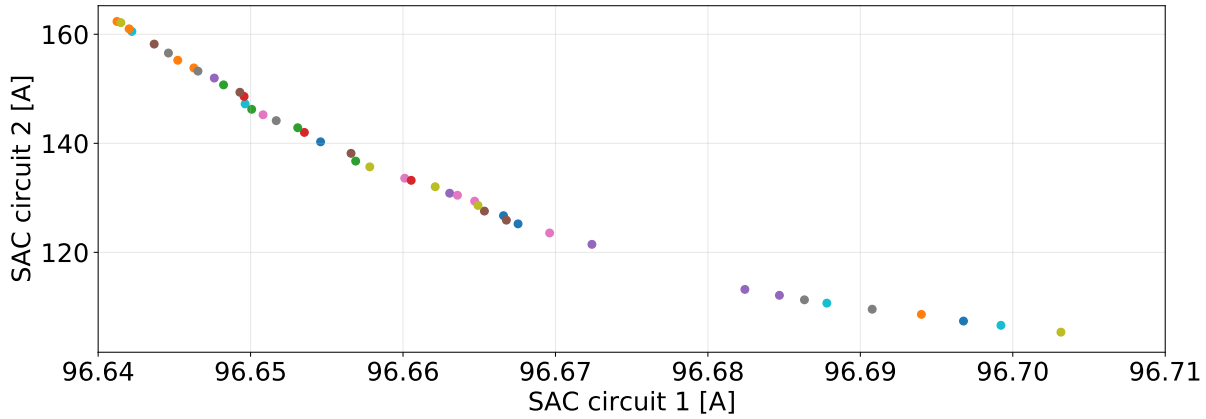

Figure 10.37 – Pareto front for the neutral reactor scheme Option 2 for the double-circuit line.

Figs. 10.38 and 10.39 show SAC and TRV response for faults along the line using the optimized neutral reactor parameters of option 2. Note that the resulting behavior is almost identical to the previous ones. This means that if the parameters of the reactors are well adjusted, the scheme 1 and 2 are equivalent.

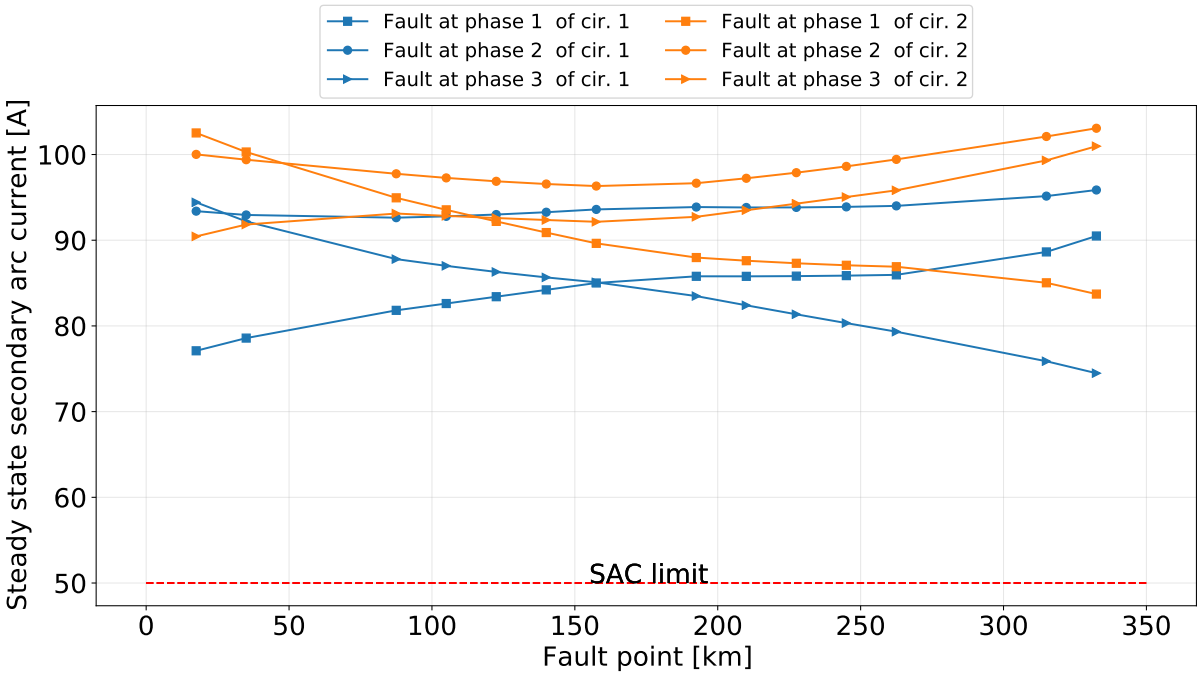

Figure 10.38 – SAC in a double-circuit line as function of the fault point, using optimized reactors for the scheme option 2.

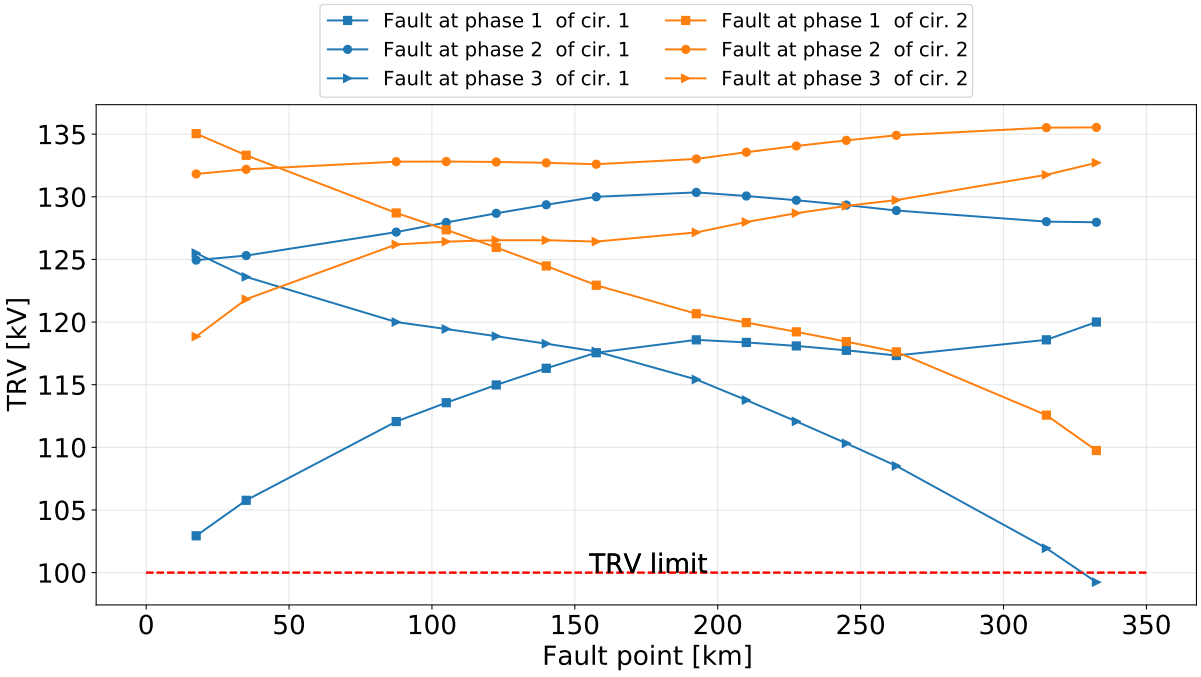

Figure 10.39 – TRV in a double-circuit line as function of the fault point, using optimized reactors for the scheme option 2.

Table 10.4 shows the reactor parameters obtained for the different neutral reactor schemes. The parameters for the reactor scheme option 2 are obtained only with optimization. Whereas, the reactor parameters for conventional four-legged reactors are calculated with both methods. Note that smaller values are obtained with the fully

connected neutral reactor. It is called option 2, or alternative 1, to establish a difference between conventional four legged reactors. The fully connected neutral reactors will require lower basic insulation levels. However, under fault conditions, overvoltages will appear in the common points with other circuits.

Table 10.4 – Obtained neutral reactor parameters in the double-circuit line in [Ω]

Reactor scheme	Method	x_{m_1}	x_{m_2}	x_{n_1}
2 circ. Option 1	Analytical	494.94	354.94	-
2 circ. Option 1	Optimization	662.81	465.46	-
2 circ. Option 2	Optimization	595.55	390.27	78.53

Table 10.5 and 10.6 show the maximum SAC and TRV for the different options.

Table 10.5 – SAC in $[A]$ obtained with the neutral reactors in the double-circuit line.

Reactor scheme	Method	$SACci_1$	$SACci_2$
2 circ. Option 1	Analytical	97.56	107.04
2 circ. Option 1	Optimization	95.85	103.53
2 circ. Option 2	Optimization	95.86	103.06

Table 10.6 – TRV in $[kV]$ obtained with the neutral reactors in the double-circuit line.

Reactor scheme	Method	$TRVci_1$	$TRVci_2$
2 circ. Option 1	Analytical	137.17	148.53
2 circ. Option 1	Optimization	130.35	135.88
2 circ. Option 2	Optimization	137.17	148.53

From the results presented in the previous figures and tables it is possible to note that even with the optimization procedure the SACs were not reduced to adequate values. Therefore, additional mitigation options should be evaluated or the transmission lines should be redesigned considering the SAC.

Since no important SAC differences were observed when using the optimized neutral reactors' parameters or the analytical parameters, it can be concluded that coupling between phases is more relevant than the coupling between circuits.

10.3.3 Triple-circuit reactors

Until this point it has been proved that conventional four-legged reactors can be optimized by solving a mono-objective problem. Therefore, instead of presenting the solutions with Pareto plots, the SAC values as function of the reactor value are shown in Fig. 10.40. One can see that the optimal points are not clearly identified. Moreover, the SAC decrease in the second circuit is almost null after 2500 Ω. Any reactor larger than

that value could be selected without impacting SAC. Further comparisons will show that in this case the coupling between circuits is very important.

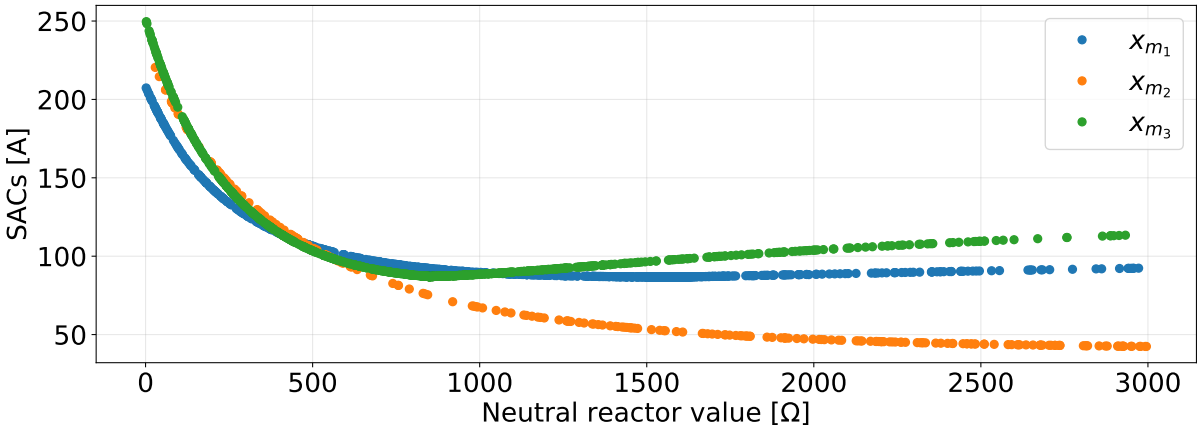

Figure 10.40 – Variation of the SAC in a triple-circuit line as function of the neutral reactor value.

Figs. 10.41 and 10.42 show the SAC and TRV profiles obtained when using four-legged neutral reactors with optimized parameters. As you can see the profiles are very different from the ones observed with parameters calculated using (10.2). The optimized values yield SAC and TRV that are below the limits in almost all cases, which is a huge improvement.

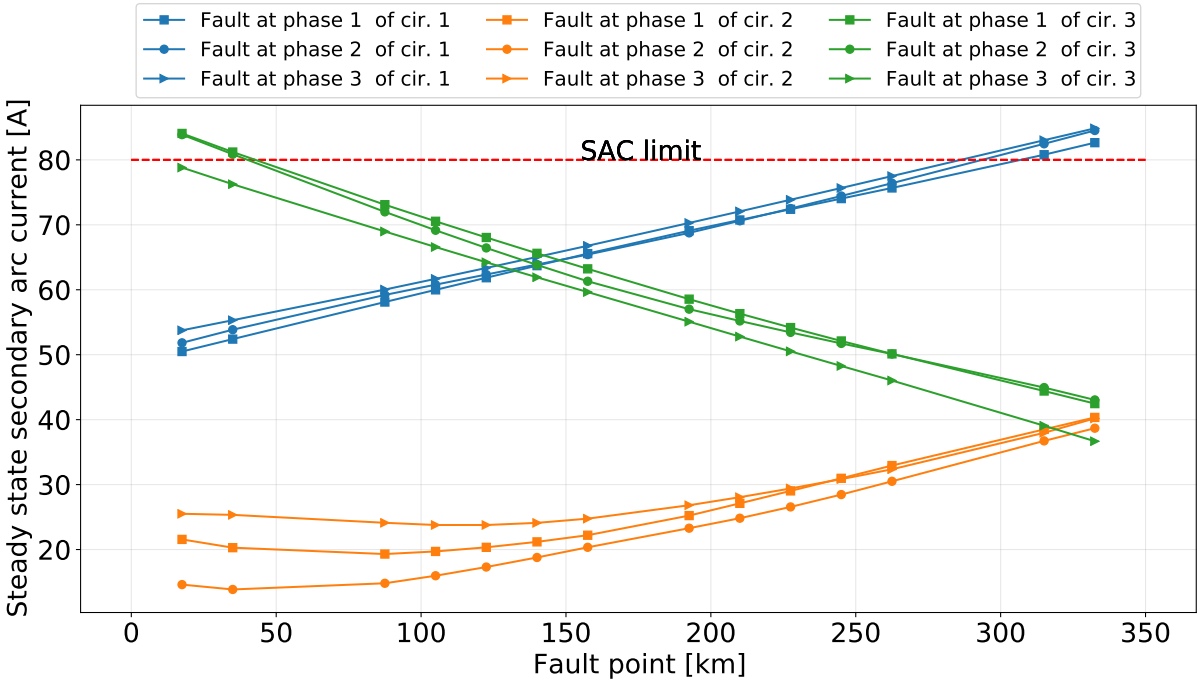

Figure 10.41 – Variation of the SAC in a triple-circuit line as function of the fault point, using optimized reactors for the scheme option 1.

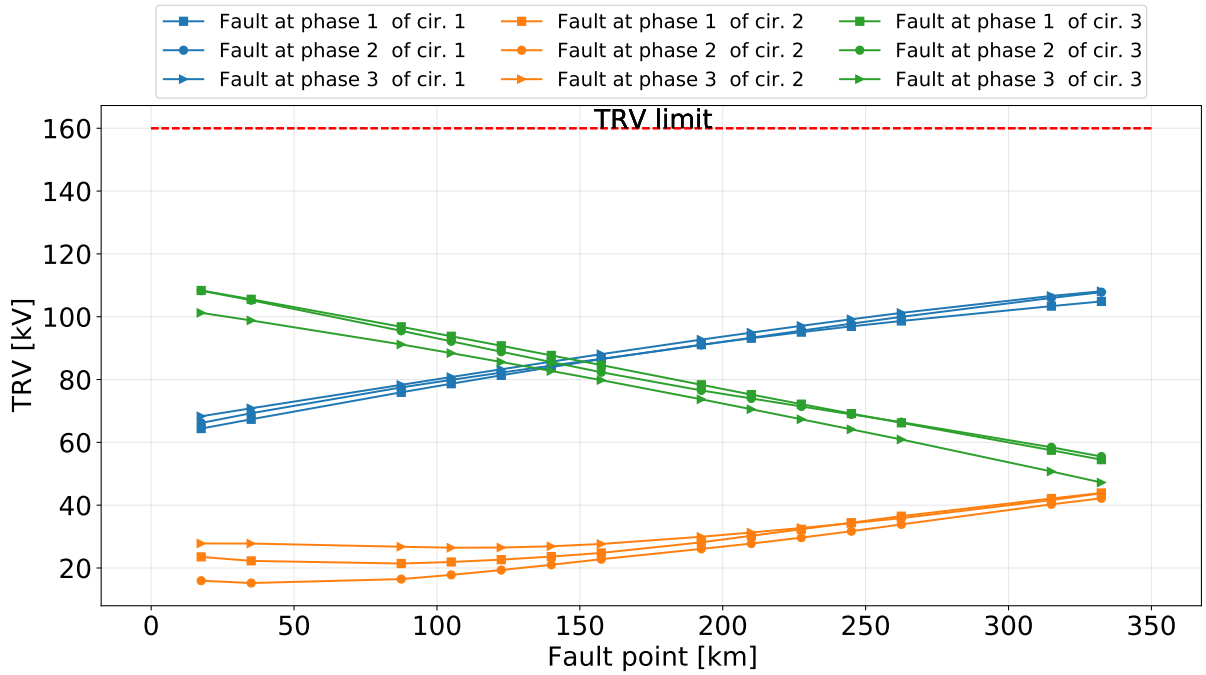

Figure 10.42 – Variation of the TRV in a triple-circuit line as function of the fault point, using optimized reactors for the scheme option 1.

As demonstrated in the previous subsection, if the neutral reactors are well designed, the SAC and TRV for all considered schemes will have similar profiles as in Figs. 10.41 and 10.42. Therefore, these figures will not be plotted again for the next reactor schemes.

The solution of the reactor scheme option 2 in the triple-circuit line connects only the first and second circuit. Therefore, a Pareto front between the SACs of circuit 1 and 2 can be obtained. The corresponding Pareto front is shown in Fig. 10.43. It shows that small changes in the optimization of the SAC in circuit 1 could yield important changes on the SAC of circuit 2. Since in this option circuit 3 is not physically connected, the optimal reactor value for that circuit can be taken from Fig. 10.40.

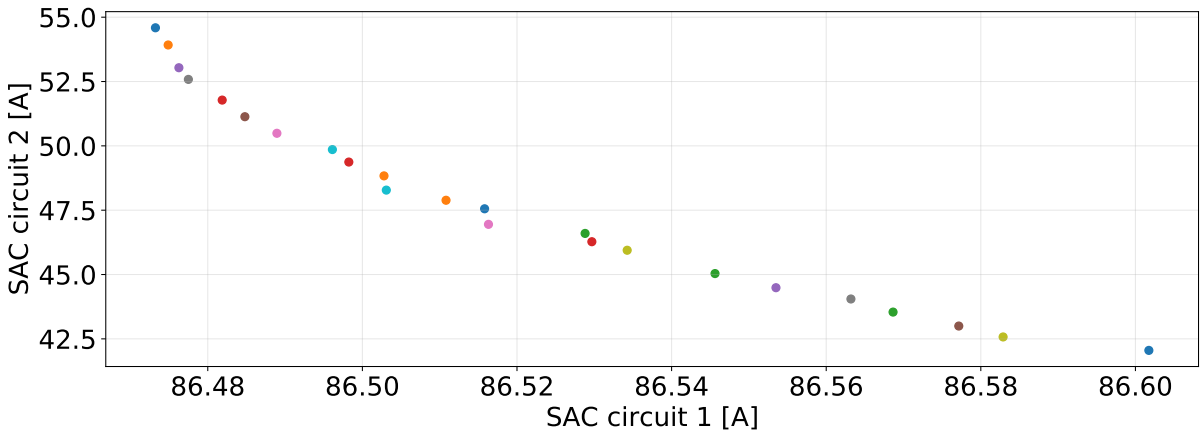

Figure 10.43 – Pareto Front between the SAC of circuit 1 and 2 using the neutral reactor scheme Option 2 for the triple-circuit line.

The final reactor scheme for the triple-circuit transmission line is a fully-connected neutral reactor. Since all reactors are physically connected, it is absolutely necessary optimize the SACs in all circuits at the same time.

Pareto fronts in 3 dimensions are not easy to visualize. Therefore, the optimization results are presented with parallel coordinated plots (WEGMAN, 1990) is presented in Fig. 10.44. One can observe the trade-off between the solutions.

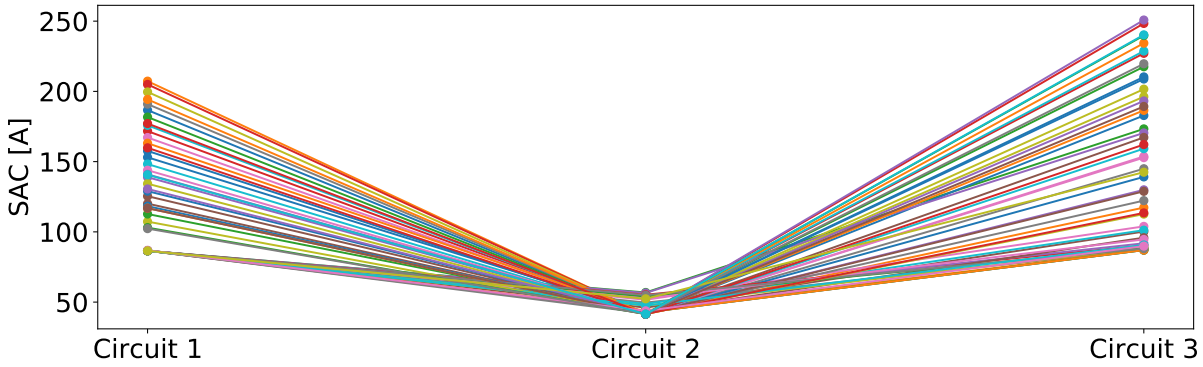

Figure 10.44 – Parallel coordinated of optimizing the neutral reactor scheme Option 3 for the triple-circuit line.

The solution with the best balance between the objectives was chosen. It is presented in Table 10.7 along with the optimal reactor parameters found for the other reactor schemes.

Table 10.7 shows the reactor parameters obtained for the different neutral reactor schemes. The parameters for the reactor scheme option 2 and 3 are obtained only with optimization. Whereas, the reactor parameters for conventional four-legged reactors are calculated analytically and with optimization. The analytically calculated parameters

are smaller than than the optimized parameters. They are clearly ignoring the coupling between circuits. The reactor parameters of the schemes 2 and 3 are very similar. However, since there are more reactances connected, the required basic insulator level of the option 3 will be the lowest.

Table 10.7 – Neutral reactor parameters in [Ω] for the triple-circuit line.

Reactor scheme	Method	x_{m_1}	x_{m_2}	x_{m_3}	x_{n_1}	x_g
3 circ. Option 1	Analytical	505.95	368.15	462.65	-	-
3 circ. Option 1	Optimization	1581.6	2995.2	849.16	-	-
3 circ. Option 2	Optimization	1035.7	2894.7	888.1	1094.8	-
3 circ. Option 3	Optimization	1060.4	2891.0	827.98	2625.4	25.34

Table 10.8 and 10.9 present the SAC and TRV for the different options. Note that there is an important reduction on the SAC and TRV of all circuits when utilizing the optimized parameters. All optimized schemes yielded to essentially the same SAC and TRV values. The circuit which was benefited the most is the circuit 2, which is the circuit located in the middle. This evidences that the mutual coupling between circuits was effectively mitigated. These results indicates that with the optimized parameters the probability of a successful SPAR within a dead time of 500 ms is high.

Table 10.8 – SAC in [A] obtained with the neutral reactors for the triple-circuit line.

Reactor scheme	Method	$SACci_1$	$SACci_2$	$SACci_3$
3 circ. Option 1	Analytical	105.03	123.9	104.85
3 circ. Option 1	Optimization	84.86	40.34	84.07
3 circ. Option 2	Optimization	85.48	39.58	84.08
3 circ. Option 3	Optimization	88.09	39.33	84.01

Table 10.9 – TRV in [kV] obtained with the neutral reactors for the triple-circuit line.

Reactor scheme	Method	$TRVci_1$	$TRVci_2$	$TRVci_3$
3 circ. Option 1	Analytical	160.68	182.93	151.03
3 circ. Option 1	Optimization	108.1	43.89	108.36
3 circ. Option 2	Optimization	107.22	42.67	107.76
3 circ. Option 3	Optimization	107.4	42.2	108.23

10.3.4 Quadruple-circuit reactors

It has been shown that the optimization of the neutral reactor scheme option 1 can be done solving a mono-objective problem. Therefore, instead of presenting the Pareto front, the variation of the SAC in each circuit according to the reactor parameter value of its circuit can be observed. The corresponding plot is presented in Fig.10.45. One

can see that the optimal reactor values for circuit 1 and 2 will be much larger than the imposed limit. However, those reactors could be difficult to obtain in real situations.

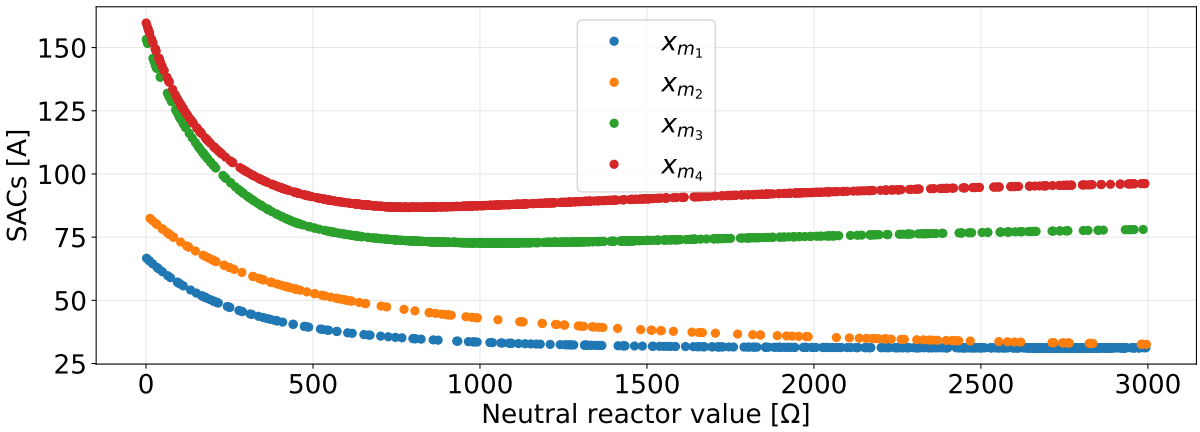

Figure 10.45 – Variation of the SAC in a quadruple-circuit line as function of the neutral reactor value.

So far, the individual analysis of each reactor scheme has been presented. However, nothing new is observed in the optimization of the reactor schemes for the quadruple-circuit line. Therefore, only the summarized results and the generalized SAC and TRV behavior in Figs. 10.46 and 10.47 using the optimized neutral reactor parameters are presented.

The reactor parameters for the different neutral reactor options in the quadruple-circuit line are presented in Table 10.10. As in the previous cases, only the parameters of the four-legged reactor were obtained analytically and with optimization. As expected, the analytically calculated neutral reactors parameters are much lower than the optimized parameters. Observing the optimized solution it is possible to see that the parameters of the reactors for circuit 1 and 2 (x_{m_1} and x_{m_2}) are very similar and close to 3000 Ω. On the other hand, the reactor parameters x_{m_3} and x_{m_4}, for circuits 3 and 4, present a larger variation in the different reactor scheme options. This indicates that the mutual coupling between those circuits is more linked to the additional neutral reactors x_{n_1}, x_{n_2} and x_g, than in the case of circuits 1 and 2.

Table 10.10 – Obtained neutral reactor parameters in a quadruple-circuit line in [Ω].

Reactor scheme	Method	x_{m_1}	x_{m_2}	x_{m_3}	x_{m_4}	x_{n_1}	x_{n_2}	x_g
4 circ. Option 1	Analytical	361.85	149.84	232.8	375.54	-	-	-
4 circ. Option 1	Optimization	2749.7	2998.9	1044.3	766.91	-	-	-
4 circ. Option 2	Optimization	2754.4	2993.4	761.1	406.84	-	699.28	-
4 circ. Option 3	Optimization	2557.7	2975.3	1024.7	1080.2	2647.3	16.88	-
4 circ. Option 4	Optimization	2666.7	2932.9	993.86	877.02	2897.5	807.0	1126.6

Table 10.11 and 10.12 present the SAC and TRV for the different options. It

can clearly be seen the importance of using the optimized parameters. The results suggest a highly probability of SPAR success in circuits 1 and 2, not reproduced in circuits 3 and 4.

Table 10.11 – SAC in $[A]$ obtained with the neutral reactors in a quadruple-circuit line.

Reactor scheme	Method	$SACci_1$	$SACci_2$	$SACci_3$	$SACci_4$
4 circ. Option 1	Analytical	42.52	69.28	98.56	95.59
4 circ. Option 1	Optimization	30.4	32.28	71.52	85.78
4 circ. Option 2	Optimization	30.4	32.29	71.74	85.63
4 circ. Option 3	Optimization	30.52	30.34	71.52	86.66
4 circ. Option 4	Optimization	30.58	30.17	73.17	89.29

Table 10.12 – TRV in $[kV]$ obtained with the neutral reactors in a quadruple-circuit line.

Reactor scheme	Method	$TRVci_1$	$TRVci_2$	$TRVci_3$	$TRVci_4$
4 circ. Option 1	Analytical	70.6	122.43	137.36	130.78
4 circ. Option 1	Optimization	37.32	36.91	76.43	101.81
4 circ. Option 2	Optimization	37.32	36.93	76.04	100.26
4 circ. Option 3	Optimization	36.55	33.96	76.47	97.44
4 circ. Option 4	Optimization	36.46	33.69	74.13	96.01

Figs. 10.46 and 10.47 present the SAC and TRV profile for faults along the line for the optimized reactor parameters. It allows to identify the fault locations with possible SPAR failure.

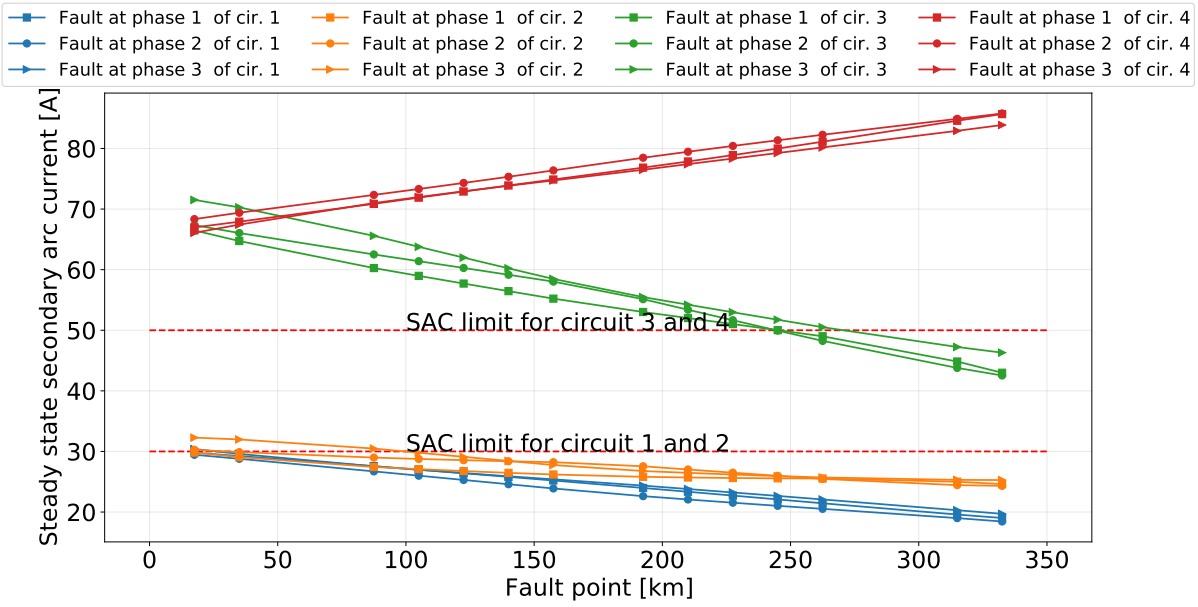

Figure 10.46 – Variation of the SAC in a quadruple-circuit line as function of the fault point, using optimized reactors for the scheme option 1.

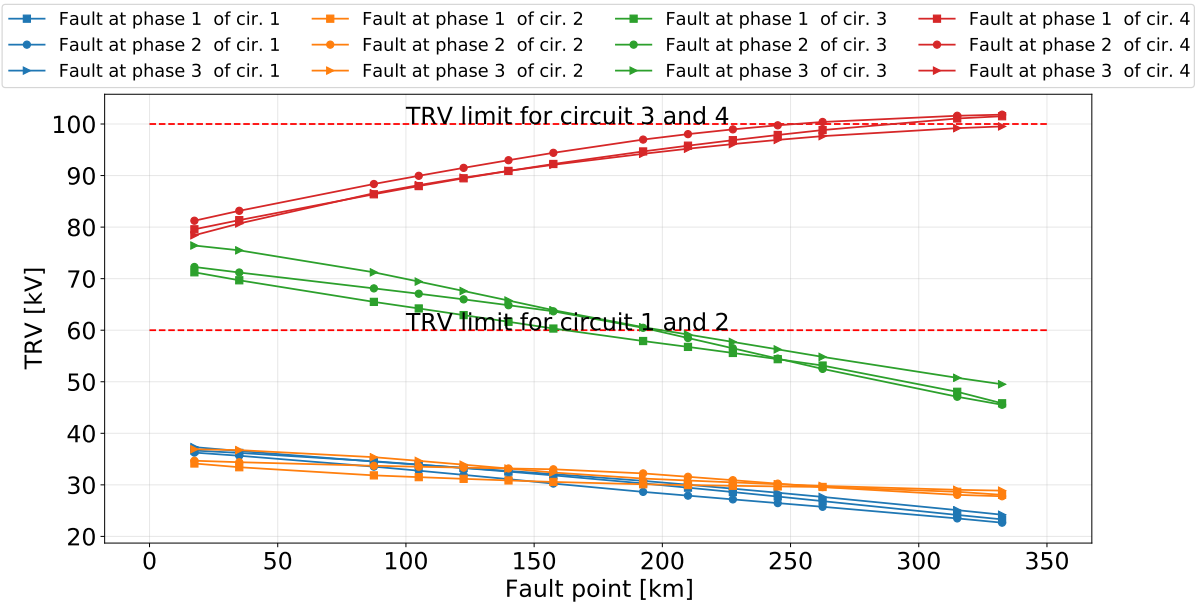

Figure 10.47 – Variation of the TRV in a quadruple-circuit line as function of the fault point, using optimized reactors for the scheme option 1.

To solve the SPAR failure, the line should be redesigned or high speed grounding switches (HSGS) should be used. However, to determine the actual SPAR success or failure, simulations with a realistic arc model should be performed.

10.4 Evaluation using an arc model

Different models to reproduce the arc behavior can be found in the literature. Mainly, there are two arc models. The Kizilcay model, that considers the thermal extinction of the arc (KIZILCAY; PNIOK, 1991; KIZILCAY, 2002; PRIKLER *et al.*, 2003), and the Johns model, that considers the electrostatic arc extinction (JOHNS; AL-RAWI, 1984; JOHNS *et al.*, 1994). The Johns' model considers the successive re-ignitions of the arc caused by the arc voltage and was used in the present research.

The dynamic arc conductance is derived in $g_k(t)$ by solving (10.9), where $G_k(t_k)$ is the stationary arc conductance at instant t_k in S and $\tau_k(t_k)$ the arc time constant at instant t_k in [s]. The sub-index $_k$ stands p for primary arc, and s for secondary arc. The arcing time t_k is measured from the initiation of the primary or secondary arc.

$$\frac{\delta g_k}{\delta t_k} = \frac{1}{\tau_k(t_k)} \left[G_k(t_k) - g_k(t_k) \right] \tag{10.9}$$

In (JOHNS *et al.*, 1994) $G_k(t)$ is calculated as in (10.10). $i_k(t)$ is the instantaneous arc current. For the primary arc, V_p is a constant equal to 15 V/cm, and $l_p(t)$ is a constant equal to 1.1 times the insulator string length (l_0). For the secondary

arc, $V_s = 75I_s^{-0.4}$ in V/cm, where I_s is the steady state peak SAC in A. Arc length $l_s(t_s)$ is $1.1l_0$ for $t_s < 0.1s$ and $1.1l_0t_s$ for $t_s \geq 0.1s$. It is important to note that the total arc is not in a straight line, because several loops occur in the arc channel (PRIKLER *et al.*, 2003).

$$G_k(t) = \frac{|i(t)|}{V_k l_k(t)} \tag{10.10}$$

The time constant τ_k is calculated as in (10.11), where I_p is the steady state peak primary arc current in A.

$$\tau_p(t_p) = \frac{2.85 \cdot 10^{-5} I_p}{l_p(t_p)} \quad \tau_s(t_s) = \frac{2.51 \cdot 10^{-3} I_s^{1.4}}{l_s(t_s)} \tag{10.11}$$

The arc extinction criterion in (JOHNS *et al.*, 1994) is based on electrostatic re-ignition verified at each SAC zero crossing. If the absolute value of the open circuit arc voltage is lower than the absolute value of the arc withstand voltage $|v_w|$ in (10.12), the arc is finally extinguished.

$$|v_w(t_s)| = \left[5 + \frac{1620T_e}{2.15 + I_s}\right](t_s - T_e) l_s(t_s) h(t_s - Te) \quad \text{in kV} \tag{10.12}$$

The extinction time T_e is a discrete value that is updated each time that the arc current has a zero crossing. Meanwhile, $h(t_r - Te)$ is a delayed step function that is 0 for $t_s < T_e$ and 1 for $t_s > T_e$ (JOHNS; AL-RAWI, 1984).

10.4.1 PSCAD simulations

The influence of the different reactor schemes in the arc extinction time was analyzed through PSCAD simulations. The original 10 Ω fault resistance was replaced by the Johns' arc model. The currents I_p and I_s, that are inputs of the model, were obtained with PSCAD simulations for solid faults. The initial length of the arc l_0 was set as 200 cm for 230 kV systems, 400 cm for 500 kV, 646 cm for 750 kV, and 954 cm for 1000 kV systems.

The Johns model yield arcs current and voltage like the ones in Figs. 10.48 and 10.49. It was obtained from a SLG fault applied at circuit 1 in the quadruple-circuit line. A conventional four-legged reactor scheme with optimized parameters was used. The non-linearity of the arc current and voltage are clearly observed. The resulting waveform from the other cases are similar, but with different extinction times.

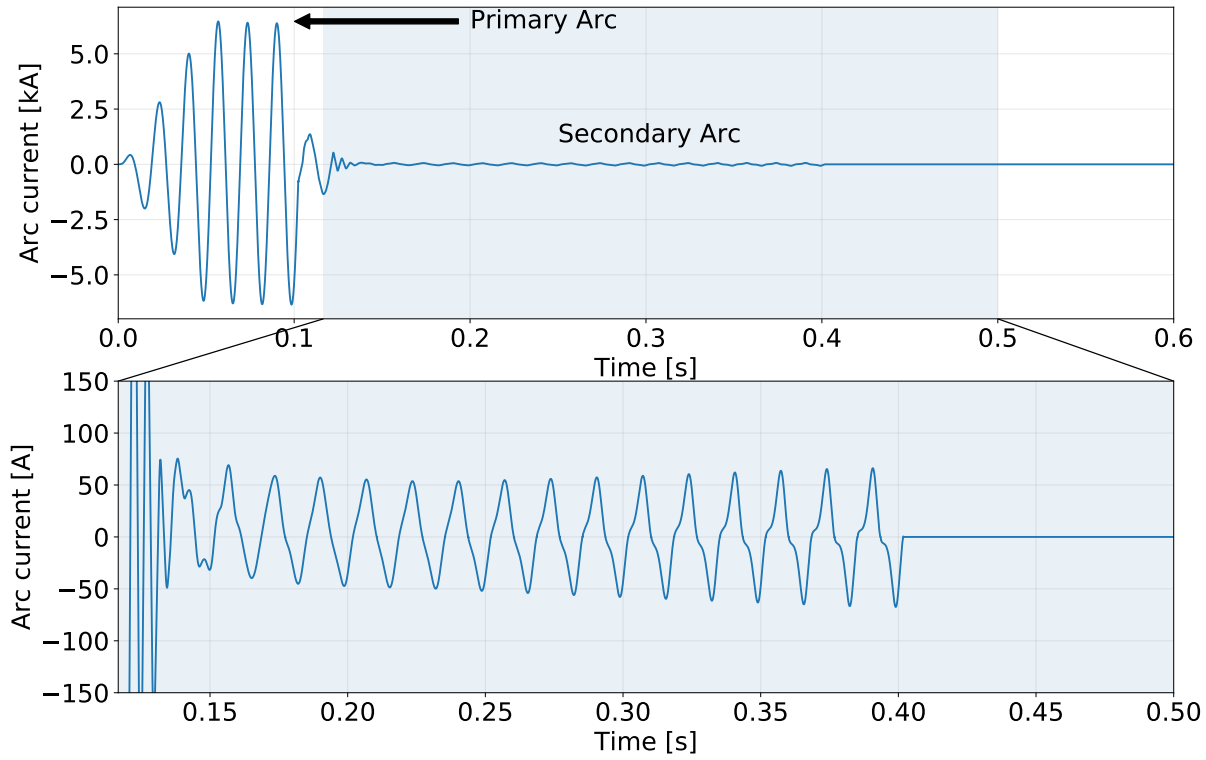

Figure 10.48 – Arc current (top) and secondary arc current (zoomed, bottom) for a fault applied on circuit 1 in the 4 circuit transmission line with conventional four-legged neutral reactor with optimized parameters.

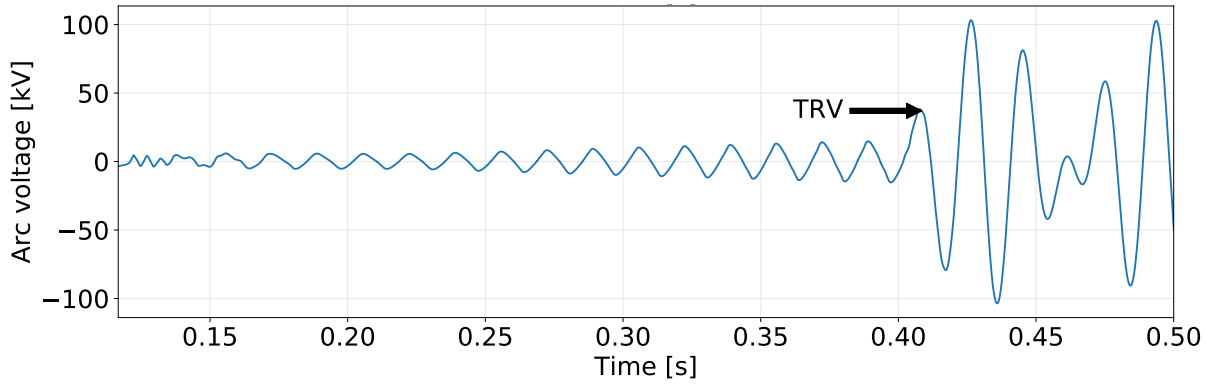

Figure 10.49 – Arc voltage for a fault applied on circuit 1 in the 4 circuit transmission line with conventional four-legged neutral reactor with optimized parameters.

Table 10.13 shows the secondary arc extinction times for the neutral reactor structures with analytical and optimized parameters. The results show that all the reactors schemes with optimized parameters yielded extinction times lower than the 500 ms criterion. On the other hand, the reactor schemes with analytically obtained parameters for the first and second circuit of the triple-circuit line would require dead times higher than 566 ms. Same happens with circuit 2 in the quadruple-circuit line when using the analytically calculated reactor parameters. Nonetheless, the other lines would have dead times under 500 ms.

Table 10.13 – Maximum secondary arc extinction times in $[ms]$ obtained with the different neutral reactor schemes.

Reactor scheme	Method	$t_{ext_{ci_1}}$	$t_{ext_{ci_2}}$	$t_{ext_{ci_3}}$	$t_{ext_{ci_4}}$
1 circ.	Analytical	196.90	-	-	-
1 circ.	Optimization	190.61	-	-	-
2 circ. Option 1	Analytical	482.70	487.81	-	-
2 circ. Option 1	Optimization	476.68	493.40	-	-
2 circ. Option 2	Optimization	476.68	493.40	-	-
3 circ. Option 1	Analytical	517.98	565.58	485.63	-
3 circ. Option 1	Optimization	453.23	289.03	403.33	-
3 circ. Option 2	Optimization	456.63	305.98	419.93	-
3 circ. Option 3	Optimization	456.98	306.13	403.33	-
4 circ. Option 1	Analytical	350.28	537.18	449.58	454.48
4 circ. Option 1	Optimization	295.48	298.18	373.13	422.23
4 circ. Option 2	Optimization	295.48	298.18	373.08	422.33
4 circ. Option 3	Optimization	295.28	289.78	373.13	422.73
4 circ. Option 4	Optimization	295.23	289.78	372.68	434.68

As observed in the present section, when the arc value is below the limit there is no need to further implement the arc model. However, when the result indicates failure it is necessary to further implement a more realistic representation of the phenomena. The optimized parameters have clear advantages compared with the analytically obtained neutral reactor parameters. Finally, since the extinction times using the optimized reactor parameters were essentially the same, no matter the neutral reactor scheme, the use of conventional four-legged reactors with optimized parameters can be applied to n-circuit transmission lines.

10.4.1.1 Disclaimer

The arc extinction times reported in Table 10.13 do not agree with the regular values observed in lines with similar RMS secondary arc currents. Since the PSCAD component used in this research only allows as input the peak value of the primary and secondary arc current, and the initial length of the arc, stochastic parameters as the arc speed elongation can not be tested. Hence, the reported times can not be taken as definitive. For practical applications the real parameters of the arc must be considered. However, the reduction in the extinction times agrees with the RMS SAC reduction, helping to observe that indeed the optimization will also reduce the arc extinction times. Therefore, further investigations should be done in future researches.

11 Optimization of MCMVTLs considering the secondary arc current

In the previous chapter it was evidenced that the optimized MCMVTLs lines proposed so far yield secondary arc currents that suggests SPAR failure for some circuits/fault locations (BALOSSI *et al.*, 1966).

To guarantee successful SPAR in the optimized lines, the SAC was considered in the optimization model of the MCMVTLs. It was included as a constraint in the mathematical model presented in section 4. In this sense, the SAC of each circuit (SAC_{ci}) is included in the constraint-set C in (4.60) as in (11.1). This forces the SAC values to be below the limits presented in Table 11.1, which has values extrapolated from (BALOSSI *et al.*, 1966).

$$SAC_{ci} \leq SAC_{ci_{limit}} \tag{11.1}$$

Table 11.1 – $SAC_{ci_{limit}}$ according the line voltage V_l.

V_l [kV]	138 to 345	440 to 500	750 to 1150
$SAC_{ci_{limit}}$ [A]	30	50	80

In this stage the SAC is analytically calculated with two-port network theory, which is several orders of magnitude faster than the EMT simulations.

11.1 Two-port network representation of the elements in the system

In chapter 9 the two-port network theory was used to calculate the values of the sending and receiving equivalent e.m.f.. However, since the voltages and currents along the lines were not required at that moment, the calculation was done with ideally transposed transmission lines and with positive sequence components for each circuit. On the other hand, in this chapter, the voltages and currents along the lines are required. Therefore, the two-port network elements are expressed for multi-phase systems, considering the actual transpositions of the lines, and the abc and modal domains.

To remember, the general representation of a two-port network element is presented in Fig. 11.1. It can be mathematically expressed in form of transmission

parameters as in (11.2). Note that since in power systems we are interested in the current that is flowing from one node to another, $\mathbf{I_2}$ must have a negative sign.

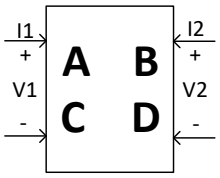

Figure 11.1 – General representation of a two-port network element.

$$\begin{bmatrix} \mathbf{V_2} \\ -\mathbf{I_2} \end{bmatrix} = \begin{bmatrix} \mathbf{A} & \mathbf{B} \\ \mathbf{C} & \mathbf{D} \end{bmatrix} \cdot \begin{bmatrix} \mathbf{V_1} \\ \mathbf{I_1} \end{bmatrix} \tag{11.2}$$

The **ABCD** parameters of Fig. 11.1 can be obtained using Eqs. (11.3) to (11.6).

$$\mathbf{A} = \left.\frac{\mathbf{V_2}}{\mathbf{V_1}}\right|_{\mathbf{I_1=0}} \tag{11.3}$$

$$\mathbf{B} = \left.\frac{\mathbf{V_2}}{\mathbf{I_1}}\right|_{\mathbf{V_1=0}} \tag{11.4}$$

$$\mathbf{C} = \left.\frac{-\mathbf{I_2}}{\mathbf{V_1}}\right|_{\mathbf{I_1=0}} \tag{11.5}$$

$$\mathbf{D} = \left.\frac{-\mathbf{I_2}}{\mathbf{I_1}}\right|_{\mathbf{V_1=0}} \tag{11.6}$$

11.1.1 Series impedance

The simplest two-port network element that we use consists of a group of series impedance as shown in Fig. 11.2. Its two-port network representation can be obtained with the equation system presented in (11.7).

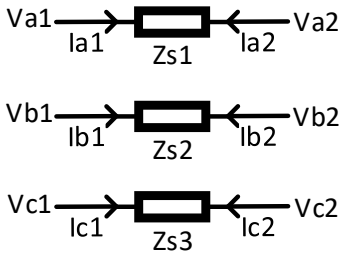

Figure 11.2 – General representation of a series impedance with a two-port network element.

$$\begin{aligned} V_{a_1} &= I_{a_1} Z_{s_1} + V_{a_2} \\ V_{b_1} &= I_{b_1} Z_{s_2} + V_{b_2} \\ V_{c_1} &= I_{c_1} Z_{s_3} + V_{c_2} \\ I_{a_1} &= -I_{a_2} \\ I_{b_1} &= -I_{b_2} \\ I_{c_1} &= -I_{c_2} \end{aligned} \tag{11.7}$$

When representing the system in a matrix form we can obtain the two-port network presented in (11.8).

$$\underbrace{\begin{bmatrix} V_{a_2} \\ V_{b_2} \\ V_{c_2} \\ -I_{a_2} \\ -I_{b_2} \\ -I_{c_2} \end{bmatrix}}_{\mathbf{VI_2}} = \underbrace{\begin{bmatrix} 1 & 0 & 0 & -Z_{s1} & 0 & 0 \\ 0 & 1 & 0 & 0 & -Z_{s2} & 0 \\ 0 & 0 & 1 & 0 & 0 & -Z_{s3} \\ 0 & 0 & 0 & 1 & 0 & 0 \\ 0 & 0 & 0 & 0 & 1 & 0 \\ 0 & 0 & 0 & 0 & 0 & 1 \end{bmatrix}}_{\mathbf{Q_s}} \cdot \underbrace{\begin{bmatrix} V_{a_1} \\ V_{b_1} \\ V_{c_1} \\ I_{a_1} \\ I_{b_1} \\ I_{c_1} \end{bmatrix}}_{\mathbf{VI_1}} \tag{11.8}$$

Generalizing for n impedance the two-port network presented in (11.9) is obtained. In (11.9) the matrix $\mathbf{Z_{s_d}}$ is the diagonal matrix comprised by the series impedance connected between $\mathbf{V_1}$ and $\mathbf{V_2}$; $\mathbf{0}$ is a $(n \times n)$ zero matrix and $\mathbf{I}$ is a $(n \times n)$ identity matrix. This two-port network representation can be used in any element modeled as a series impedance, such as network equivalents and switch states, in whose case Z_{s_d} would be 10^6 if open, and 0 if closed.

$$\mathbf{Q_s} = \begin{bmatrix} \mathbf{I} & -\mathbf{Z_{s_d}} \\ \mathbf{0} & \mathbf{I} \end{bmatrix} \tag{11.9}$$

11.1.2 Transmission lines

The two-port network element for a single-phase transmission line can be represented as in (11.10), where l is the line length, $\gamma = \sqrt{zy}$, and $z_c = \sqrt{zy^{-1}}$. The line impedance and admittance are z and y per unit length, respectively. For this calculus, only the imaginary part of z and y is considered.

$$\begin{bmatrix} V_2 \\ -I_2 \end{bmatrix} = \begin{bmatrix} A & B \\ C & D \end{bmatrix} \cdot \begin{bmatrix} V_1 \\ I_1 \end{bmatrix} = \begin{bmatrix} cosh(\gamma l) & -z_c\ sinh(\gamma l) \\ \frac{-sinh(\gamma l)}{z_c} & cosh(\gamma l) \end{bmatrix} \cdot \begin{bmatrix} V_1 \\ I_1 \end{bmatrix} \tag{11.10}$$

Extending the analysis to the three-phase transmission line case, the ABCD parameters acquire dimensions of 3×3 and are represented with their modal parameters as in (11.11) to (11.14).

$$\mathbf{A_{modal}} = \begin{bmatrix} cosh(\gamma_{mode_1} l) & 0 & 0 \\ 0 & cosh(\gamma_{mode_2} l) & 0 \\ 0 & 0 & cosh(\gamma_{mode_3} l) \end{bmatrix} \tag{11.11}$$

$$\mathbf{B_{modal}} = \begin{bmatrix} -Z_{c_{mode_1}}\ sinh(\gamma_{mode_1} l) & 0 & 0 \\ 0 & -Z_{c_{mode_2}}\ sinh(\gamma_{mode_2} l) & 0 \\ 0 & 0 & -Z_{c_{mode_3}}\ sinh(\gamma_{mode_3} l) \end{bmatrix} \tag{11.12}$$

$$\mathbf{C_{modal}} = \begin{bmatrix} \frac{-sinh(\gamma_{mode_1} l)}{Z_{c_{mode_1}}} & 0 & 0 \\ 0 & \frac{-sinh(\gamma_{mode_2} l)}{Z_{c_{mode_2}}} & 0 \\ 0 & 0 & \frac{-sinh(\gamma_{mode_3} l)}{Z_{c_{mode_3}}} \end{bmatrix} \tag{11.13}$$

$$\mathbf{D_{modal}} = \begin{bmatrix} cosh(\gamma_{mode_1} l) & 0 & 0 \\ 0 & cosh(\gamma_{mode_2} l) & 0 \\ 0 & 0 & cosh(\gamma_{mode_3} l) \end{bmatrix} \tag{11.14}$$

For obtaining the modal parameters the relationship presented in (11.15) to (11.18) are used. It is important to note that one can only calculate $\mathbf{T_v}$ or $\mathbf{T_i}$ with (11.17) or (11.18). The remainder $\mathbf{T_v}$ or $\mathbf{T_i}$ must be calculated with (11.19) or (11.20).

$$\mathbf{Z_{mode}} = \mathbf{T_v^{-1}} \cdot \mathbf{Z_{abc}} \cdot \mathbf{T_i} \tag{11.15}$$

$$\mathbf{Y_{mode}} = \mathbf{T_i^{-1}} \cdot \mathbf{Y_{abc}} \cdot \mathbf{T_v} \tag{11.16}$$

where:

$$\mathbf{T_v} = eigvec(\mathbf{Z_{abc}Y_{abc}}) \tag{11.17}$$

$$\mathbf{T_i} = eigvec(\mathbf{Y_{abc}Z_{abc}}) \tag{11.18}$$

With $\mathbf{T_v}$ and $\mathbf{T_i}$ related according (11.19) and (11.20).

$$\mathbf{T_v^{-1}} = \mathbf{T_i^{transpose}} \tag{11.19}$$

$$\mathbf{T_v} = inv(\mathbf{T_i^{transpose}}) \tag{11.20}$$

Hence, the two-port network of a three-phase transmission line with modal parameters is defined as in (11.21). To extend the result to the multi-circuit transmission line case, the **ABCD** matrices must have dimensions of $(3n_{circ} \times 3n_{circ})$ using the corresponding modal parameters of each circuit.

$$\mathbf{Q_{TL_{modal}}} = \begin{bmatrix} \mathbf{A_{modal}} & \mathbf{B_{modal}} \\ \mathbf{C_{modal}} & \mathbf{D_{modal}} \end{bmatrix} \tag{11.21}$$

To be able to use the two-port network of the transmission line with the rest of the system, it is necessary to obtain its phase two-port network representation. To do that, it is necessary to use the following phase/mode voltage/current transformation:

$$\mathbf{V_{phase}} = \mathbf{T_v} \cdot \mathbf{V_{mode}} \quad \Rightarrow \quad \mathbf{V_{mode}} = \mathbf{T_v^{-1}} \cdot \mathbf{V_{phase}} \tag{11.22}$$

$$\mathbf{I_{phase}} = \mathbf{T_i} \cdot \mathbf{I_{mode}} \quad \Rightarrow \quad \mathbf{I_{mode}} = \mathbf{T_i^{-1}} \cdot \mathbf{I_{phase}} \tag{11.23}$$

This leads to:

$$\mathbf{A_{mode}} = \left.\frac{\mathbf{V_{2_{mode}}}}{\mathbf{V_{1_{mode}}}}\right|_{\mathbf{I_{1_{mode}}=0}} \Rightarrow \mathbf{A_{phase}} = \mathbf{T_v} \cdot \mathbf{A_{mode}} \cdot \mathbf{T_v^{-1}} \tag{11.24}$$

$$\mathbf{B_{mode}} = \left.\frac{\mathbf{V_{2_{mode}}}}{\mathbf{I_{1_{mode}}}}\right|_{\mathbf{V_{1_{mode}}=0}} \Rightarrow \mathbf{B_{phase}} = \mathbf{T_v} \cdot \mathbf{B_{mode}} \cdot \mathbf{T_i^{-1}} \tag{11.25}$$

$$\mathbf{C_{mode}} = \left.\frac{-\mathbf{I_{2_{mode}}}}{\mathbf{V_{1_{mode}}}}\right|_{\mathbf{I_{1_{mode}}=0}} \Rightarrow \mathbf{C_{phase}} = \mathbf{T_i} \cdot \mathbf{C_{mode}} \cdot \mathbf{T_v^{-1}} \tag{11.26}$$

$$\mathbf{D_{mode}} = \left.\frac{-\mathbf{I_{2_{mode}}}}{\mathbf{I_{1_{mode}}}}\right|_{\mathbf{V_{1_{mode}}=0}} \Rightarrow \mathbf{D_{phase}} = \mathbf{T_i} \cdot \mathbf{D_{mode}} \cdot \mathbf{T_i^{-1}} \tag{11.27}$$

11.1.3 Transpositions

Long transmission lines require transposition to reduce the voltage and line current unbalance among phases. The two-port network representation of a transposition can be easily obtained knowing that after a transposition each one of the phases will be located at the other phase position, so phase a will be in the position of phase b, b in the position of c, and c the position of a. This can be mathematically represented in a matrix form as in (11.28).

$$\underbrace{\begin{bmatrix} V_{c_2} \\ V_{a_2} \\ V_{b_2} \\ -I_{c_2} \\ -I_{a_2} \\ -I_{b_2} \end{bmatrix}}_{\mathbf{VI_2}} = \underbrace{\begin{bmatrix} 0 & 0 & 1 & 0 & 0 & 0 \\ 1 & 0 & 0 & 0 & 0 & 0 \\ 0 & 1 & 0 & 0 & 0 & 0 \\ 0 & 0 & 0 & 0 & 0 & 1 \\ 0 & 0 & 0 & 1 & 0 & 0 \\ 0 & 0 & 0 & 0 & 1 & 0 \end{bmatrix}}_{\mathbf{Q_{120}}} \cdot \underbrace{\begin{bmatrix} V_{a_1} \\ V_{b_1} \\ V_{c_1} \\ I_{a_1} \\ I_{b_1} \\ I_{c_1} \end{bmatrix}}_{\mathbf{VI_1}} \tag{11.28}$$

Therefore, a single transposition is represented in (11.29), whereas as a full transposition cycle in (11.30).

$$\mathbf{VI_2} = \mathbf{Q_{120}} \cdot \mathbf{VI_1} \tag{11.29}$$

$$\mathbf{VI_2} = \mathbf{Q_{120}} \cdot \mathbf{Q_{120}} \cdot \mathbf{Q_{120}} \cdot \mathbf{VI_1} \tag{11.30}$$

In a generalized form for N circuits $\mathbf{Q_{120}}$ follows the form presented in (11.31) to (11.33) with $\mathbf{rot_{120}}$ defined in (11.34) and $\mathbf{0}$ in (11.35). The matrix $\mathbf{Q_{120}}$ for single circuit lines is represented in (11.31), for double circuit lines in (11.32), and for triple circuit lines in (11.33). $\mathbf{Q_{120}}$ for quadruple circuit lines it is not represented because the deduction is straightforward using the previous examples. As you may guess, any number of circuits can be represented following the same procedure.

$$\mathbf{Q_{120}} = \begin{bmatrix} \mathbf{rot_{120}} & \mathbf{0} \\ \mathbf{0} & \mathbf{rot_{120}} \end{bmatrix} \tag{11.31}$$

$$\mathbf{Q_{120}} = \begin{bmatrix} \mathbf{rot_{120}} & \mathbf{0} & \mathbf{0} & \mathbf{0} \\ \mathbf{0} & \mathbf{rot_{120}} & \mathbf{0} & \mathbf{0} \\ \mathbf{0} & \mathbf{0} & \mathbf{rot_{120}} & \mathbf{0} \\ \mathbf{0} & \mathbf{0} & \mathbf{0} & \mathbf{rot_{120}} \end{bmatrix} \tag{11.32}$$

$$\mathbf{Q_{120}} = \begin{bmatrix} \mathbf{rot_{120}} & \mathbf{0} & \mathbf{0} & \mathbf{0} & \mathbf{0} & \mathbf{0} \\ \mathbf{0} & \mathbf{rot_{120}} & \mathbf{0} & \mathbf{0} & \mathbf{0} & \mathbf{0} \\ \mathbf{0} & \mathbf{0} & \mathbf{rot_{120}} & \mathbf{0} & \mathbf{0} & \mathbf{0} \\ \mathbf{0} & \mathbf{0} & \mathbf{0} & \mathbf{rot_{120}} & \mathbf{0} & \mathbf{0} \\ \mathbf{0} & \mathbf{0} & \mathbf{0} & \mathbf{0} & \mathbf{rot_{120}} & \mathbf{0} \\ \mathbf{0} & \mathbf{0} & \mathbf{0} & \mathbf{0} & \mathbf{0} & \mathbf{rot_{120}} \end{bmatrix} \tag{11.33}$$

$$\mathbf{rot_{120}} = \begin{bmatrix} 0 & 0 & 1 \\ 1 & 0 & 0 \\ 0 & 1 & 0 \end{bmatrix} \tag{11.34}$$

$$\mathbf{0} = \begin{bmatrix} 0 & 0 & 0 \\ 0 & 0 & 0 \\ 0 & 0 & 0 \end{bmatrix} \tag{11.35}$$

11.1.4 Faults

In this section, the two-port network elements of different fault types are modeled, and in the end a generalized two-port network element for any fault type is proposed.

11.1.4.1 Single line to ground (SLG) Faults

The simplest two-port network representation for faults correspond to a SLG fault. To obtain the two-port network it is analyzed the scheme presented in Fig. 11.3 for an C-G fault.

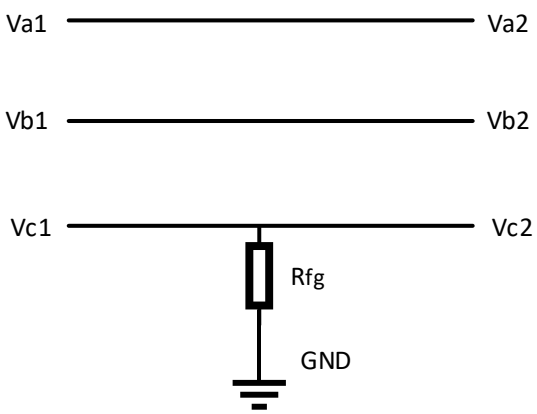

Figure 11.3 – CG fault representation.

The equations that describe the system are presented in (11.36). Note that g was used to represents the conductance, notation that will be maintained along all this section.

$$\begin{aligned} V_{a_1} &= V_{a_2} \\ V_{b_1} &= V_{b_2} \\ V_{c_1} &= V_{c_2} \\ I_{a_1} &= -I_{a_2} \\ I_{b_1} &= -I_{b_2} \\ I_{c_1} &= -I_{c_2} + g_{f_g} V_{c_1} \end{aligned} \tag{11.36}$$

Based on the previous equation system, a generalized two-port network for SLG faults is presented in (11.37), where the sub-index $1, 2, 3$ refer to the number of the phase.

$$\begin{bmatrix} V_{a_2} \\ V_{b_2} \\ V_{c_2} \\ -I_{a_2} \\ -I_{b_2} \\ -I_{c_2} \end{bmatrix} = \begin{bmatrix} 1 & 0 & 0 & 0 & 0 & 0 \\ 0 & 1 & 0 & 0 & 0 & 0 \\ 0 & 0 & 1 & 0 & 0 & 0 \\ -g_{f_{g1}} & 0 & 0 & 1 & 0 & 0 \\ 0 & -g_{f_{g2}} & 0 & 0 & 1 & 0 \\ 0 & 0 & -g_{f_{g3}} & 0 & 0 & 1 \end{bmatrix} \cdot \begin{bmatrix} V_{a_1} \\ V_{b_1} \\ V_{c_1} \\ I_{a_1} \\ I_{b_1} \\ I_{c_1} \end{bmatrix} \tag{11.37}$$

11.1.4.2 Line to Line (L-L) Faults

To deduce the two-port network of a L-L fault the, A-B fault example in Fig.(11.4) is used.

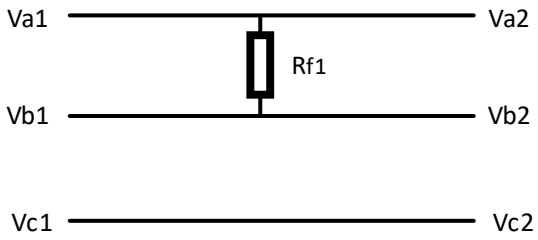

Figure 11.4 – AB fault representation.

The equations that describe the system are presented in (11.38), leading to the two-port network representation in (11.39). This representation allows to deduce any L-L fault.

$$\begin{aligned} V_{a_1} &= V_{a_2} \\ V_{b_1} &= V_{b_2} \\ V_{c_1} &= V_{c_2} \\ I_{a_1} &= -I_{a_2} + g_{f_1}(V_{a_1} - V_{b_1}) \\ I_{b_1} &= -I_{b_2} + g_{f_1}(V_{b_1} - V_{a_1}) \\ I_{c_1} &= -I_{c_2} \end{aligned} \tag{11.38}$$

$$\begin{bmatrix} V_{a_2} \\ V_{b_2} \\ V_{c_2} \\ -I_{a_2} \\ -I_{b_2} \\ -I_{c_2} \end{bmatrix} = \begin{bmatrix} 1 & 0 & 0 & 0 & 0 & 0 \\ 0 & 1 & 0 & 0 & 0 & 0 \\ 0 & 0 & 1 & 0 & 0 & 0 \\ -g_{f_1} & g_{f_1} & 0 & 1 & 0 & 0 \\ g_{f_1} & -g_{f_1} & 0 & 0 & 1 & 0 \\ 0 & 0 & 0 & 0 & 0 & 1 \end{bmatrix} \cdot \begin{bmatrix} V_{a_1} \\ V_{b_1} \\ V_{c_1} \\ I_{a_1} \\ I_{b_1} \\ I_{c_1} \end{bmatrix} \tag{11.39}$$

11.1.4.3 ABC Fault

The ABC fault presented in Fig. 11.5 can be described by the system in (11.40), generating the two-port network representation in (11.41).

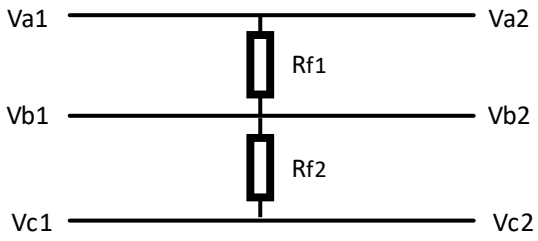

Figure 11.5 – ABC fault representation.

$$\begin{aligned}
V_{a_1} &= V_{a_2} \\
V_{b_1} &= V_{b_2} \\
V_{c_1} &= V_{c_2} \\
I_{a_1} &= -I_{a_2} + g_{f_1}(V_{a_1} - V_{b_1}) \\
I_{b_1} &= -I_{b_2} + g_{f_1}(V_{b_1} - V_{a_1}) + g_{f_2}(V_{b_1} - V_{c_1}) \\
I_{c_1} &= -I_{c_2} + g_{f_2}(V_{c_1} - V_{b_1})
\end{aligned} \tag{11.40}$$

$$\begin{bmatrix} V_{a_2} \\ V_{b_2} \\ V_{c_2} \\ -I_{a_2} \\ -I_{b_2} \\ -I_{c_2} \end{bmatrix} = \begin{bmatrix} 1 & 0 & 0 & 0 & 0 & 0 \\ 0 & 1 & 0 & 0 & 0 & 0 \\ 0 & 0 & 1 & 0 & 0 & 0 \\ -g_{f_1} & g_{f_1} & 0 & 1 & 0 & 0 \\ g_{f_1} & -(g_{f_1} + g_{f_2}) & g_{f_2} & 0 & 1 & 0 \\ 0 & g_{f_2} & -g_{f_2} & 0 & 0 & 1 \end{bmatrix} \cdot \begin{bmatrix} V_{a_1} \\ V_{b_1} \\ V_{c_1} \\ I_{a_1} \\ I_{b_1} \\ I_{c_1} \end{bmatrix} \tag{11.41}$$

11.1.4.4 ABC-G Fault

The ABC-G fault presented in Fig. 11.6 can be described by the system in (11.42), generating the two-port network representation in (11.43).

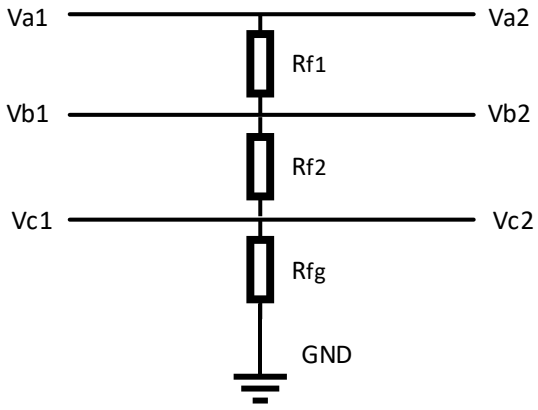

Figure 11.6 – ABC-G fault representation.

$$\begin{aligned}
V_{a_1} &= V_{a_2} \\
V_{b_1} &= V_{b_2} \\
V_{c_1} &= V_{c_2} \\
I_{a_1} &= -I_{a_2} + g_{f_1}(V_{a_1} - V_{b_1}) \\
I_{b_1} &= -I_{b_2} + g_{f_1}(V_{b_1} - V_{a_1}) + g_{f_2}(V_{b_1} - V_{c_1}) \\
I_{c_1} &= -I_{c_2} + g_{f_2}(V_{c_1} - V_{b_1}) + g_{f_g} V_{c_1}
\end{aligned} \tag{11.42}$$

$$\begin{bmatrix} V_{a_2} \\ V_{b_2} \\ V_{c_2} \\ -I_{a_2} \\ -I_{b_2} \\ -I_{c_2} \end{bmatrix} = \begin{bmatrix} 1 & 0 & 0 & 0 & 0 & 0 \\ 0 & 1 & 0 & 0 & 0 & 0 \\ 0 & 0 & 1 & 0 & 0 & 0 \\ -g_{f_1} & g_{f_1} & 0 & 1 & 0 & 0 \\ g_{f_1} & -(g_{f_1}+g_{f_2}) & g_{f_2} & 0 & 1 & 0 \\ 0 & g_{f_2} & -(g_{f_2}+g_{f_g}) & 0 & 0 & 1 \end{bmatrix} \cdot \begin{bmatrix} V_{a_1} \\ V_{b_1} \\ V_{c_1} \\ I_{a_1} \\ I_{b_1} \\ I_{c_1} \end{bmatrix} \tag{11.43}$$

11.1.4.5 Generalized two-port network for any single-circuit fault

The specific two-port network representation shown so far can be used according to the fault type. However, a generalized two-port network for any type of fault can be obtained using the scheme presented in Fig. 11.7. The equations that describe this system are presented in (11.44).

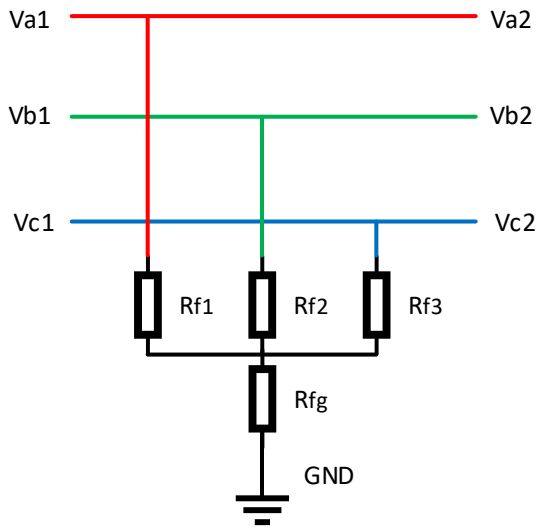

Figure 11.7 – Generalized fault scheme.

$$\begin{aligned} V_{a_1} &= V_{a_2} \\ V_{b_1} &= V_{b_2} \\ V_{c_1} &= V_{c_2} \\ I_{a_1} &= -I_{a_2} + g_{f_1}(V_{a_1} - V_n) \\ I_{b_1} &= -I_{b_2} + g_{f_2}(V_{b_1} - V_n) \\ I_{c_1} &= -I_{c_2} + g_{f_3}(V_{c_1} - V_n) \end{aligned} \tag{11.44}$$

To get the two-port network the previous scheme, the equation system must be expressed only in terms of its input/output voltages and currents. Therefore, it is necessary to find the voltage at the neutral point (V_n) in terms of the input/output

voltage and currents. Hence, knowing that $V_n = I_n R_{f_g}$ we obtain the next equations:

$$\begin{aligned} V_n &= (g_{f_1}(V_{a_1} - V_n) + g_{f_2}(V_{b_1} - V_n) + g_{f_3}(V_{c_1} - V_n))R_{f_g} \\ V_n &= -V_n(g_{f_1} + g_{f_2} + g_{f_3})R_{f_g} + g_{f_1}V_{a_1}R_{f_g} + g_{f_2}V_{b_1}R_{f_g} + g_{f_3}V_{c_1}R_{f_g} \\ V_n(1 &+ (g_{f_1} + g_{f_2} + g_{f_3})R_{f_g}) = g_{f_1}V_{a_1}R_{f_g} + g_{f_2}V_{b_1}R_{f_g} + g_{f_3}V_{c_1}R_{f_g} \end{aligned} \tag{11.45}$$

If we define a variable $M = 1 + R_{f_g}(g_{f_1} + g_{f_2} + g_{f_3})$ we can finally find the value of V_n as:

$$V_n = \frac{g_{f_1}V_{a_1}R_{f_g}}{M} + \frac{g_{f_2}V_{b_1}R_{f_g}}{M} + \frac{g_{f_3}V_{c_1}R_{f_g}}{M} \tag{11.46}$$

Then, the new equation system, represented with the the two-port network element, is presented in (11.47). Note that it could be easily extended to faults in multi-circuit transmission lines just by following the same form of $\mathbf{Q_{fault}}$.

$$\begin{bmatrix} V_{a_2} \\ V_{b_2} \\ V_{c_2} \\ -I_{a_2} \\ -I_{b_2} \\ -I_{c_2} \end{bmatrix} = \underbrace{\begin{bmatrix} 1 & 0 & 0 & 0 & 0 & 0 \\ 0 & 1 & 0 & 0 & 0 & 0 \\ 0 & 0 & 1 & 0 & 0 & 0 \\ -g_{f_1} + \frac{g_{f_1}^2 R_{f_g}}{M} & \frac{g_{f_1}g_{f_2}R_{f_g}}{M} & \frac{g_{f_1}g_{f_3}R_{f_g}}{M} & 1 & 0 & 0 \\ \frac{g_{f_2}g_{f_1}R_{f_g}}{M} & -g_{f_2} + \frac{g_{f_2}^2 R_{f_g}}{M} & \frac{g_{f_2}g_{f_3}R_{f_g}}{M} & 0 & 1 & 0 \\ \frac{g_{f_3}g_{f_1}R_{f_g}}{M} & \frac{g_{f_3}g_{f_2}R_{f_g}}{M} & -g_{f_3} + \frac{g_{f_3}^2 R_{f_g}}{M} & 0 & 0 & 1 \end{bmatrix}}_{\mathbf{Q_{fault}}} \cdot \begin{bmatrix} V_{a_1} \\ V_{b_1} \\ V_{c_1} \\ I_{a_1} \\ I_{b_1} \\ I_{c_1} \end{bmatrix} \tag{11.47}$$

11.1.5 Shunt compensation

Fig. 11.8 represents the two-port network scheme of a single-circuit compensation reactor. Parameters **A**, **B**, and **D** are simple to calculate with Eqs. (11.48) to (11.50), in which **I** is the identity matrix and **0** a zero matrix, both with dimensions of $(3n_{circ} \times 3n_{circ})$. However, **C** matrix in Eq. (11.51) requires more mathematical development.

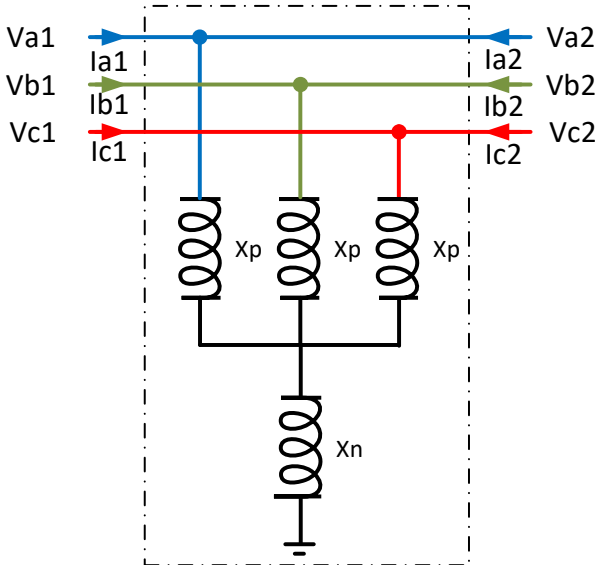

Figure 11.8 – Four legged reactor scheme for two port network analysis.

$$\mathbf{A} = \left.\frac{\mathbf{V_2}}{\mathbf{V_1}}\right|_{\mathbf{I_1=0}} = \mathbf{I} \tag{11.48}$$

$$\mathbf{B} = \left.\frac{\mathbf{V_2}}{\mathbf{I_1}}\right|_{\mathbf{V_1=0}} = \mathbf{Z} \tag{11.49}$$

$$\mathbf{D} = \left.\frac{-\mathbf{I_2}}{\mathbf{I_1}}\right|_{\mathbf{V_1=0}} = \mathbf{I} \tag{11.50}$$

$$\mathbf{C} = \left.\frac{-\mathbf{I_2}}{\mathbf{V_1}}\right|_{\mathbf{I_1=0}} \tag{11.51}$$

To obtain $\mathbf{C}$ it is necessary to write the equations that describe the system when $\mathbf{I_1} = 0$. In this situation all the current will flow through the compensation scheme, given the equation system presented in (11.52).

$$\begin{aligned} V_{a_2} &= j(I_{a_2}x_p + I_{a_2}x_n + I_{b_2}x_n + I_{c_2}x_n) \\ V_{b_2} &= j(I_{b_2}x_p + I_{a_2}x_n + I_{b_2}x_n + I_{c_2}x_n) \\ V_{c_2} &= j(I_{c_2}x_p + I_{a_2}x_n + I_{b_2}x_n + I_{c_2}x_n) \end{aligned} \tag{11.52}$$

In a matrix form Eq. 11.53 represents the system under the specified conditions.

Therefore, $\mathbf{C}$ can be expressed as in (11.54).

$$\underbrace{\begin{bmatrix} V_{a_2} \\ V_{b_2} \\ V_{c_2} \end{bmatrix}}_{\mathbf{V_2}=\mathbf{V_1}} = j \underbrace{\begin{bmatrix} x_p + x_n & x_n & x_n \\ x_n & x_p + x_n & x_n \\ x_n & x_n & x_p + x_n \end{bmatrix}}_{\mathbf{X_{comp}}} \cdot \underbrace{\begin{bmatrix} I_{a_2} \\ I_{b_2} \\ I_{c_2} \end{bmatrix}}_{\mathbf{I_2}} \tag{11.53}$$

$$\mathbf{C} = -\mathbf{X}_{\mathbf{comp}}^{-\mathbf{1}} \tag{11.54}$$

The form of $\mathbf{X_{comp}}$ can be easily extended to all of the proposed reactor schemes. In real situations, the neutral reactors have a resistance, so $\mathbf{X_{comp}}$ must be replaced with $\mathbf{Z_{comp}}$. In a general form, the two-port network representation of the compensation schemes is as in (11.55).

$$\mathbf{Q_{comp}} \begin{bmatrix} \mathbf{I} & \mathbf{0} \\ -\mathbf{Z}_{\mathbf{comp}}^{-\mathbf{1}} & \mathbf{I} \end{bmatrix} \tag{11.55}$$

Additionally, note that this result could also be used in the fault analysis case using (11.56) and (11.57).

$$\underbrace{\begin{bmatrix} V_{a_2} \\ V_{b_2} \\ V_{c_2} \end{bmatrix}}_{\mathbf{V_2}=\mathbf{V_1}} = \underbrace{\begin{bmatrix} r_{a_f} + r_{g_f} & r_{g_f} & r_{g_f} \\ r_{g_f} & r_{b_f} + r_{g_f} & r_{g_f} \\ r_{g_f} & r_{g_f} & r_{c_f} + r_{g_f} \end{bmatrix}}_{\mathbf{R_{fault}}} \cdot \underbrace{\begin{bmatrix} I_{a_2} \\ I_{b_2} \\ I_{c_2} \end{bmatrix}}_{\mathbf{I_2}} \tag{11.56}$$

$$\mathbf{C} = -\mathbf{R}_{\mathbf{fault}}^{-\mathbf{1}} \tag{11.57}$$

11.2 Calculation of the secondary arc current

The system illustrated in Fig. 11.9 can be represented in two-port network elements as in Fig. 11.10. All the elements of the systems are calculated as in the previous chapter.

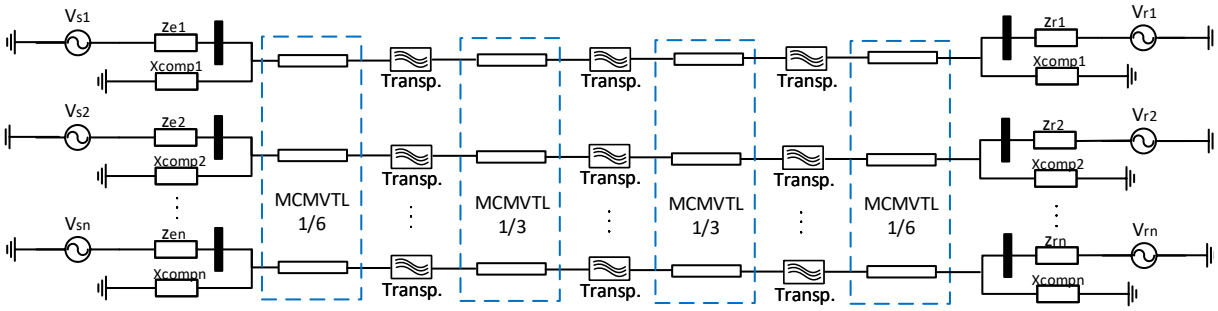

Figure 11.9 – Scheme of the test systems.

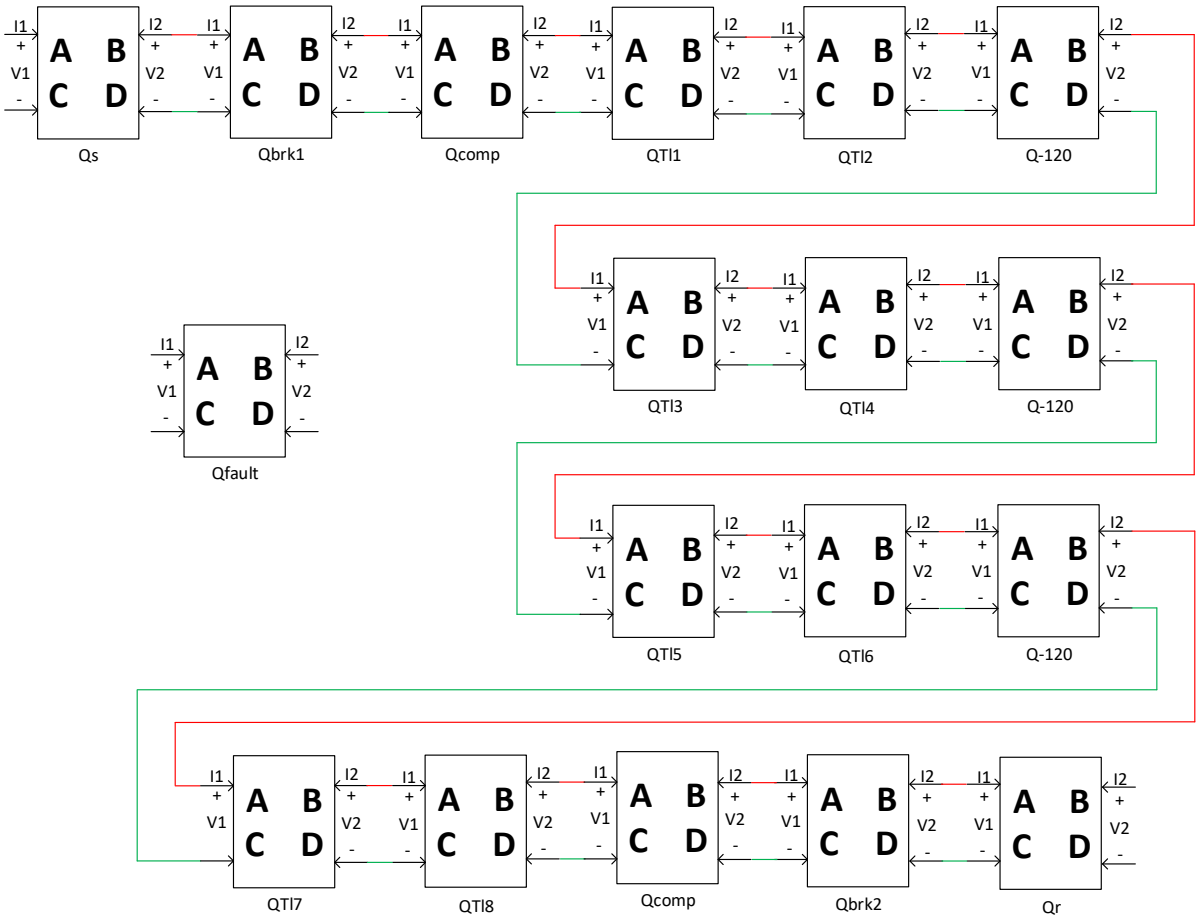

Figure 11.10 – Two port network representation of the entire system.

The description of the two-port networks elements is as follows:

- $\mathbf{Q_s}$ and $\mathbf{Q_r}$ are the two-port networks of the sending and reception fonts.
- $\mathbf{Q_{brk_1}}$ and $\mathbf{Q_{brk_2}}$ are the two-port networks that represents the line breakers status.
- $\mathbf{Q_{comp}}$ is the two-port network compensation element.
- $\mathbf{Q_{Tl_1}}$ to $\mathbf{Q_{Tl_8}}$ are the two-port networks of the transmission line segments

- $\mathbf{Q_{-120}}$ is the two-port network element of transposition.
- $\mathbf{Q_{fault}}$ is the two-port network fault component.

Note that the transmission line is fully transposed and each line segment was represented with two two-port networks elements. This allows to put the fault two-port network element at any line point.

The system in Fig. 11.10 can be represented also as in Fig. 11.11, in which $\mathbf{Q_1}$ is the equivalent two-port network at left side of the fault, where as $\mathbf{Q_2}$ is the equivalent two-port network at right side of the fault.

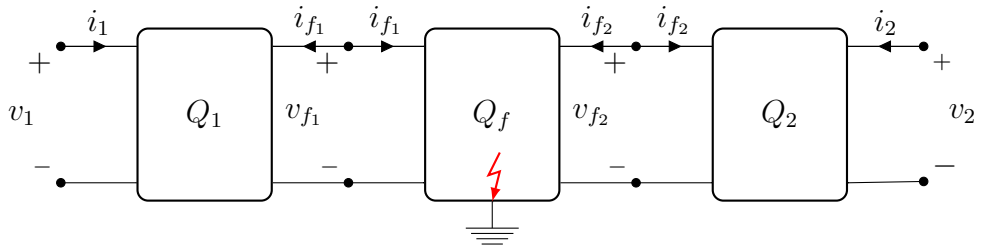

Figure 11.11 – Two port network equivalent of the entire system.

Eqs. (11.58) to (11.60) describe the two-port network dynamics of the system in Fig. 11.11.

$$\begin{aligned} \mathbf{V_2} &= \mathbf{A_2 V_{f_2}} + \mathbf{B_2 I_{f_2}} \\ -\mathbf{I_2} &= \mathbf{C_2 V_{f_2}} + \mathbf{D_2 I_{f_2}} \end{aligned} \tag{11.58}$$

$$\begin{aligned} \mathbf{V_{f_2}} &= \mathbf{A_f V_{f_1}} + \mathbf{B_f I_{f_1}} \\ -\mathbf{I_{f_2}} &= \mathbf{C_f V_{f_1}} + \mathbf{D_f I_{f_1}} \end{aligned} \tag{11.59}$$

$$\begin{aligned} \mathbf{V_{f_1}} &= \mathbf{A_1 V_1} + \mathbf{B_1 I_1} \\ -\mathbf{I_{f_1}} &= \mathbf{C_1 V_1} + \mathbf{D_1 I_1} \end{aligned} \tag{11.60}$$

If we replace (11.60) in (11.59) we have:

$$\begin{aligned} \mathbf{V_{f_2}} &= \mathbf{A_f}(\mathbf{A_1 V_1} + \mathbf{B_1 I_1}) - \mathbf{B_f}(\mathbf{C_1 V_1} + \mathbf{D_1 I_1}) \\ -\mathbf{I_{f_2}} &= \mathbf{C_f}(\mathbf{A_1 V_1} + \mathbf{B_1 I_1}) - \mathbf{D_f}(\mathbf{C_1 V_1} + \mathbf{D_1 I_1}) \end{aligned} \tag{11.61}$$

Now, if we replace (11.61) in (11.58) we have:

$$\begin{aligned}
\mathbf{V_2} = \quad & \mathbf{A_2}[\mathbf{A_f}(\mathbf{A_1V_1} + \mathbf{B_1I_1}) - \mathbf{B_f}(\mathbf{C_1V_1} + \mathbf{D_1I_1})] \\
& -\mathbf{B_2}[\mathbf{C_f}(\mathbf{A_1V_1} + \mathbf{B_1I_1}) - \mathbf{D_f}(\mathbf{C_1V_1} + \mathbf{D_1I_1})] \\
-\mathbf{I_2} = \quad & \mathbf{C_2}[\mathbf{A_f}(\mathbf{A_1V_1} + \mathbf{B_1I_1}) - \mathbf{B_f}(\mathbf{C_1V_1} + \mathbf{D_1I_1})] \\
& -\mathbf{D_2}[\mathbf{C_f}(\mathbf{A_1V_1} + \mathbf{B_1I_1}) - \mathbf{D_f}(\mathbf{C_1V_1} + \mathbf{D_1I_1})]
\end{aligned} \tag{11.62}$$

Since $\mathbf{V_1}$ and $\mathbf{V_2}$ in (11.62) are known it is possible to get $\mathbf{I_1}$ as in (11.63) and find all the unknown variables.

$$\begin{aligned}
\mathbf{M_1} = \quad & (\mathbf{A_2A_fB_1} - \mathbf{A_2B_fD_1} + \mathbf{B_2D_fD_1} - \mathbf{B_2C_fB_1})^{-1} \\
\mathbf{M_2} = \quad & (\mathbf{V_2} - \mathbf{A_2A_fA_1V_1} + \mathbf{A_2B_fC_1V_1} + \mathbf{B_2C_fA_1V_1} - \mathbf{B_2D_fC_1V_1}) \\
\mathbf{I_1} = \quad & \mathbf{M_1^{-1}M_2}
\end{aligned} \tag{11.63}$$

Finally, the fault current I_f is expressed as in (11.64)

$$\mathbf{I_f} = \mathbf{I_{f_1}} + \mathbf{I_{f_2}} \tag{11.64}$$

11.3 Optimization results

To show the advantages of including the SAC as a restriction in the mathematical model that formalizes the optimization of MCMVTLs, double-circuit lines operating at 500 kV were optimized. These lines were chosen based on previous chapter results where the line with the highest steady state SAC value was the double-circuit line.

The lines were optimized considering a four-legged reactor scheme with analytically calculated parameters (KIMBARK, 1964). An optimization of the reactor parameters was not performed because it would increase the simulation time significantly. The SAC was calculated for a condition of a load of 90% of the line SIL. The equivalents of the systems were set to have a SCR of 25 in the strong source and 15 in the weak source, considering a SCR = 1 for the current at 100% of the line SIL.

Fig. 11.12 shows the selected optimized line. For the sake of comparison, Fig. 11.13 shows the optimized line analyzed in the previous chapter, which does not include the SAC in the mathematical model. The data of the neutral reactors are available at Table 11.2. As you can see, the two lines are considerably different. The advantages of including the SAC in the mathematical model are clearly evidenced. While the line in Fig. 11.12 yielded a maximum SAC of 28 and 24 A in circuit 1 and 2, respectively, the line in Fig. 11.13 presented maximum values of 100 and 109 A. Therefore, an average SAC reduction of 75% was achieved.

Certainly, the SAC reduction can not be achieved without cost. In this case, the SAC reduction was achieved by increasing the right of way (ROW) and height of the line. On the other hand SIL is higher and the cost is lower. As any multi-objective optimization problem there exists a trade-off between objectives and it is responsibility of the designer to choose the solution that fits the best the desired objectives.

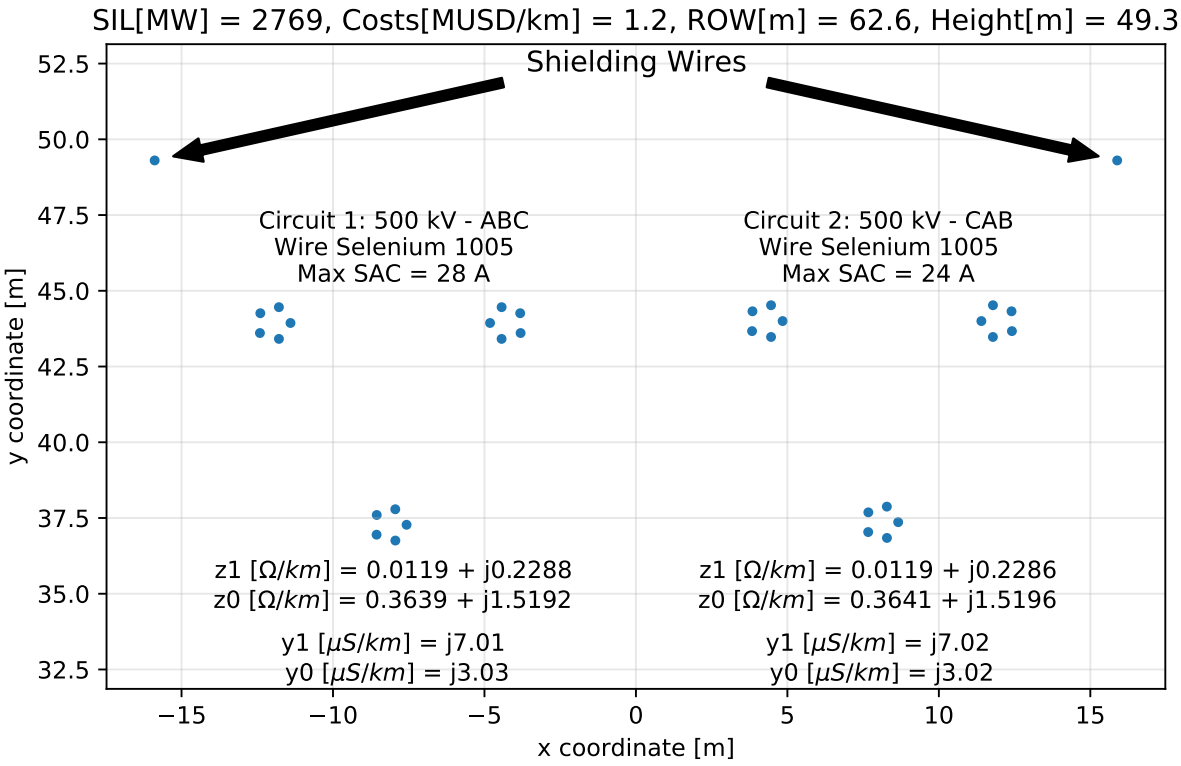

Figure 11.12 – Optimal double-circuit line including SAC optimization.

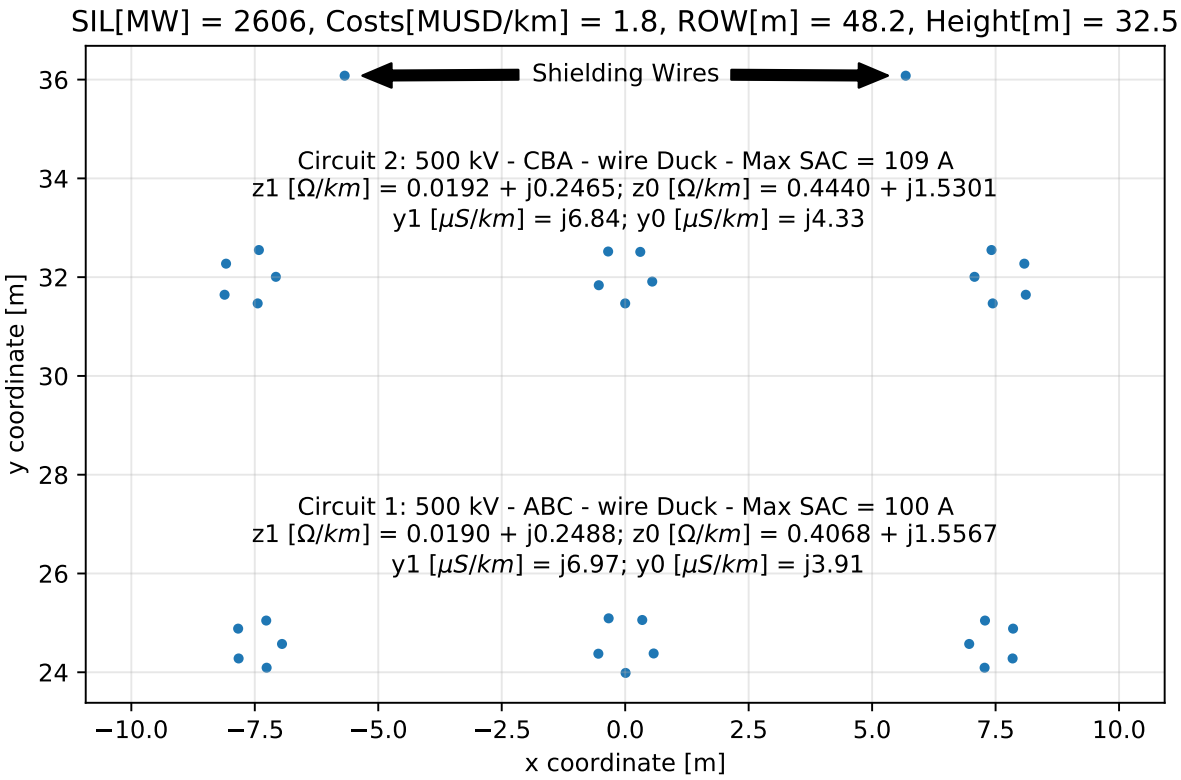

Figure 11.13 – Optimal double-circuit line without SAC optimization.

Table 11.2 – Neutral reactor comparison between the line with and without SAC optimization.

Line Type	$x_{p_1}[\Omega]$	$x_{p_2}[\Omega]$	$x_{m_1}[\Omega]$	$x_{m_2}[\Omega]$
Fig. 11.12	1144.32	1143.19	1443.17	1454.34
Fig. 11.13	1197.99	1171.95	494.94	354.94

Figs. 11.14 and 11.15 show the SAC as a function of the fault point and fault phase in both transmission lines. One can clearly see that at any fault location of the line in Fig. 11.12 (optimized with the SAC as a constraint) the SAC is way below the acceptable limit. Also, the response for faults in different phases is quite similar. On the contrary, the profile for the line in Fig. 11.13 shows higher values for every fault point, and presents an irregular profile.

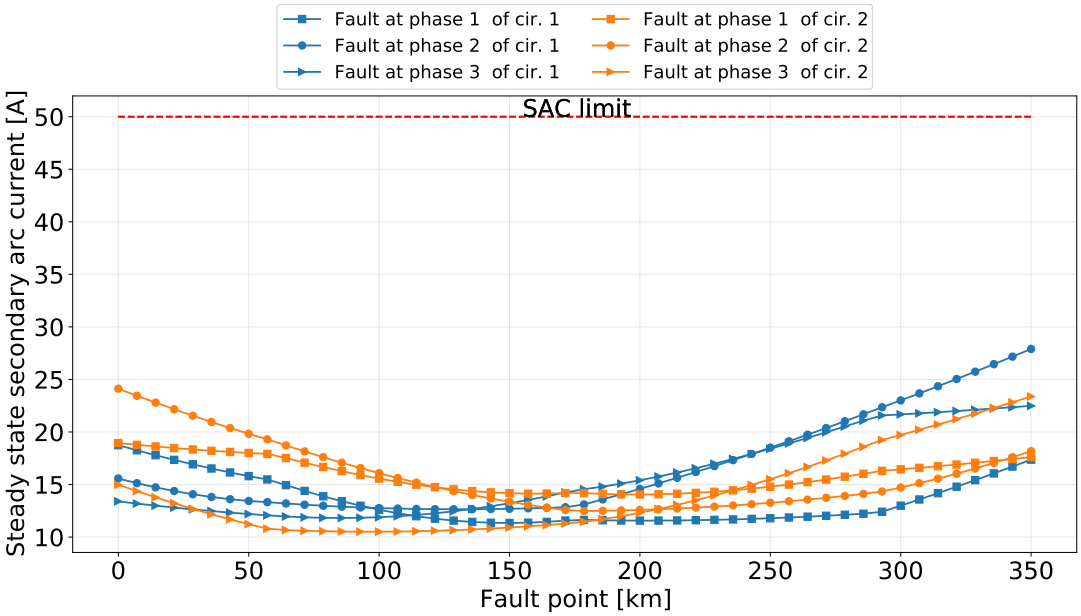

Figure 11.14 – Secondary arc current along an optimized double-circuit line with SAC restriction.

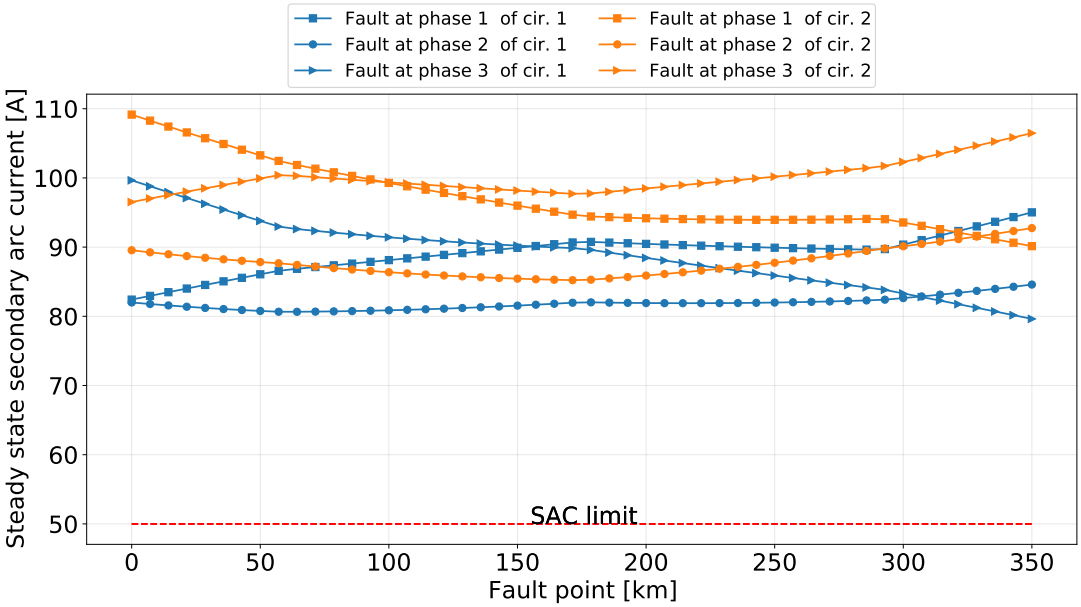

Figure 11.15 – Secondary arc current along an optimized double-circuit line without SAC restriction.

Figs. 11.16 and 11.17 show the TRV as a function of the fault point and fault phase in both transmission lines. The conclusions are the same as in the SAC case. Also, it is evident that the SAC restriction inclusion also influenced positively on the TRV reduction.

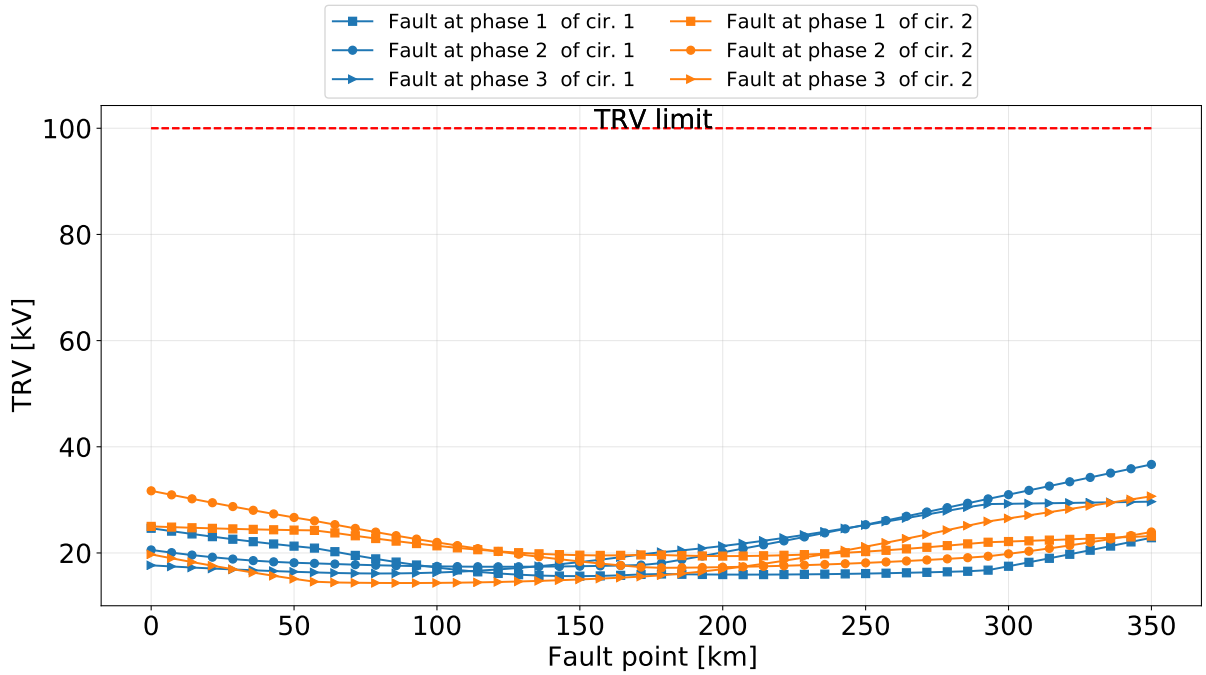

Figure 11.16 – TRV along an optimized double-circuit line with SAC restriction.

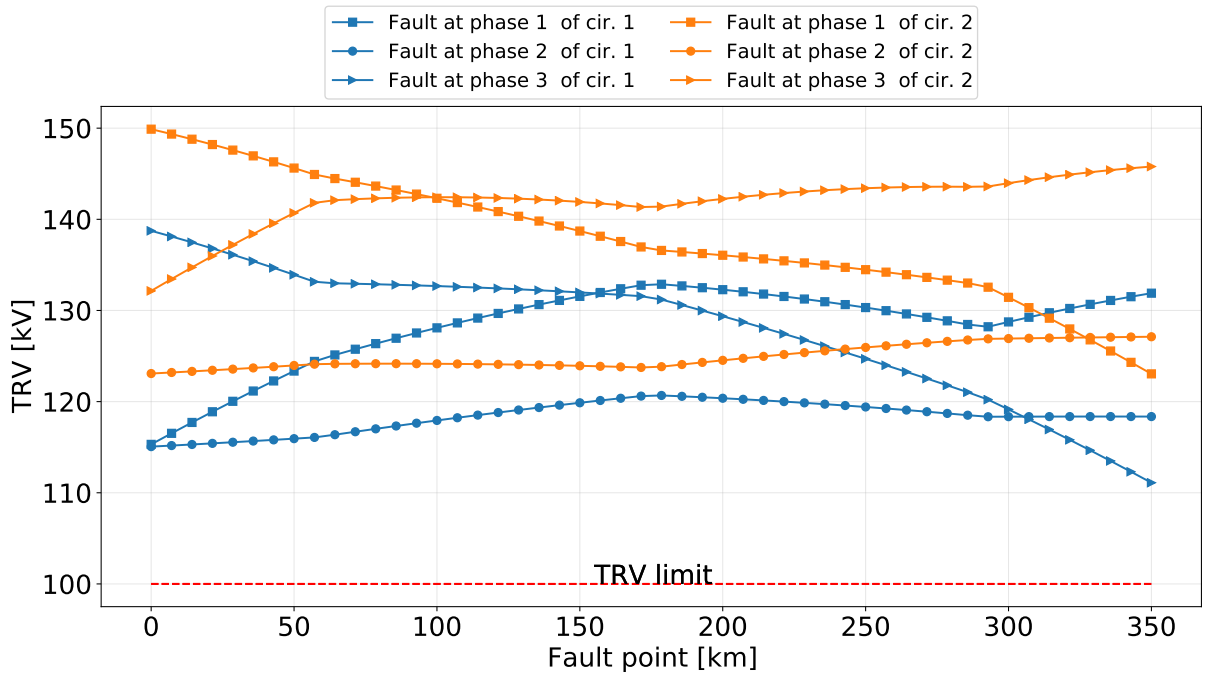

Figure 11.17 – TRV along an optimized double-circuit line without SAC restriction.

As stated before, in multi-objective problems there exists a trade-off between objectives. It is possible to find another trade-off making a comparison of the voltage at the neutral point of the neutral reactors in each line. Figs. 11.18 and 11.19 show the peak voltage at the neutral point of the reactors that belong to the lines in Fig. 11.12 and 11.13, respectively.

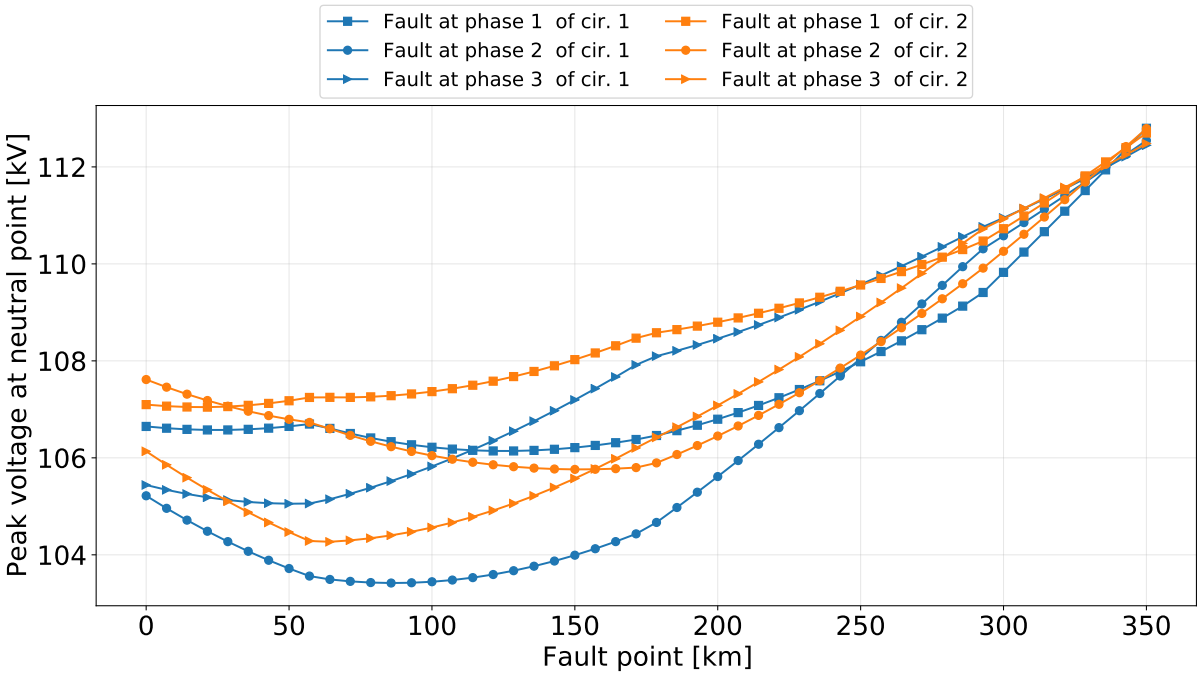

Figure 11.18 – Peak voltage at neutral reactor neutral point for faults along the double-circuit line optimized with SAC restriction.

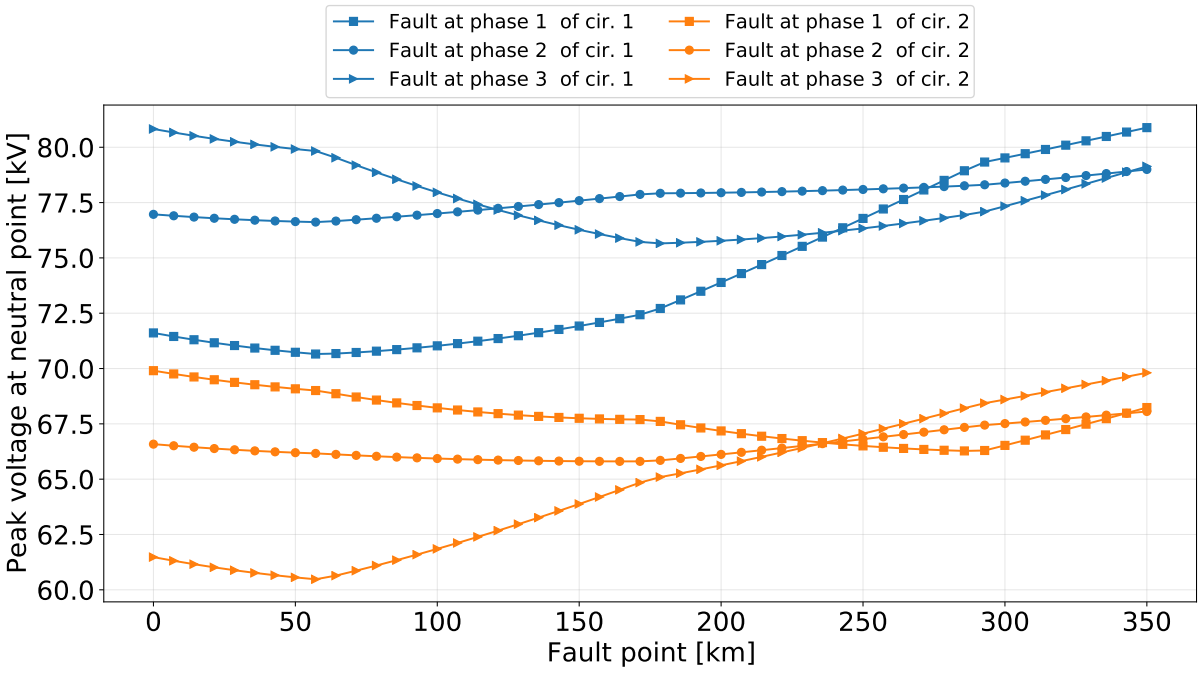

Figure 11.19 – Peak voltage at neutral reactor neutral point for faults along the double-circuit line optimized without SAC restriction.

It can be seen that the line optimized considering the SAC presents a maximum peak voltage of 113 kV (79.76 kV rms) in both neutral reactors. Meanwhile, the line optimized without considering the SAC as a restriction presented values of 81 kV (57.19 kV rms) and 70 kV (49.43 kV rms). This means that the line optimized considering the SAC

will require surge arresters larger than the other line, and slightly larger than the regular ones. The normal withstand rms voltage of neutral reactors in systems of 500 kV is 72.5 kV (CAMARA, 2010).

These results highlight the importance and advantages of considering the SAC in the optimization model. The lines designed with this methodology are more prone to have successful SPAR. Additional research could be done for specifying the most adequate neutral reactor in order to reduce its size.

All the results presented in this chapter can be extended to the other kind of MCMVTLs studied during this research. They will have similar behavior. With this, one step further to make the MCMVTLs feasible in different situations has been taken.

12 Conclusions and future work

12.1 Conclusions

Regarding the continuous growing of population, density and power demand, there is a need of increasing the SIL of the transmission lines and reducing their ROW. Thus, a good option is to use multi-circuit lines instead of single-circuit lines. Additionally, if the multi-circuit lines are non-conventional, the benefits will be higher. Therefore, in this document it was presented a mathematical model and an algorithm to effectively improve the transmission lines considering four objectives: increase of the transmission line SIL, and reduce: costs, ROW and height.

The optimization is done using two different approaches: the Weighted sum and a Pareto approach. The model is adaptive, so it is able to optimize multi-circuit lines from 1 to any quantity of circuits. The new lines are named as non-conventional multi-circuit transmission lines. As example, lines from 1 to 4 circuits were optimized. The initial results showed that the non-conventional multi-circuit transmission lines are better in values up to 152% than parallel single-circuit transmission lines. Even in the case of single-circuit lines, the algorithm produced non-conventional lines, so better results were obtained (up to 66%).

When compared the Weighted sum approach and the NSGA-II vectorized, similar results are obtained in execution time and objective function values. The final values are slightly better when used the NSGA-II approach. However, Weighted sum approach does not provide an entire Pareto front in a single run. Therefore, the NSGA-II approach becomes superior because in a single run it is generated a Pareto front that can be used in the final choice of the geometry, according to the needs of specific problems.

After identifying the importance of the phase sequence in modifying the electromagnetic environment, the phase sequence was included in the optimization model. As a result, the phase sequence was optimized and an increment on the fitness value was achieved. The increment is up-to 30% compared with the optimization without consider the phase sequence. The increment is mainly because the phase sequence helps to reduce the ROW and the transmission line height.

From transient studies it was observed that the voltage and current in neighbor circuits experienced much severe coupling in multi-circuit transmission lines, imposing important requirements for the protection system. It is important to highlight that the phase sequence has an important influence on the systems, helping to mitigate the induced

overvoltage and secondary arc current in some cases.

The analysis of the secondary arc current (SAC) lead to explore alternatives to reduce the SAC. The first alternative investigated was to optimize different neutral reactor schemes. A comparison between them evidenced that it was possible to reduce the SAC to the same value with any reactor scheme as long the reactor parameters were optimized, including the typical four-legged reactor. The SAC using the optimized reactor parameters achieved reductions of up-to 50% compared with the analytically calculated neutral reactors.

An additional enhancement was implemented to include SAC reduction as a restriction in the optimization model. As a result, new transmission lines ready to perform single phase auto reclosing were achieved. The new lines have a SAC considerable lower than the original lines that do not include the SAC in the optimization model.

The geometries presented in this research are different from those presented in the previous literature and have better qualities related to the proposed objectives. Additionally, the proposed mathematical model allows to optimize and generate geometries that are not hard to implement in real projects. That is because of the symmetry of tower and phases, and because of adequate distances design considering insulation coordination restrictions.

Finally, we can conclude that the obtained lines are good options to implement in real projects, because they meet all the electrical safety distance and constraints, reduce the ROW and height, and increment the SIL. Moreover, because of the ROW reduction, the lines are environmentally friendly.

12.2 Future work

Although we understand a very broad research covering different topics of HSIL multi-circuit multi-voltage transmission lines was developed, and perhaps provoked by that, we foresee that the below topics could be considered for further improvements:

1. The protection system needs to be carefully studied and probably new algorithms will be necessary to properly cope with the stronger inter-circuit and intra-circuit coupling.

2. The new structures should have a proper lightning study.

3. Although all towers have the mass center properly positioned, it is necessary to implement a mechanical feasibility analysis.

4. The presented transient study was implemented for some selected conditions. It should be further enlarged in order to include different loading levels and consider power flow in a broader variation.

5. In the present research the electric field limits were properly considered, however the magnetic field was not analyzed. As the transmission lines have HSIL, it is necessary to investigate the magnetic field under normal operation and also when operation is closer to thermal limits.

6. Other optimization algorithms, such as the NSGA-III or the SMS-EMOA, should be evaluated.

Bibliography

ABETTI, P. A. Bibliography on extra-high-voltage systems. *Trans. Am. Inst. Electr. Eng. Part III Power Appar. Syst.*, v. 77, n. 3, p. 1517–1535, apr 1958. ISSN 0097-2460. Referenced in page 32.

ACOSTA, J. S.; TAVARES, M. C. Methodology for optimizing the capacity and costs of overhead transmission lines by modifying their bundle geometry. *Electr. Power Syst. Res.*, oct 2017. ISSN 03787796. Referenced 5 times in pages 33, 67, 81, 82, and 125.

AGRASAR, M.; URIONDO, F.; HERNANDEZ, J. R.; ALVAREZ, R. A useful methodology for analyzing distance relays performance during simple and inter-circuit faults in multi-circuit lines. *IEEE Trans. Power Deliv.*, v. 12, n. 4, p. 1465–1471, 1997. ISSN 08858977. Referenced in page 34.

ALEXANDROV, G. N.; PODPORKYN, G. V. Improvement of the efficiency of 35 to 220 kV lines. *Int. Conf. AC DC Power Transm.*, n. 5, p. 226–231, 1991. ISSN 0025-7028. Referenced 2 times in pages 32 and 33.

BALOSSI, A.; MALAGUTI, M.; OSTANO, P. Laboratory full-scale tests for determination of the secondary arc extinction time in high-speed reclosing. In: *IEEE Summer Power Meet. July 10-15*. New Orleans: [s.n.], 1966. Referenced 2 times in pages 151 and 187.

BEUME, N.; NAUJOKS, B.; EMMERICH, M. SMS-EMOA : Multiobjective selection based on dominated hypervolume. *European Journal of Operational Research*, v. 181, p. 1653–1669, 2007. Referenced 2 times in pages 57 and 58.

CAMARA, A. *Modeling of electric arc in the air. Power system applications (in portuguese)*. 1–333 p. Tese (PhD.) — Federal University of Rio de Janeiro, 2010. Referenced in page 209.

CORNE, D.; KNOWLES, J.; OATES, M. The Pareto Envelope-Based Selection Algorithm for Multiobjective Optimization. *Schoenauer M. al. Parallel Probl. Solving from Nat. PPSN VI*, v. 1917, 2000. Referenced 2 times in pages 57 and 59.

CORNE, D. W.; JERRAM, N. R.; KNOWLES, J. D.; MARTIN, J. PESA-II : Region-based Selection in Evolutionary Multiobjective Optimization. In: *Proc. Genet. Evol. Comput. Conf.* [S.l.]: Morgan Kaufmann Publishers, 2001. p. 283—-290. Referenced in page 57.

DEB, K.; PRATAP, A.; AGARWAL, S.; MEYARIVAN, T. A fast and elitist multiobjective genetic algorithm: NSGA-II. *IEEE Trans. Evol. Comput.*, v. 6, n. 2, p. 182–197, 2002. ISSN 1089778X. Referenced 4 times in pages 53, 57, 59, and 85.

DERI, A.; TEVAN, G.; SEMLYEN, A.; CASTANHEIRA, A. The Complex Ground Return Plane a Simplified Model for Homogeneous and Multi-Layer Earth Return. *IEEE Trans. Power Appar. Syst.*, PAS-100, n. 8, p. 3686–3693, 1981. ISSN 0018-9510. Referenced in page 65.

DIAS, O.; TAVARES, M. C. Comparison between traditional single-phase auto reclosing and adaptive technique based on harmonic content measurement. *IET Gen., T&D*, v. 11, n. 4, p. 905–914, 2016. Referenced in page 150.

DOMMEL, H. W. Electromagnetic Transients Program Theory Book. *Bonnev. Power Adm.*, p. 483, 1986. Referenced in page 66.

DUBANTON, C. Calcul approché des parametres primaires et secondaires d'une ligne de transport. *EDF Bull. Direct. Etudes Rech.*, v. 1, p. 53—-62, 1969. Referenced in page 65.

Electric Power Research Institute. *EPRI AC Transmission Line Reference Book–200 kV and Above, Third Edition*. [S.l.]: EPRI, 2005. 1–1074 p. Referenced 8 times in pages 38, 65, 67, 70, 72, 77, 117, and 121.

FLEISCHER, M. The measure of pareto optima applications to multi-objective metaheuristics. In: FONSECA, C. M.; FLEMING, P. J.; ZITZLER, E.; THIELE, L.; DEB, K. (Ed.). *Evolutionary Multi-Criterion Optimization*. Berlin, Heidelberg: Springer Berlin Heidelberg, 2003. p. 519–533. ISBN 978-3-540-36970-7. Referenced in page 58.

FOGARTY, T. C. Varying the probability of mutation in the genetic algorithm. In: *Proceedings of the Third International Conference on Genetic Algorithms*. San Francisco, CA, USA: Morgan Kaufmann Publishers Inc., 1989. p. 104–109. ISBN 1-55860-006-3. Disponível em: <http://dl.acm.org/citation.cfm?id=93126.93162>. Referenced in page 52.

FONSECA, C. M.; FLEMING, P. J. Genetic Algorithms for Multiobjective Optimization: Formulation Discussion and Generalization. In: *Proc. 5th Int. Conf. Genet. Algorithms*. Urbana-Champaign, IL, USA: [s.n.], 1993. Referenced in page 56.

FORTESCUE, C. L. Method of Symmetrical Co-Ordinates Applied to the Solution of Polyphase Networks. *Trans. Am. Inst. Electr. Eng.*, XXXVII, n. 2, p. 1027–1140, jul 1918. ISSN 0096-3860. Referenced in page 65.

GHASSEMI, M. High Surge Impedance Loading (HSIL) Lines: A Review Identifying Opportunities, Challenges, and Future Research Needs. *IEEE Trans. Power Deliv.*, IEEE, v. 34, n. 5, p. 1909–1924, 2019. ISSN 19374208. Referenced in page 34.

GOLDBERG, D. E. *Genetic Algorithms in Search, Optimization, and Machine Learning*. 1 edition. ed. [S.l.]: Addison-Wesley Professional; 1 edition, 1989. ISBN 978-0201157673. Referenced in page 56.

GOLDBERG, D. E.; RICHARDSON, J. Genetic algorithms with sharing for multimodal function optimization. In: *Proceedings of the Second International Conference on Genetic Algorithms on Genetic Algorithms and Their Application*. Hillsdale, NJ, USA: L. Erlbaum Associates Inc., 1987. p. 41–49. ISBN 0-8058-0158-8. Disponível em: <http://dl.acm.org/citation.cfm?id=42512.42519>. Referenced in page 56.

Gomes Junior, S. *Otimização De Linhas Aéreas De Transmissão Considerando Novas Concepções Construtivas Para Os Feixes De Condutores*. Tese (Doutorado) — Universidade Federal do Rio de Janeiro, 1995. Referenced in page 33.

GUIHONG, F.; YANXIN, W.; BINGYI, Z. Study on electromagnetic environment of multi-circuit transmission lines on same tower. *Int. Conf. Power Syst. Technol. POWERCON IEEE Power India Conf. POWERCON*, 2008. Referenced 2 times in pages 34 and 35.

Haisheng Liang; Chaojie Zhu; Xiaorong Li; Xuhang Zhang; Wei Cao. Simulation research of the unbalanced factor under the mutual influence of the multi voltage level quadruple-circuit sharing the same tower. In: *2016 IEEE Int. Conf. Power Renew. Energy*. IEEE, 2016. p. 144–150. ISBN 978-1-5090-3068-2. Disponível em: <http://ieeexplore.ieee.org/document/7871190/>. Referenced in page 35.

HAJELA, P.; LIN, C. Y. Genetic search strategies in multicriterion optimal design. *Struct. Optim.*, v. 4, n. 2, p. 99–107, jun 1992. ISSN 0934-4373. Disponível em: <http://link.springer.com/10.1007/BF01759923>. Referenced in page 57.

HORN, J.; NAFPLIOTIS, N.; GOLDBERG, D. E. A niched pareto genetic algorithm for multiobjective optimization. In: *Proc. First IEEE Conf. Evol. Comput. IEEE World Congr. Comput. Intell.* [S.l.: s.n.], 1994. p. 82–87 vol.1. Referenced in page 57.

IEEE. National electrical safety code 2002 edition. *IEEE Std C2-2002*, p. 1–324, Aug 2001. Referenced 2 times in pages 73 and 74.

IEEE Standards association. *IEEE Standard for Calculating the Current-Temperature Relationship of Bare Overhead Conductors*. 2013. 1–72 p. Referenced 2 times in pages 64 and 79.

JOHNS, A.; AL-RAWI, A. Developments in the simulation of long-distance single-pole-switched EHV systems. *IEE Proc. C Gener. Transm. Distrib.*, v. 131, n. 2, p. 67, 1984. ISSN 01437046. Disponível em: <https://digital-library.theiet.org/content/journals/10.1049/ip-c.1984.0010>. Referenced 2 times in pages 183 and 184.

JOHNS, A. T.; AGGARWAL, R. K.; SONG, Y. H. Improved techniques for modelling fault arcs on faulted EHV transmission systems. *IEE Proc. Gener. Transm. Distrib.*, v. 141, n. 2, p. 148–154, 1994. ISSN 13502360. Referenced 2 times in pages 183 and 184.

KIMBARK, E. W. Suppression of Ground-Fault Arcs on Single-Pole- Switched EHV Lines by Shunt Reactors. *IEEE Transactions on Power Apparatus and Systems*, v. 83, n. 3, p. 285–290, 1964. Referenced 5 times in pages 150, 152, 163, 170, and 203.

KIZILCAY, M. Improved Secondary Arc Models Based on Identification of arc parameters from staged fault test records. In: *14th PSCC*. Sevilla, Spain: [s.n.], 2002. p. 24–28. Referenced in page 183.

KIZILCAY, M.; NEUMANN, C. Backflashover Analysis for 110-kV Lines at Multi-Circuit Overhead Line Towers. *Int. Conf. Power Syst. Transients*, p. 4–9, 2007. Referenced 2 times in pages 34 and 35.

KIZILCAY, M.; PNIOK, T. Digital simulation of fault arcs in power systems. *Eur. Trans. Electr. Power*, v. 1, n. 1, p. 55–60, 1991. ISSN 15463109. Referenced in page 183.

KNOWLES, J. D.; CORNE, D. W. Approximating the nondominated front using the pareto archived evolution strategy. *Evol. Comput.*, MIT Press, Cambridge, MA, USA, v. 8, n. 2, p. 149–172, jun. 2000. ISSN 1063-6560. Disponível em: <http://dx.doi.org/10.1162/106365600568167>. Referenced in page 57.

KNUDSEN, N. Single Phase Switching of Transmission Lines Using Reactors For Extinction of The Secondary Arc. In: *Conférence Internationale des Grands Réseaux Électriques à Haute Tension*. Paris - France: [s.n.], 1962. v. 33, p. 1–7. Referenced 2 times in pages 150 and 152.

KOCOT, H. Impedance models of multi-circuit multi-voltage overhead power lines. *PRZEGLĄD ELEKTROTECHNICZNY*, v. 1, n. 12, p. 259–262, dec 2019. ISSN 0033-2097. Disponível em: <http://sigma-not.pl/publikacja-123740-2019-12.html>. Referenced in page 35.

KOEHLER, N. S.; HARI, S.; GUTMAN, R. Breakthrough Overhead Line Design (BOLD): System and Performance Considerations. In: *CIGRE US Natl. Committee, Grid Futur. Symp.* [S.l.: s.n.], 2016. Referenced in page 34.

KONAK, A.; COIT, D. W.; SMITH, A. E. Multi-objective optimization using genetic algorithms : A tutorial. *ELSEVIER Reliab. Eng. Syst. Saf.*, v. 91, p. 992–1007, 2006. Referenced in page 57.

KRON, G. *Tensor analysis of networks*. London: MacDonald, 1939. 635 p. Referenced in page 65.

LI, B.; HE, J.; LI, Y.; ZHENG, Y. Multi-circuit transmission lines. In: *Prot. Technol. Ultra-High-Voltage AC Transm. Syst.* Elsevier, 2020. p. 189–213. ISBN 9780128162057. Disponível em: <https://linkinghub.elsevier.com/retrieve/pii/B978012816205700011X>. Referenced in page 34.

LI, B.; WANG, W.; WEN, W.; YAO, B.; HE, J.; WANG, X. Unbalanced currents of EHV multi-circuit lines and coordination of zero-sequence overcurrent relayings. *Int. J. Electr. Power Energy Syst.*, Elsevier Ltd, v. 126, n. PA, p. 106607, 2021. ISSN 01420615. Disponível em: <https://doi.org/10.1016/j.ijepes.2020.106607>. Referenced in page 35.

LI, H. The Optimal Phase Sequence Arrangement of Multi- circuit Transmission Lines on the Same Tower. *2017 13th Int. Conf. Nat. Comput. Fuzzy Syst. Knowl. Discov.*, IEEE, p. 2525–2529, 2017. Referenced in page 35.

LI, W.; ZHANG, B.; HE, J.; ZENG, R.; CHEN, S. Ion Flow Field Calculation of Multi-circuit DC Transmission Lines. *Int. Conf. High Volt. Eng. Appl.*, n. 3, p. 16–19, 2008. Referenced in page 34.

LI, X.; LI, F.; LIU, P.; CAI, W.; CAI, Z. Modeling Approach for Short-Transmission Lines on the same Tower with Different Wire Parameters and Tower Structure. In: *2018 Int. Conf. Power Syst. Technol.* Guangzhou,China: IEEE, 2018. p. 376–383. ISBN 978-1-5386-6461-2. Disponível em: <https://ieeexplore.ieee.org/document/8601542/>. Referenced in page 35.

LI, Z.; YU, Z.; WANG, X.; HE, J. A design of unbalanced insulation to improve the lightning performance of multi-circuit transmission lines. *31st Int. Conf. Light. Prot. ICLP*, p. 0–3, 2012. Referenced in page 34.

LIEW, A. C.; THUM, P. C. Comparative Studies Of Lightning Performance Of A Quadruple-circuit Dual Voltage 275/132KV Transmission Line Design With Wooden Crossarms. *IEEE Trans. Power Deliv.*, v. 8, n. 4, p. 1973–1980, 1993. ISSN 19374208. Referenced in page 34.

LIU, W.; PAN, M.; LIU, K.; XU, G. Research on electromagnetic character of 500/220kV mixed-voltage quadruple-circuit transmission line. *12th Int. Conf. Environ. Electr. Eng. EEEIC*, p. 227–231, 2013. Referenced 2 times in pages 34 and 35.

LV, X. C.; SUN, Q. Q.; LI, Q. M.; SHI, W. Multi-objective parameter optimization of shunt reactors for multi-circuit transmission lines on the same tower. In: *4th Int. Conf. Electr. Util. Deregul. Restruct. Power Technol.* [S.l.: s.n.], 2011. p. 271–276. ISBN 9781457703638. ISSN 02588013. Referenced in page 35.

MACIEL, R. P. *Maximization of Characteristic Power of Transmission Lines using a non-linear optimization method (in portuguese).* Tese (Master Thesis) — University of Campinas, Brazil, 2013. Referenced 2 times in pages 33 and 73.

MACKOW, A.; KIZILCAY, M.; MALICKI, P. Lightning performance of overhead hybrid transmission line. *IEEE Eindhoven PowerTech, PowerTech*, 2015. Referenced 2 times in pages 34 and 35.

MALICKI, P.; MACKOW, A.; KIZILCAY, M. Estimating the lightning performance of a multi-circuit transmission tower. In: *33rd Int. Conf. Light. Prot. ICLP.* [S.l.: s.n.], 2016. ISBN 9781509058433. Referenced in page 34.

MARJERRISON, M. Electric Transmission Tower Design. *J. Power Div.*, v. 95, n. 2, p. 357–359, oct 1969. ISSN 0569-8030. Disponível em: <http://ascelibrary.org/doi/10.1061/JPWEAM.0000935>. Referenced in page 69.

MILLER, C. J. The Calculation of Radio and Corona Characteristics of Transmission-Line Conductors. *Trans. Am. Inst. Electr. Eng. Part III Power Appar. Syst.*, v. 76, n. 3, p. 461–472, 1957. ISSN 0097-2460. Referenced in page 77.

MURATA, T.; ISHIBUCHI, H. MOGA: multi-objective genetic algorithms. In: *Proc. 1995 IEEE Int. Conf. Evol. Comput.* IEEE, 1995. v. 1, p. 289. ISBN 0-7803-2759-4. Disponível em: <http://ieeexplore.ieee.org/document/489161/>. Referenced in page 57.

NOVITSKIY, A.; WESTERMANN, D. Interaction of multi-circuit overhead transmission lines of different voltages located on the same pylons. In: *Electr. Power Qual. Supply Reliab.* [S.l.]: IEEE, 2012. p. 1–4. ISBN 978-1-4673-1979-9. Referenced 2 times in pages 34 and 35.

PORTELA, C.; GOMES, S. Analysis and optimization of non conventional transmission trunks, considering new technological possibilities. In: *Proc. VI SEPOPE Salvador Bras.* Salvador, BA, Brasil: [s.n.], 1998. SP-092, n. 1, p. 1–6. Referenced in page 73.

PRIKLER, L.; KIZILCAY, M.; BÁN, G.; HANDL, P. Modeling secondary arc based on identification of arc parameters from staged fault test records. *Int. J. Electr. Power Energy Syst.*, v. 25, n. 8, p. 581–589, 2003. ISSN 01420615. Referenced 2 times in pages 183 and 184.

REICHELT, D.; SCHERER, R.; LINES, M.-c. Magnetic Field Reduction Measures for Transmission Lines Considering Power Flow Conditions. In: *Proc. IEEE Transm. und Distrib. Conf.* Los Angeles, United States: [s.n.], 1996. p. 0–6. ISBN 0780335228. Referenced in page 35.

RIBEIRO, M. F.; VASCONCELOS, J. A.; TEIXEIRA, D. A. Optimization of compact overhead lines of 138/230kV: Optimal selection and arrangement of cables and definition of the best transmission line tower topology. In: *17th IEEE Int. Conf. Environ. Electr. Eng. 1st IEEE Ind. Commer. Power Syst. Eur. EEEIC / I CPS Eur.* [S.l.: s.n.], 2017. ISBN 9781538639160. Referenced in page 35.

SALARI, J. C. *Optimizing Transmission Lines Conductors Bundle Geometries (in Portuguese)*. 397 p. Tese (Master Thesis) — Federal University of Rio de Janeiro, Brazil, 1993. Referenced 2 times in pages 33 and 73.

SANDELL, D. H.; SHEALY, A. N.; WHITE, H. B.; SANDELL, D. H. Bibliography on Bundled Conductors. *IEEE Trans. Power Appar. Syst.*, v. 82, n. 69, p. 1115–1128, 1963. ISSN 00189510. Referenced in page 32.

SARMIENTO, J. S. A.; TAVARES, M. C. Enhancement the overhead transmission lines' capacity by modifying the bundle geometry using heuristics algorithms. In: *IEEE PES Asia-Pacific Power Energy Eng. Conf.* [S.l.]: IEEE, 2016. Decem, p. 646–650. ISBN 978-1-5090-5418-3. ISSN 21574847. Referenced in page 33.

SCHAFFER, J. D. *Some Experiments in Machine Learning Using Vector Evaluated Genetic Algorithms (Artificial Intelligence, Optimization, Adaptation, Pattern Recognition)*. Tese (Doutorado) — computer, Nashville, TN, USA, 1984. AAI8522492. Referenced in page 56.

SRINIVAS, N.; DEB, K. Muiltiobjective optimization using nondominated sorting in genetic algorithms. *Evolutionary Computation*, v. 2, n. 3, p. 221–248, Sept 1994. ISSN 1063-6560. Referenced in page 56.

STARR; LLOYD; PEEK. An investigation of corona loss: Law of corona and dielectric strength. *J. AIEE*, v. 46, n. 12, p. 1457–1461, 1927. ISSN 0095-9804. Referenced in page 77.

SUN, Q.; WANG, G.; LI, Q.; LI, Q. Calculation and analysis of the coupling effects of the ultra high voltage double-circuit transmission lines. *2008 Int. Conf. High Volt. Eng. Appl. ICHVE 2008*, IEEE, v. 3, n. 1, p. 366–370, 2008. Referenced in page 35.

TANG, C.; YIN, X.; ZHANG, Z.; LONG, M. Research on the unbalance degree of four-circuit overhead lines on the same tower with different phase sequence arrangements. *Electr. Power Syst. Res.*, Elsevier B.V., v. 163, p. 774–781, 2018. ISSN 0378-7796. Disponível em: <http://dx.doi.org/10.1016/j.epsr.2017.06.003>. Referenced in page 35.

TEVAN, G.; DERI, A. Some remarks about the accurate evaluation of the Carson integral for mutual impedances of lines with earth return. *Arch. Elektrotech.*, v. 67, n. 1, p. 83–90, 1984. Referenced in page 65.

THOMAS, P. H. Output and Regulation in Long-Distance Lines. *Trans. Am. Inst. Electr. Eng.*, XXVIII, n. 1, p. 615–640, 1909. ISSN 0096-3860. Referenced in page 32.

WANG, X.; LI, Z.; HE, J. Impact of Coupling Ground Wire on Lightning Protection Effect of Multi-circuit Tower. In: *Int. Conf. Light. Prot.* Vienna, Austria: [s.n.], 2012. ISBN 9781467318976. Referenced in page 34.

WANG, Y. H.; MENG, S. M.; TANG, B. Study on Type Design of Multi-Circuit Transmission Line Tower. *Adv. Mater. Res.*, v. 594-597, p. 900–903, 2012. ISSN 1662-8985. Referenced in page 34.

WEGMAN, E. J. Hyperdimensional Data Analysis Using Parallel Coordinates. *J. Am. Stat. Assoc.*, v. 85, n. 411, p. 664–675, sep 1990. ISSN 0162-1459. Disponível em: <http://www.tandfonline.com/doi/abs/10.1080/01621459.1990.10474926>. Referenced in page 179.

WEI, S.; QINGMIN, L.; LIANG, Z.; LI, Z.; XINCHANG, L. Research on lightning performance of AC/DC hybrid transmission lines on the same tower. *Iet Gener. Transm. Distrib.*, v. 7, n. 2, p. 166–174, 2013. ISSN 1751-8687. Referenced in page 34.

XI, W.; LI, Z.; HE, J. Improving the lightning protection effect of multi-circuit tower by installing coupling ground wire. *Electr. Power Syst. Res.*, Elsevier B.V., v. 113, p. 213–219, 2014. ISSN 03787796. Disponível em: <http://dx.doi.org/10.1016/j.epsr.2014.03.018>. Referenced in page 35.

Yang Changhui; Wang Luyang; Wang Yufei; Xue Hua; Yang Xiu; Yan Tianyou; Huang Yetong. Computation of unbalance factors for six-circuit transmission line on the same tower. In: *2011 IEEE Power Eng. Autom. Conf.* IEEE, 2011. v. 2, p. 217–220. ISBN 978-1-4244-9690-7. Disponível em: <http://ieeexplore.ieee.org/document/6134941/>. Referenced in page 35.

YANG, Q.; SIMA, W.; YANG, M.; WANG, R.; YUAN, T. Secondary arc current of ultra-high voltage transmission line with a mixed voltage of 1000/500 kV on a single tower. *IET Gener. Transm. Distrib.*, v. 9, n. 7, p. 686–693, 2015. ISSN 1751-8687. Referenced 2 times in pages 34 and 35.

ZEVALLOS, M. E. *Otimização de Linhas de Transmissão para Manobra de Abertura Monopolar - Análise da Influência dos Parâmetros Transversais do Sistema de Compensação Reativa*. 1–161 p. Tese (Doutorado) — Universidade Estadual de Campinas, 2013. Referenced 3 times in pages 137, 138, and 144.

ZHAO, Y.; SU, J.; GU, S.; REN, H.; ZHAO, C. Influence of different coupling ground wire erecting mode on lightning withstand performance for multi-circuit transmission line in a tower. *Int. Conf. Light. Prot. ICLP*, p. 1036–1040, 2014. Referenced in page 34.

ZHEREN, Z.; QING, Y.; LIBIN, Y.; WENXIA, S.; TAO, Y. Lightning back-flash performance of 220kV AC quadruple-circuit transmission lines on the same tower. *Asia-Pacific Symp. Electromagn. Compat. APEMC*, p. 1570–1573, 2010. Referenced in page 34.

ZITZLER, E.; MARCO, L.; THIELE, L. *SPEA2: Improving the Strength Pareto Evolutionary Algorithm For Multiobjective Optimization*. 1–6 p. Tese (Doutorado) — Swiss Federal Institute Techonology, 2002. Referenced in page 57.

ZITZLER, E.; THIELE, L. Multiobjective Evolutionary Algorithms : A Comparative Case Study and the Strength Pareto Approach. *IEEE Trans. Evol. Comput.*, v. 3, n. 4, p. 257–271, 1999. Referenced in page 57.

ZUO, X. F.; KURIBYASHI, H. Protection of parallel multi-circuit transmission lines. In: *Proc. 6th lnternauunal Conferr. Adv. Power Spm Control. Oper. hlanagcmenr*. Hong Kong: [s.n.], 2003. p. 630–634. Referenced in page 34.

APPENDIX A – Parallel simulations in PSCAD

A.1 PSCAD Volley simulations with master and slave projects

To implement volley simulations in PSCAD it is necessary to take into account that the maximum number of parallel simulations that can be executed is $n_{cores} - 1$. It is because PSCAD needs a *master* project to control the *slave* projects, i.e., a core will be always used for control, meanwhile the other cores will be used to simulate copies of the *slave* project but with different parameters. This kind of parallelism is known as *embarrassingly parallel*, which means that the simulation of each project is completely independent of the others.

The *master* project control looks like in Fig. A.1, while the slave project control looks line in Fig. A.2. The *master* project is designed to send a different simulation number (using transmitters) to each one of the parallel *slave* projects, and wait for their ending signal. On the other hand, the *slave* projects use transmitters to receive the signal number sent by the *master* project. Then, using the signal number and the PSCAD *X-Y table* component, the reactor parameters are extracted from the solution file created in Python. In the same *slave* projects the extracted parameters are assigned and simulated. Once a simulation in any *slave* project finish, two actions are performed. Firstly, with the PSCAD *Multiple Run Additional Recording* component an individual output file is filled with the maximum secondary arc current from a specific time. Secondly, a signal of *Ok* is sent back to the *master* project, to indicate that that simulation is done. The *master* project will wait for all *Ok* signals to send the next simulation batch.

Once all simulations in PSCAD are done, the $n_{cores} - 1$ files created by PSCAD are sorted and merged into one, with the objective of assign the objective function values for each one of the solutions sent with Python. This process will be repeated until reach the stop criteria of the NSGA-II, which in this case is the maximum number of generations.

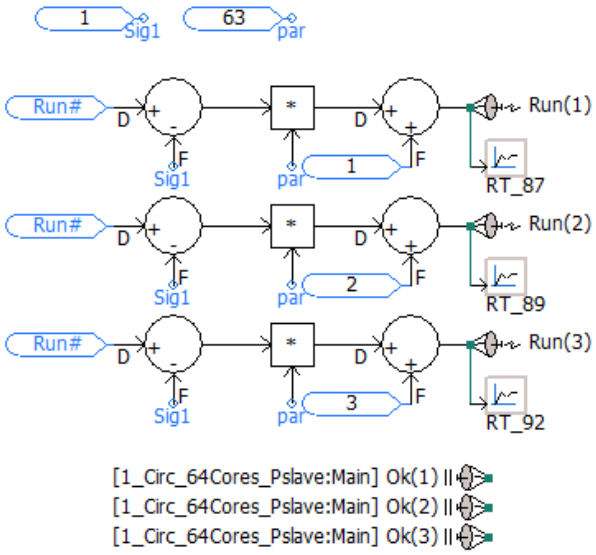

Figure A.1 – Master project configuration in PSCAD.

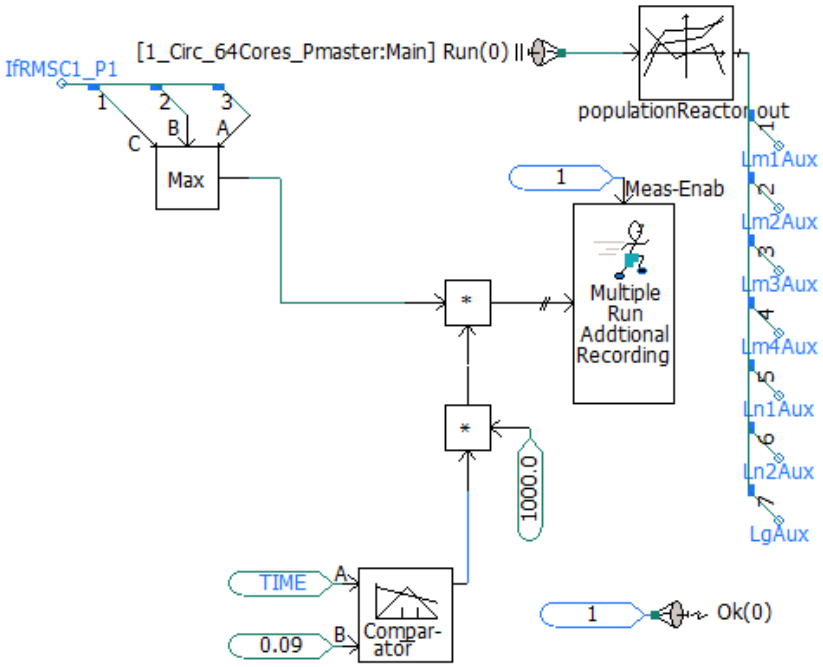

Figure A.2 – Slave project control configuration in PSCAD.

To make a comparison between serial and parallel approach, firstly Table A.1 shows the time used to evaluate 126 solutions of the neutral reactor scheme 3 for the quadruple transmission line and the neutral reactor scheme of the single circuit transmission line when using 1 to 64 cores. Secondly, Table A.2 shows the time consumed to evolve a population of 60 solutions over 20 generations for the same previous cases. In this tests, the faults were applied only in one point and one phase.

As a result, an important reduction in the simulation time was achieved with

the parallel approach. However, the reduction in the simulation time was not linear. The reason for this will be explained ahead.

Note that the results presented in Table A.1 do not use the optimization algorithm, whereas, simulations in Table A.2 do. This allows to see that the impact of the optimization algorithm in the speed up is low, which means that the non-linearity in the speed-up is caused by PSCAD. The main reason is that each system is compiled sequentially.

This fact can be observed in both tables comparing the results when using 32 cores and 64 cores in the single and quadruple circuit transmission line. In the first case, when 64 cores were used, the speed-up was lower that with 32 cores. However, in the second case, a higher speed-up was obtained with 64 cores. It is because in the first case, which is a simpler case than the second, the time to compile the 64 parallel projects dominate over speed-up of running all projects in parallel. On the contrary, the second case is more complex than the first case, so the time to compile the 64 cases remains non-dominant over the speed-up. This is also the reason why higher speed-ups are obtained in the quadruple circuit transmission line.

Table A.1 – Simulation time for evaluating 126 solutions of the reactor scheme option 3 proposed for the quadruple transmission line, and the reactor scheme for the single circuit transmission.

Cores	1 circuit Line		4 circuit Line	
	Time	Speed-up [times]	Time	Speed-up [times]
1	2min 43s ± 4.18s	-	12min 55s ± 11s	-
4	57.8s ± 969ms	2.82	4min 54s ± 1.88s	2.64
8	41.6s ± 589ms	3.92	2min 16s ± 1.06s	5.70
16	23.3s ± 285ms	7.0	1min 17s ± 1.29s	10.06
32	21.7s ± 256ms	7.51	59.2s ± 713ms	13.09
64	26.6s ± 337ms	6.13	52.9s ± 672ms	14.65

Table A.2 – Simulation time for evolving 60 solutions of the reactor scheme option 3 proposed for the quadruple transmission line, and the reactor scheme for the single circuit transmission line during 20 generations.

Cores	1 circuit Line		4 circuit Line	
	Time	Speed-up [times]	Time	Speed-up [times]
1	54min 41s	-	18h 36min 19s	-
4	26min 53s	2.03	7h 17min 45s	2.55
8	17min 42s	3.09	3h 45min 36s	4.95
16	15min 57s	3.43	2h 19min 31s	8.00
32	15min 35s	3.51	1h 52min 53s	9.89
64	16min 20s	3.35	1h 45min 50s	10.55

A.2 PSCAD Volley simulations with standalone projects

The way in which PSCAD suggest to perform parallel simulations a core always have to be used to control the master project, reducing the number of cores to be used in the actual simulation. Furthermore, it is necessary to stabilize a master/slave radio link data transmission, removing the truly embarrassingly parallel state, and increasing the simulation time.

To solve this problem, a straightforward logic was created in PSCAD, allowing to perform the parallel simulations in with a Standalone project. The logic created in PSCAD is presented in Fig. A.3, in which the main components are the rank number ($Rank_{\#}$ which is the core used), the run number, the total number of runs and the X-Y table component. The logic follows Eq. (A.1), that as a result gives the number of a solution ($solution_{ID}$) to be explored and extracted from the X-Y table component.

With this approach the communication between projects is eliminated, leading to a truly embarrassingly parallel solution that allows to use all available cores. An additional advantage of this approach is that each core will save the solutions in sequential files (e.g. if $maxRuns = 10$, core 1 will analyze the first 10 solutions, core 2, the next 10, and so on), so the data processing in Python is easier, because the result files can be joined without sorting.

$$solution_{ID} = (Rank_{\#} - 1)maxRuns + Run_{\#} \tag{A.1}$$

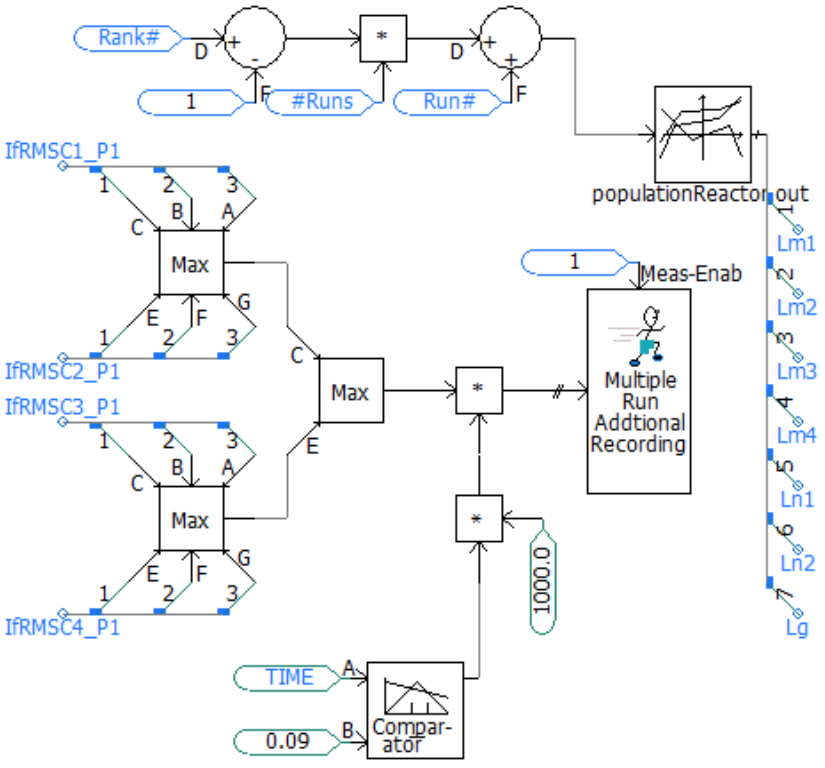

Figure A.3 – Slave project control configuration in PSCAD.

Table A.3 shows the average time consumed when simulated seven times 128 solutions of the reactor scheme option 3 proposed for the quadruple transmission line, and the reactor scheme for the single circuit transmission, with the truly embarrassingly parallel approach proposed. On the other hand, table A.4 shows the average time consumed to evolve a population of 61 solutions over 20 generations for the same previous cases, with the truly embarrassingly parallel approach proposed.

Table A.3 – Statistical simulation time for evaluating 128 solutions of the reactor scheme option 3 proposed for the quadruple transmission line, and the reactor scheme for the single circuit transmission, using a true embarrassingly parallel approach.

Cores	1 circuit Line		4 circuit Line	
	Time	Speed-up [times]	Time	Speed-up [times]
1	1min 22s ± 3.14s	-	10min 42s ± 7.26s	-
4	26.9s ± 125ms	3.05	3min 19s ± 252ms	3.23
8	15.3s ± 117ms	5.36	1min 43s ± 217ms	6.23
16	10.7s ± 253ms	7.66	1min 1s ± 1.16s	10.52
32	9.71 ± 172 ms	8.44	40.3s ± 339ms	15.93
64	11.1 ± 106ms	7.39	33s ± 246ms	19.45

Table A.4 – Simulation time for evolving 60 solutions of the reactor scheme option 3 proposed for the quadruple transmission line, and the reactor scheme for the single circuit transmission line during 20 generations, using a true embarrassingly parallel approach.

Cores	1 circuit Line		4 circuit Line	
	Time	Speed-up [times]	Time	Speed-up [times]
1	54min 41s	-	18h 36min 19s	-
4	15min 3s	3.63	5h 2s	3.72
8	11min 34s	4.73	2h 53min 58s	6.42
16	9min 44s	5.62	1h 56min 9s	9.61
32	9min 26s	5.8	1h 36min 25s	11.58
64	10min 7s	5.41	1h 11min 19s	15.62

As you can observe, the speed-up with this approach is almost 150% higher than in the previous case. This means that the communication between projects is an important pipeline in the simulation time and should be avoided.